Dissertation

submitted to the
Combined Faculties for the Natural Sciences and for Mathematics
of the Ruperto-Carola University of Heidelberg, Germany
for the degree of
Doctor of Natural Sciences

presented by

Diplom-Physicist Marc Schartmann
born in: Ulm, Germany

Oral examination: February 7th, 2007

Models of Dust and Gas Tori in Active Galactic Nuclei

Referees: **Prof. Dr. Klaus Meisenheimer**
Prof. Dr. Ralf S. Klessen

Modelle für Staub- und Gastori in Aktiven Galaktischen Kernen

Zusammenfassung Das Ziel der vorliegenden Arbeit ist die realistische Modellierung der Verteilung von Gas und Staub in den Zentralbereichen Aktiver Galaktischer Kerne. Vereinheitlichende Schemata benötigen einen Staubtorus, um zwei Beobachtungsklassen geometrisch in einem Modell zu vereinigen (Blick entlang und senkrecht zur Torusachse). Realistische Torusmodelle sind notwendig, um interferometrische Beobachtungen naher Seyfertgalaxien im nahen und mittleren Infrarotbereich (MIDI, AMBER) beschreiben zu können. In einem ersten Schritt untersuchen wir ein analytisches Torusmodell, das sogenannte *Turbulente Torus Modell*, durch Anwendung von Strahlungstransportsimulationen. Es zeigt sich gute Übereinstimmung sowohl mit der Gesamtemission von Seyfertgalaxien, als auch räumlich hochaufgelöster Beobachtungen im Nahinfrarotbereich. Probleme ergeben sich jedoch durch zu ausgeprägte Silikatemission bei Beobachtung entlang der Torusachse. Überwunden werden diese Diskrepanzen durch Modellierung drei-dimensionaler klumpiger Staubtori in einem zweiten Schritt. Dabei legen wir besonderen Wert auf die Unterschiede zwischen klumpigen und homogenen Modellen und deren Signaturen in interferometrischen Beobachtungen. In einem letzten Schritt folgen wir der zeitlichen Entwicklung eines nuklearen Sternhaufens im Rahmen von Hydrodynamiksimulationen. Durch dessen Massen- und Energieeintrag in das umgebende Medium und Gaskühlung entsteht auf natürliche Weise ein filamentartiger, klumpiger Gasstrom, der zum Minimum des effektiven Potenzials hin gerichtet ist. Dieses wird gebildet aus dem Gravitationspotenzial des Schwarzen Loches, des Sternhaufens selbst und der Rotation des Gases. Dort bildet sich eine massive, turbulente Scheibe aus. Anschließende Strahlungstransportsimulationen spiegeln spektrale Energieverteilungen von Seyfertgalaxien (Spitzer) gut wieder. Probleme, die unsere kontinuierlichen Torusmodelle mit der Beschreibung der beobachteten Relation zwischen der Stärke der Silikatcharakteristik und der H I Säulendichte haben, können mittels dieser neuartigen Modellierung ausgeräumt werden.

Models of Dust and Gas Tori in Active Galactic Nuclei

Abstract The goal of this thesis is to gain theoretical understanding of the distribution of dust and gas in the innermost parsecs of Active Galactic Nuclei. Unified Schemes demand a circum-nuclear disk or *torus* to geometrically unify two separate classes of observed objects (face-on and edge-on view onto the torus). In a multi-step approach, we work towards the establishment of realistic simulations of this massive and dense gas and dust reservoir, in order to be able to interpret near- and mid-infrared interferometric observations (MIDI, AMBER), which are able to resolve dust structures in the centres of Seyfert galaxies. In a first step, we investigate an analytical torus model (the so-called *Turbulent Torus Model*) with the help of radiative transfer calculations and find gross agreement with large aperture, as well as high-resolution observations of Seyfert galaxies. However, the model SEDs show too pronounced silicate emission features in the face-on case. This can be overcome with the help of three-dimensional clumpy tori, calculated in a second step. Special emphasis is put on the differences of clumpy and continuous dust distributions, also concerning interferometric observations. In a further step, we apply hydrodynamic simulations to trace the evolution of a nuclear star cluster, which provides energy via discrete supernova explosions and mass from stellar mass loss. With these ingredients, a highly dynamical system forms, with gas streaming inward, in form of long filaments, which cool due to radiative energy losses. In the vicinity of the minimum of the effective potential (caused by gravity of the nuclear stellar cluster and black hole, as well as rotation of the gas), a turbulent disk forms, surrounded by a less dense clumpy and filamentary toroidal structure. Subsequent radiative transfer calculations yield good agreement with Seyfert galaxy spectral energy distributions (observed with the Spitzer space telescope). Problems of the comparison of continuous models with the silicate feature strength to H I column density relation can be overcome with the help of our new approach.

Contents

Chapter 1

Introduction

In this chapter, we give a general introduction into the topic of this thesis and motivate our work. After a few words about the class of Active Galactic Nuclei with special emphasis on Seyfert galaxies, we present observational facts which lead to the current knowledge of these objects. The actual work presented in this thesis is separated into a three-step approach: In Chapter 2, we start with radiative transfer calculations of an analytical torus model, the so-called *Turbulent Torus Model*, where the density distribution results from hydrostatic equilibrium. Pressure forces due to random cloud motion are balanced by forces due to an effective potential. This potential is made up of the gravitational potential of the central black hole, the surrounding nuclear stellar cluster and the centrifugal potential due to orbital motion of the gas clouds, resulting from the rotating stellar cluster. This has the great advantage of determining the shape and the density distribution from physical principles, in contrast to radiative transfer models so far, where density and shape were set up with a purely geometrical model in order to fulfil observational constraints. In a second step (Chapter 3), we organise the dust into clumps within our tori. This is not only a more physical approach, but also suggested by recent observations. We especially focus on the comparison with continuous torus models and the possible differentiation between them with the help of the mid-infrared interferometric instrument (MIDI). Finally, in Chapter 4 of this thesis, we realise an extended version of the *Turbulent Torus Model* with three-dimensional hydrodynamic simulations. Subsequent radiative transfer calculations enable us the direct comparison with observational data.

1.1 Active Galactic Nuclei

Active galaxies are among the most energetic objects in the universe. With current knowledge, these objects – although containing up to 60 different variations (Ward 2003) – can be described by a small number of models. The differences between them are mainly ascribed to geometrical effects, which cause their aspect-dependent appearance. The most common model is called the *Unified Scheme* (Antonucci 1993) of Active Galactic Nuclei (AGN), see Fig. 1.1. According to this scheme, several components can be distinguished: A supermassive black hole (10^6 - $10^{10}\,M_\odot$) in the centre is surrounded by an accretion disk, reaching from the marginally stable orbit up to thousands of Schwarzschild radii. By turbulent processes, material is accreted and the gas in the disk is heated to several hundred thousand Kelvin. Hence, the spectrum of the emitted radiation

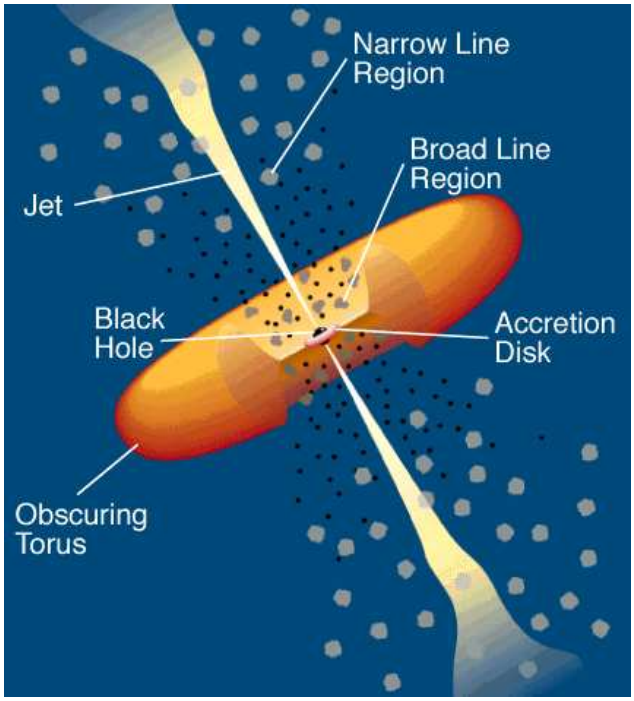

Figure 1.1: *Sketch of the Unified Scheme of Active Galactic Nuclei and its major constituents. Figure courtesy of Urry & Padovani (1995).*

peaks in the UV/optical wavelength range. In the outer part, the temperature of the disk drops to about 1000 K and merges into a larger and geometrically thicker gas reservoir. The dust embedded into this gas torus produces a characteristic bump in the IR spectral range (hereafter the *Infrared Bump*). The torus is made up of a mixture of phases: cold gas in the torus is intermixed with dust and a hot, tenuous medium. This will be described in more detail in Section 4.5.4. Additionally, hard X-ray radiation is produced within the central region. It emanates from a hot plasma above the accretion disk, often referred to as a *hot corona*. With the help of Compton upscattering events, mainly UV-optical radiation from the accretion disk is transferred in the X-ray wavelength regime. Whereas dust primarily absorbs the radiation of the accretion disk, the X-ray radiation is attenuated by the gaseous component (mainly neutral hydrogen and neutral and singly ionised helium).

The Unified Scheme distinguishes between two different types of active galaxies: The spectral energy distributions (SEDs) of type I objects show the so-called Big Blue Bump, arising from the direct radiation of the accretion disk mentioned above. Broad emission lines with full width half maximum (FWHM) of several thousand km/s overlay the continuum spectral energy distribution. They result from the so-called *Broad Line Region (BLR)* near the centre of the object, within the low-density funnel of the torus (dark grey clouds in Fig. 1.1). Within this area, streams of gas are moving at high velocities due to the deep potential well of the central black hole and emit broad spectral lines. Excitation arises from the ionising radiation of the nearby accretion disk. Type II objects show a very weak or even no Big Blue Bump. Narrow spectral lines, arising from orbiting gas streams further away from the gravitational centre (depicted as light grey blobs in Fig. 1.1) are visible in both types of galaxies. After broad spectral lines were observed in the polarised light of type II objects (Antonucci & Miller 1985), it was proposed that both AGN types belong to the same class of objects with a dust reservoir located in a torus which blocks the direct view to the centre and the *BLR* within the opening of the torus for the case of type II objects. Polarised light is then produced by electrons and tenuous dust above the open cone of the actual dust torus (depicted as

black dots in Fig. 1.1). Therefore, the type of object simply depends on the viewing angle towards the axis of the torus.

The main parameters, determining the activity of a galactic nucleus are the black hole mass M_{BH} and the accretion rate $\dot{M}$. The first is mainly characterised by the accretion history and probably by mergers in the past. The latter depends on the current supply of fuel for the accretion process. Within this process, gravitational energy of infalling matter within the deep potential well is transformed to radiation with some efficiency ϵ. Thereby, the accretion rate determines the resulting luminosity:

$$L_{\mathrm{N}} = \epsilon \, \dot{M} \, c^2 \approx 1.2 \cdot 10^{12} \, L_{\odot} \, \frac{\epsilon}{0.1} \, \frac{\dot{M}}{M_{\odot}/yr}, \tag{1.1}$$

where ϵ is the efficiency of the transformation of matter to radiation energy, which amounts to roughly 10% for an optically thick accretion disk around a nuclear black hole. Accretion is a self-regulated process in a sense that with increasing infall of matter not only the luminosity increases, but additionally the radiation pressure, which tends to push material outwards and finally stops the accretion process. This leads to a (theoretical) upper limit for the central luminosity, named after Arthur Stanley Eddington:

$$L_{\mathrm{max}} \leq L_{\mathrm{Edd}} = \frac{4 \, \pi \, G \, M_{\mathrm{BH}} \, m_{\mathrm{p}} \, c}{\sigma_{\mathrm{T}}} \approx 3.27 \cdot 10^{11} \, L_{\odot} \, \frac{M_{\mathrm{BH}}}{10^7 \, M_{\odot}}, \tag{1.2}$$

where m_{p} is the mass of the proton, experiencing gravitational attraction. σ_{T} is the Thomson cross section, characterising the interaction between electrons and photons, which gives the main contribution to the radiation pressure. The respective other combinations are negligible (gravitational attraction of electrons and radiation pressure acting on protons). As these calculations imply spherical accretion, super-Eddington accretion rates are possible, if the accretion happens within a disk, for example.

A further ingredient of the unified scheme is a so-called jet, which is a narrow collimated outflow of high energetic particles. Impinging on the inter-galactic medium, synchrotron radiation is emitted in the radio regime and the jet diameter broadens (see Fig. 1.1). Depending on the amount of radio emission in relation to the bolometric luminosity of the objects, they are classified radio-loud quasars and bright radio galaxies or radio-quiet quasars and Seyfert galaxies.

1.2 Seyfert galaxies

In this thesis, we concentrate on the nuclear regions of Seyfert galaxies. Galaxies of this class of AGN are amongst the closest to us and, therefore, a good target for interferometric observations with the MIDI instrument (see Section 1.3), capable of revealing the structure of dusty tori. These observations can then be compared to our modelling. In Seyfert galaxies, the nuclear activity is of the same order as the brightness of the stellar content (roughly $10^{11} \, L_{\odot}$). This is in contrast to quasars, where the nucleus outshines the stellar content by a factor of approximately 100. Therefore, quasars have a similar appearance as stars – hence their name *quasi-stellar radio sources*

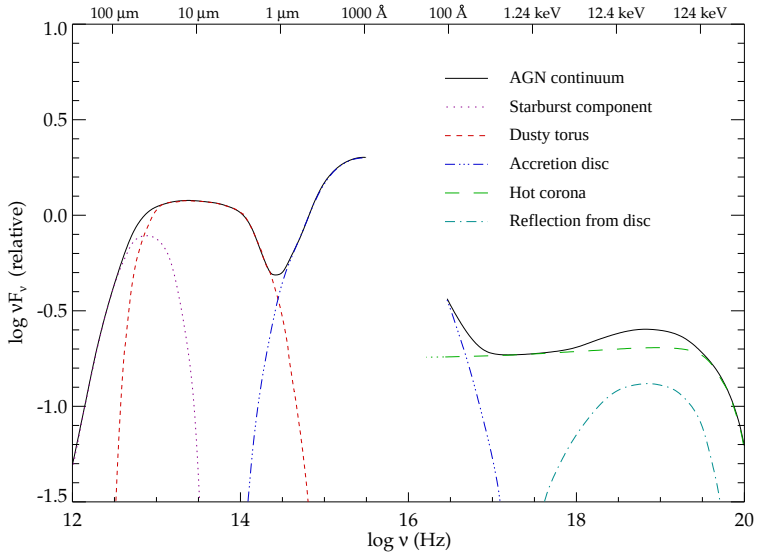

Figure 1.2: *Sketch of an AGN continuum spectrum of the nuclear region, where the stellar contribution has been subtracted. Three distinct bumps can be distinguished: the Big Blue Bump at low frequencies, the Infrared Bump and an X-ray tail. Figure courtesy of Manners (2002).*

(quasars). Furthermore, Seyfert galaxies are mostly normal spiral galaxies with enhanced central luminosity, or in other words, they are normal galaxies with tremendous fuelling rates towards their central black hole. This is the case for roughly 1% of all spirals. The first spectrum of a Seyfert galaxy – the type II source NGC 1068 – was obtained by E. A. Fath in his PhD-thesis in 1908. The class of Seyfert galaxies was formed by Carl Seyfert in 1943 by selecting galaxies with stellar-like cores and characteristic high-excitation nuclear emission lines.

The spectra of AGN span a wide range in frequency from hard X-rays to the far-infrared with almost identical power per decade of frequency. A schematic continuum spectral energy distribution is given by the black solid line in Fig. 1.2. Several distinct features are visible, starting at low frequencies up to high frequencies:

① **Infrared Bump**
It is comprised of several components. Dominant is the emission of hot and warm dust from the dusty torus (depicted by the red dashed line) and cold dust from outer galactic regions. Enhanced star formation (starburst activity) contributes only in the far-infrared regime (purple dotted line), leading to a shallower decrease of the Infrared Bump towards sub-millimeter wavelengths. At larger frequencies, the bump is limited by a minimum in the total flux at typically 1 to 1.5 µm called *near-infrared inflection*, which is due to the sublimation temperature of dust grains (Neugebauer et al. 1987).

② **Big Blue Bump**
Towards shorter wavelengths, the minimum turns over into the *Big Blue Bump* (blue dashed-triple-dotted line), arising from thermal emission of hot gas (5 000 – 100 000 K) in the accretion disk, heated by turbulent viscous processes. The gap in the bump results from missing data due to absorption of neutral hydrogen within the Galaxy. Most of the radiation of the Big Blue Bump is transferred to the infrared wavelength regime, and, thereby, powers the Infrared Bump.

③ **X-ray Tail**
Finally, X-ray emission from a hot corona above the accretion disk and reflection off the disk is shown with the green dashed line and the blue dashed-dotted line, respectively.

1.3 Observations of AGN tori

In the past - due to the enormous distances to active galaxies (the closest is Centaurus A with $d = 3.8\,\mathrm{Mpc}$, Rejkuba 2004), large aperture photometry and spectroscopy, which cover several kiloparsec, have been the only observational methods applicable in the mid-infrared.

As already mentioned above, the Unified Scheme was proposed after broad optical emission lines (a characteristic of type I AGN) have been found in spectropolarimetric observations of Seyfert II galaxies (Antonucci & Miller 1985). In Fig. 1.3 an example is given for the case of the Seyfert II galaxy NGC 1068, which shows broad Balmer lines and broad Fe II blends (a mixture of several Fe II lines) in the polarised light, both characteristics of type I AGN. This means that it harbours a Seyfert I nucleus, which is only visible in light that has most probable been scattered by free electrons and dust beyond the torus funnel and, therefore, is not affected by extinction. The same mechanism enables that the shape of the UV-optical (AGN) continuum remains a powerlaw with the same slopes as in the Seyfert I case (Kinney et al. 1991), but smaller fluxes relative to the stellar continuum. Observed through dust, the slopes would be altered by dust reddening. A torus was

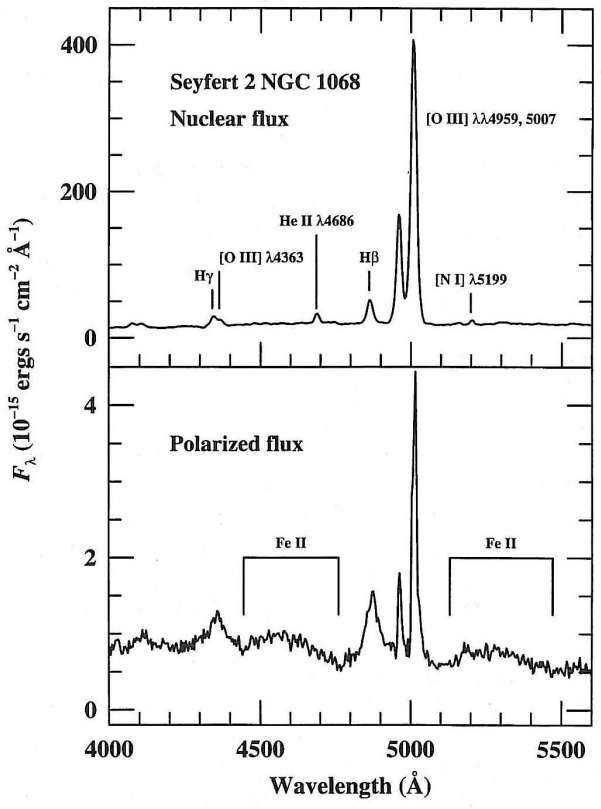

Figure 1.3: *Total flux nuclear spectrum of the Seyfert II galaxy NGC 1068 (upper panel) and its linearly polarised flux in the lower panel (Miller et al. 1991). The polarised SED is similar to the SED of a type I galaxy: broad Balmer lines (Hβ and Hγ) and characteristic Fe II blends.*

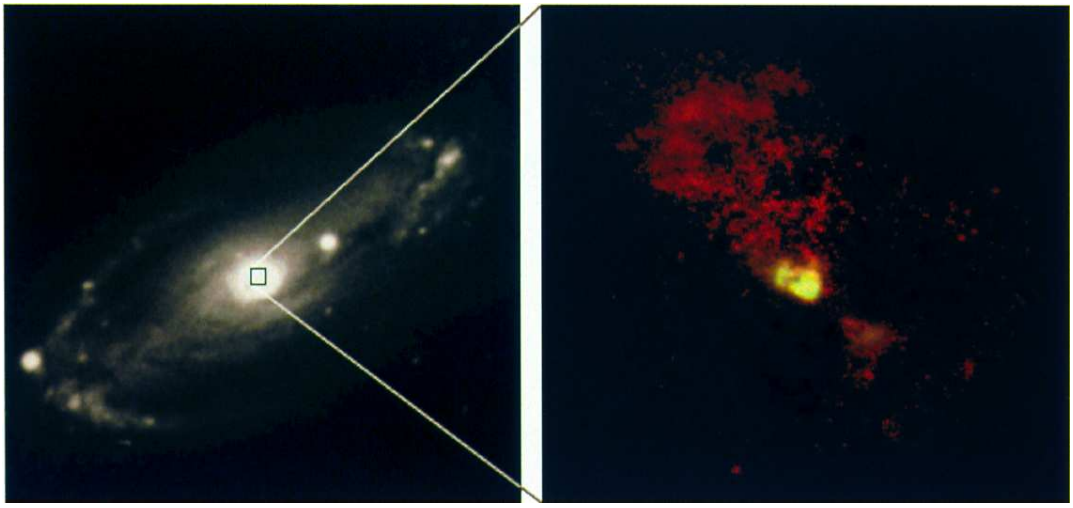

Figure 1.4: *Ground-based, optical image of the Seyfert galaxy NGC 5728 (left panel) and* [O III] *emission line image obtained with the help of the WFPC onboard the Hubble Space Telescope. Taken from the Hubble Archive, data courtesy of Wilson et al. (1993).*

assumed, as it is the most simple morphology one can think of, which is capable of explaining the observations given above.

Longwards of 10 µm, the spectral energy distributions (measured in large apertures) of both type I and type II objects are very similar, as was shown in mid- to far-infrared observations with the IRAS satellite and the Infrared Space Observatory (ISO). This provides further support for the Unified Scheme, as central AGN-heated dust structures (*tori*) seem to exist in both types.

The opening angle of the dust-free cones can be inferred from number statistics of type I and type II sources. Maiolino & Rieke (1995) find a ratio between Sy II and Sy I of 4:1 in their sample, which results in an opening angle of the dust-free cones of 74°, in concordance with many observations of ionisation cones of individual galaxies. As an example, the right panel of Fig. 1.4 shows the ionisation cones of the Seyfert galaxy NGC 5728 in form of a [O III] emission line image, which was obtained with the *Wide Field Planetary Camera* onboard the Hubble Space Telescope (Wilson et al. 1993). The most probable explanation is that gas in and above the low-density funnel of the torus is highly excited by the ionising continuum of the accretion disk. The cone-like structure is then attributed to shadowing effects of the dusty torus. The cone in north-eastern direction appears much longer compared to the cone in south-western direction. This can be explained by absorption within the galactic disk.

Indications for a clumpy nature of the circumnuclear gas distribution comes from X-ray measurements of the absorbing column density. Risaliti et al. (2002) claim that the observed variability of these measurements on timescales from months to several years can be explained by a clumpy structure of the gaseous circumnuclear material with a scale well below one parsec.

Direct support for the idea of geometrically thick tori comes from recent interferometric observations (e. g. Jaffe et al. 2004; Tristram et al. 2007; Meisenheimer et al. 2007). Pioneering work was done by Jaffe et al. (2004). With these measurements, the existence of geometrically thick dust distributions in the Seyfert II galaxy NGC 1068 could be proven and, thereby, further support for the unification principle was provided. The interferometric data reveals two different dust components: a hot component in the centre with a diameter of less than 1 pc and a temperature of

more than 800 K and warm dust within an elongated structure perpendicular to the jet axis with a temperature of approximately 320 K and a size of 3.4 pc times 2.1 pc perpendicular and parallel to the torus axis, respectively. In the meantime, detailed interferometric studies of the three brightest mid-infrared AGN, visible from the VLT, are on their way: The Circinus galaxy, which at only 4 Mpc distance is the nearest Seyfert II galaxy, thus enabling studies with $\simeq 0.1$ pc resolution (Tristram et al. 2007), and on the radio galaxy Centaurus A, which shows only faint hints of nuclear dust emission (Meisenheimer et al. 2007) and NGC 1068 (Jaffe et al. 2004; Poncelet et al. 2006). Remarkably, some of these observations show similar spatial extent and identical orientation as observations of water maser emission, which reveal parsec-sized warped disks (e. g. Greenhill et al. 2003). In addition, MIDI has succeeded in observing the first Seyfert I galaxies, which are on average more distant. Nevertheless, first indications for the existence of central, AGN-heated dust structures have been found. This new observational technique which provides spatially resolved spectral information between $\lambda = 8$ and 13 µm opens up entirely new possibilities to probe the central dust tori. Thus, state-of-the-art models need to predict not only global SEDs, but maps of the dust emission and the temperature distribution.

Furthermore, with the advent of the Spitzer Space Telescope, silicate features in emission have been detected for the first time in type I AGN (Fig. 1.5) (Siebenmorgen et al. 2005; Hao et al. 2005; Sturm et al. 2005; Weedman et al. 2005). High resolution photometric data, e. g. from NACO put further constraints on spectral energy distributions of the dust reemission of the innermost region.

1.4 Connection to galactic scales

Still a matter of debate is the link between AGN activity and starburst activity. Many NACO observations reveal starburst rings reaching into the nuclear region. E.g. in the Seyfert II galaxy Circinus, a nuclear starburst can be seen close to the centre. When comparing the typical stellar luminosities with the central AGN luminosities, one finds that they are of comparable size. As most of the detected starbursts are found to be very young in a range between 50-100 Myr, it suggests itself the conclusion that both kinds of activity happen at the same time, or one might even trigger the other. This means that in a global model of the nuclear region of AGN, starbursts have to be taken into account as well.

Within the last years it has been found that processes in the very centres of AGN are intimately linked to large scale phenomena in the galactic bulges or disks. The most prominent examples are the so-called *Magorrian* or M_{BH}-σ relation (Gebhardt et al. 2000; Ferrarese & Merritt 2000) and the M_{BH}-M_{bulge} relation (Häring & Rix 2004), showing the close connection between the mass of the central black hole and the kiloparsec sized galactic bulge. Other studies indicate that supermassive black hole growth, nuclear activity, star formation as well as global galaxy evolution cannot be treated as separate processes, but are tightly interwoven (Hopkins et al. 2006; Robertson et al. 2006), which further underlines the complexity of the problem.

For a more detailed and complete introduction into the wide field of active galaxies, we refer to Peterson (1997), Krolik (1999) and Osterbrock & Ferland (2006).

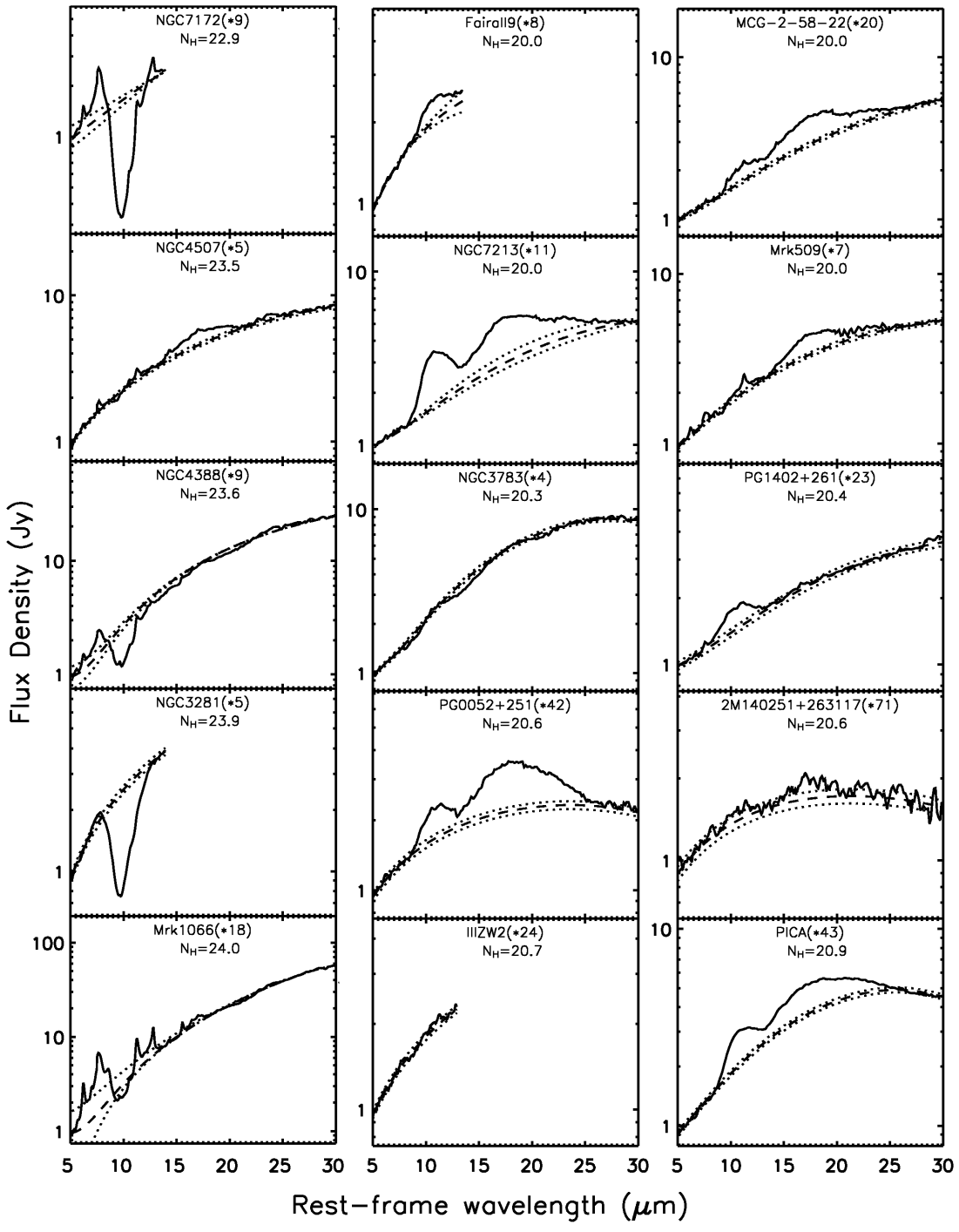

Figure 1.5: *Spitzer IRS (Infrared Spectrograph) spectra for a number of AGN, showing silicate features in emission as well as in absorption. Narrow emission lines have been removed. The dashed lines are the spline-fitted continua with uncertainties as given by the dotted lines. All spectra are normalised at* 5 μm*. The factor for this normalisation process is given in brackets behind the name. Below, the* H I *column density in units of* cm^{-2} *is given.*

Chapter 2

Radiative transfer models for continuous tori

In this chapter, we explore physically self-consistent models of dusty molecular tori in Active Galactic Nuclei (AGN) with the goal of interpreting VLTI observations and fitting high resolution mid-IR spectral energy distributions (SEDs). The input dust distribution is analytically calculated by assuming hydrostatic equilibrium between pressure forces – due to the turbulent motion of the gas clouds – and gravitational and centrifugal forces as a result of the contribution of the nuclear stellar distribution and the central black hole. For a fully three-dimensional treatment of the radiative transfer problem through the tori we employ the Monte Carlo code MC3D. We find that in homogeneous dust distributions the observed mid-infrared emission is dominated by the inner funnel of the torus, even when observing along the equatorial plane. Therefore, the stratification of the distribution of dust grains – both in terms of size and composition – cannot be neglected. In the current study we only include the effect of different sublimation radii which significantly alters the SED in comparison to models that assume an average dust grain property with a common sublimation radius, and suppresses the silicate emission feature at $9.7\,\mu$m. In this way we are able to fit the mean SED of both type I and type II AGN very well. Our fit of special objects for which high angular resolution observations ($\leq 0.3''$) are available indicates that the hottest dust in NGC 1068 reaches the sublimation temperature while the maximum dust temperature in the low-luminosity AGN Circinus falls short of 1000 K.

2.1 Introduction

The first more detailed radiative transfer simulations for the case of dusty tori were carried out by Pier & Krolik (1992). They used the most simple dust configuration to describe the observations available at that time, consisting only of spectral energy distributions – due to the large distances (several tens of Mpc) and small sizes (less than 100 pc) of these objects: a cylindrical shape with a cylindrical hole in the middle. Although pointing out that dust – in order to avoid destruction by hot gas – must be contained in clumps, they applied a homogeneous dust distribution. Characteristics of their modelling are the small sizes of a few pc in diameter and very high dust densities. The small amount of cold dust leads to a too narrow dust temperature range, resulting in spectra insufficiently extended towards longer wavelengths, compared to observations. Granato & Danese (1994) pre-

ferred larger wedges (tens to hundreds of pc in diameter) and thereby solved the problem of the too narrow IR bumps compared to observations. Further difficulties when comparing calculations with data emerge from the so-called silicate feature problem. The silicate feature is a resonance in the spectral energy distributions at 9.7 μm, arising from the stretching modes in silicate tetrahedra. For optically thin configurations, this feature is seen in emission. Looking at optically thick tori, two cases have to be distinguished: The feature appears in emission, if the temperature decreases along the line of sight away from the observer and an absorption feature is seen for the case of increasing temperature along the line of sight. Between those two cases, at an optical depth $\tau_{9.7\,\mu m} \approx 1$, a mixture of both – so-called self-absorption – is visible (Henning 1983). Therefore, for typical torus geometries, the feature is expected to arise in absorption for type II objects and in emission in type I sources. At the time of these simulations, no observation of a type I object has shown the feature in emission. Therefore, a primary goal of modelling was to get rid of the prominent silicate emission features. In both studies mentioned, a significant reduction of the silicate emission feature could be found for the case of type I galaxies. However, a lot of fine tuning of the parameters was needed. Within this discussion, Granato & Danese (1994) point out that small silicate grains are selectively destroyed by radiation pressure induced shocks in the inner part of the torus close to the central source. Therefore, they set up a depletion radius for small silicate grains and are able to reduce the silicate emission at 9.7μm. Manske et al. (1998) succeeded in avoiding the feature by using a toroidal density distribution comparable to the one of Granato & Danese (1994) with a large optical depth in combination with a strong anisotropic radiation source, which is a more physical approach to describe the accretion disk. Another more realistic way to cope with the silicate feature problem was proposed by Nenkova et al. (2002). They employed 1D radiative transfer for single clouds, in combination with a statistical method of combining these clumps to a wedge-like shaped torus. Their calculations reproduce large-aperture observations rather well and showed evidence for the reduction of the silicate feature in emission for a wide range of parameters. A distribution of the dust and gas within independent clumps not only allows dust grains to survive the inhospitable conditions close to the hard radiation of the accretion disk but also explain why the gas maintains a geometrically thick distribution rather than settling into the equatorial plane, as Krolik & Begelman (1988) point out. Another possibility to investigate AGN torus models is the simulation of polarisation maps and their comparison with observations. For a first approach see Wolf & Henning (1999).

In this chapter, we present radiative transfer calculations for a hydrostatic model of dusty tori. We use the so-called *Turbulent Torus Model*, introduced by Camenzind (1995). The great advantage of this model arises from the fact that the dust density distribution and the geometrical shape of the torus do not have to be set up arbitrarily and independent from each other, but both result from physically reasonable assumptions. Our calculations combine structure modelling and fully three-dimensional Monte Carlo radiative transfer simulations. The following section will summarise the structure modelling together with all ingredients needed to perform the radiative transfer simulations. Section 2.3 deals with the results we obtained with the first approach. Spectral energy distributions and surface brightness maps are calculated and discussed for part of the simulation series we conducted. Subsequently in Section 2.4 we discuss comparisons of our model results with large aperture data as well as with very high spatial resolution data.

2.2 The model

2.2.1 The Turbulent Torus Model

It is known that many spiral galaxies harbour young nuclear star clusters (e.g. Gallimore & Matthews 2003; Walcher et al. 2004; Böker et al. 2002, 2004). Especially during late stages of stellar evolution, stars release large amounts of gas through stellar winds and the ejection of planetary nebulae. With increasing distance from the star, dust forms from the gas phase. Due to the origin of the dust from ejection processes of single stars, we expect the dust torus to consist of a cloudy structure. As even current interferometric instruments are not able to resolve single clouds of the dust distribution, they are assumed to be small. For the sake of simplicity, we treat the torus as a continuous medium in this chapter. The dust clouds are ejected by the stars and, therefore, take over the stellar velocity dispersion σ_*. As we neglect interaction effects between these clouds, we can assume that they possess the same velocity as the stars, called the turbulent velocity v_t ($v_\mathrm{t} \approx \sigma_*$).

We are dealing with stationary models only. Therefore, the presence of continuous energy feedback by supernovae explosions as well as continuously injected mass by stellar winds is not taken into account. The dust clouds are embedded into hot gas, which leads to the destruction of dust grains by sputtering effects. Therefore, dust has a finite lifetime and it is likely that the composition differs from the one found in interstellar dust within our galaxy (see Sect. 2.2.3). The effects of magnetic fields on charged dust particles are neglected. The radiation pressure of the extreme radiation field of the central AGN exerted on the dust grains only affects the very innermost part of the dust density distribution and is, therefore, not taken into account within our simulations.

Due to their environment, the dusty clouds are subject to gravitational forces. Together with centrifugal forces – because of the rotation of the central star cluster – an effective potential can be formed. In the following, the three main components will be discussed: First, the gravitational potential of the supermassive black hole. As the torus extends to several hundred thousands of Schwarzschild radii from the centre, we can treat the black hole as a point-like source of gravitation with a Newtonian potential, given in cylindrical coordinates:

$$\phi_\mathrm{BH}(R,z) = -\frac{G\,M_\mathrm{BH}}{\sqrt{R^2+z^2}}. \tag{2.1}$$

The second contribution we take into account is the gravitational potential of the nuclear star cluster, dominating the contribution by stars in the galaxy core. From high resolution observations of the centres of galactic nuclei (e. g. Gebhardt et al. 1996) a surface brightness distribution profile can be derived. This can be well fitted by a two-component power law, the so-called Nuker law, given by the following equation (Lauer et al. 1995; Byun et al. 1996; Gebhardt et al. 1996; Faber et al. 1997a):

$$\begin{aligned} I(R,z) &= 2^{\frac{\beta-\delta}{\alpha}}\, I_\mathrm{c} \left(\frac{R_\mathrm{c}}{\sqrt{R^2+z^2}}\right)^{\delta} \\ &\quad \left[1+\left(\frac{\sqrt{R^2+z^2}}{R_\mathrm{c}}\right)^{\alpha}\right]^{\frac{\delta-\beta}{\alpha}}, \end{aligned} \tag{2.2}$$

where R_c is the core radius (or break radius), β the slope of the surface brightness distribution outside R_c, δ the slope inside R_c, α characterises the width of the transition region and I_c is the surface brightness at the location of R_c.

When assuming a constant mass-to-light ratio, this distribution mirrors the projected mass density distribution directly. By applying a least-square fitting procedure, one can obtain the 3D density profile, for which an analytical expression can be given. This is the so-called Zhao density profile family (Zhao 1997):

$$\rho_*(R,z) = \frac{M_*}{4\,\pi\,R_\mathrm{c}^3}\,\frac{C\left(\tilde{\alpha},\tilde{\beta},\tilde{\delta}\right)}{\left(R^2+z^2\right)^{\frac{\tilde{\delta}}{2}}\,\left(1+\left(R^2+z^2\right)^{\frac{\tilde{\alpha}}{2}}\right)^{\frac{\tilde{\beta}-\tilde{\delta}}{\tilde{\alpha}}}}, \tag{2.3}$$

where the parameters $\tilde{\alpha}$, $\tilde{\beta}$ and $\tilde{\gamma}$ are complicated functions of the parameters α, β and γ of the Nuker law. The quantity C is a constant, depending on these parameters.

By solving the Poisson equation, the gravitational potential of the nuclear star cluster can be obtained. Throughout this chapter, all simulations use the special case of the Hernquist profile (Hernquist 1990). According to observed profiles of cores of spiral galaxies, the exponent of the density distribution within the core radius is close to 1 in most cases (corresponding to the Hernquist profile). Recent simulations of dark matter halos by Williams et al. (2004) – which belong to the same family of stellar systems – also give an upper limit for the exponent of the density distribution within the core radius between 1.5 and 1.7 in the inner part.
With the parameters $\tilde{\alpha}=1$, $\tilde{\beta}=4$ and $\tilde{\delta}=1$, we finally get the needed gravitational potential:

$$\phi_\mathrm{Hernquist}(R,z) = -\frac{G\,M_*}{\sqrt{R^2+z^2}+R_\mathrm{c}}. \tag{2.4}$$

The third part of the effective potential is the centrifugal potential. Apart from the turbulent velocity, the stars – and therefore the dust clouds – possess an additional velocity component from the rotational motion around the gravitational centre. Due to the lack of observational data, we adopt the following distribution of specific angular momentum for such a stellar system:

$$j_\mathrm{spec} = \sqrt{G\left(M_\mathrm{BH}+M_*(R_\mathrm{T})\right)R_\mathrm{T}}\left(\frac{R}{R_\mathrm{T}}\right)^{\gamma}. \tag{2.5}$$

Here, R_T is the torus radius, defined as the location, where the effective potential reaches its minimal value. This corresponds to an equilibrium of centrifugal and gravitational forces in our solution, where the angular momentum attains the Keplerian value. Therefore, a distribution of the specific angular momentum is needed, which fixes the value at the location of the torus radius to the Keplerian value. We used a less steep decline of the specific angular momentum beyond the torus radius than for the Keplerian case, which is in agreement with expectations for elliptical star clusters. Such toroidal gas distributions are expected to be unstable on time scales larger than the dynamical time at the torus radius. The torus is however steadily refilled so that a quasi-stationary configuration results.

By integrating over the centrifugal force – under the assumption of constant angular velocity on cylinders – we obtain the centrifugal potential:

$$\phi_\mathrm{CF}(R,z) = \frac{G\left(M_\mathrm{BH}+M_*(R_\mathrm{T})\right)}{2\,R_\mathrm{T}\,(1-\gamma)}\left(\frac{R}{R_\mathrm{T}}\right)^{2(\gamma-1)}. \tag{2.6}$$

The effective potential and its three single components are shown in Fig. 2.1 for the case of our standard model (described in Sect. 2.2.2) in the equatorial plane. As can be seen, the effective potential (given by the solid line) in the outer part of the torus is dominated by the potential of the

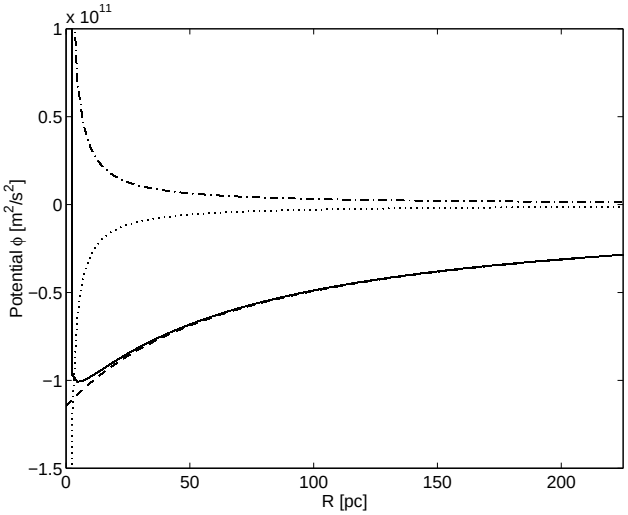

Figure 2.1: *Comparison of the contributions of the three components of the effective potential for the parameters of our standard model in the equatorial plane. The solid line corresponds to the effective potential, the dotted line to the BH-potential, the dashed line to the potential of the nuclear star cluster and the dashed-dotted line to the centrifugal potential.*

nuclear star cluster (dashed line). Moving closer to the centre, the black hole potential (dotted line) would lead to a further bending down of the potential, but the centrifugal potential (dashed-dotted line) dominates. The latter is the only repulsive term and leads to a centrifugal barrier close to the centre, preventing the models to be gravitationally unstable.

The force given by the effective potential has to be balanced by the turbulent pressure in hydrostatic equilibrium. This pressure results from the turbulent motion of the dust clouds and can be expressed by the following (isothermal) equation of state:

$$P(\rho_\mathrm{d}) = \rho_\mathrm{d}\, v_\mathrm{t}^2. \tag{2.7}$$

After inserting this into the equation for the hydrostatic equilibrium and solving the differential equation under the assumption that v_t is constant, we obtain the dust density distribution:

$$\rho_\mathrm{d} = \rho_\mathrm{d}^0 \exp\left[\frac{G\,M_*}{v_\mathrm{t}^2\,R_\mathrm{c}}\left\{\frac{M_\mathrm{BH}/M_*}{\sqrt{\frac{R^2+z^2}{R_\mathrm{c}^2}}} + \frac{1}{1+\sqrt{\frac{R^2+z^2}{R_\mathrm{c}^2}}} - \frac{R_\mathrm{c}\,(M_\mathrm{BH}+M_*(R_\mathrm{T}))}{2\,M_*\,R_\mathrm{T}(1-\gamma)}\left(\frac{R}{R_\mathrm{T}}\right)^{2(\gamma-1)}\right\}\right]. \tag{2.8}$$

Here, ρ_d^0 is a measure for the total dust mass. From this equation, some basic features of the model can be derived: First of all, equipotential surfaces have the same shape as surfaces of constant density, so-called isopynic surfaces. The shape of these surfaces only depends on the reduced parameter M_BH/M_* and the reduced coordinates R/R_c, R/R_T and z/R_c and the exponent of the angular momentum distribution γ. As mentioned above, the torus radius is connected with the minimum of the potential, the maximum of the density and the maximum of pressure and lies within the equatorial plane, due to symmetry considerations.

2.2.2 Parameters of the model

The introduced standard model will be used to represent the core of a typical Seyfert galaxy. Therefore, we calculated the mean black hole mass and mean luminosity of a large sample of Seyfert galaxies, given in Woo & Urry (2002). We find mean values of $\langle M_{\rm BH}\rangle = 6.6 \cdot 10^7\, M_\odot$ and $\langle L_{\rm disk}\rangle = 1.2 \cdot 10^{11}\, L_\odot$. After calculating a set of simulations with different dust density distributions, leading to different density contrasts between the maximum density and the outer part of the distribution, we found that a relatively shallow density distribution is needed in order to obtain SEDs extending to wavelengths longer than 10-20 µm. To achieve this, a relatively steep radial distribution of specific angular momentum is required ($\gamma = 0.5$ leads to the steepest – but still stable – distribution). But this gives only a fairly small effect. It is more efficient to increase the core radius, which leads to a broadening of the density distribution, due to the flattening of the potential of the star cluster in the outer part of the torus. A change of the total mass of the stars mainly scales the potential of the stellar cluster and, therefore, finally the density distribution. By taking this into account, we chose the core radius for our mean model to be 75 pc with a mass of the nuclear star cluster of $2 \cdot 10^9\, M_\odot$.

To constrain the other parameters, one can use the fact that not all of them are independent from each other. Comparable to the fundamental plane of global galaxy parameters, the cores of ellipticals and bulges of spiral galaxies span the so-called core fundamental plane, relating the parameters core radius R_c, the central surface brightness μ_0 and the central velocity dispersion σ_* (Kormendy 1987; Faber et al. 1997b). These studies give several relations between relevant parameters. The relation between the core radius and the central velocity dispersion of the stars is interesting for us:

$$\sigma_* \approx 201 \left(\frac{R_{\rm c}}{75\,{\rm pc}}\right)^{0.18} \frac{\rm km}{\rm s}. \tag{2.9}$$

As already mentioned above, the dusty clouds are produced by the stars and take over their velocity dispersion. Therefore, we choose the turbulent velocity of the clouds $v_{\rm t}$ to be equal to the velocity dispersion of the stars in the central region of the galaxy. According to equation (2.9) the value $v_{\rm t} = 201\,{\rm km\,s^{-1}}$ is obtained. Interactions between the different phases (dust, molecular and hot gas) within the torus and between other dust clouds, which may alter their velocity distribution are not taken into account at present. The outer radius of the torus is chosen to be three times the core radius of the nuclear star cluster, where the density distribution has already reached an approximately constant value. An upper limit for the total mass of the nuclear star cluster is determined by the Jeans equation, which relates structural with dynamical parameters for an isothermal model of the

Parameter	Value	Parameter	Value
$M_{\rm BH}$	$6.64 \cdot 10^7\, M_\odot$	$M_{\rm dust}$	$5.79 \cdot 10^5\, M_\odot$
$R_{\rm c}$	75 pc	$\tau_{9.7\,\mu{\rm m}}$	2.0
M_*	$2.0 \cdot 10^9\, M_\odot$	$R_{\rm out}$	225 pc
$L_{\rm disk}$	$1.23 \cdot 10^{11}\, L_\odot$	$v_{\rm t}$	$201\,{\rm km\,s^{-1}}$
$L_{\rm disk}/L_{\rm Edd}$	6%	γ	0.5
$R_{\rm T}$	5 pc	d	45 Mpc

Table 2.1: *Parameters used for the simulation of our mean Seyfert model.*

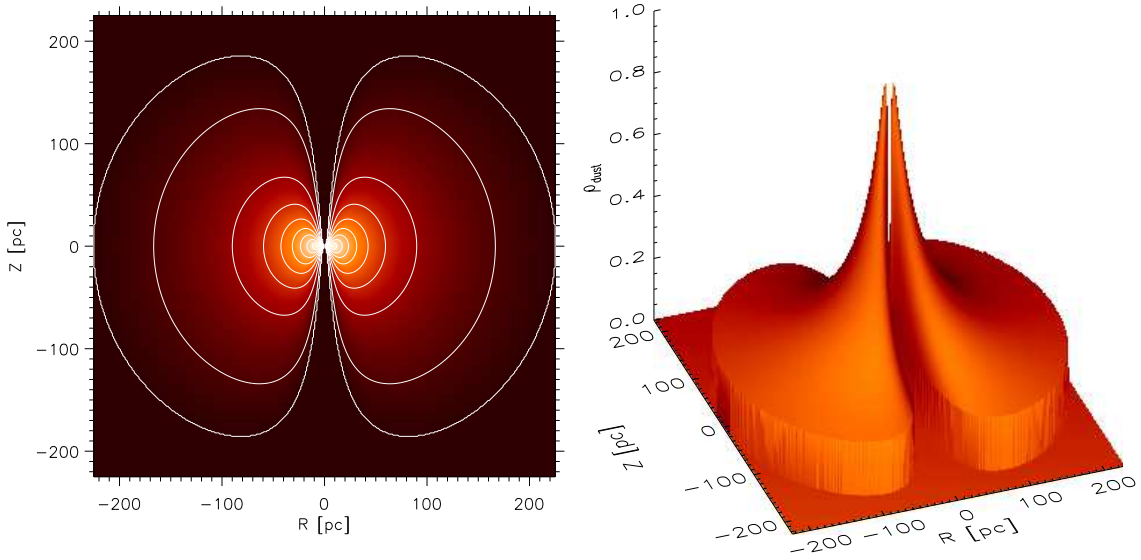

Figure 2.2: *Visualisation of our standard model:* **a)** *Isopynic line plot (logarithmically equidistant) in a meridional plane of the torus.* **b)** *Relative dust density distribution in a meridional plane.*

central stellar distribution under the assumption of a constant velocity dispersion. The remaining two parameters R_T and γ are chosen such that the dust density distribution remains flat enough to obtain IR bumps, which are broad enough to compare with data and to obtain a torus model with an inner radius small enough to allow the majority of the grain species to reach their sublimation temperatures. Finally, the mass of the dust, enclosed into the torus, is determined by the depth of the silicate feature at 9.7 µm. We chose $M_{\rm dust} = 5.79 \cdot 10^5\ M_\odot$ (corresponding to an optical depth of $\tau_{9.7\,\mu{\rm m}} = 2.0$), which yields depths comparable to observed spectra.

The parameters we assumed for our standard model are summarised in Table 2.1 and the resulting model is shown in Fig. 2.2. As can be seen, the torus has a relatively dense core and the density distribution gets shallow in the outer part. The maximum is reached in the equatorial plane (due to symmetry considerations) at the torus radius R_T and the models possess a more or less pronounced cusp at the inner end of the torus. The dust-free cone with quite steep walls will be called funnel in the following. The turbulent velocity always tends to increase the height of the torus, while the angular momentum tends to flatten it.

2.2.3 Dust properties

Although the very extreme physical conditions near the central source make it likely that the dust composition may be altered compared to interstellar dust in our own galaxy, we assume – for the sake of simplicity and comparability – a typical dust extinction curve of interstellar dust. We use the model of Mathis et al. (1977) which fits well the observed extinction curve of the interstellar medium.

They found a number density distribution (MRN-distribution hereafter), which is proportional to the grain radius to the power of - 3.5 and a range of grain radii between 0.005 µm and 0.25 µm. We use 15 different grains[1], containing a mixture of 5 silicate and 10 graphite grains – each species

[1]The number of dust grains increases the computational time for simulating the temperature distribution, therefore

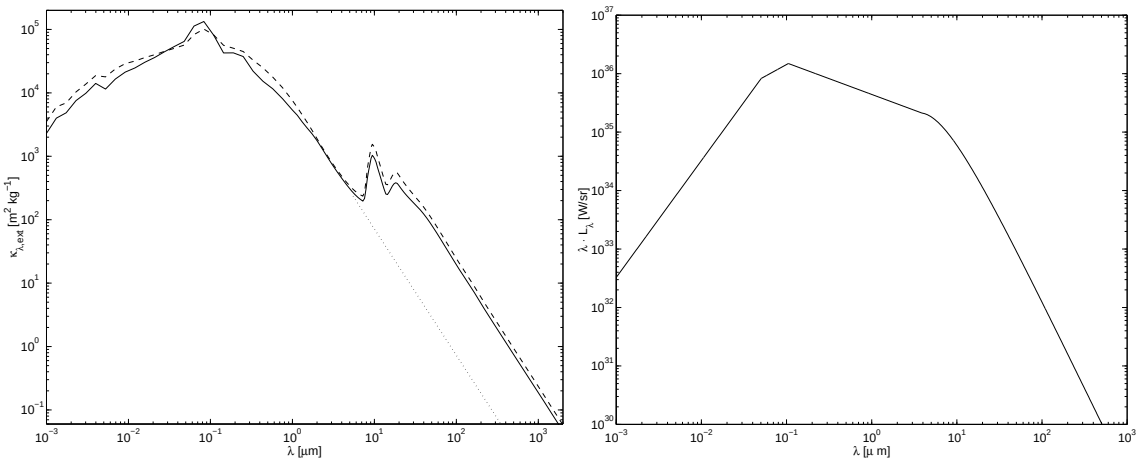

Figure 2.3: *Input parameters of our simulations:* **a)** *Course of the mass extinction coefficient plotted against the wavelength for the averaged dust model (dashed line) and single grains (solid line): composition of silicate and graphite grains with varying grain radii (for details see text). The dotted straight line is meant to clarify the offset in the continuum extinction curve.* **b)** *SED of the central accretion disk, used as the primary energy source.*

with different grain radii according to the MRN grain size distribution – and a mass fraction of 62.5% silicate and 37.5% graphite. Because of the anisotropic behaviour of graphite, two different sets of optical constants are necessary: one where the electric field vector oscillates parallel to the crystal axis of the grain (5 grains) and another one, where it oscillates perpendicular to it (5 grains). For them, the standard $\frac{1}{3} - \frac{2}{3}$ approximation is used, which is valid exactly in the Rayleigh limit and reproduces extinction curves reasonably well, as shown by Draine & Malhotra (1993). Optical data (refraction indices) are taken from Draine & Lee (1984), Laor & Draine (1993) and Weingartner & Draine (2001) and the scattering matrix elements and coefficients are calculated under the assumption of spherical grains using the routines of Bohren & Huffman (1983) within the radiative transfer code MC3D, which will be discussed in Sect. 2.2.6.

In addition, a comparison was made between a split into 15 different grains and the usage of only one grain, but with weighted mean values for the extinction, absorption and scattering cross sections and the Stokes parameters, which describe the intensity and the polarisation state of the photon package. The weights result from the abundance and the size distribution of the respective material (for details about the averaging see Wolf 2003a). The resulting extinction curves of these two cases are shown in Fig. 2.3a, where the solid line corresponds to the split model and the dashed line to the model with mean characteristics. For every dust species (type of material and grain size) the temperature distribution is determined separately. In Fig. 2.3a one can clearly see the two silicate features at 9.7 µm and 18.5 µm. The extinction curves drop down quite steeply at longer wavelengths and an offset can be recognised around the wavelengths of the two features between the continuum spectra shortward of 10 µm and longward of 20 µm, emphasised by the dotted line fragment.

we tried to minimise the number of grains. Simulations, where we doubled the number of grains showed no significant differences in the spectral energy distributions.

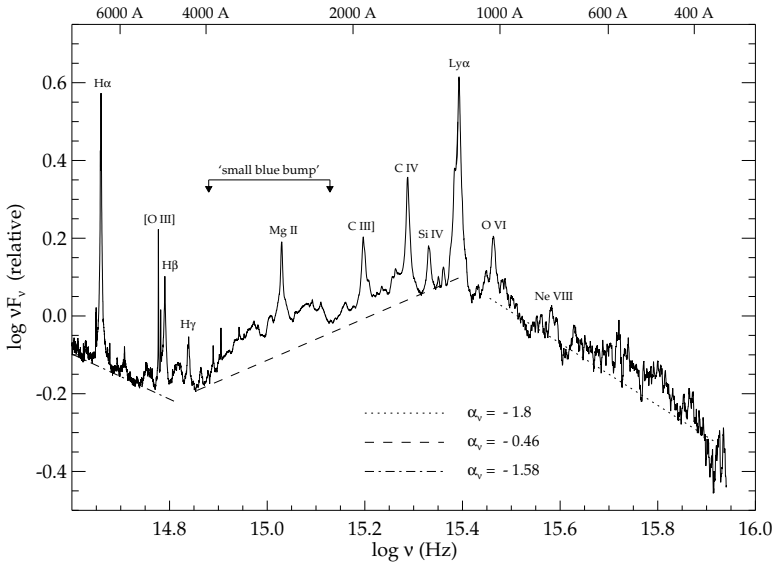

Figure 2.4: *Mean quasar SED: composed of data from the Sloan Digital Sky Survey (SDSS, Vanden Berk et al. 2001) for frequencies below the Lyman α line and from HST/FOS observations of radio-quiet quasars at frequencies larger than Lyman α (Zheng et al. 1997). Figure courtesy of Manners (2002).*

2.2.4 Primary source

In our modelling, the dust in the torus is solely heated by an accretion disk in the centre of the model space. In most of the simulations we use a point-like, isotropically radiating source with a luminosity of $1.2 \cdot 10^{11}\, L_\odot$ in our standard model, which corresponds to roughly 6% of the Eddington luminosity. The spectral energy distribution (SED) is composed of different power laws and a Planck curve as follows. In the ultraviolet to optical wavelength regime, we use the composite mean quasar spectrum from Manners (2002), see Fig. 2.4. For wavelengths longer than Lyman alpha, it includes data from 2200 quasars of the Sloan Digital Sky Survey (Vanden Berk et al. 2001), which results in a power law with a spectral index of $\alpha_\nu = -0.46$ [2]. Shortwards of Lyman alpha, data from radio-quiet quasars (Zheng et al. 1997), taken with the HST Faint Object Spectrograph, is used. The data leads to a spectral index of $\alpha_\nu = -1.8$. For wavelengths longer than 10 μm, we use a decline of the spectrum according to the Rayleigh-Jeans branch of a Planck curve with an effective temperature of 1000 K, reflecting the smallest temperatures expected from the thermal emission of the accretion disk. At shorter wavelengths, the spectrum decays with a spectral index of $\alpha_\nu = -3$. Due to the lack of observational data in this wavelength range, the index is chosen in agreement with theoretical modelling of accretion disk spectra performed by Hubeny et al. (2000). Taking this shape and normalising to the chosen bolometric luminosity of the accretion disk yields the input spectrum shown in Fig. 2.3b.

2.2.5 Radiative transfer equation

The underlying equation for this kind of modelling is the radiative transfer equation. It can be derived from the phase space distribution function of photons with the help of the Boltzmann equation.

[2] α_ν is defined as $F_\nu \propto \nu^{\alpha_\nu}$

The following form results:

$$\begin{aligned}\frac{1}{c}\frac{\partial I_\nu(\vec{x},\vec{n})}{\partial t} + \vec{n}\cdot\vec{\nabla}I_\nu(\vec{x},\vec{n}) &= \frac{1}{4\pi}\rho_d(\vec{x})\, j_\nu(\vec{x},T) \\ &\quad - \rho_d(\vec{x})\,\{\kappa_{\nu,\mathrm{abs}}(T) + \kappa_{\nu,\mathrm{sca}}(T)\}\, I_\nu(\vec{x},\vec{n}) \\ &\quad + \rho_d(\vec{x}) \int\limits_{4\pi} d\Omega'\, \Phi(\vec{n},\vec{n}')\,\kappa_{\nu,\mathrm{sca}}(T)\, I_\nu(\vec{x},\vec{n}')\end{aligned} \tag{2.10}$$

The time dependence is not shown explicitly for clarity reasons. $I_\nu(\vec{x},\vec{n})$ is the monochromatic, specific, total intensity at the spatial coordinate $\vec{x}$ in direction $\vec{n}$. $\kappa_{\nu,\mathrm{abs}}(T)$ and $\kappa_{\nu,\mathrm{sca}}(T)$ are the mass absorption and mass scattering coefficients. $j_\nu(\vec{x},T)$ is the specific emissivity of the dust. $\rho_d(\vec{x})$ is the dust mass density at the spatial point $\vec{x}$. $\Phi(\vec{n},\vec{n}')$ denotes the normalised probability that a photon from direction $\vec{n}'$ is scattered in direction $\vec{n}$.

$$\int \Phi(\vec{n},\vec{n}')\, d\Omega' = 1, \tag{2.11}$$

where $d\Omega'$ is the solid angle element.

A temporal or spatial change of the specific intensity (left hand side of equation 2.10) has to be balanced by source and sink terms (right hand side of equation 2.10). In the form of source terms, we have the emission of dust at the location $\vec{x}$ (first term) as well as radiation, which is scattered from any direction $\vec{n}'$ into direction $\vec{n}$ (third row in equation 2.10). As sink terms (and, therefore with negative sign) appear the absorption at the location $\vec{x}$ (first term, second row in equation 2.10) and the intensity, which is scattered out of the line of sight (second row, second term).

The radiative transfer equation is a seven dimensional partial integro-differential equation with the variables: three spatial coordinates $\vec{x}$, two angles θ and φ, the frequency ν and time t.

As the light travel times within the torus volume are small compared to the evolutionary time of the torus, we assume stationarity. With $\frac{\partial}{\partial t} = 0$, the first term vanishes and for a fixed point in space, the equation of local energy equilibrium has to be fulfilled:

$$\int\limits_{4\pi} d\Omega' \int\limits_0^\infty d\nu\, \kappa_{\nu,\mathrm{abs}}(T(\vec{x}))\, I_\nu(\vec{x},\vec{n}') = \int\limits_0^\infty d\nu\, j_\nu(\vec{x}) \tag{2.12}$$

This means that all absorbed energy has to be re-emitted. It is the zeroth moment of the radiative transfer equation and, therefore, results from integration of equation 2.10 over all solid angles. All contributions from scattering cancel out each other due to the normalisation condition (equation 2.11). This means that scattering does not contribute to the heating of dust grains. A further simplification is the assumption of local thermodynamic equilibrium. Then, the Kirchhoff law is

valid and the emissivity can be described in terms of the mass absorption coefficient and the Planck function:

$$j_\nu(\vec{x}) = 4\,\pi\,\kappa_{\nu,\mathrm{abs}}(T(\vec{x}))\,B_\nu(T(\vec{x})) \tag{2.13}$$

where

$$B_\nu(T(\vec{x})) = \frac{2\,h\,\nu^3}{c^2}\,\frac{1}{e^{\frac{h\nu}{k_\mathrm{B}T}} - 1} \tag{2.14}$$

is the Planck function. Inserted into equation 2.12, the dust temperature distribution can be determined. Finally, neglecting the temperature dependence of the dust coefficients, only the right hand side of the equation depends on the temperature, which is a numerical simplification. This is a good approximation within the wavelength and grain size range we are interested in.

2.2.6 The radiative transfer code MC3D

MC3D is a three-dimensional continuum radiative transfer code based on the Monte Carlo approach (Wolf et al. 1999). It is able to manage arbitrary three-dimensional dust and electron configurations and different primary sources of radiation. Diverse shapes and species of dust grains can be implemented as well. Working in the particle picture, the bolometric luminosity of the central source is divided into photon packages, so-called weighted photons. They are fully described by their wavelength λ and their Stokes vector, describing the intensity and the polarisation state of the particle. According to a provided radiation characteristic and spectral energy distribution of the source, such a weighted photon is emitted. Within the dust or electron configuration, absorption and scattering take place, where Thomson scattering, Rayleigh and Mie scattering is applied to the weighted photon. In a last step, these photons are detected after leaving the convex model space. According to this procedure, temperature distributions as well as – in a second step – spectral energy distributions and surface brightness distributions can be calculated. Temperature distributions have to be calculated using real radiative transfer. In order to minimise CPU time and get smoother surface brightness distributions, a raytracer (also inherent in MC3D) can be used to obtain SEDs and maps.

Details about MC3D and the built-in features can be found in Wolf et al. (1999), Wolf & Henning (2000), Wolf (2001) and Wolf (2003b).

Pascucci et al. (2004) tested MC3D for 2D structures against various other continuum radiative transfer codes, where they found good agreement. We also performed a direct comparison for the special case of AGN dust tori with the simulations of Granato & Danese (1994), one of the standard torus models to compare to, calculated with their grid based code. The results are displayed in Fig. 2.5, where the solid line corresponds to the calculation with MC3D and the dashed line to the original SED of Granato. The underlying model is a wedge geometry with dust of constant density. The ratio between outer and inner radius is set to 100 with a half opening angle of the dust-free cone of 40 ° and an optical depth of 0.3 at 9.7 µm (for details of the model setup see Granato & Danese 1994). The original spectrum of Granato's code is taken from the library of SEDs described in Galliano et al. (2003).

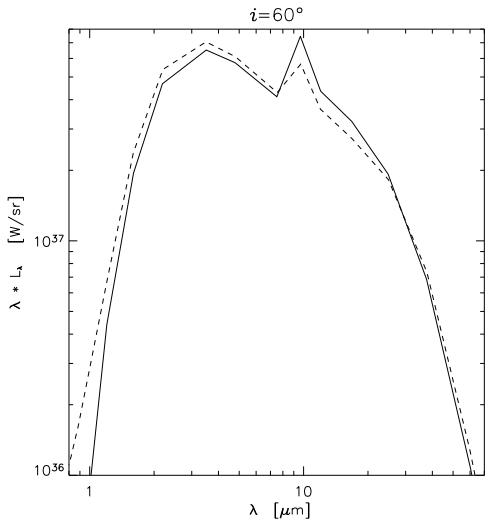

Figure 2.5: *Comparison of MC3D (solid line) with the code of Granato & Danese (1994) (dashed line).*

As can be seen in Fig. 2.5, good agreement between the two codes is found with deviations smaller than 30% within the relevant wavelength range. The reason for the remaining differences between the two SEDs is due to the fact that only standard calibrations of the code-parameters were used and no fine tuning was performed. Minor differences of the model setup are responsible for the remaining discrepancies among the SEDs.

2.3 Results and discussion

First, the use of single dust grains is motivated, before we introduce our model by presenting temperature distributions and an inclination angle study. After that, several parameters of our standard model have been varied and the resulting effects will be discussed.

If not noted otherwise, all of the SEDs shown are pure dust re-emission spectra. The direct radiation from the central source is always omitted, as we are only interested in the mid-infrared wavelength range, where the torus emission dominates the SED. Optical depths are given for lines of sight within the equatorial plane from the centre outwards.

2.3.1 Averaged dust mixture versus single grains

Detailed Monte Carlo simulations are always very time consuming. In order to reduce the CPU time, an averaged dust grain mixture (Wolf 2003a) is often considered instead of a real mixture of single grains. However, temperature distributions have to be computed for every single grain. Therefore, computation time strongly scales with the number of dust grains considered. As Wolf (2003a) showed for the case of protoplanetary disks and we also confirmed for AGN tori, an averaged dust model works perfectly well, if the inner radius of the disk/torus is larger than the sublimation radii of the grains (see discussion later). But for most of our models, this is not the case, as the inner radii of the tori are often determined by sublimation themselves. These sublimation radii follow an approximative formula for the local thermodynamic equilibrium. It only takes emission of the central source and extinction by dust species with smaller inner radii into account. Although the resulting maximal temperatures for the single grains differ by up to 10%

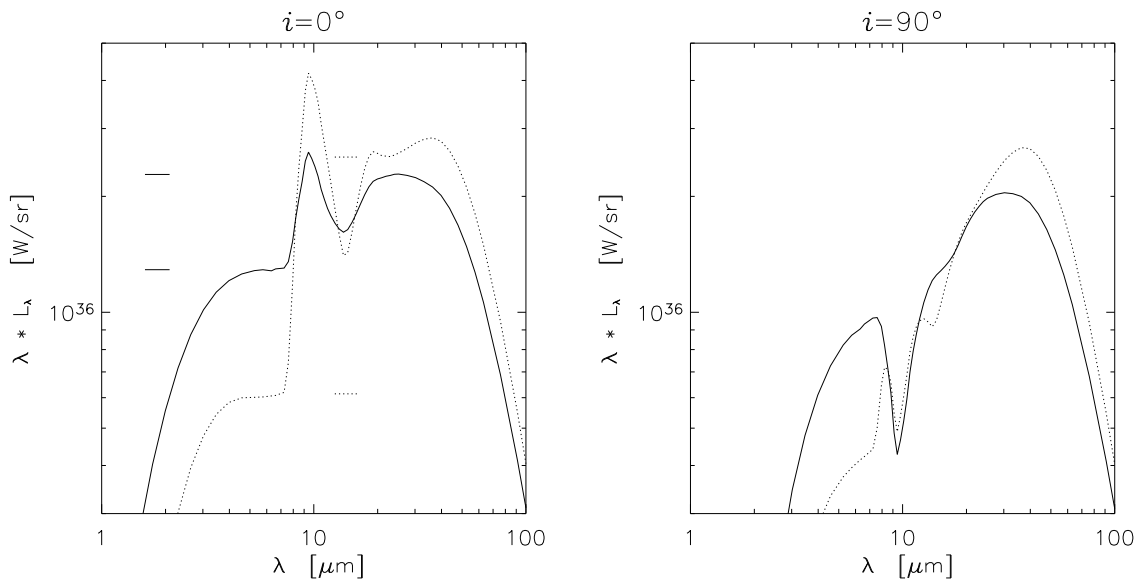

Figure 2.6: *SEDs at inclination angles of 0° and 90° for the case of averaged dust properties (dotted line) and dust split in grains of different species and sizes (solid line). The horizontal line segments in the left panel indicate the offset of the continuum SEDs of the individual curves.*

relative to the assumed sublimation temperatures of silicate and graphite grains, this seems to be an adequate procedure, as sublimation temperatures are not very well known. With this new dust model, the situation looks much different, as shown in Fig. 2.6, although the overall shape of the extinction curve looks similar compared to the one of the averaged grain model (see Fig. 2.3a). The typical shape of the resulting SEDs will be described in more detail in Sect. 2.3.3. In the following, we address just the major differences between these two cases. The solid line corresponds to our standard model (see Fig. 2.6) with a dust mixture containing 15 different grains (3 different grain species – silicate and two orientations of graphite grains – with 5 varying grain radii each), while the dotted line is calculated for the same torus parameters, but the dust model is given by a single grain type with averaged properties concerning chemical composition and grain size. Using the averaged grain model, the silicate features are much more pronounced compared to the other case. The same happens with the offset in the SED shortwards of the 9.7 μm feature. The reason for this is the varying sublimation temperatures of the different dust species. Silicate grains sublimate at about 1000 K, while graphite grains sublimate at around 1500 K. Smaller particles are heated more efficiently than larger grains. Therefore, smaller grains reach the sublimation temperature earlier and the inner radius of their density distribution must be larger than the one for the distribution of large grains. This effect leads to a layering of grain species and sizes, where silicate grains are further out (in the radial direction) than graphite grains and the distribution of smaller grains is shifted outwards compared to the distribution of larger grains. Neglecting this layering and using averaged properties within one grain leads to the effects shown in Fig. 2.6. The reason for these effects is that some of the dust species, represented by the grain, are heated to temperatures higher than their sublimation temperatures. This is an unphysically treatment of these components. Especially affected are the smallest silicate grains, which are the most abundant ones in our dust model. The effects are mainly more explicitly visible characteristics of the dust extinction curve properties of silicate grains – especially the offset in the continuum spectrum near the feature (demonstrated by the horizontal lines in Fig. 2.6) and the strength of the feature itself. Reaching only the permitted smaller temperatures, these effects are partially balanced by the contribution of the other grain

types. Using the minimum of sublimation temperatures of the mean grain components leads to a Wien branch shifted to longer wavelengths.

Being mainly interested in the mid-infrared wavelength range, we decided to split the dust model in single grains for all of the models shown in this chapter. All species obey the same density distribution, according to physical reasoning (see Sect. 2.2.1) and the mass fraction of the individual species, derived from the power law number density distribution.

The inner radius of the distribution of every dust species is calculated using the formula for the local energy equilibrium and taking extinction by all other dust species into account. Spheres with these radii around the central source are left vacant concerning these particular dust species. The rest of the calculated equipotential surfaces are filled with dust, according to the dust model used.

2.3.2 Temperature distribution

Fig. 2.7 shows the temperature distribution of our standard Seyfert model for the smallest silicate grain component, which is also the most abundant one (see Sect. 2.2.3). In the left panel, radial temperature distributions for an equatorial line of sight (solid line), an inclination angle of $i = 30\,^\circ$ (dotted line) and $i = 20\,^\circ$ (dashed line) are plotted. With increasing inclination angle, the intersection of the respective line of sight with the torus moves to larger distances from the central source (compare to Fig. 2.9b). Therefore, the maxima of the temperature distributions move further out and the maximum temperature decreases as well. The smaller the inclination, the smaller the dust density at the point of the intersection of the line of sight with the torus. This causes shallower temperature distributions with decreasing inclination.

The right panel of Fig. 2.7 shows various cuts in θ-direction through the temperature distribution at radial distances from the centre of 2 pc, 5 pc and 20 pc. A minimum curve is expected because

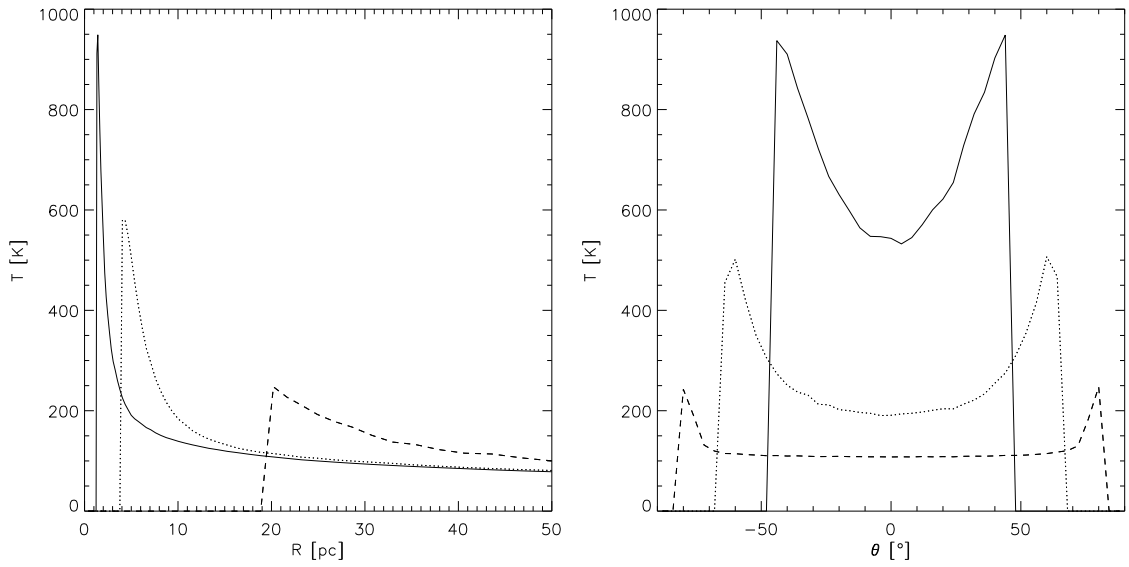

Figure 2.7: *Temperature distributions of the smallest silicate grain component:* **a)** *Radial temperature distributions. The solid line corresponds to an equatorial line of sight, the dotted line to an inclination angle of $i = 30\,^\circ$ and the dashed line to $i = 20\,^\circ$.* **b)** *Temperature distributions in θ-direction. The solid line corresponds to a radial distance to the centre of 2 pc, the dotted line to 5 pc and the dashed line to 20 pc.*

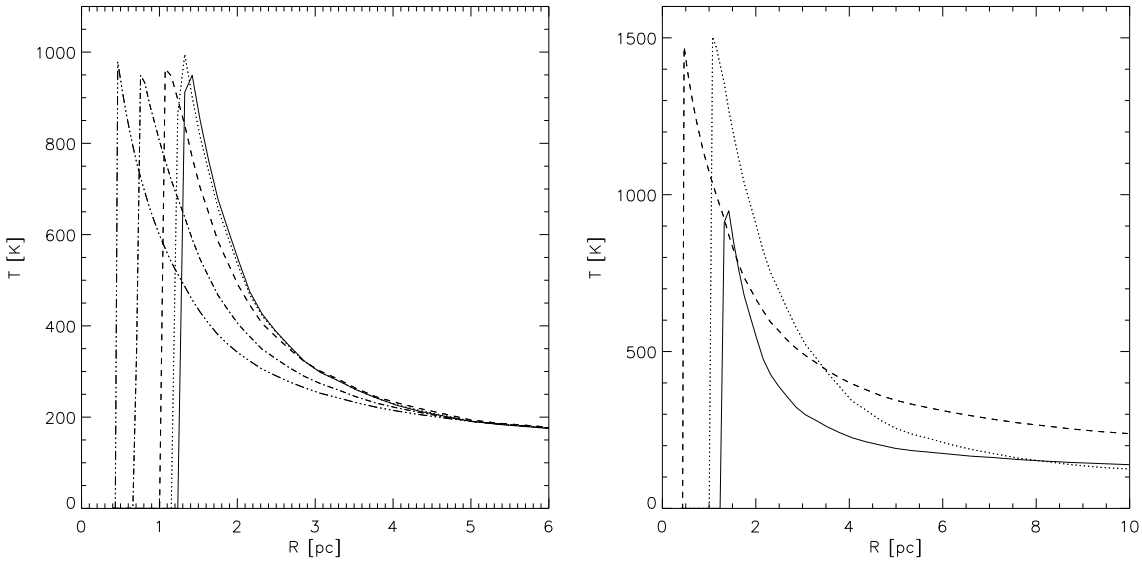

Figure 2.8: *Comparison of the temperature distributions of different dust species within the equatorial plane:* **a)** *Temperature distributions for differently sized silicate grains: $a = 0.005\,\mu m$ (solid line), $a = 0.013\,\mu m$ (dotted line), $a = 0.035\,\mu m$ (dashed line), $a = 0.094\,\mu m$ (dashed-dotted line), $a = 0.25\,\mu m$ (dashed-dotted-dotted-dotted line).* **b)** *Temperature distributions for different dust species: the smallest silicate component (solid line), the smallest graphite component with $E \parallel c$ and the smallest graphite component with $E \perp c$ (dashed line).*

of the direct illuminated – and therefore hotter – funnel walls. In the outer part of the torus, the temperature contour lines get spherical symmetric, as can be seen by the flattening of the curve at 20 pc distance from the centre.

Fig. 2.8 displays the temperature distributions within the equatorial plane for different kinds of grains. In the left panel, the layering of differently sized silicate grains can be read off. The smallest grains (given by the solid line in Fig. 2.8a) are heated more efficiently and, therefore, their distribution possesses the largest sublimation radius. Fig. 2.8b compares the temperature distributions within the equatorial plane for the smallest grains of the three dust species. The solid line corresponds to silicate grains, the dotted and dashed curve to graphite with the two orientations of the polarisation vector relative to the optical axis. Silicate grains are heated more efficiently than graphite grains.

2.3.3 Inclination angle study for SEDs

In Fig. 2.9a we show an inclination study for SEDs. The uppermost curve belongs to an angle of 0 °, which corresponds to an extreme Seyfert I case, where we see the torus face-on. Typical inclination angles of Seyfert I galaxies are between 10 °and 20 °. Then, the inclination angle is increased up to 90 °, the edge-on case, in steps of 10 °. Some of the inclinations are visualised in Fig. 2.9b for the case of our standard model. Only dust re-emission SEDs are shown, which result in the so-called IR bump. It arises from dust at different temperatures within the toroidal distribution. The two characteristic silicate features at 9.7 µm and 18.5 µm are present in the SED. The 18.5 µm feature is less pronounced and partially hidden in the global maximum of the IR bump. Just looking at the continuum spectrum and neglecting the silicate bands for a second, an offset in the flux is visible.

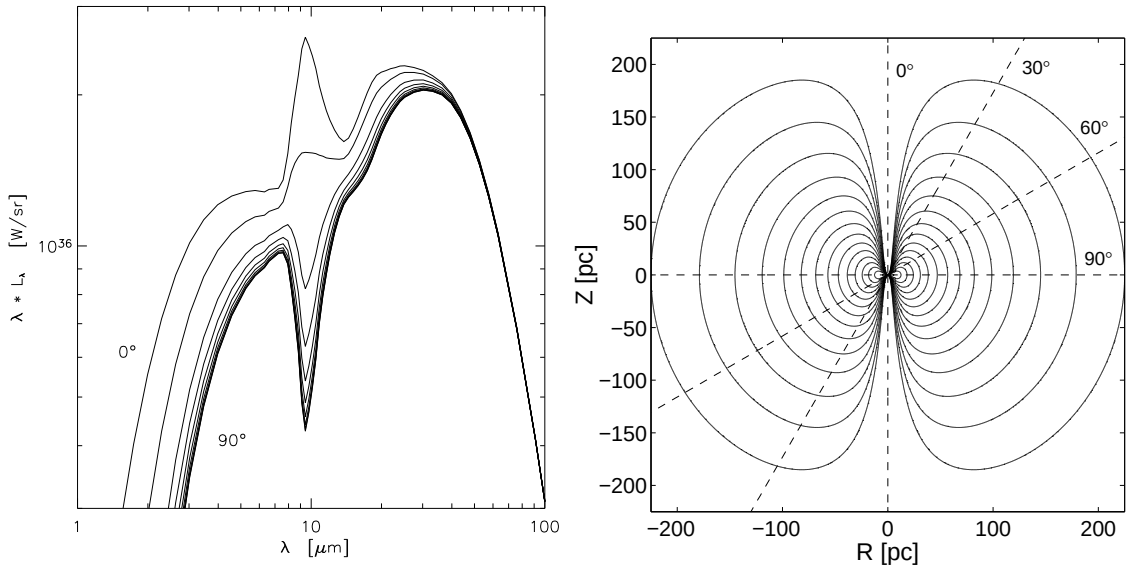

Figure 2.9: *Inclination angle study for our standard model:* **a)** *SEDs of the dust re-emission. The inclination varies from 0° (upper curve) to 90° (lowermost curve) in steps of 10°.* **b)** *Illustration of some inclination angles of lines of sight frequently used for our standard model.*

This offset (explained in Sect. 2.3.1 and visualised in Fig. 2.6) is again due to the offset in the extinction curve (see Fig. 2.3a) and especially visible for the case of silicate grains.

For $i = 0°$, we directly see the torus and the primary source and, therefore, expect the silicate feature in emission. Moving to higher inclination angles, the extinction to occur along the line of sight, mainly caused by cold dust in the outer part of the torus, increases. Less and less of the hotter, directly illuminated parts of the torus can be seen directly. Therefore, the silicate feature changes from emission to absorption. With rising extinction along the line of sight, the increase of the SEDs at small wavelengths is shifted to longer wavelengths and the IR bump gets more and more narrow. The increase at small wavelengths can be explained by a Planck curve with the highest occurring dust temperatures (at the very inner end of the cusp) altered by rising extinction along the line of sight. For our modelling, the torus gets optically thin between 40 and 50 μm (due to the steep decrease of the extinction curve, compare to Fig. 2.3a). Therefore, all curves coincide and the dust configuration emits radiation isotropically for longer wavelengths.

When we look at the extinction in the visual wavelength range plotted against the inclination angle, A_V reaches about 5 at an inclination angle of 10°. This means that the opening angle of our torus model is too small compared to simple estimates of the torus opening angle using the ratio between Seyfert I and II galaxies, e. g. Osterbrock & Shaw (1988) find a half opening angle between 29°and 39°.

2.3.4 Inclination angle study for surface brightness distributions

In the following section, an inclination study for surface brightness distributions is presented. The underlying model is our standard model introduced earlier. As wavelength we chose $\lambda = 13.18$ μm, which lies in the continuum spectrum outside the silicate feature and still belongs to the wavelength range covered by MIDI (Leinert et al. 2003). Using the Wien law as a rough estimate of the

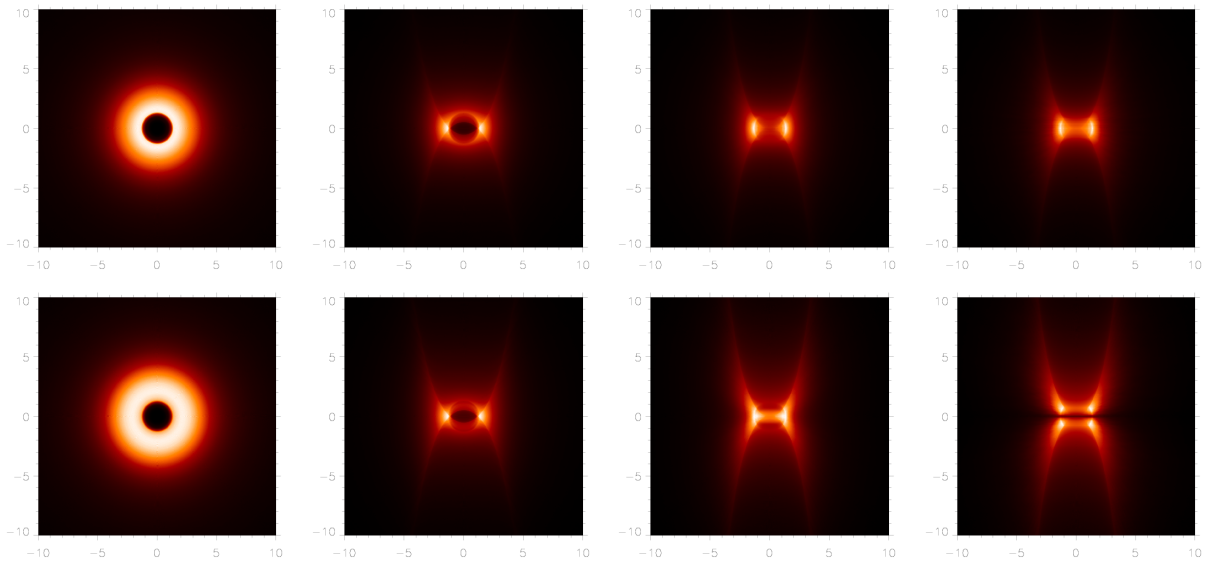

Figure 2.10: *Surface brightness distributions of our standard model with an isotropically radiating central source (first row) and with a* $|\cos\theta|$ *- radiation characteristic (second row) at inclination angles of 0°, 30°, 60° and 90° given with a linear colour scale ranging from 0 to the maximum value of the respective image.*

temperature, where the dust emits the maximal radiation at this wavelength, we get about 230 K. Looking at the steep radial temperature distributions of the various grains (see Fig. 2.8b), we expect the radiation to come from the direct vicinity of the inner radius of the torus. The resulting surface brightness distributions for inclination angles of 0°, 30°, 60° and 90° are shown in the upper row of Fig. 2.10. The images are given in a linear colour scale emphasising areas of maximum surface brightness. The axis labelling denotes the distance to the centre of the AGN in pc. When we consider flux scales, the object is always assumed to be at a distance of 45 Mpc, which is a typical value for Seyfert galaxies, which will be observed with MIDI.

Looking at the image with an inclination angle of 90 °(the last image in the first row of Fig. 2.10), the most central part of the torus funnel is visible. As already mentioned above, the dust species sublimate at different distances from the central source. Within these inner radii, no such grains can survive. Therefore, a layering of dust grains exists in the vicinity of the cusp. This is partly visible here. While the very inner end of the torus appears quite faint due to the depletion of many grain species (especially the most abundant small silicate grains and also the smallest graphite grains), a semilunar feature is visible further out. At this point, the dust density increases strongly, because the sublimation radii of small silicate grains are reached. They provide the highest mass fraction of all dust species (for this dust model, the two smallest silicate grain populations carry about 43% of the total mass). Apart from this, an x-shaped emission area appears. Here we see the directly illuminated funnel walls. As the dust density peaks further out at a distance of 5 pc in the equatorial plane, the dust density next to the funnel (outer equipotential lines) is quite low. Hence, only an x-shaped feature remains from the emission of the walls, which arises from a summation effect along the lines tangential to these walls of the funnel. The two maxima are connected via an emission band, which gets fainter and more narrow towards the centre, again due to a summation effect, which is stronger for the case of a line of sight tangential to the ring than perpendicular.
At an inclination angle of 60 °, the same features remain, but the two semilunar areas of maximal emission get connected via thin and faint bows, due to the different line of sight to the ring-like structure. This effect further increases at $i = 30°$. Now, the whole ring of the main dust grain

contributors is visible. We see here the intersection of the sublimation sphere of these kind of grains with the torus.

In the face-on case ($i = 0\,^\circ$), we get the expected ring-like structure. In the central area no emission is present, because in our modelling the funnel of the dusty torus itself is free of any material. The maximum surface brightness does not result from the innermost part of the torus – although these dust grains possess the highest temperatures – because of the summation effect already mentioned above. Only very little dust can exist here because of the density model itself and because the sublimation radii of the main dust contributors lie further out. Summing up along the line of sight results in the shown distribution of surface brightness.

2.3.5 Wavelength study for surface brightness distributions

In Fig. 2.11 we show surface brightness distributions at different wavelengths for the face-on and the edge-on view on our mean Seyfert torus model. Images for the same inclination angles are given with the same logarithmic colour scale and a dynamic range between the global maximum at the respective inclination angle and $10^{-3}\%$ of this value. Again, only re-emission spectra of the dust configuration are shown. The direct radiation of the energy source is neglected. When we would take this into account, the centre would always yield the highest brightness in the surface brightness distribution. The wavelengths are chosen as follows: We start with 7.22 µm, located outside the silicate feature at 9.7 µm, but closest to 8 µm, where the wavelength range of the MIDI (Leinert et al. 2003) instrument starts. The next is the wavelength of the feature itself, then between the two silicate features (at 13.18 µm) at the upper end of the MIDI wavelength range and finally we chose the overall maximum of the SEDs (30.2 µm).

At wavelengths smaller than approximately 2 µm, re-emission of dust can be neglected and pure emission of the central source remains, attenuated by the dust. The surface brightness distributions at varying wavelengths highlight explicitly the different temperature domains. According to Wien's

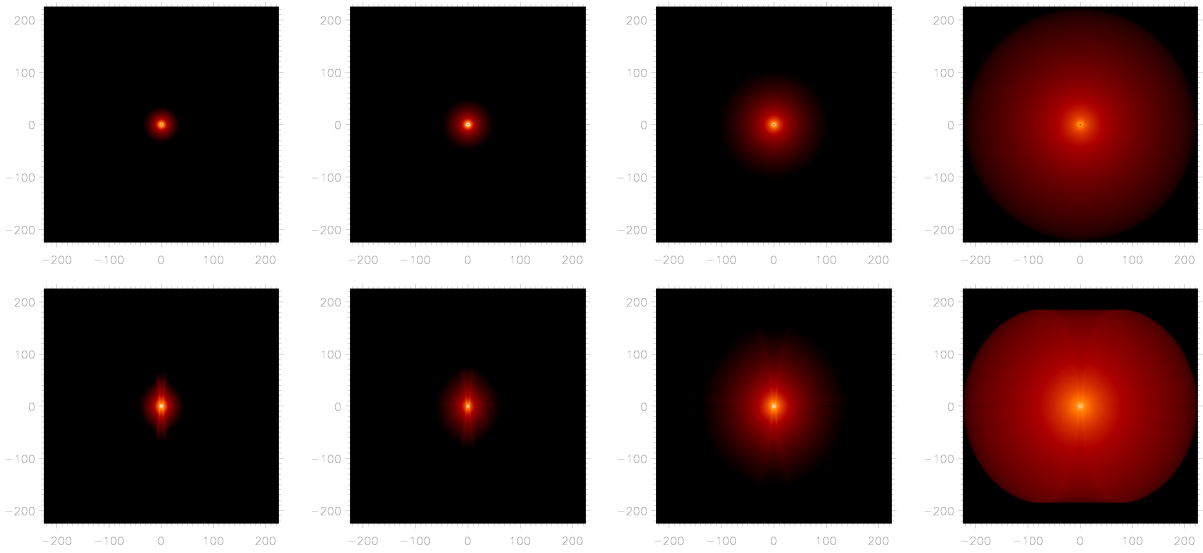

Figure 2.11: *Surface brightness distributions of our standard model for different wavelengths from left to right (*7.22 µm, 9.7 µm, 13.18 µm, 30.2 µm*). Maps are given in logarithmic scale for inclination angles of $i = 0\,^\circ$ (upper row) and $i = 90\,^\circ$ (lower row). See text for a detailed description.*

law, the maximum surface brightness at a wavelength of about 7 μm is emitted by dust of a temperature of around 400 K. This area is concentrated to the innermost part of the dust distribution, caused by the very steep radial temperature curve there. Dust heated to about 100 K – which is reached in the flattening part of the temperature distribution – has its maximum radiation at a wavelength of around 30 μm. Therefore, emission can be seen from a large fraction of the torus volume. The same behaviour is also visible in the case of an inclination of 90 °. While for small wavelengths basically the x-shaped structure is visible, at longer wavelengths one can see the whole torus. This is also due to the fact that the extinction curve drops off very steeply and, therefore, we expect emission from all over the torus body.

2.3.6 Implementation of a radiation characteristic

A further step towards a more physical model was the introduction of a radiation characteristic of the accretion disk (see also Manske et al. 1998). We wanted to check if this yields less steep radial temperature distributions, helping us to explain the increasing depth of the silicate feature seen in correlated flux measurements performed by MIDI (Jaffe et al. 2004). In an extended optically thick accretion disk, a significant part of the radiation arises from the surface. Therefore, in a simple approach, we implemented a radiation characteristic following the same $|\cos(\theta)|$ law for all wavelengths. After emission of a photon package from the central source, the direction of emission is chosen by chance, but in accordance with this radiation characteristic.

In Fig. 2.12, the differences in the temperature distributions of the smallest silicate dust component are visualised. Here, one can directly see that compared to the isotropic radiating case, the $|\cos(\theta)|$ characteristic for the photon emission leads to hotter areas near the funnel walls, while the tempera-

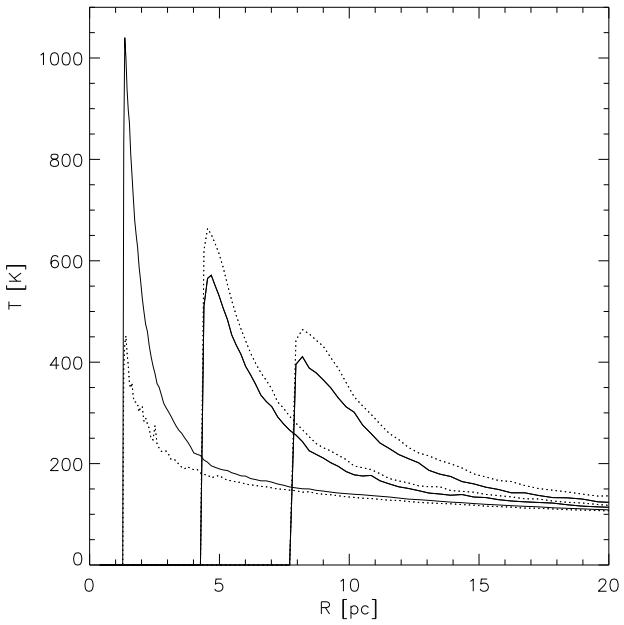

Figure 2.12: *Comparison of the temperature distribution of our standard model (solid lines) with the model with an anisotropically radiating accretion disk (dotted lines). The respective pairs of radial temperature distributions for the smallest silicate grain component are shown. From left to right: within the equatorial plane, for an inclination angle of 30° and an inclination angle of 20°.*

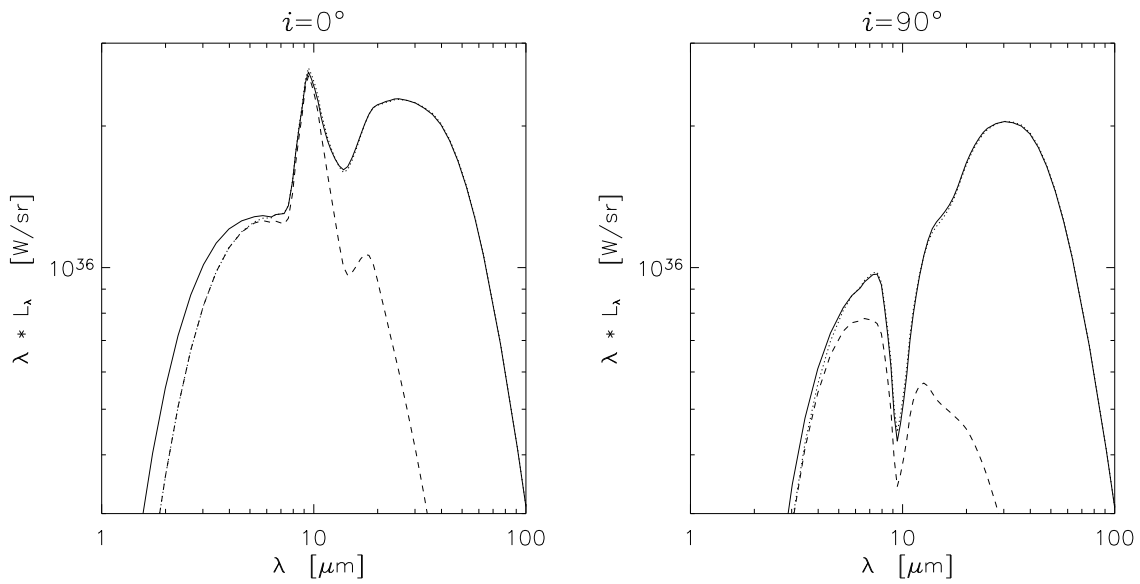

Figure 2.13: *SEDs at inclination angles of 0° and 90° for our standard model with an isotropically radiating accretion disk (given by the solid line) and for the same model but with an accretion disk with a $|cos(\theta)|$ - radiation characteristic, without zoom (dotted line) and zooming into the inner 10 pc in radius (dashed line).*

ture within the equatorial plane gets lower. This is understandable, because the midplane is mainly heated by indirect reradiation of the dust in this case.

In Fig. 2.13, SEDs of our standard model with an isotropically radiating accretion disk (given by the solid line) are compared to the case of an accretion disk with a $|\cos\theta|$ - radiation characteristic (dotted line). The dashed line corresponds to the model with a radiation characteristic, but zoomed into the central 10 pc in radius and will be discussed in Sect. 2.3.10. As the maximum dust temperature is smaller when implementing a radiation characteristic, the left branch of the IR bump is slightly shifted to longer wavelengths. The dotted line coincides here with the dashed line. With increasing inclination, this effect gets less important due to increasing extinction along the line of sight. In disagreement with Manske et al. (1998), we cannot find any change of the depth of the silicate feature, when comparing the SED with an isotropically radiating accretion disk with the anisotropic case. This is caused by the different geometry in the innermost part of the torus and other values of the optical depth of our modelling compared to their approach. The cusp of the torus, which is only present in our modelling leads to a more pronounced silicate feature in emission for small inclination angles.
In the second row of Fig. 2.10, surface brightness distributions at different inclination angles are shown for the case of our standard torus model, illuminated by the accretion disk described above. Here, one can directly see that the radiation characteristic leads to an enhanced heating of the funnel walls. This is best seen when comparing the images at an inclination angle of 0°. The area of maximum emission increases for the case of an implemented radiation characteristic, because more energy is emitted into the relevant solid angle and can, therefore, heat the funnel efficiently up to a larger height. In contrast to this, the equatorial plane can only be heated by re-emitted photons and, therefore, only smaller temperatures are reached. This effect is visible directly when looking at the image for the edge-on view towards the torus. The midplane appears as a narrow absorption band.

2.3.7 Dust mass variation study for SEDs

To study the impact of changing the dust mass, which is enclosed in the torus, we started with our standard model (given by the solid line in Fig. 2.14) with an optical depth of $\tau_{9.7\,\mu m} = 2.0$ within the midplane, doubled the mass (dotted line, $\tau_{9.7\,\mu m} = 4.0$) and halved it twice (dashed line with $\tau_{9.7\,\mu m} = 1.0$ and dashed-dotted line with $\tau_{9.7\,\mu m} = 0.5$). The resulting SEDs are shown in Fig. 2.14 for the Seyfert I and Seyfert II case with inclination angles of $0\,^\circ$ and $90\,^\circ$ respectively. As the optical depth is given by the integral of the product of the dust density and the mass extinction coefficient along the line of sight, it scales linearly with the enclosed dust mass:

$$\tau_{\mathrm{ext}} = \int_{\zeta} \rho_{\mathrm{d}}\, \kappa_{\mathrm{ext}}\, ds. \tag{2.15}$$

When we choose a line of sight within the dust-free hole of the torus – corresponding to the Seyfert I case – the whole temperature range of the dust in the torus can be seen. With increasing optical depth, more and more photons are absorbed within a decreasing volume near the funnel of the torus and re-emitted in the infrared wavelength range. This leads to a rise of the temperature of dust near the funnel. But due to the high optical depths, less photons reach the outer part of the torus and, therefore, the temperature drops. Altogether, a steeper temperature distribution in radial direction results. Smaller minimum temperatures lead to a shift of the Rayleigh-Jeans branch to longer wavelengths and larger maximum temperatures lead to a shift of the Wien branch to shorter wavelengths. Altogether, the IR bump gets broader. The higher temperatures in the inner region also cause more flux at short wavelengths, while the larger amount of cold dust produces more flux at longer wavelengths. The global maximum of the IR bump is shifted to higher wavelengths because of the smaller temperatures at the point of the maximum of the dust density.

For an inclination angle of $90\,^\circ$, which corresponds to a Seyfert II-like case, there is always dust on the line of sight. Only the outer and, therefore, the coldest part of the torus can be seen directly.

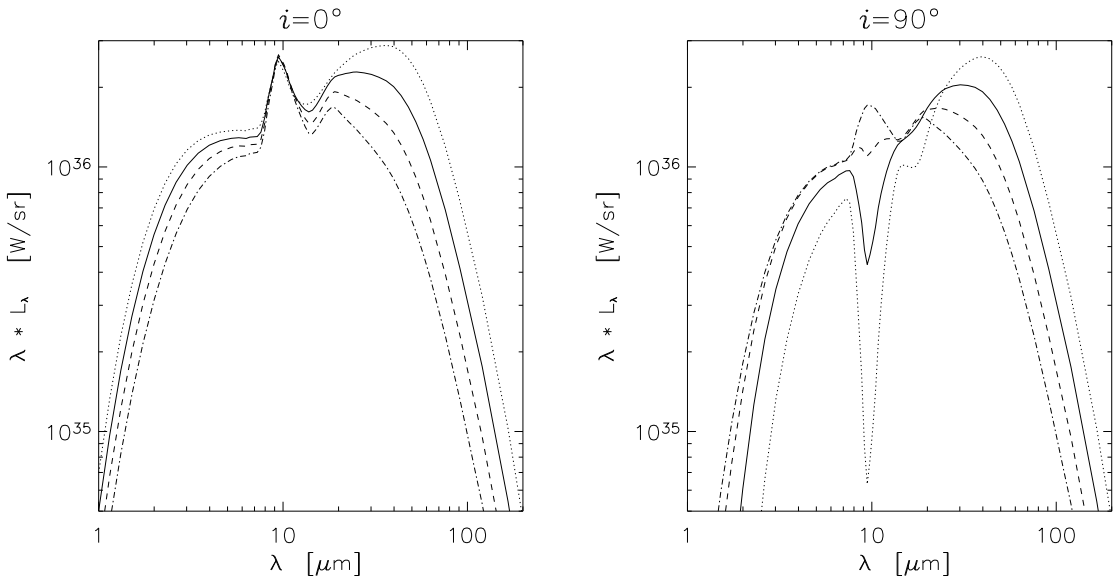

Figure 2.14: *SEDs at inclination angles of $0\,^\circ$ and $90\,^\circ$ for different optical depths along an equatorial line of sight: $\tau_{9.7\,\mu m} = 4.0$ (dotted line), $\tau_{9.7\,\mu m} = 2.0$ (solid line – our standard model), $\tau_{9.7\,\mu m} = 1.0$ (dashed line) and $\tau_{9.7\,\mu m} = 0.5$ (dashed-dotted line).*

That is why we can use the reasoning for the Seyfert I case for the long wavelength region. The innermost (and therefore hottest) part of the torus can only be seen through an increasing amount of dust. The higher the extinction the less we can look into the torus and the less hot areas of the torus can be seen. Therefore, the left branch of the IR bump is shifted to higher wavelengths when the extinction increases. The 9.7 μm silicate feature changes from emission over partial absorption to total absorption, comparable to large inclination angles in the study shown in Sect. 2.3.3. As discussed above, increasing dust mass affects the optical depth linearly. When $\tau = 1$ is reached, the torus gets optically thick, and, therefore, the feature changes from emission to absorption. Between these two cases, a smooth transition region is visible, where the feature can be seen in partial absorption and emission, called self-absorption (Henning 1983). Intersecting the $\tau = 1$ line with the optical depth plotted against the wavelength though displays the expected behaviour of the silicate feature in the spectrum. The same holds for the second silicate feature at 18.5 μm but in alleviated form as it is much weaker and partially covered by the global maximum of the IR bump.
The study shows that the SEDs are very sensitive to changes in the dust mass. Already a change by a factor of four changes the feature from emission to complete absorption (see solid line compared to dashed-dotted line in Fig. 2.14). Therefore, the silicate feature is a quite sensitive tool to distinguish the optical depth along the line of sight.

2.3.8 Dust mass variation study for surface brightness distributions

To study the impacts of changing the optical depth along the line of sight on surface brightness distributions, we used the same dust masses as in Sect. 2.3.7 for the case of spectral energy distributions to gain comparability, but doubled the highest mass again. This means that coming from our standard model, we doubled the enclosed dust mass twice and halved it twice. Again, we chose the same wavelength of 13.18 μm. The results are shown in Fig. 2.15. The different optical depths ($\tau_{9.7\,\mu m} = 0.5$, $\tau_{9.7\,\mu m} = 1.0$, $\tau_{9.7\,\mu m} = 4.0$, $\tau_{9.7\,\mu m} = 8.0$) are shown in different columns, while the inclination angle changes are shown in different rows, starting from 0° in the upper row to 90° in the lower row. Our standard model is omitted here, please compare to Fig. 2.10. All of the images are given in a linear colour scale, with a dynamic range between zero and the maximum value of the respective map in order to show the changes in the distribution of maximum surface brightness for the different optical depths. The absolute values for the pixels are given in Fig. 2.16, which shows a cut through the maps of the dust mass variation study from the centre along the positive x-axis for an inclination of 0° and 90°. The fluxes are given in Jansky per square milliarcsecond for an assumed distance of the object of 45 Mpc. For the case of 0°, all graphs show the same trend: coming from the centre, one can see a sharp rise of surface brightness with a sharp peak and a flatter decrease in the outer part. Between 4 and 5 pc, all of the curves meet into a single curve, independent of the optical depth. The latter is due to the fact that our model features very steep funnel walls. As indicated by the temperature distribution, we expect most of the emission for this wavelength next to the torus boundary. The intersection of all curves then indicates the distance from the centre, where the density has decreased that much that a doubling of it does not change the emitted flux anymore and the expected surface brightness distribution is independent of the optical depth within our sample. By increasing the optical depth, the maximum is shifted towards the centre and to higher values and the curves get steeper. As already discussed in the previous section, the higher the optical depth is, the steeper the drop of the temperature distribution in radial direction is, because the photon mean free path length decreases and most of the photon packages get absorbed within a reduced volume of the dust torus (steepening of the inner part) and, therefore,

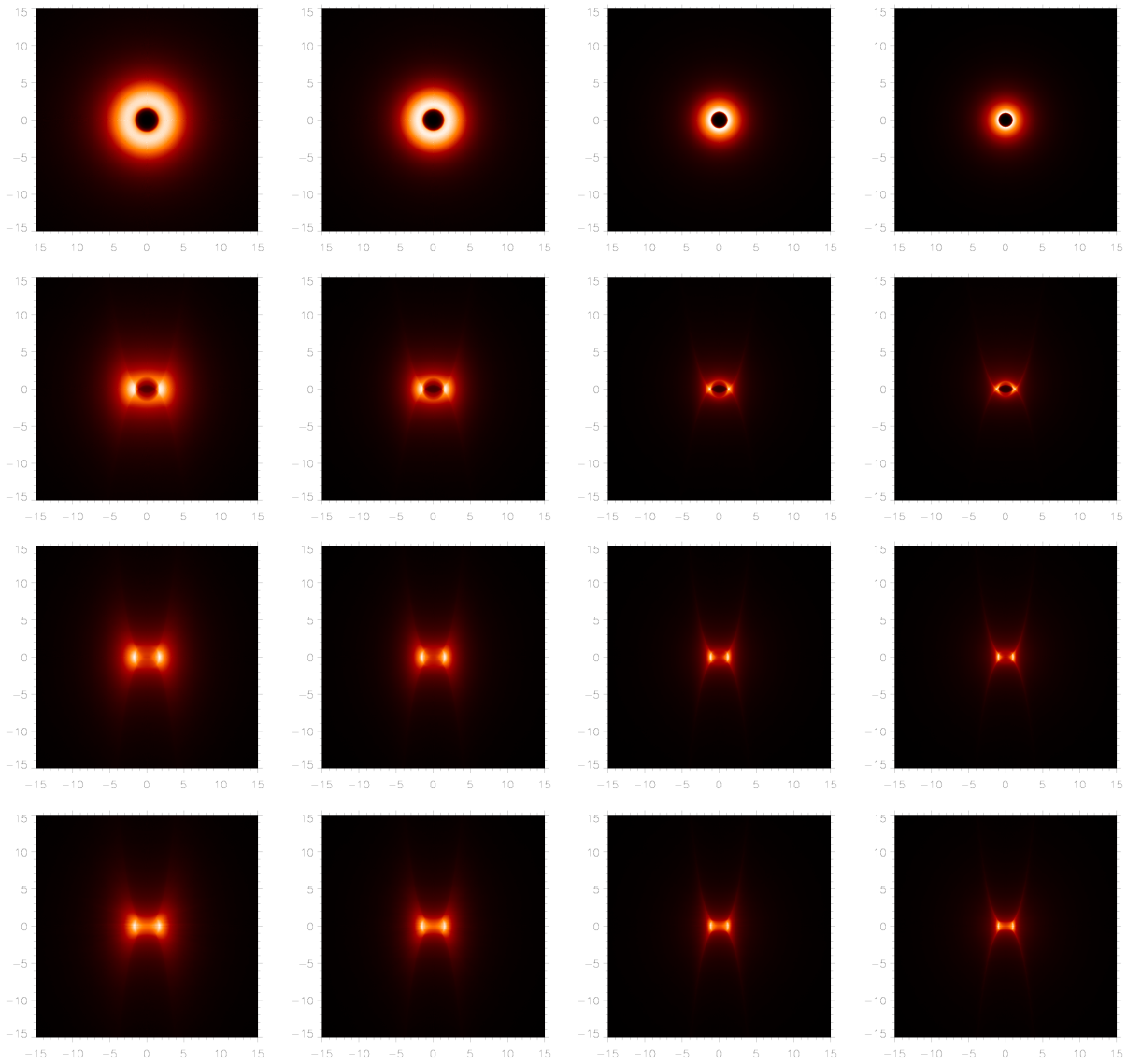

(a) $\tau_{9.7\,\mu m} = 0.5$ (b) $\tau_{9.7\,\mu m} = 1.0$ (c) $\tau_{9.7\,\mu m} = 4.0$ (d) $\tau_{9.7\,\mu m} = 8.0$

Figure 2.15: *Surface brightness distributions at a wavelength of* $\lambda = 13.18\,\mu m$ *for models with different optical depths. The values for the optical depth are* $\tau_{9.7\,\mu m} = 0.5$ *(left column),* $\tau_{9.7\,\mu m} = 1.0$*,* $\tau_{9.7\,\mu m} = 2.0$*,* $\tau_{9.7\,\mu m} = 4.0$ *and* $\tau_{9.7\,\mu m} = 8.0$ *(right column) and inclination angles change from* $0°$ *(upper row) to* $90°$ *(lower row) in steps of* $30°$*. Each step in* τ *means doubling the included dust mass. The images with* $\tau_{9.7\,\mu m} = 2.0$ *is omitted (please compare to Fig. 2.10). All images are given with a linear colour scale reaching from zero to the maximum of the respective image.*

only re-emitted photons in the IR reach the outer region (flattening of the outer part). To estimate the surface brightness, one has to take into account all emission by dust until $\tau = 1$ is reached. This can also be directly seen in Fig. 2.15 in the decreasing size of the region of maximum emission. The apparent shift of the inner radius of the torus is caused by the increase of the *atmosphere* around the dense core of the torus or the growth of the denser core, respectively.

At the other inclination angles one can again see that the area of maximal emission changes. At smaller optical depths, it is a diffuse, wide distribution within the torus volume. Increasing the optical depth leads to a spreading, which is more located in the direct vicinity of the inner funnel

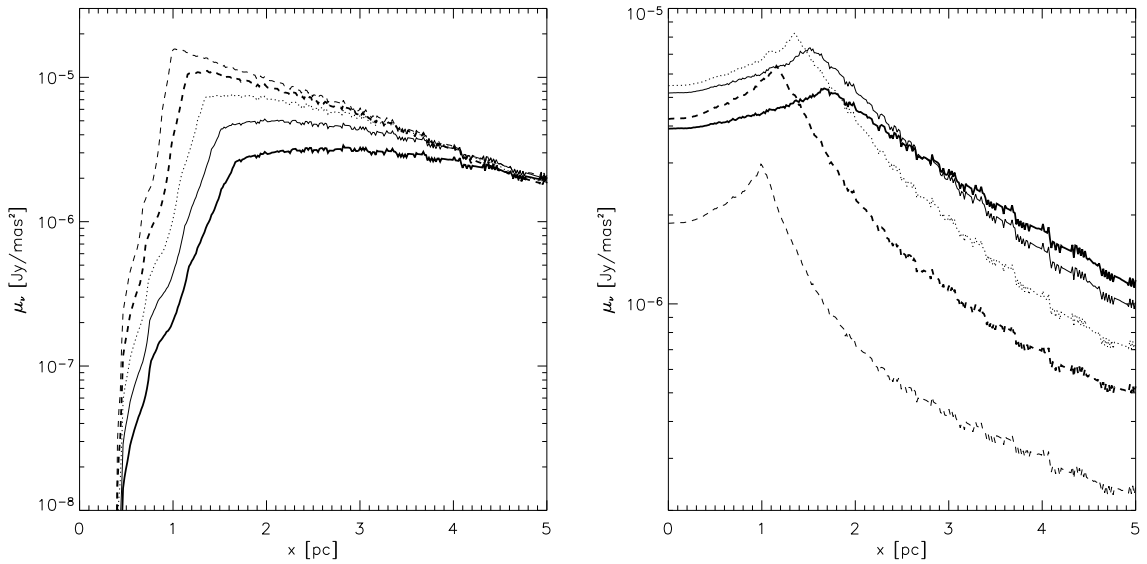

Figure 2.16: *Cut through the surface brightness distributions μ_ν at a wavelength of $\lambda = 13.18\,\mu$m along the positive x-axis for inclination angles of 0° and 90°. The thick solid line corresponds to the case with $\tau_{9.7\,\mu\mathrm{m}} = 0.5$, the thin solid line to $\tau_{9.7\,\mu\mathrm{m}} = 1.0$, the dotted line to our standard model with $\tau_{9.7\,\mu\mathrm{m}} = 2.0$, the thick dashed line to $\tau_{9.7\,\mu\mathrm{m}} = 4.0$ and the thin dashed line to $\tau_{9.7\,\mu\mathrm{m}} = 8.0$. The fluxes shown are given in Jansky per square milliarcsecond for an assumed distance of the object of 45 Mpc.*

border. This leads to the sharply emerging inner borders of the funnel, which are now visible in the typical x-shaped form. These appearances have been seen in a similar dust configuration around a double system, the so-called Red Rectangle (Tuthill et al. 2002), which can be explained by a dusty torus as well (Men'shchikov et al. 2002). It is located in a distance of only 330 pc, much closer than Seyfert galaxies and can therefore be resolved.

At higher inclination angles, two effects have to be taken into account. With increasing amount of dust along the line of sight, first of all, we expect a larger surface brightness, but the extinction along the line of sight increases as well. The value of the maximum of the cut along the positive x-axis of the maps with the highest optical depth is not the brightest anymore. It decreases with increasing inclinations. In Fig. 2.16 the case for an inclination angle of 90° is shown. Here, the model with the highest dust mass (thin dashed line) has the smallest surface brightness and the curve of the second heaviest torus (thick dashed line) has also shifted significantly to smaller values. The shape of these graphs also changes when changing from the Seyfert I ($i = 0°$) case to the Seyfert II ($i = 90°$) case. As the directly illuminated parts of the funnel are not directly visible anymore, the decreasing curve further away from the centre decreases faster. With increasing optical depth, the outer part of the torus gets colder and colder, which can be seen by the decreasing flux and the steepening of the curves there. In the innermost part, the curves flatten, which is due to the emission band of the innermost ring of the funnel. As less photons reach the outer part, statistic gets poorer there and therefore the graphs get more noisy.

2.3.9 Variation of dust properties

As already pointed out in Sect. 2.2.3, the dust composition in the extreme environment of an AGN may be altered compared to interstellar dust in our own galaxy. The main effects here are sputter-

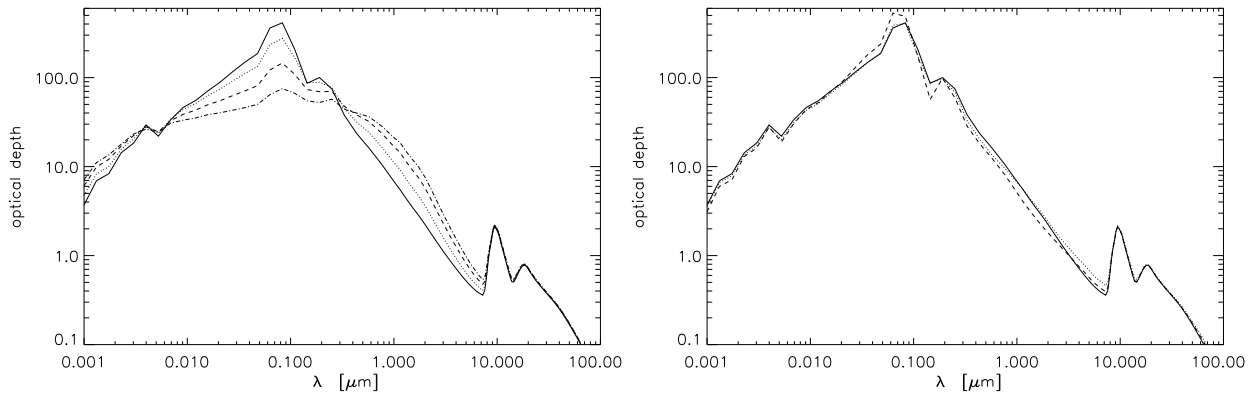

Figure 2.17: *Optical depth within the equatorial plane for different dust models:* **a)** *Increasing the exponent of the number density distribution of grain sizes, from* -3.5 *(our standard model, given by the solid line) over* -3.0 *(dotted line) and* -2.5 *(dashed line) to* -2.0 *(dashed-dotted line).* **b)** *Changing the range of grain sizes, from* $0.005 \ldots 0.25\,\mu$m *(our standard model, given by the solid line) to* $0.005 \ldots 10\,\mu$m *(dotted line) and to* $0.001 \ldots 10\,\mu$m *(dashed line).*

ing due to interaction of the dust grains with the hot surrounding gas, the presence of the strong radiation field of the central source, destruction of dust grains due to shocks, etc.

All of the mentioned effects mainly impact the population of small grains. Therefore, some authors (e. g. Laor & Draine 1993; Maiolino et al. 2001) claim that within an AGN dust model, small grains should be depleted. In the following section, we test this by first of all changing the exponent of the number density distribution of grain sizes and later by widening the grain size distribution in both directions. By doing this, a transition is made between the standard MRN galactic dust model – which we have adopted as our standard dust model – and the dust model proposed by van Bemmel & Dullemond (2003). In this section, we are especially interested in the behaviour of the 9.7 μm silicate feature, as it was claimed that the depletion of smaller grains may solve the problem that the feature has never been seen in emission in AGN. On the other hand, one needs to check whether other constraints are violated by this change of the dust model, e. g. the appearance of the feature in absorption, as observed.

Changing the exponent of the number distribution of grain sizes

Different exponents of the number density distribution of the grains were tested by van Bemmel & Dullemond (2003) for their torus model. They finally adopt a somehow more shallow distribution with an exponent of -2 to be their standard dust model.

In this section, we also study different slopes of the distribution for our standard torus geometry (see Sect. 2.2.2). We start with our standard dust model with a slope of -3.5 (given by the solid line in Fig. 2.17a) and Fig. 2.18) and test shallower distributions by changing the exponent in steps of 0.5 up to -2.0 (dashed-dotted line) used by van Bemmel & Dullemond (2003). Due to renormalisation of the dust density after changing the exponent, this means that a flatter distribution leads to more large grains compared to small grains. This produces a flatter course of the optical depth (see Fig. 2.17a) at small wavelengths – compared to our standard model – because of the less efficient heating of larger grains, which dominate the dust composition more and more during the variation. Consequently, the temperature distributions flatten.

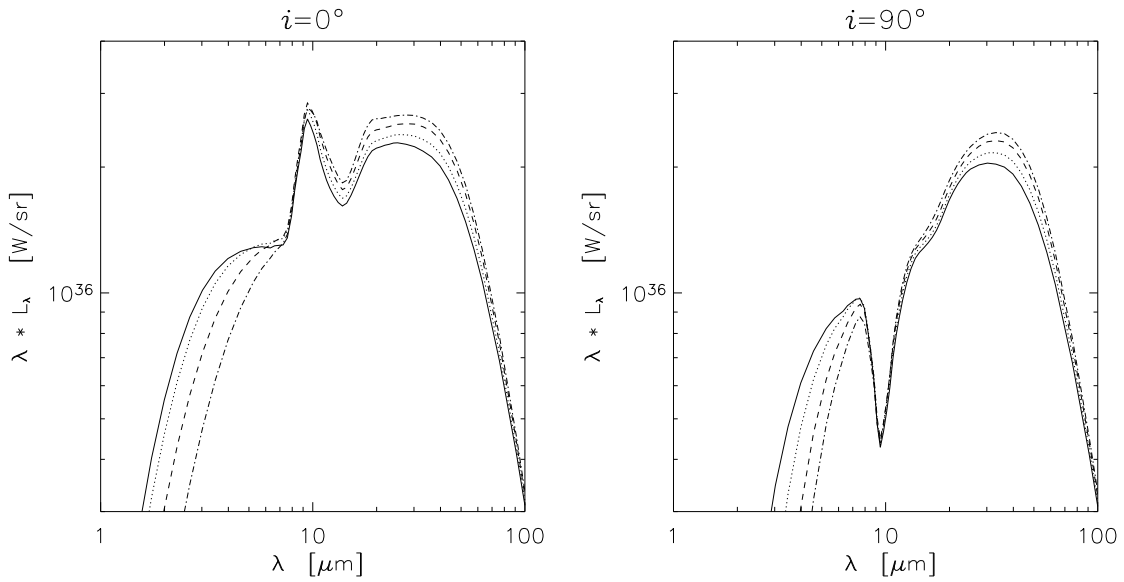

Figure 2.18: *Consequences on the SEDs at inclination angles of* 0° *and* 90° *of changing the exponent of the dust grain number density distribution. The exponent changes from* −3.5 *(solid line) in steps of* 0.5 *to* −2.0 *(dashed-dotted line).*

In the SEDs (see Fig. 2.18a), this can be seen by the decreasing fluxes at the rise of the IR-bump at small wavelengths and the increasing fluxes at wavelengths around the maximum (20−30 μm) of the infrared bump (see Fig. 2.18a). The stratification of dust grains concerning sizes and composition and the increasing extinction caused by the large grain population (with smaller sublimation radii) lead to larger sublimation radii for the other components. In contradiction to the modelling of van Bemmel & Dullemond (2003), a significant change of the silicate feature cannot be found in our simulations. For the case of an inclination angle of 90° (see Fig. 2.18b), any change is simply due to the fact that there is too little dust left that has temperatures higher than about 300K – the temperature which is required for the emission feature at 9.7μm.

Changing the width of the grain size distribution

In a further dust parameter study, we test the effects of a broadening of the grain size distribution. The corresponding courses of the optical depths with wavelength within the equatorial plane are plotted in Fig. 2.17b) and the resulting SEDs in Fig. 2.19b). Starting from the MRN model (given by the solid line), we first extend the grain size range towards larger grains (dotted line) up to 10 μm size and later additionally towards smaller grains down to 0.001 μm (dashed line). By doing this, we finally get the dust model used by van Bemmel & Dullemond (2003).

As can be seen from Fig. 2.17b), only minor changes of the optical depth are visible. Conspicuous is the smaller relative depth of the silicate feature towards shorter wavelengths after including also large grains (dotted line). This can also be seen in the SEDs, displayed in Fig. 2.19b). While the differences for an inclination angle of 0° are nearly negligible, the reduced relative depth of the silicate feature towards smaller wavelengths is clearly visible in the SED for edge-on view (i = 90°). In the last step of our study – the inclusion of pronounced slightly smaller grains – the effects of extending the size distribution towards larger grains is partly compensated.

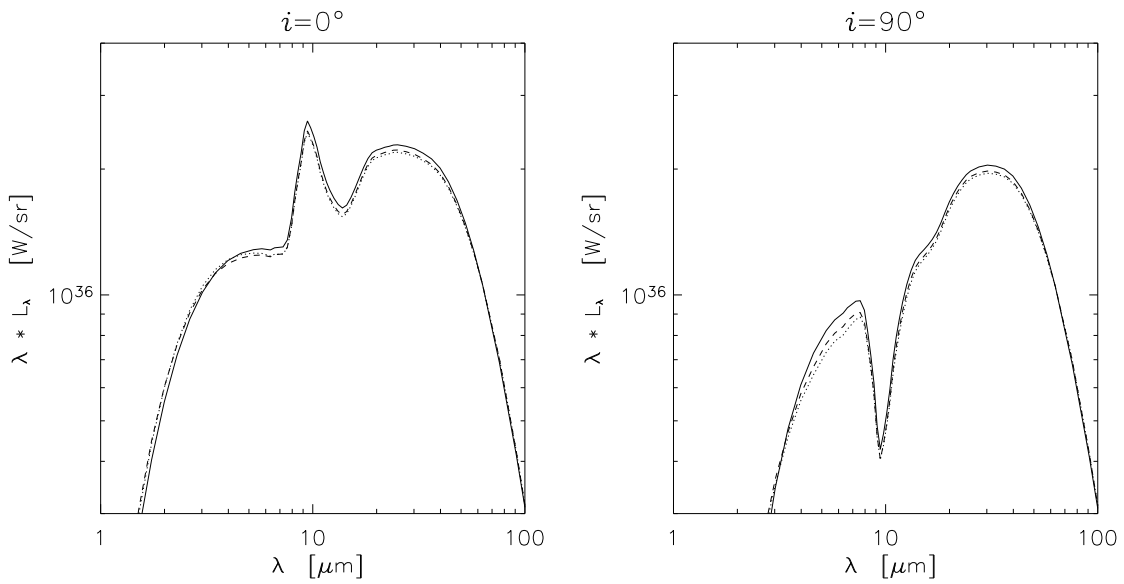

Figure 2.19: *Consequences on the SEDs at inclination angles of* 0° *and* 90° *of changing the width of the dust grain size distribution from* 0.005 . . . 0.25 µm *(solid line) over* 0.005 . . . 10 µm *(dotted line) and finally to* 0.001 . . . 10 µm *(dashed line).*

2.3.10 Zooming into the torus

Another simulation series we made was to investigate the impact of zooming into the torus, resembling a certain aperture of the telescope. To do this, we again started from our standard model and zoomed into the central 10 pc and 1 pc in radius. This corresponds to a resolution of the observing

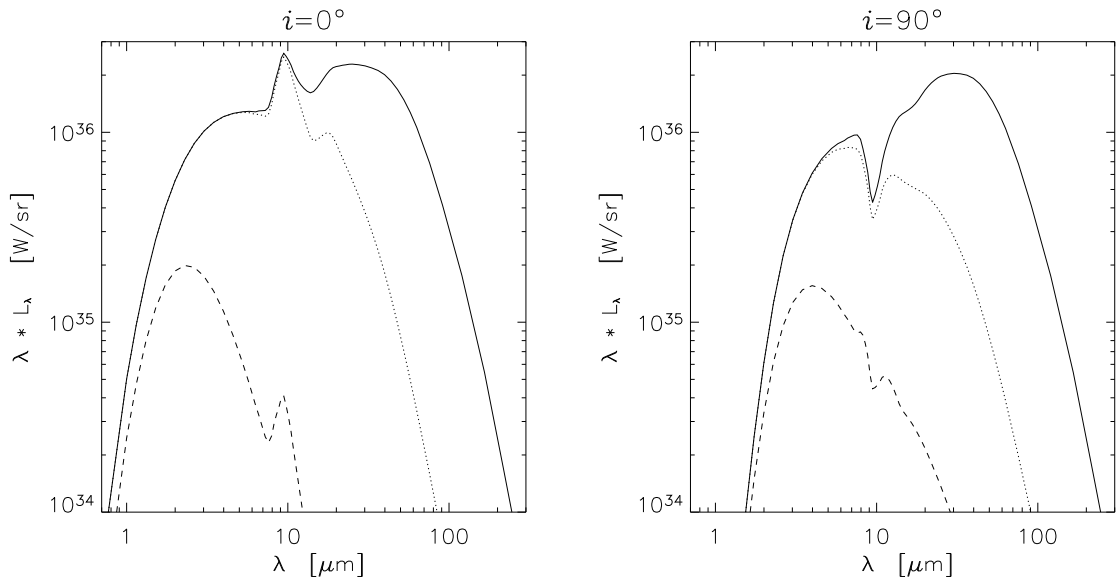

Figure 2.20: *Dependence of SEDs on the beamsize of the observing device. The solid line corresponds to our standard model, the dotted line to the resolution obtainable with a single-dish telescope (100 mas) for a distance to the object of 45 Mpc and the dashed line to the resolution of the MIDI interferometer (10 mas). The left panel shows SEDs for an inclination angle* $i = 0\,^\circ$ *and the right panel for* $i = 90\,^\circ$.

instrument of 100 mas and 10 mas for an object at a distance of 45 Mpc. These are typical values for the largest single-dish telescopes (100 mas) and the first interferometers in this wavelength range like MIDI (10 mas). The results of this study are shown in Fig. 2.20. In terms of surface brightness distributions compare to Fig. 2.10.

When we decrease the aperture, we concentrate more and more on the central parts of the torus emission. As our temperature distribution is very steep, it is expected that cold dust in the outer part of the torus is excluded from the field of view. Therefore, the smaller the aperture, the less total flux we obtain, which is taken from the large wavelengths part of the spectrum. For the case of 10 mas resolution, only the inner pc in radius is visible. This is even less than the sublimation radius of the smallest silicate grains (approximately 1.3 pc).

For the silicate feature, one notices a decrease of the relative depth rather than the expected increase, as seen with MIDI (compare to Fig. 2 in Jaffe et al. 2004). This might be due to a too steep radial temperature distribution of our models. Introducing a cloudy structure, which leaves unobscured channels up to the outer part of the torus, may lead to a direct heating of clouds further outside and therefore to a broader temperature distribution. Zooming into the centre then means for the Seyfert II case to exclude areas, where emission features are produced and a deepening of the silicate absorption feature is expected to take place.

2.4 Comparison with observations

In this section, simulated spectral energy distributions are compared to available observational data for the case of large aperture SEDs and high spatial resolution SEDs.

2.4.1 Comparison with large aperture spectra of type I galaxies

In Fig. 2.21 we compare the resulting SEDs of our standard model (different line styles) for an axial view on the torus (typically, Seyfert I galaxies have inclination angles between 10 °and 20 °) with varying enclosed dust masses (as described in Sect. 2.3.7 and shown in Fig. 2.14) to different sets of mean large aperture data for type I objects. The green plus signs refer to a mean spectrum, extrapolated from 29 radio quiet quasars, provided by Elvis et al. (1994), the blue squares correspond to 16 Seyfert galaxies, reported by Granato & Danese (1994). The red triangles and diamonds represent radioquiet type I PG quasars with bolometric luminosity larger and smaller than $10^{12}\,L_{\odot}$ respectively (Sanders et al. 1989). All of these data sets are scaled in order to get fluxes comparable to our simulations.

As can be seen from this, our models compare well to the overall shape of the UV to FIR wavelength range of these mean AGN spectra. An exception is the pronounced feature at 9.7 μm. As already discussed before, it has never been observed in emission in SEDs of Seyfert galaxies at the time of this work – as well not in SEDs of higher spectral resolution. The introduction of a clumpy structure of the dust distribution, which is also a more physical solution, will help to remove these large emission features of our models as we will see in Chapter 3. A comparison with high spatial resolution SEDs of type II sources is given in the next section for some selected objects.

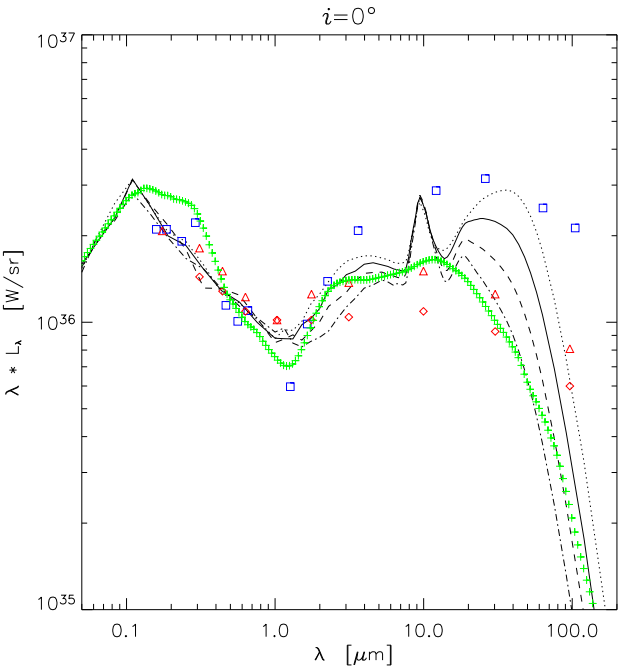

Figure 2.21: *Comparison of our standard model (different line styles correspond to varying dust masses) with large aperture spectra for type I objects. The green plus signs refer to 29 radio quiet quasars (Elvis et al. 1994), the blue squares to 16 Seyfert I galaxies (Granato & Danese 1994) and the red diamonds and triangles to PG Quasars (Sanders et al. 1989) with luminosity smaller (diamonds) and larger (triangles) than* $10^{12}\,L_\odot$*. For a typical Seyfert I galaxy (*$10° < i < 20°$*), the silicate feature looks much less pronounced (see Fig. 2.9a).*

2.4.2 Comparison with special Seyfert II galaxies

To specify as many of our simulation parameters as possible for these special objects, we started with a literature study. Some of the remaining variables could be chosen according to conditional relations as mentioned in Sect. 2.2.2. The value of the enclosed dust mass was assumed such that the relative depth of the 10 μm-feature appears comparable to the observations of the correlated flux with a baseline of 78 m done with MIDI for the case of NGC 1068 and comparable to the depth of the feature in the MIR spectrum of Roche et al. (1991) for the Circinus galaxy. As zooming into our torus does not reproduce the deepening of the silicate feature as seen by MIDI, this seems to be a reasonable procedure and explains the deviations concerning wavelengths around the feature for the case of NGC 1068. It results in an optical depth in the equatorial plane at 9.7 μm of $\tau = 3.3$ for NGC 1068 and $\tau = 3.9$ for the Circinus galaxy. The free parameters finally were chosen to obtain a reasonable dust distribution and a good comparison with the data.

Parameter	Value	Reference	Parameter	Value
$M_{\rm BH}$	$8.3 \cdot 10^6\,M_\odot$	Greenhill et al. (1996)	$\tau_{9.7\,\mu\rm m}$	3.3
$R_{\rm c}$	24 pc	Gallimore & Matthews (2003)	$R_{\rm out}$	72 pc
M_*	$6.5 \cdot 10^8\,M_\odot$	Thatte et al. (1997)	$v_{\rm t}$	164 km s^{-1}
$L_{\rm disk}$	$5.42 \cdot 10^{10}\,L_\odot$		$L_{\rm disk}/L_{\rm Edd}$	20%
d	14.4 Mpc	Galliano et al. (2003)	γ	0.5
i	85 °	Crenshaw & Kraemer (2000)	$R_{\rm T}$	3 pc
$M_{\rm dust}$	$7.8 \cdot 10^4\,M_\odot$			

Table 2.2: *Parameters used for the simulation of NGC 1068.*

Wavelength μm	Band	Flux Jy	Aperture (diameter) arcsec	Reference
1.30	J	5e-4	0.20	R98
1.70	H	6e-3	0.20	R98
2.20	K	5.6e-2	0.27	P04
3.79	L	1.5	0.70	M03
4.47	M	2.5	0.27	P04
7.99	N	4.23	0.20	B00
9.99	N	3.33	0.20	B00
11.99	N	7.1	0.20	B00
24.98		9.4	0.20	B00

Table 2.3: *High resolution data of NGC 1068. The compilation was done by M. A. Prieto. The references are R98 (Rouan et al. 1998), P04 (Prieto, private communication), M03 (Marco & Brooks 2003) and B00 (Bock et al. 2000).*

NGC 1068

NGC 1068 is a nearby Seyfert II galaxy at a distance of 14.4 Mpc (Galliano et al. 2003). Therefore, it has been studied extensively and we were able to find at least some of the needed simulation parameters in literature. The procedure described above led to the parameters summarised in Table 2.2. The inclination angle of $i = 85\,^\circ$ was chosen in agreement with the tilt of the outflow cone of ionised gas reported by Crenshaw & Kraemer (2000). For our comparison, we use a compilation of high resolution data done by M. A. Prieto, given in Table 2.3. Fig. 2.22 shows the result of the adaptation of the model given in Table 2.2 to this data set. The line corresponds to a zoomed-in view of the torus by a factor of 10, which resembles the aperture of 0.2″ in diameter of most of the datapoints (given by the triangles) in Fig. 2.22. The diamonds correspond to a slightly larger aperture of 0.27″. The L-band flux, which corresponds to an aperture of 0.7″ in diameter is given by the square symbol. In addition, we added the total flux (dashed-dotted line) – corresponding to

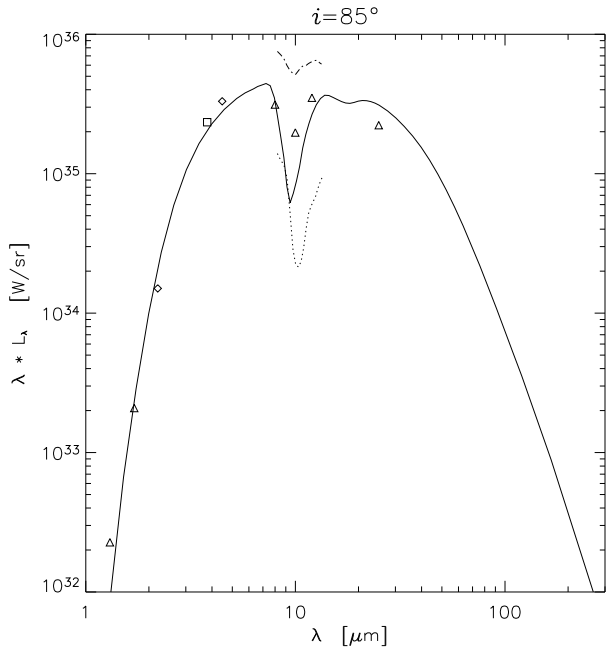

Figure 2.22: *Comparison of one of our models (described by the parameters given in Table 2.2 and plotted with a solid line) to a set of data (given in Table 2.3) from high spatial resolution observations of NGC 1068, compiled by M. A. Prieto. The various symbols correspond to slightly different apertures. The dashed-dotted line gives the total flux spectrum obtained with MIDI and the dotted line corresponds to the correlated flux spectrum obtained with MIDI for a baseline of 78 m (Jaffe et al. 2004).*

Parameter	Value	Reference	Parameter	Value
$M_{\rm BH}$	$1.7 \cdot 10^6\,M_\odot$	Greenhill et al. (2003)	$R_{\rm c}$	10 pc
M_*	$2.0 \cdot 10^8\,M_\odot$		$L_{\rm disk}$	$8.4 \cdot 10^9\,L_\odot$
$L_{\rm disk}/L_{\rm Edd}$	15%		$R_{\rm T}$	3.5 pc
$M_{\rm dust}$	$2.0 \cdot 10^4\,M_\odot$		$\tau_{9.7\,\mu{\rm m}}$	3.9
$R_{\rm out}$	30 pc		$v_{\rm t}$	140 km s^{-1}
d	4.2 Mpc	Freeman et al. (1977)	γ	0.5
i	90 °	Crenshaw & Kraemer (2000)		

Table 2.4: *Parameters used for the simulation of the Circinus galaxy.*

an aperture of $0.6 \times 0.6''$ – and the correlated flux spectrum for a baseline of 78 m (dotted line) – corresponding to an aperture in diameter of approximately 30 *mas* (Jaffe et al. 2004). As can be seen in this figure, observations are in good agreement with our model except of the wavelength region around the 9.7 µm silicate characteristic. As already mentioned before, zooming into our model torus does not reproduce the trend of MIDI-observations, which means a deepening of the silicate feature. We therefore adapted the depth of our feature to the depth observed in correlated flux measurements of MIDI with a baseline of 78 m. This was also necessary in order to describe the datapoints at the smaller wavelengths.

Circinus

The Circinus galaxy is one of the nearest spiral galaxies, which harbours an Active Galactic Nucleus. As it is the second extragalactic object, which has been observed by MIDI and also with NAOS/CONICA (Prieto et al. 2004), we also carried out a comparison with one of our models.

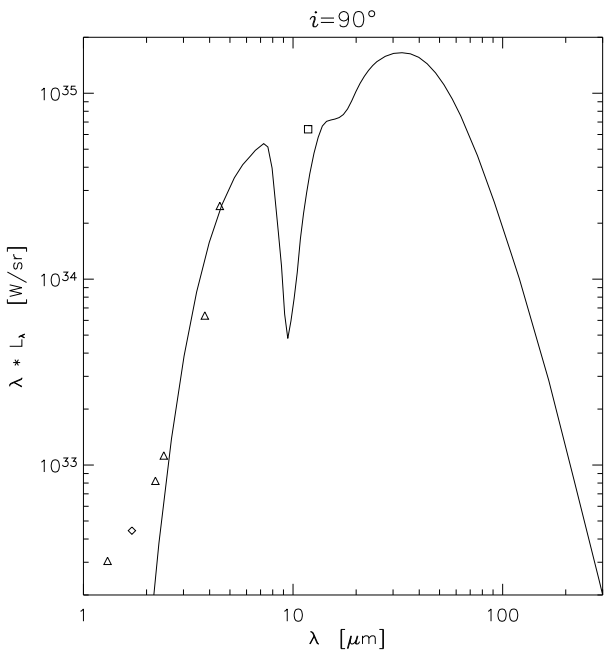

Figure 2.23: *Model comparison with high spatial resolution data of the Circinus galaxy taken with the NACO camera at the VLT. Data courtesy of Prieto et al. (2004). The data was corrected for foreground extinction by $A_{\rm V} = 6$ mag. The various symbols correspond to different apertures (see Table 2.5).*

Wavelength μm	Band	Flux mJy	Aperture (diameter) arcsec
1.30	J	≲7.9	0.38
1.70	H	15.0	0.10
2.20	K	36.0	0.38
2.42		54.0	0.38
3.79	L	480.0	0.38
4.47	M	2200.0	0.38
11.80	N	15000.0	1.00

Table 2.5: *High resolution data of the Circinus galaxy. The data was corrected for foreground extinction by $A_V = 6$ mag. Data courtesy of Prieto et al. (2004).*

From the first results of these observations (Prieto et al. 2004) and also from previous modelling of the dusty torus by Ruiz et al. (2001), we know that it harbours a relatively small sized toroidal dust distribution. Therefore, we used a scaled down version of our standard model described above. The simulation was done with the parameters summarised in Table 2.4.

Fig. 2.23 shows the result of the comparison of this model (given by the solid line plot) with data taken with the NACO camera at the VLT (Prieto et al. 2004). Various symbols represent different apertures (see Table 2.5). Fluxes, corrected for foreground extinction by $A_V = 6$ mag, are used.

The graph corresponds to a torus model with an inner radius of approximately 0.9 pc and a luminosity of the central source of 15% of the Eddington luminosity. The modelling leads to a maximum temperature lower than the sublimation temperatures of the dust grains. Models with smaller inner radii and, therefore, higher maximum temperatures can be excluded. For models with higher maximum temperature, the rise of the IR bump at small wavelengths is moved towards smaller wavelengths. In order to avoid this, we would have to increase the amount of dust, leading to a deeper silicate feature, in contradiction to available observations. This shows that sublimation temperatures of the dust grains are only reached in some of the torus configurations. Our model fits well to the observations, except for the small wavelength part of the SED. This excess can not be due to torus emission within this model. The increased fluxes are most probable caused by light from the central source, scattered above the torus by material (dust and electrons) within the opening of the torus.

Our attempts to model observational data showed once more the inherent ambiguity: The same SED can be modelled with different parameter sets or even models. Therefore, additional information from observations is needed in order to be able to distinguish between different torus models.

2.5 Conclusions

In this chapter we present new radiative transfer simulations for dust tori of Active Galactic Nuclei. The dust density distribution and the geometrical shape of the torus model result from a hydrostatic equilibrium in which gravitational and centrifugal forces of the nuclear stellar distribution and the central black hole are balanced by pressure forces due to the turbulent motion of the clouds. Spectral energy distributions (SEDs) and surface brightness distributions are obtained by a fully three-dimensional treatment of the radiative transfer problem.

After fixing as many parameters of the model as possible by observational constraints, we undertake an extensive parameter study by varying dust properties, dust masses and other factors. It shows that our modelling is able to explain mean observed spectral energy distributions (SEDs) for classes of Active Galactic Nuclei as well as for individual objects.

Obviously, the innermost part of the tori close to the central energy source is crucial for the determination of SEDs in the mid-infrared wavelength range. Specifically, we found that any realistic model has to incorporate the fact that sublimation radii for varying dust grain sizes and dust composition differ considerably. Using mean dust characteristics according to the MRN dust model (see Sect. 2.2.3) instead leads to incorrect temperature distributions and SEDs. Even with this refinement, the model cannot explain the recent interferometric observations of the MIDI instrument, as reported by Jaffe et al. (2004), which show a deepening of the silicate absorption feature in the correlated flux – effectively sampling the central few parsec of the dust distribution. In order to reproduce these results, a temperature distribution shallower than in our model would be required. We find that introducing a $|\cos\theta|$ radiation characteristic for the primary radiation source does not yield significant changes. In a next step, we will introduce a clumpy structure of our dust configuration (see Chapter 3). Gaps within the dust distribution should then lead to direct heating of clumps in the outer part of the torus and thus producing a shallower mean temperature distribution. Biasing the grain size distribution of the dust towards larger grains as proposed by several authors (e. g. Laor & Draine 1993; Maiolino et al. 2001) does not yield a reduction of the emission feature of type I objects for the case of our dust density distribution.

With the present examination of the *Turbulent Torus Model* for dust distributions in AGNs, we made a first step towards the introduction of more physics into the modelling of the torus emission. We demonstrated that a model based on physical assumptions reproduces the SEDs both on kiloparsec and parsec scales as well as previous models in which the shape and size of the dust distribution are free parameters (*e.g.* Pier & Krolik (1993); Granato & Danese (1994); Manske et al. (1998); Nenkova et al. (2002); van Bemmel & Dullemond (2003)).

As pointed out in Sect. 2.2.1, this kind of stationary modelling cannot account for all physical effects present in such an environment. In a further step, hydrodynamic simulations in combination with radiative transfer calculations should enable us to take at least some of these uncertainties into account. The main effects are continuous energy feedback by supernovae explosions and mass injection by stellar winds (see Chapter 4).

With the first interferometric observations at hand, however, the problem becomes more challenging: the wide range in observable scales from hundreds of parsec down to *one parsec* requires not only to reproduce global SEDs of the torus but also to describe its shape, structure and temperature stratification correctly. In addition, these detailed observations are an essential step to resolve the ambiguities that are present in current global models of dusty tori in Active Galactic Nuclei.

The work of this chapter has already been published in Schartmann et al. (2005).

Chapter 3

Clumpy models of AGN tori

In this chapter, we present three-dimensional models of clumpy AGN-tori, where the torus is modelled as a wedge-like shaped disk. Dusty clouds are randomly distributed throughout the volume, by taking the dust density distribution of the corresponding continuous model into account. We calculate spectral energy distributions as well as surface brightness distributions with the help of the three-dimensional Monte Carlo radiative transfer code MC3D. Subsequently, visibilities can be obtained and the principal differences between clumpy and continuous models are investigated. We find that the existence of the silicate 10 μm-feature in absorption or in emission depends delicately on the distribution and optical depth of clouds in the innermost part of the dust distribution. With this explanation, failure and success of previous modelling efforts can be understood. This is underlined with the help of several parameter variations. After adapting our clumpy standard model to the circumstances of the Seyfert II Circinus galaxy, it can qualitatively explain recent mid-infrared interferometric observations done with MIDI, as well as high resolution spectral data.

3.1 Introduction and motivation

As already discussed in Chapter 2, most groups working in the field concentrated on smooth dust distributions in their simulations so far (e. g. Pier & Krolik 1992; Granato & Danese 1994; van Bemmel & Dullemond 2003; Schartmann et al. 2005). This is mainly caused by the lack of appropriate (3D) radiative transfer codes and computational power. Such models are able to describe the gross observable features of these objects (see Chapter 2). Problems arise from too strong emission features of silicate dust (SiO) compared to the observations, when looking directly onto the inner rims of the model structures (face-on views). They had never been observed at that time, although nearly all models showed them for the face-on view. Therefore, large theoretical effort was undertaken in order to find models showing SiO absorption features in the edge-on case, but no SiO feature at all in the face-on case. The most promising idea was to solve the problem naturally by splitting the dust distribution into single clouds. This was first attempted by Nenkova et al. (2002). They used a one-dimensional code for the simulation of radiative transfer through single clumps and, in a second step, assembled the torus and its emitted spectral energy distribution by adding many clouds of different aspect angles with the help of a statistical method. They could show that

a clumpy dust distribution of this kind can significantly smear out the prominent SiO emission feature of the SEDs of type I objects (face-on view onto the torus) at 10 μm for a large range of parameter values. No more fine-tuning was needed, like in the previously proposed solutions with the help of continuous models. Real two-dimensional radiative transfer calculations were undertaken by Dullemond & van Bemmel (2005). Clouds were modelled as concentrical rings. A direct comparison between these kind of clumpy models and the corresponding continuous models did not show evidence for a strong suppression of the silicate feature in emission of clumpy models compared to continuous ones.

Meanwhile, silicate features in moderate emission were found with the help of the Infrared Spectrograph (IRS) onboard the Spitzer space telescope (e. g. Siebenmorgen et al. 2005; Hao et al. 2005; Sturm et al. 2005; Weedman et al. 2005). For these kind of studies, it is superior to other available facilities, due to its high sensitivity and the coverage of a wavelength range including both silicate features (at 9.7 μm and 18.5 μm) and the surrounding continuum emission. SiO emission features in different kind of objects were found, ranging from very luminous quasars down to week LINERS. These findings are in good agreement with a geometrical unification with an optically thick dusty torus, as silicate emission features can already be produced even in the simplest models.

Therefore, new challenges for detailed three-dimensional radiative transfer simulations arise: Depending on the focused object, the silicate emission features have to be present or not and the underlying physical mechanism for the different appearances has to be found. The same model has to be able to explain the X-ray variability and all the predictions of the unification principle, as discussed in Section 1.3.

A first step in this direction was undertaken by Hönig et al. (2006). They apply a similar method as Nenkova et al. (2002), but use a 2D radiative transfer code for the simulation of SEDs of individual spherical clumps at various positions in the torus and with various illumination patterns: directly illuminated and/or illuminated by reemitted light of surrounding clouds. In a second step, these clouds are distributed according to analytical models by Vollmer et al. (2004) and Beckert & Duschl (2004) and their illumination pattern there. A comparison of the resulting spectral energy distributions (SEDs) and images with spectroscopic and interferometric observations shows good agreement. In this scenario, dust is accreted from further out of the galaxy due to angular momentum transport triggered by cloud-cloud collisions. The clumps are self-gravitating and close to the shear-limit given by the gravitational potential of a nuclear star cluster and a supermassive black hole, which puts constraints on the cloud mass and size. This model is characterised by a large number of small clouds with a very large optical depth, especially close to the centre. We compare our models with recent models of Hönig et al. (2006) in Section 3.4.3.

In this chapter, we address the question of the different appearance of the relative strength of the silicate features by implementing fully three-dimensional radiative transfer calculations through a clumpy dust distribution and discuss the possible mechanisms causing this behaviour. In Section 3.2, a description of the model we use is given, before we present the basic results (Section 3.3) of several parameter studies and discuss the findings (Section 3.4), as well as differences and similarities to other models. In Section 3.5 we interpret our results in terms of MIDI interferometric observations and compare them to data of the Circinus galaxy. In the last Section (3.6), we draw our conclusions.

3.2 The model

In this section, we first motivate the construction of our standard model. Then, a short overview over the used method is presented, before we discuss numerical limitations.

3.2.1 Assembly of our clumpy standard model

In this chapter, we aim at working out the different behaviour and special signatures of a three-dimensional clumpy dust arrangement in comparison with continuous dust distributions. Therefore, we apply a very simple, wedge-like torus geometry. As the opening angle directly coincides with the model space itself, this helps to gain resolution, compared to our previously used *TTM*-models, where the simulation of the whole θ-range is necessary.

The cloudy dust distribution is set up on a spherical three dimensional grid. To obtain the clumpy density structure, the following procedure is applied: A random number generator (RAN2 taken from Press et al. 1992) determines the radial coordinate of the clump centre, which is equally distributed between the inner and outer radius. The θ and ϕ coordinates are chosen such that the resulting points are equally distributed on spherical shells [1]. In a second step, the spatial distribution found so far is coupled to the dust density distribution of the continuous model:

$$\rho_{\mathrm{cont}}(r, \theta, \phi) = \rho_0 \, r^{\alpha} \tag{3.1}$$

Clump radii vary with distance from the centre according to a distribution

$$a_{\mathrm{clump}} = a_0 \, r_{\mathrm{clump}}^{\beta}. \tag{3.2}$$

All cells within this clump radius are homogeneously filled with dust, while all clumps possess the same optical depth, measured along a radial ray through the clump centre. An additional side condition is that clumps always have to be completely contained within the model space, but are allowed to intersect. Such a combination of intersecting clumps will be called *cloud* from now on. These intersecting clumps can cause overdensities where the intersection happens, as there, the density is added up. This results in effects, visible in surface brightness distributions, as can be seen below. A clump size distribution as described above seems to be reasonable, as shear forces due to the differential rotation increase towards the centre. Therefore, clouds get more easily disrupted in the inner part of the torus. Furthermore, clouds get compressed when moving towards the centre due to the increasing ambient pressure.

All other routines and algorithms used in this chapter are identical with the model described in 2.2.1 and will only be mentioned briefly in Section 3.2.2.

The main model parameters of the continuous and clumpy distributions are summarised in Tab. 3.1. The numerical values refer to our clumpy standard model. With these parameters, the dust density distribution shown in Fig. 3.1 results. The torus possesses a volume filling factor of 30% and the dust mass was chosen such that the optical depth of the torus within the equatorial plane (averaged

[1] This procedure leads to a concentration of clouds in the inner part of the computational domain, compared to an equal distribution within the whole volume. Though, it helps to obtain the desired effects, as we will see below.

both models		additional in clumpy model	
Parameter	Value	Parameter	Value
$R_{\rm sub}$	0.39 pc	$N_{\rm clump}$	400
$R_{\rm out}$	50 pc	β	1.0
$\theta_{\rm op}$	45°	a_0	0.2 pc
$\left\langle \tau^{\rm equ}_{9.7\,\mu{\rm m}} \right\rangle_\phi$	2.0	$\tau_{9.7\,\mu{\rm m}}$	0.38
α	-0.5		

Table 3.1: *Main model parameters for continuous and clumpy models: inner ($R_{\rm sub}$) and outer ($R_{\rm out}$) radius of the torus, half opening angle of the torus ($\theta_{\rm op}$), optical depth within the equatorial plane of the whole torus $\left(\left\langle \tau^{\rm equ}_{9.7\,\mu{\rm m}} \right\rangle_\phi\right)$ and the exponent of the radial density distribution of the continuous model (α). Additional parameters of the clumpy models: Number of clumps ($N_{\rm clump}$), exponent (β) and proportionalisation constant (a_0) of the clump size distribution and the optical depth of each clump ($\tau_{9.7\,\mu{\rm m}}$).*

over all angles ϕ) reaches a value of 2 at 9.7 µm. The resulting absorption column densities are in concordance with observations done with the IRS spectrometer onboard Spitzer (see e. g. Shi et al. 2006), when assuming a gas-to-dust-ratio of 250.

Following Nenkova et al. (2002), all clumps originally possess the same optical depth. For the case of our standard model, this is $\tau_{9.7\,\mu{\rm m}} = 0.38$ along a radial ray through the centre of the clump. As clumps are allowed to intersect, larger optical depths can occur within clouds, as densities are simply added up. The clumps intersect in approximately equal measure all over the radial range, slightly more at larger radii, where clouds are much larger in the standard model. Therefore, our procedure yields in some regions a continuous medium with clumpy structure embedded. But especially in the innermost part, single clumps can be distinguished. The corresponding continuous model has the same geometrical structure, continuously filled with dust according to the density distribution given in equation 3.1. Therefore, it is different to the continuous TTM-model in Chapter 2,

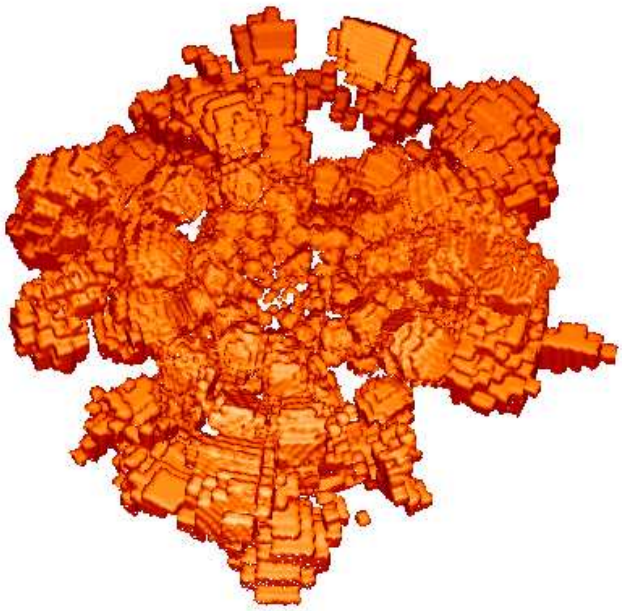

Figure 3.1: *3D visualisation of an illuminated surface of constant density (3% of the maximum value) of our standard clumpy torus model. The inclination angle of* 30° *corresponds to a Seyfert I type view onto the torus.*

which was a density distribution resulting from physical assumptions. These 2D-models showed a radial as well as a θ-dependence of the dust distribution, resulting in a density enhancement at the torus radius close to the midplane. Thus, many differences arise, as partly discussed below.

3.2.2 Further preconditions and methods

A very brief overview over the dust composition, the heating source and the numerical method of radiative transfer will be given in this section.

Concerning the dust composition, several authors claim that it should be altered towards larger grains and different composition compared to the dust within the interstellar medium of our direct vicinity. This was found for example with the help of interferometric (Jaffe et al. 2004) and spectrographic (Sturm et al. 2005) observations of AGN. From the theoretical point of view, this seems to be a reasonable detection as small particles are likely to be destroyed in the very close environment of the central energy source of the AGN. These kind of changes in the dust composition and the grain size distribution can account for different shapes of the silicate features as e. g. found by Jaffe et al. (2004). As we are more interested in the behaviour of the height or depth of the silicate feature and for the sake of simplicity and comparability, we use the standard galactic dust model proposed by Mathis et al. (1977), but we split it into 3 different grain species with 5 different grain sizes each. Taking different sublimation radii of the various grains into account then partially accounts for the destruction of small grains as mentioned above, as they possess larger sublimation radii.

The dust distribution is heated by a point-like, central accretion disk with a compiled spectral energy distribution, which resembles a mean quasar spectrum (see Fig. 2.4). The radiation characteristic is chosen to follow a $|\cos(\theta)|$-law for all wavelengths. For the simulations shown in this chapter, the resulting distribution is normalised to a bolometric luminosity of $1.2 \times 10^{11}\,L_{\odot}$, if not stated otherwise.

In order to obtain the temperature, spectral energy distributions as well as surface brightness distributions of the dusty torus, we use the three-dimensional radiative transfer code MC3D (Wolf et al. 1999). We apply the Monte-Carlo procedure mainly for the calculation of temperature distributions, whereas spectral energy distributions and the surface brightness maps for dust reemission are obtained with the included raytracer. The code itself has been tested extensively against other codes for 2D structures (Pascucci et al. 2004) and we also performed a direct comparison for the special case of AGN dust tori with the simulations of Granato & Danese (1994), one of the standard torus models to compare to, calculated with his grid based code (see Fig. 2.5). The main advantage compared to other codes is MC3D's capability to cope with real three-dimensional dust density distributions, needed for a realistic modelling of the dust reemission from a clumpy torus. We added procedures, so that the sublimation surfaces of the different grains of our dust model can be calculated after inserting the density distribution of the clumps. In a three-dimensional, discontinuous model, we also expect the sublimation to happen along unequally shaped surfaces.

3.2.3 Resolution study

For most of the simulations shown in this chapter, we use a separation of the computational domain into 31 cells in θ direction. The number of cells in ϕ and radial direction are chosen to be 120 and 97, respectively. With this choice, the cells have comparable extension in every coordinate

direction. In total, this results in 360 840 cells. This is about the largest grid size possible on our opteron machines without parallelisation and without giving up the important separation of the dust distribution into several grain species (see Section 3.2.2). It results in a memory usage of approximately 26 Gigabytes. In Fig. 3.17 the number of cells per clump is plotted against the radial position of that clump. The clumps have on average 272 cells varying between 245 and 311 cells per clump, independent of radial position. This is achieved by the combination of a logarithmically spaced grid in radial direction and because clumps grow linearly with distance from the centre.

In order to check limitations of radiative transfer problems due to resolution, different approaches are made. Hönig et al. (2006) use a very stringent criterion for the radiative transfer simulations of their single clump models. Namely, they demand convergence of the temperature difference between the inner and outer rim of the cloud. This is necessary, as their model features very high optical depths ($\tau_{0.55\,\mu m} \approx 250$ for a clump at the sublimation radius of the torus with a radial size of $a_{clump} = 0.02$ pc), much larger than in our standard model with a clump optical depth of $\tau_{0.55\,\mu m} \approx 3$ for a clump size of 0.08 pc near the sublimation radius.

The temperature distribution

Another condition often referred to is that temperature gradients should be well resolved and temperature differences between neighbouring cells should not exceed 10 to 20%. Therefore, in radiative transfer simulations where the main heating of the dust results from a central source, the grid is logarithmically divided in radial direction. Fig. 3.2a) shows a histogram of the relative temperature differences of all cells of our standard model in radial and polar direction (only differences between dust filled cells are taken into account). After integration, one finds that less than 7% (2.5%) of the temperature differences in radial direction are steeper than 10% (20%). In polar direction we find 11% (5%) for the case of temperature gradients larger than 10% (20%). The polar direction is slightly worse, as the grid is equally spaced in this direction, while a primary source with a $|\cos(\theta)|$-radiation characteristic is used. Finally, it should be noted that the temperature distribution discussed here is only one out of 15 temperature distributions, which are calculated separately. Therefore, the signal-to-noise-ratio of the single temperature distribution is reduced appreciably when calculating the spectral energy distribution or the surface brightness distributions.

Dependence on the number of photon packages and resolution of the whole torus model

In all SEDs presented below, only pure dust reemission is shown. If not stated otherwise, we use an azimuthal viewing angle of 45°. In the upper panel of Fig. 3.2b), we show dust reemission SEDs for our standard clumpy model (blue curves, $2 \cdot 10^5$ monochromatic photon packages) and for the same model, but with twice as many photon packages used for the simulation of the temperature distribution (red graphs). Despite the noise in the single temperature distributions, we find almost identical behaviour. This is understandable, as the SED results from the temperature distributions of the 15 different grains. Only slight deviations are visible at small wavelengths for the face-on case. In the lower panel of Fig. 3.2b), a resolution study is shown, where the red curve shows the result for our high resolution standard model (red curves) and the blue lines refer to a model with a factor of roughly three less grid cells. Small deviations are only visible below and beyond the mid-infrared wavelength region, we are mostly interested in. We obtain identical results within the range of the silicate feature.

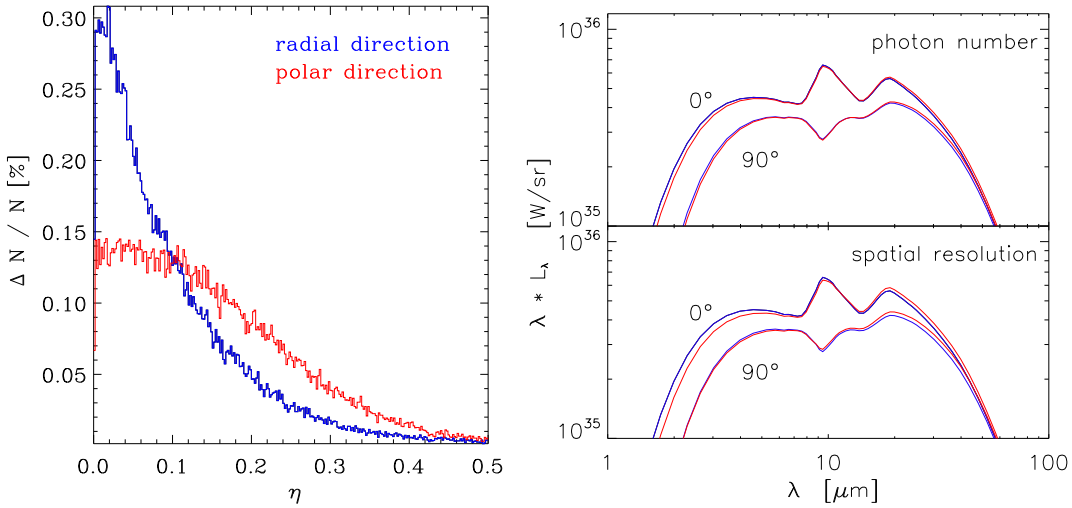

Figure 3.2: *Quality tests:* **a)** *Histogram of relative differences in the temperatures of neighbouring grid cells (for the smallest silicate grains) split into radial and polar direction. See text for further explanation.*
b) *Upper panel: SEDs for a photon number study. The blue curves refer to our standard model and the red graphs result after doubling the number of photon packages. Lower panel: SEDs for a resolution study: high resolution (red curves – our standard model) and a factor of 3 reduced number of grid cells (blue curves). Shown are the inclination angles* 0° *and* 90°.

Single clumps

Looking at the SEDs of a single clump at our standard resolution and a twice as high resolution in all coordinate directions for the case of our standard clumpy model and a clump size of 0.4 pc in radius in a distance of 2 pc from the centre (see Fig. 3.3a), one finds that the differences in the integrated total flux are roughly 4% for the SEDs with $i = 0$. The higher resolution models are shifted towards shorter wavelengths due to the higher temperatures reached in the innermost[2] cells of the clump in the higher resolved model, which are averaged out in case of lower resolution. The relative height of the silicate feature as well as its appearance stays roughly the same. The same can be said about the models with four times higher optical depth (see Fig. 3.3b). The largest errors occur at short wavelengths. This is where the direct radiation of the central source would dominate over dust reemission for some of the inclination angles, which is not shown in our calculations.

These kind of steep temperature gradients only appear in directly illuminated clumps of the very vicinity of the radiation source. Some of these differences also occur from deviations of the shape of the clump's rim with resolution. Integrated over a number of clumps, such differences decrease, as can be seen in the resolution study for the whole torus model in Fig. 3.2b (see also the case of our clumpy and filamentary hydrodynamics models in Fig. 4.40). Though, a higher spatial resolution would be favourable, but is not manageable with a serial code and the currently available computational power. Therefore, we focus on relative changes within the parameter studies in this chapter.

[2] closest to the central radiation source

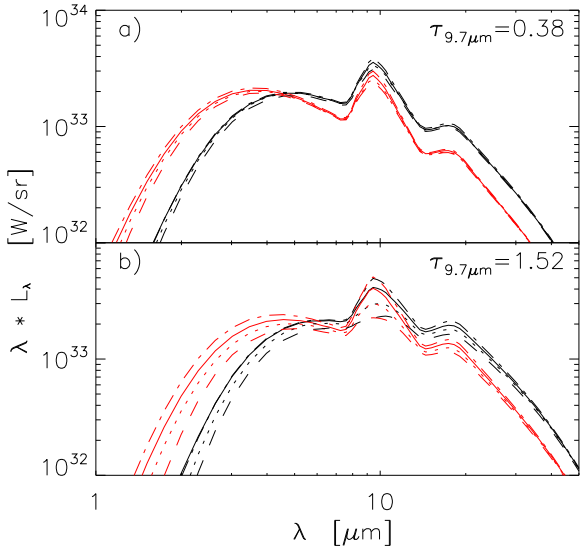

Figure 3.3: *SEDs for a single clump at two different optical depths, as indicated in the upper and lower panel. It is located at a distance of* 2 *pc and has a radius of* 0.4 *pc, is simulated with the resolution of our standard model (black) and 2 times the resolution in every coordinate direction (red curves). For each simulation, four inclination angles (in the sense of the usual torus inclination angles) are shown:* $i = 0°$ *(solid line),* 45° *(dotted line),* 90° *(dashed line, behind the clump) and* 270° *(dash-dotted line, heating source in front of the clump).*

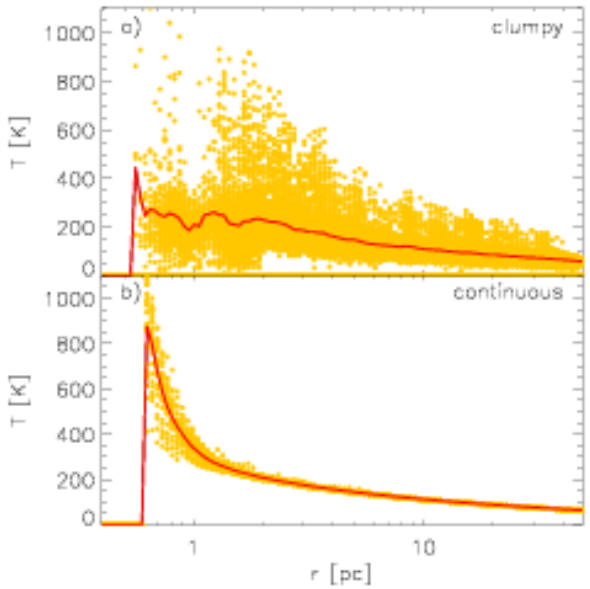

Figure 3.4: *Comparison between radial temperature distributions (for the smallest silicate grains) for all cells of the clumpy standard model (panel a) with the temperature distribution of the corresponding continuous model (panel b). The red curve indicates the temperature averaged over all angles* θ *and* ϕ*.*

3.3 Results

In the following, we mainly concentrate on parameter studies showing the differences between our clumpy and the corresponding continuous models. The main focus will lie on the behaviour of the silicate feature. With the new Spitzer results (see Section 1.3), theoretical models have to be able to explain silicate features in absorption as well as moderate emission, when looking face-on onto the torus. At the same time, moderate silicate absorption features for the Sy II case have to be obtained. Within the discussion section, we present a possible explanation for the reduction of the silicate feature. In all SEDs discussed below, only pure dust reemission SEDs are shown. If not stated otherwise, we use a single azimuthal viewing angle of 45°.

3.3.1 Temperature distribution

In Fig. 3.4, the temperature distribution in all θ and ϕ directions is plotted for the clumpy standard model and in comparison for the continuous model. The red curves give the radial temperature profile, averaged over all (θ, ϕ)-directions with nonzero temperature. It is evident that the spread of temperature values is much larger for the clumpy models, as it highly depends on how single

clumps are illuminated. Concerning the continuous model, the temperature values of the single cells approach the average value from 2 pc outwards. Further in, the scatter is higher, which is caused by the radiation characteristic of the primary source in θ-direction. This leads to higher temperatures further away from the midplane.

3.3.2 Viewing angle dependence of our standard model

Fig. 3.5a) shows the dependence of the spectral energy distributions on the inclination of the torus. One can only see a clear distinction between lines of sight within the dust free funnel and within the wedge-shaped disk. Therefore, the 0° and 30° inclinations are nearly identical, as well as the 60° and the 90° angles. In this respect, our clumpy models resemble the continuous wedge models, as already reported by Granato & Danese (1994). This is caused by the relatively large volume filling fraction and the large clouds in the outer part of the torus. In Fig. 3.5b), the azimuthal angle is varied for a constant inclination angle of 60°. Nearly identical SEDs result. This can also be explained by the large volume filling factor.

Fig. 3.6 shows the dependence on the inclination angle for images. Especially interesting is that the different inclination angles look much more similar compared to the continuous case (see Fig. 3.14). There, the images at larger inclination angles are dominated by the boundaries of the disk, which are not as well defined in the clumpy case. In the close-up (Fig. 3.7), the basic features of our model are directly visible, as one can see the different illumination patterns of clouds: Clouds in the innermost part are fully illuminated and, therefore, show bright inner rims and cold outer parts. Other clouds are partly hidden behind clouds further in and appear with bright spots only. A second effect comes from intersecting clumps, increasing the dust density at these locations, which then results in a steeper temperature gradient compared to neighbouring clouds. In Fig. 3.7, the central source is shown as well together with the dust reemission. Noteworthy, at all of the inclination angles, it possesses the highest surface brightness, even in the case of edge-on view, which in this particular case is caused by an optically thin line of sight ($\tau_{9.7\,\mu m} = 0.71$) towards the central point source.

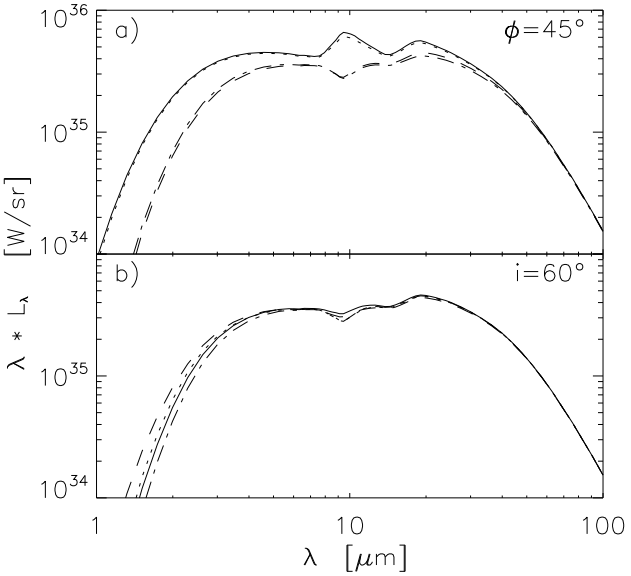

Figure 3.5: *Dependence of the spectral energy distributions on the viewing angle:* **a)** *different inclination angles for a common azimuthal angle* $\phi = 45°$. *Inclination angles shown are:* 0° *(solid line),* 30° *(dotted line),* 60° *(dashed line),* 90° *(dashed-dotted line),* **b)** *different azimuthal angles* ϕ *for a common inclination angle of* $i = 60°$. *Azimuthal angles shown are:* 0° *(solid line),* 45° *(dotted line),* 180° *(dashed line),* 110° *(dashed-dotted line).*

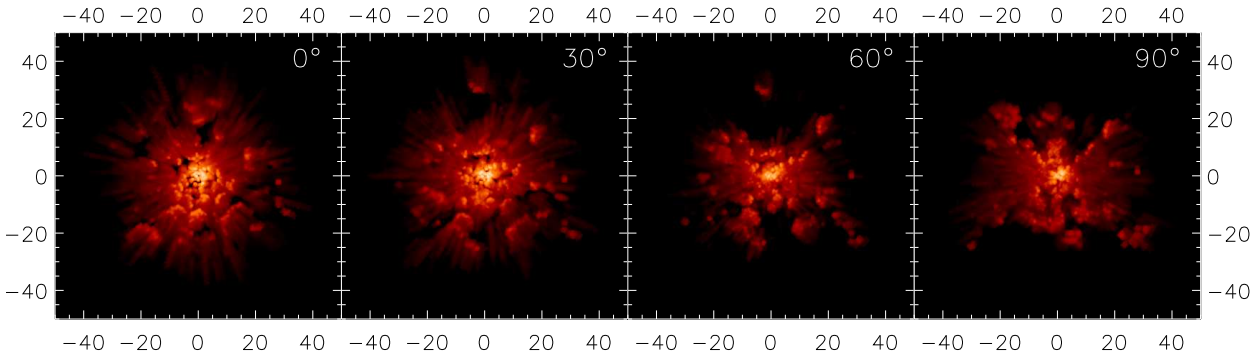

Figure 3.6: *Dependence of the surface brightness distributions on the inclination angle for a wavelength of 12.0 µm. Inclination angles shown are:* 0°, 30°, 60°, 90°. *The images are given in logarithmic scaling with a range of values between the maximum value of all images and the* 10^{-5}*th fraction of it. The physical scale is given in pc.*

3.3.3 Different realisations of the clumpy distribution

As previously discussed, SEDs of dust reemission depend delicately on the distribution of dust in the innermost region. Changing the random arrangements of clumps – as done in this section – therefore, is expected to cause huge changes of the SEDs, especially for the case of a small number of clouds. The second important parameter is the optical depth[3] of the single clumps. The larger it is, the stronger the dependence on the dust distribution in the innermost region. For the case of our modelling, the small number of clouds is expected to cause huge differences in the observed SEDs. But this effect is partially compensated by – in most of the simulations – optically thin individual clumps, leading to more similar behaviour.

In Fig. 3.8, three different random distributions are directly compared in terms of SEDs (first column) and images at a wavelength of 12 µm. The images in the second column correspond to the solid line, the third column to the dotted line and the fourth column to the dashed line. The first row shows the face-on view ($i = 0°$), the second row an inclination angle of $i = 60°$ and the last row the edge-on view ($i = 90°$) of the torus. Looking at the simulated SEDs and matching them

[3] If not stated otherwise, optical depth always refers to a wavelength of 9.7 µm.

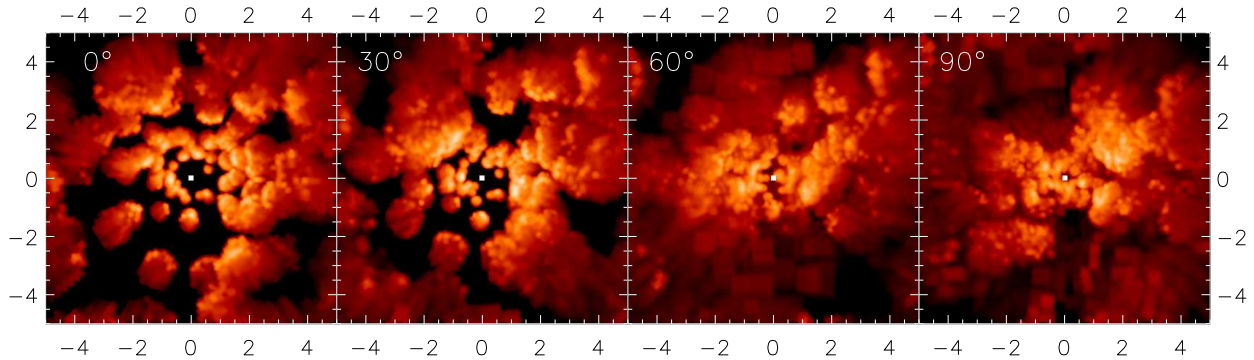

Figure 3.7: *Close-up of an inclination angle study for a wavelength of 12.0 µm (with inclusion of the central heating source). Inclination angles shown are:* 0°, 30°, 60°, 90°. *The images are given in logarithmic scaling with a range of values between the maximum of all images and the* 10^{-3}*rd part of it. The labels are given in pc.*

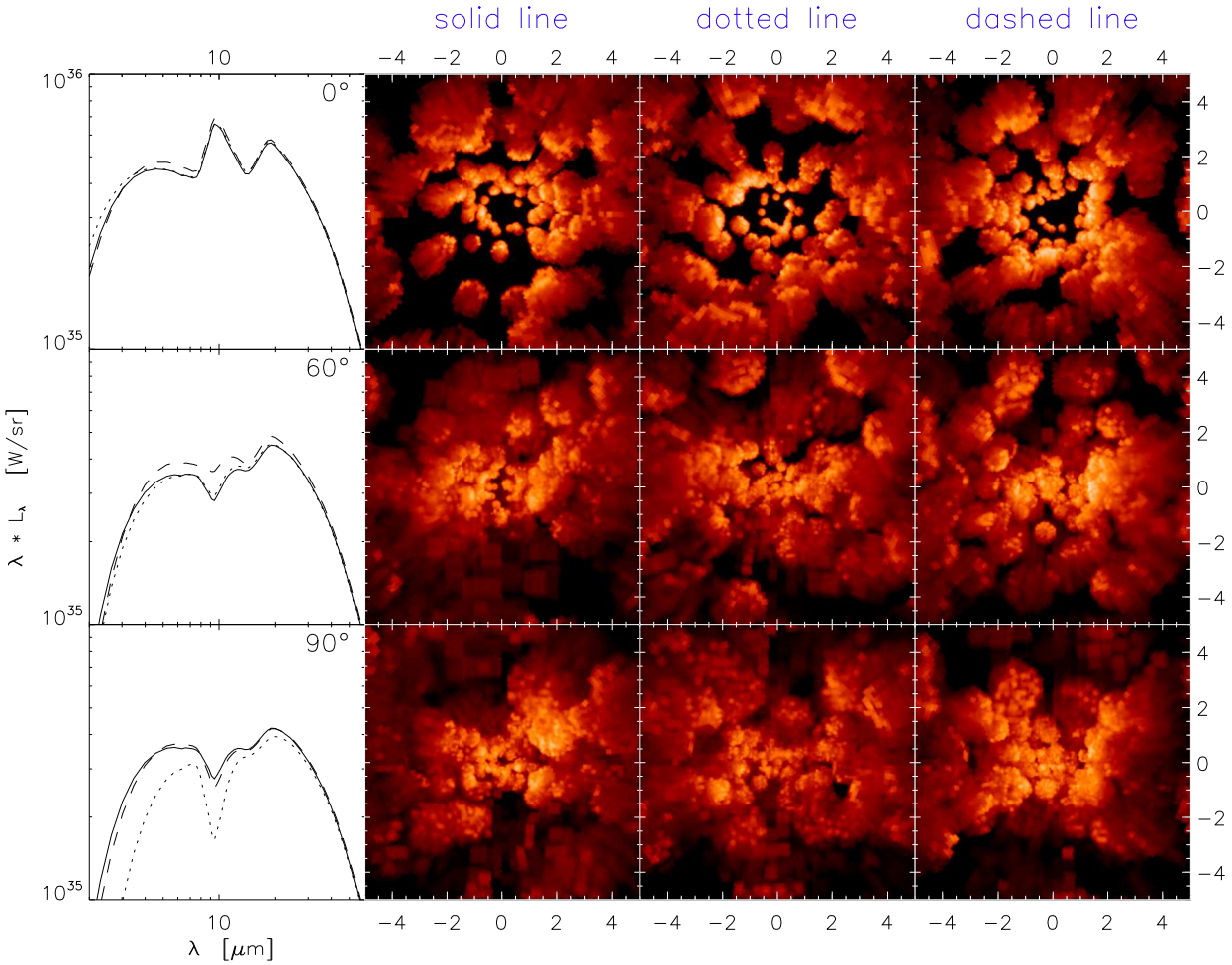

Figure 3.8: *Different random arrangements of clumps. The rows show three different inclination angles:* 0° *(first row),* 60° *(second row),* 90° *(third row). Given in columns are the spectral energy distributions (first column) and the images at* 12 µm *for the three different random cloud arrangements (column 2 to 4). Here, the solid line in the SED corresponds to the first column of images, the dotted line to the second and the dashed line to the third column. Images are given in logarithmic color scale ranging from the maximum of all images to the* 10^{-3}*rd part of it. Labels denote distance to the centre in pc.*

with the images, the following results can be read off (compare to Fig. 3.8):

At 0° inclination angle (upper row), we observe nearly identical spectral energy distributions. The dotted line (corresponding to the third column) shows slightly enhanced flux at short wavelengths, as a larger number of clouds is close to the central source. In the last column, we have enhanced density in an almost ring-like structure with a radius of roughly 2 pc, resulting in an enhancement of flux around 5 µm. For the case of the middle row ($i = 60°$), larger deviations are only visible for the case of the dashed line (fourth column). Here, the silicate absorption feature nearly vanishes, as more primarily illuminated clouds are directly visible (brighter in the centre) and, therefore, partly compensates the absorption feature. At an inclination angle of 90° (third row), the dotted line shows a much deeper silicate feature in absorption and the Wien branch is shifted to longer wavelengths, which is an indication of stronger extinction on the line of sight. This can also be seen in the dimmer central part of the middle image (less direct radiation can be obtained from the central directly illuminated clouds). The other curves show almost identical behaviour.

3.3.4 Wavelength dependency

Fig. 3.9 shows the wavelength dependence of our standard model. At short wavelengths, the hottest inner parts are the brightest and in addition to that, some spots further out are visible. These spots are either directly illuminated clumps and/or possess extraordinarily high dust density due to intersecting clumps. At the longest wavelengths, emission arises from clumps all over the torus, as colder dust emits maximally at these wavelengths. This dust is spread over a larger volume, due to the steeply decreasing temperature distribution at small radii. Furthermore, the extinction curve has dropped by a large factor at these wavelengths and, therefore, the torus gets optically thin and the whole range of cloud sizes is visible.

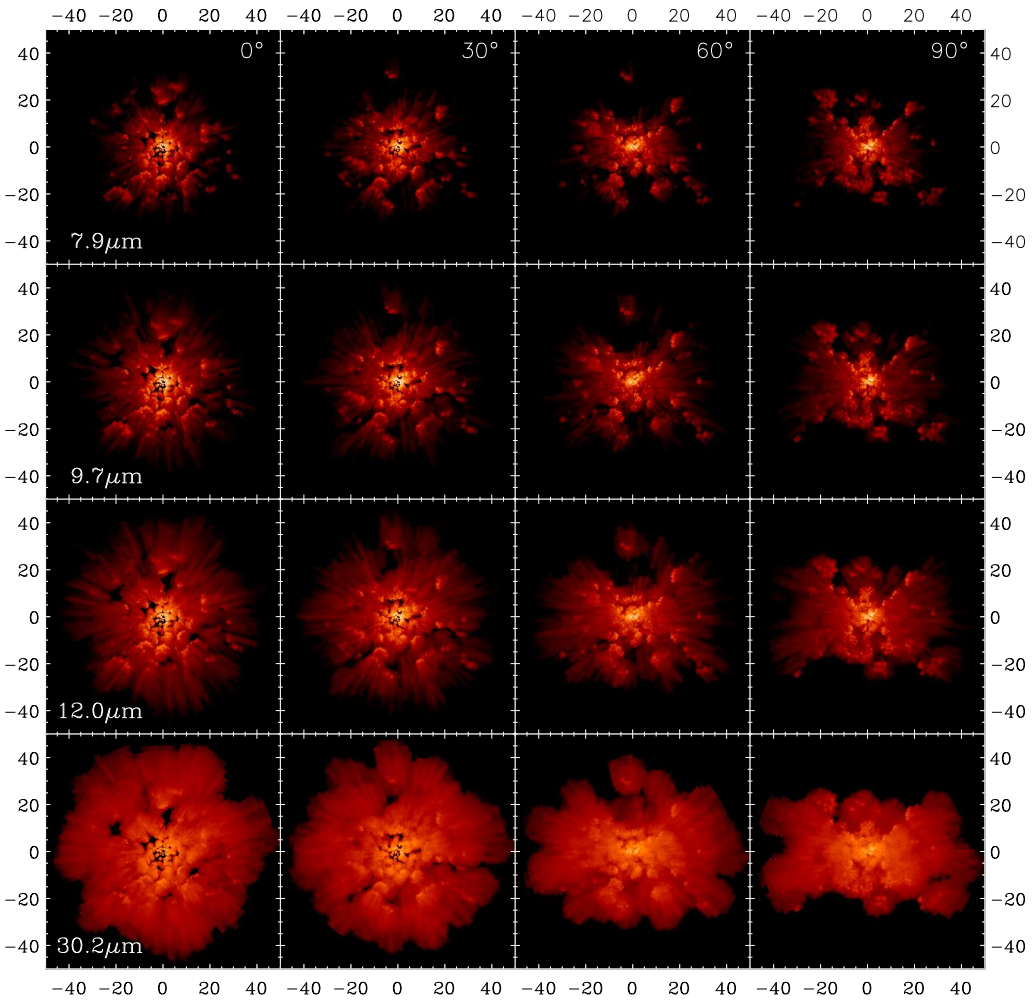

Figure 3.9: *Wavelength dependence of the surface brightness distributions:* $\lambda = 7.9\,\mu$m *(upper row),* $\lambda = 9.7\,\mu$m *(second row),* $\lambda = 12.0\,\mu$m *(third row) and* $\lambda = 30.2\,\mu$m *(lower row). Within the rows, the inclination angle changes from face-on view (leftmost panel) over* $i = 30°$ *and* $60°$ *to* $90°$ *(rightmost panel). The images are given in logarithmic scaling with a range of values between the global maximum of all images and the* 10^{-5}th *fraction of it.*

3.3.5 Study of different volume filling factors

Within this parameter study, the volume filling factor is changed. Starting from the standard model with a volume filling factor of 30% and 400 clumps within the whole model space, we halved it once by distributing only 160 clumps within the calculation domain and doubled it, for which 1500 clumps were needed due to the applied procedure of randomly distributing clumps.

The resulting surface brightness distributions at $\lambda = 12.0\,\mu$m are shown in Fig. 3.10 with the three models given in different rows and for four different inclination angles: $i = 0°$, 30°, 60°, 90°. In the case of the lowest volume filling factor, individual clouds are visible. The distribution of surface brightness of these individual clouds clearly resembles the temperature structure within single clumps. The directly illuminated clumps are hotter and, therefore, appear brighter. When adding more and more clumps (increasing the volume filling factor), the chance to directly illuminate clumps further out decreases and at higher filling factors it is only possible for clumps close to the funnel. This is clearly visible at higher inclination angles: the higher the volume filling factor, the clearer the x-shaped feature appears, as only clumps within or close to the funnel can be directly illuminated. At a volume filling factor of 60%, the surface brightness distribution looks very similar to the one of the corresponding homogeneous model (compare to Fig. 3.14). At large factors and close to edge-on, substructure is only visible from clouds in viewing direction towards the cones.

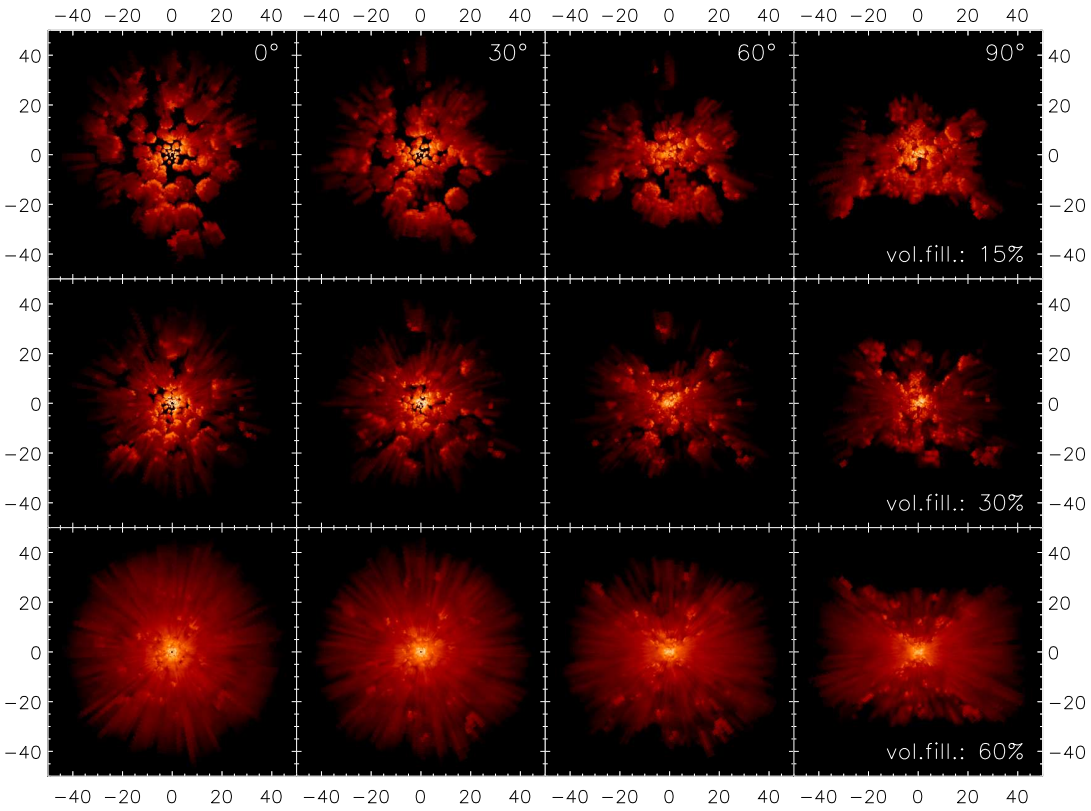

Figure 3.10: *Different volume filling factors:* 15% *(upper row),* 30% *(middle row),* 60% *(lower row) for* $\lambda = 12.0\,\mu$m*. From left to right, the inclination angle changes:* $i = 0°$, 30°, 60°, 90°*. The scaling is logarithmic with a range between the maximum value of all images and the* 10^{-5}*th fraction of it. Length scales are given in pc.*

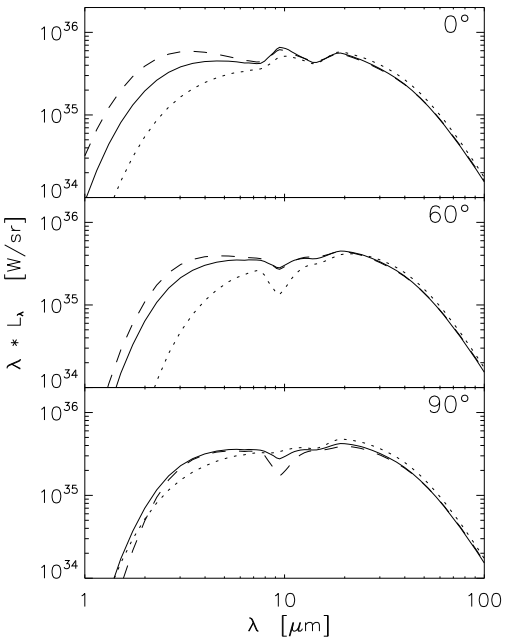

Figure 3.11: *Different volume filling factors:* 15% *(dotted line),* 30% *(solid line),* 60% *(dashed line). Rows show various inclination angles: i* = 0°, 60°, 90°. *The viewing angle in* ϕ*-direction is always* 45°.

The corresponding SEDs are shown in Fig. 3.11. In our model, the distribution of clumps is further concentrated in the central part of the torus (see Sec. 3.2) and the change of the volume filling factor is achieved by varying the number of clumps. Therefore, to double the volume filling factor, nearly a factor of four more clumps are needed, because of the decreasing volume of clumps towards the inner part and the less probable case of dicing a clump position in the outer part of the torus. This means that adding clumps in the inner part does not increase the volume filling fraction by a large amount. But filling the inner part with dust has large implications on the spectral energy distribution at short wavelengths, as we have seen in Chapter 2. This can also be seen in Fig. 3.11. The higher the volume filling fraction, the further the shape of the clumpy model SEDs resemble the corresponding continuous model (compare to Fig. 3.12). Concerning the silicate feature, it decreases in emission as the amount of dust at the appropriate temperature decreases as well. The silicate absorption feature at higher inclinations strongly depends on the viewing angle and especially for the model with the least number of clumps on the different distribution of clumps, as can be seen in the various strengths of the silicate feature for this model at the two Seyfert II inclinations.

3.3.6 Dust mass study

To study the dependence of the spectral energy distributions on the optical depth of the torus, we halved the enclosed dust mass of our standard model and also doubled it twice. This leads to an optical depth at 9.7 μm within the equatorial plane, averaged over all angles of ϕ of $\left\langle \tau^{\mathrm{equ}}_{9.7\,\mu\mathrm{m}} \right\rangle_{\phi}$ = 1.0, 2.0, 4.0 and 8.0. Single clumps then change from optically thin to optically thick ($\tau^{\mathrm{clump}}_{9.7\,\mu\mathrm{m}} = 0.19, 0.38, 0.76, 1.52$).

This causes the behaviour of the SEDs shown in Fig. 3.12, where it is also compared to the corresponding continuous models. Concerning the silicate feature in emission for the face-on case, we see a very similar behaviour of the SEDs of the clumpy and continuous model. Increasing the total optical depth leads to a flattening of the SED around the silicate feature. In addition to that, a slight shift of the maximum of the silicate feature towards longer wavelengths is visible for the case of

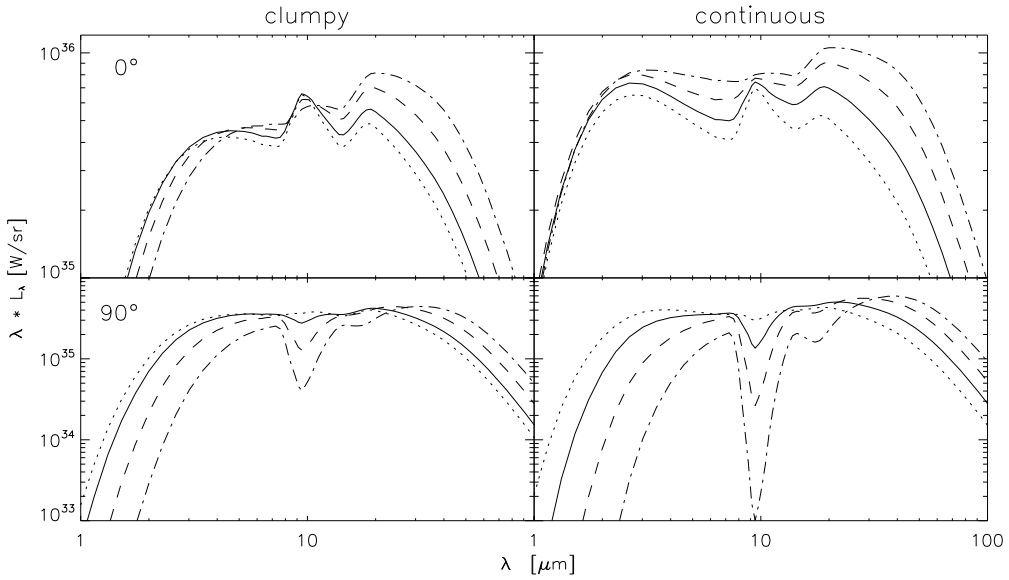

Figure 3.12: *SEDs for different enclosed dust masses. The first column shows the case for the clumpy models and face-on view (upper row) as well as edge-on view (lower row). In the second column continuous models are displayed. The solid line corresponds to the standard model, the dotted to half of the mass, the dashed double the mass and the dash-dotted to four times the mass.*

the highest dust mass, visible in the zoom-in of Fig. 3.12 around the silicate feature (see Fig. 3.13). This is simply due to the increasing underlying continuum towards longer wavelengths. Although the behaviour of the silicate feature is identical, the reasons differ. In the case of a wedge-like torus, the inner, directly illuminated walls are only visible through a small amount of dust. From step to step, the walls get more opaque and shield the directly illuminated inner rim better and better, decreasing the height of the silicate feature. This was not the case for our continuous *TTM*-models in Chapter 2. With them, it was not possible to significantly reduce the silicate feature height within reasonable optical depth ranges. This was caused by the totally visible, directly illuminated inner funnel (compare to Fig. 2.14). Therefore, in the wedge-shaped continuous models, the reduction of the feature is an artefact caused by the unphysical, purely geometrically motivated shape. Furthermore, it also involves very deep silicate absorption features for the edge-on case (see lower right

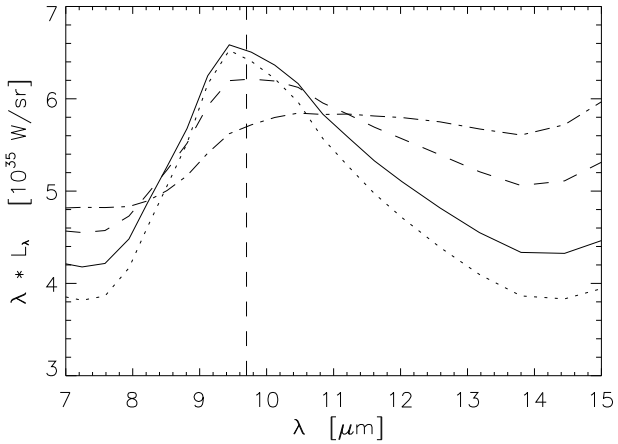

Figure 3.13: *Close-up of the spectrum between 7 and* 15 µm *of the face-on case of the dust mass study for the clumpy model in linear display. The lines are defined as in Fig. 3.12.*

panel in Fig. 3.12). Concerning the clumpy model, the explanation will be given in Sec 3.4.1.

Furthermore, one can see opposite behaviour of the Wien branches of the models: For the case of the clumpy torus model, increasing the optical depth means that the Wien branch moves to larger wavelengths, like expected for the edge-on case. This is understandable, when most of the directly illuminated surfaces of the clouds are then hidden behind other clouds, an argument which naturally is not valid if the clouds are too optically thin in the inner part.
For the edge-on case, we get qualitatively a comparable behaviour as in the continuous case, because of the large number of clumps and the same optical depth within the equatorial plane. But a very important difference can be seen in the appearance of the silicate feature in absorption: when we want to have only very weak silicate emission features in the Seyfert I case, a large optical depth is needed, resulting in an unphysically deep silicate feature in absorption in the Seyfert II case of the continuous models, whereas the silicate feature remains moderate for many lines of sight for the clumpy model, where we see a large scatter for different random arrangements of clumps (compare to Fig. 3.8).

Concerning surface brightness distributions (see Fig. 3.14), one can see that the objects appear

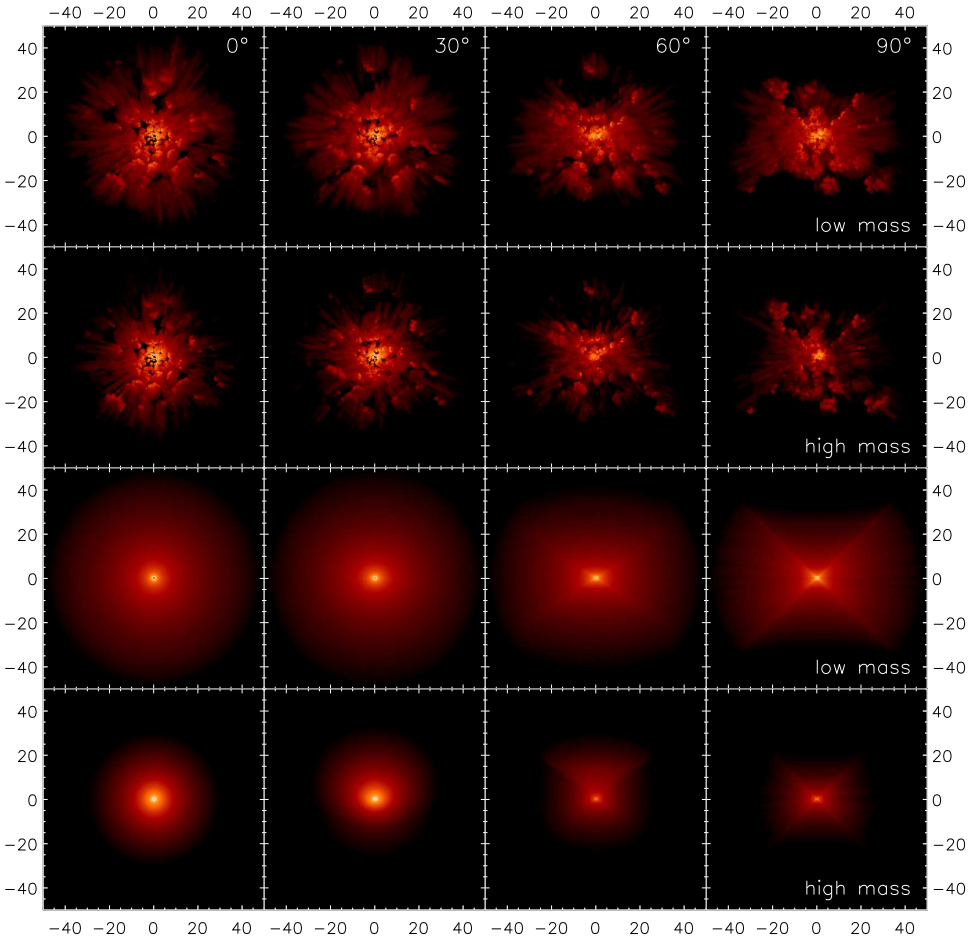

Figure 3.14: *Comparison of images at* 12 µm *for clumpy models (first two rows) and continuous models (last 2 rows) with half of the mass of the standard model and four times the mass. The inclination angles* $i = 0°$, $30°$, $60°$, $90°$ *are shown in different columns.*

smaller at mid-infrared wavelengths for the case of higher dust masses: the larger the optical depth, the brighter the inner region and the dimmer the outer part. This is caused by a steepening of the radial dust temperature distribution with increasing mass of the objects, as the probability of photon absorption increases in the central region. Especially for the continuous case, the asymmetry at intermediate inclination angles gets visible for larger optical depths, caused by extinction on the line of sight due to cold dust in the outer parts of the torus.

3.3.7 Concentration of clumps in radial direction

As already described in the model section (3.2), clump positions are chosen also in accordance with the density distribution of the corresponding continuous model. Therefore, changing the slope of this radial density distribution[4] leads to a different concentration of clumps along radial rays. In this section, we vary the slope of the distribution α from a homogeneous dust distribution ($\alpha = 0.0$) over $\alpha = -0.5$ to $\alpha = -1.0$. This leads to an enhancement of the clump number density towards the central region. In order to keep the volume filling fraction at a constant level of 30%, we need to increase the number of clumps, as their size decreases towards the central region. All clumps possess the same optical depth. Therefore, the total dust mass has to be decreased, in order to have a constant mean optical depth in the midplane. For an overview over the modified parameters see Table 3.2. This behaviour can be seen directly from the simulated images at 9.8 µm in Fig. 3.15,

[4]reminder: the density distribution was defined to be $\rho_{\rm cont}(r, \theta, \phi) = \rho_0\, r^{\alpha}$, see also Section 3.2.

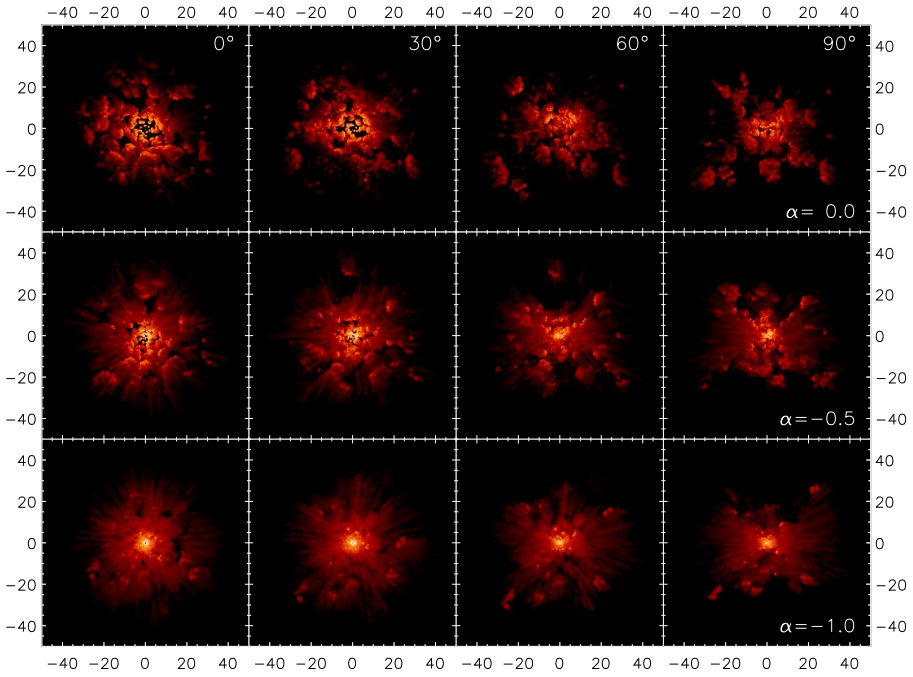

Figure 3.15: *Different slopes of the density distribution ($\rho_{\rm cont} \propto r^{\alpha}$) in the corresponding continuous model leading to different concentrations of clumps in radial direction. The slopes are: $\alpha = 0.0$ (upper row), $\alpha = -0.5$ (middle row), $\alpha = -1.0$ (lower row). From left to right, the inclination angle increases from face-on to edge-on: $i = 0°, 30°, 60°, 90°$. Shown are images at 9.8 µm with a logarithmic color scale ranging from the maximum of all images to the 10^{-5}th part of it. Labels denote distance to the centre in pc.*

Parameter	$\alpha = 0$	$\alpha = -0.5$	$\alpha = -1$
No. of clumps	250	400	900
Dust mass [$M_\odot$]	22950	12562	6418

Table 3.2: *Varied parameters of the clump concentration study.*

especially in the face-on case. In the upper panel, single reemitting clumps are visible in the central region. This changes more and more to a continuous emission for the case of the highest cloud concentration in the centre due to multiple clumps along the line of sight and intersecting clumps. At higher inclination angles, the stronger concentration leads to a sharper peak of the surface brightness.

The same behaviour is visible in the corresponding spectral energy distributions shown in Fig. 3.16. Decreasing the amount of dust in the centre near the heating source leads to decreasing flux at near-infrared wavelengths, whereas the flux at far-infrared wavelengths increases.

3.3.8 Dependence on the clump size distribution

In our clumpy standard model, a radially changing clump size proportional to the radial distance to the centre was chosen, in order to obtain an equal number of cells per clump due to the logarithmically spaced grid. In this section, we test the effects of decreasing the slope β[5] of the radial size distribution of the clumps. This is done in a way that the volume filling fraction as well as the optical depth in the midplane, averaged over all azimuthal angles ϕ remain constant. It is achieved by changing the proportionalisation constant of the clump size distribution a_0 and the total dust mass of the torus. Doing this leads to very well resolved clumps in the inner part (see Fig. 3.17). Beyond a distance of approximately 25 pc, the number of clumps drops below the value for our standard model.

Surface brightness distributions for the extreme case of a constant clump size are shown in Fig. 3.18.

[5]Please remember: $a_{\mathrm{clump}} = a_0\, r^{\beta}_{\mathrm{clump}}$, see also Section 3.2.1.

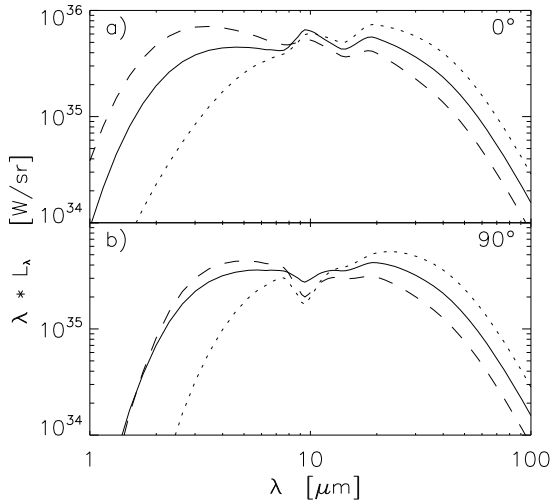

Figure 3.16: *Different slopes of the density distribution ($\rho_{\mathrm{cont}} \propto r^{\alpha}$) in the corresponding continuous model, leading to different concentrations of clumps in radial direction. The slopes are: $\alpha = 0.0$ (dotted line), $\alpha = -0.5$ (solid line), $\alpha = -1.0$ (dashed line):* **a)** *face-on,* **b)** *edge-on.*

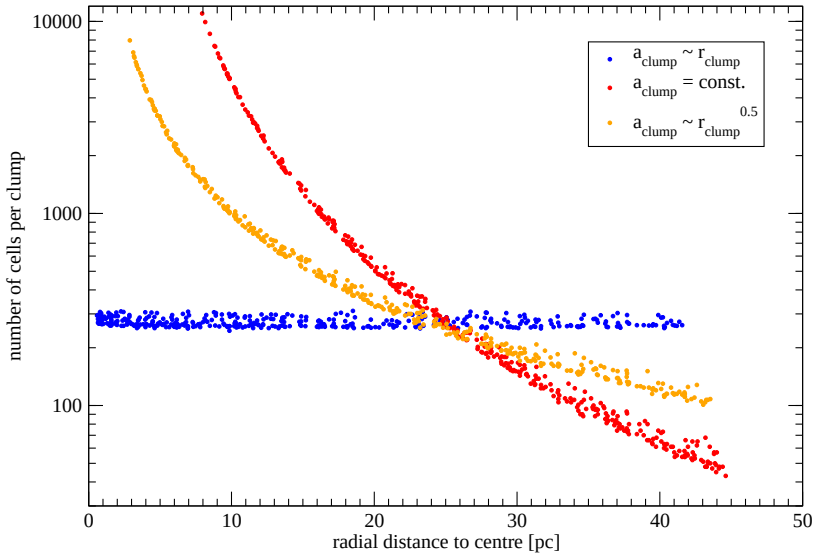

Figure 3.17: *Comparison of cell numbers per clump of models with different slopes of the radial clump size distribution.*

Due to the large clump radius of 5 pc even in the central region, and that fractions of clumps at the model space boarder are prohibited, it leads to a density distribution with a quite large, unevenly shaped central cavity, as can be seen in the face-on view (Fig. 3.18 a). The inner rim is given by only a few, intersecting clumps, instead of the otherwise defined spherical central cavity. Therefore, in the edge-on case, the surface brightness distribution shows an inner boundary, which is bend towards the centre (convex shaped). In these models, due to the large clump size in the inner region, many clumps intersect, producing a nearly continuous dust distribution at the inner boundaries, which lets the – for continuous models – typical x-shaped structure slightly appear again. For the same reason, the extinction band due to the $|\cos(\theta)|$-radiation characteristic is visible in the edge-on view. Especially at the 60° inclination angle in this series of images, single clumps are directly visible (above and below the centre). In these cases, their shading directly shows the illumination pattern due to the primary source (accretion disk), emission from other clumps and extinction from the foreground dust distributions.

The corresponding SEDs (see Fig. 3.19) mainly reflect the increase of the inner cavity and, therefore, the lack of flux at short wavelengths. The convex shape of that region causes a larger directly

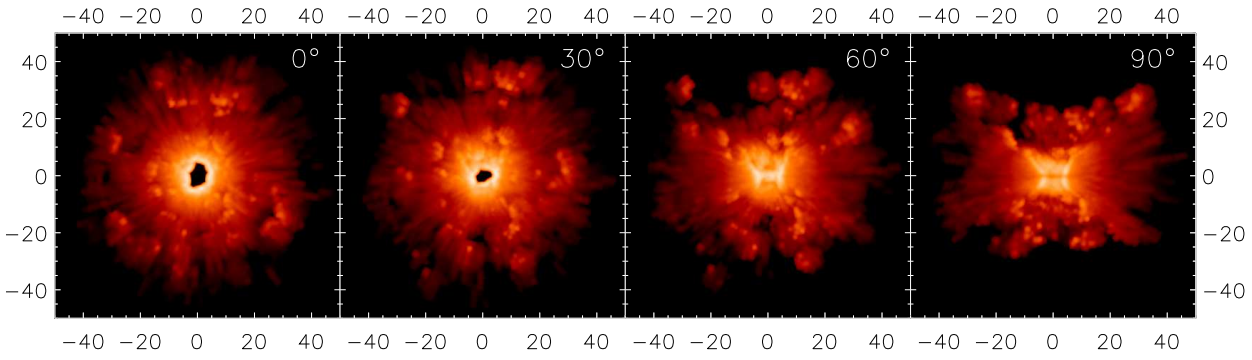

Figure 3.18: *Images at* 12 µm *and inclination angles* $i = 0°, 30°, 60°, 90°$ *for a clumpy distribution with a constant clump size, independent of the radial position.*

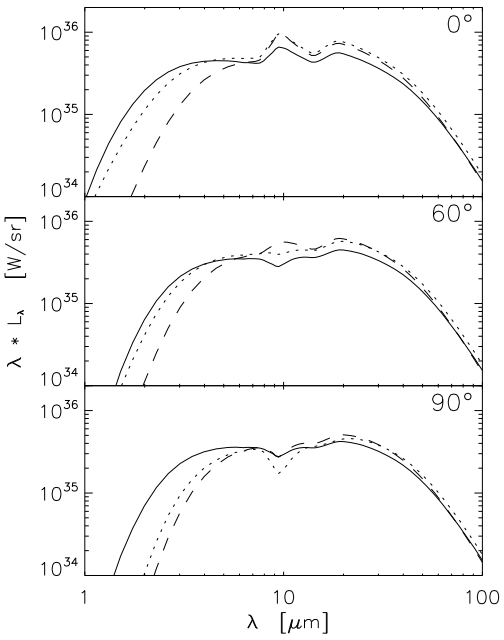

Figure 3.19: *Dependence on the clump size for different inclination angles (rows: 0°, 60°, 90°). The solid line corresponds to our standard model with $\beta = 1$. For the dashed line, clumps have equal size ($a_{\mathrm{clump}} = 5\,pc$, $\beta = 0$), independent of the radial position and the dotted line corresponds to an intermediate model with $\beta = 0.5$.*

illuminated area at the funnel walls and, therefore, strengthens the silicate emission feature in face-on view. Further interesting is the different appearance (emission/absorption) of the 10 μm feature at $i = 60°$ (middle panel). This is due to the lower number density of clumps in the inner part, enforced by the restriction of having only whole clumps within the model space.

In Fig. 3.20, a dust mass study is shown for the large, constant diameter clump model ($\beta = 0$). Whereas the edge-on case (Fig. 3.20a) shows qualitatively the same behaviour as discussed in Section 3.3.6, the face-on case differs: only the relative height of the silicate feature changes slightly. This was already observed in our *TTM*-models in Chapter 2 and is due to the now inward bent inner walls of the funnel, here caused by the very large and spherical clumps in the innermost torus region.

3.3.9 Radial dependence of the optical depth of the clumps

The origin of the clouds within the torus is still under debate. Therefore, we study a different radial dependence of the optical depth of the clumps in this section. Assuming that the clouds result from stellar processes of violent mass loss, e. g. the ejection of planetary nebulae, the assumption, that all clumps possess similar masses might be sensible. When we apply this to our model and assure the same total optical depth within the equatorial plane, averaged over all angles of ϕ, the comparison as shown in Fig. 3.21 emerges. The solid line corresponds to our standard model and the dotted line is the model described above with a mass of each clump of approximately $1.04\,M_{\odot}$. Now, the optical depth is concentrated to the central part of the torus and scales in radial direction as $\tau \propto a_{\mathrm{clump}}^{-2}$. This means that – although the total optical depth within the equatorial plane, averaged over all angles ϕ stays constant – SEDs of all simulated inclination angles appear optically thin. The reason for this is the small optical depth in the outer part due to the clumps' large volumes there. Clumps in the inner part of the torus are extremely optically thick, but enough lines of sight remain open to keep the mean torus optically thin. For the face-on view, the smaller amount of dust in the direct vicinity of the heating source leads to a shift of the Wien branch towards longer wavelengths. The missing flux at FIR wavelengths can be explained by the smaller clump mass in

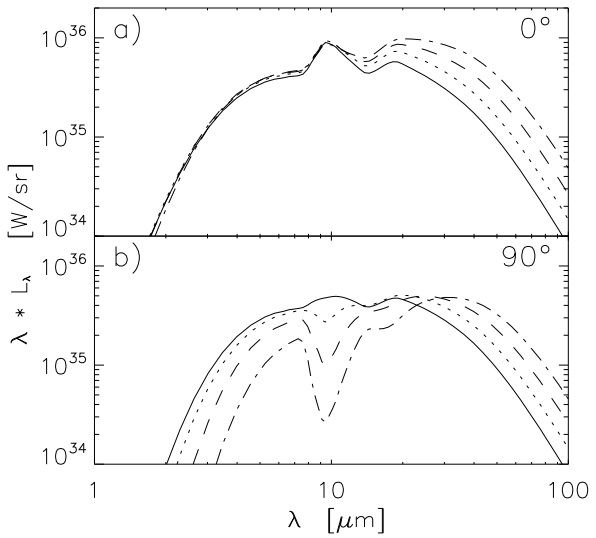

Figure 3.20: *Dust mass study for the model with constant clump size. The optical depth increases from the solid line to the dash-dotted line. Compare to Fig. 3.12.*

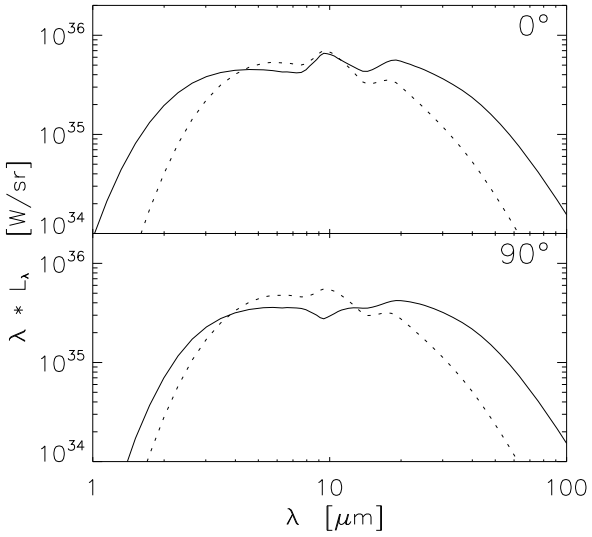

Figure 3.21: *Dependence of the SEDs on the radial distribution of the optical depth of the clumps. The solid line corresponds to our standard model, where all clumps possess the same optical depth along lines of sight through the centre of the clumps and the dotted line to a model, where all clumps have the same mass.*

the outer part, compared to the standard model, where the clump mass scales with the square of the radial position.

3.4 Discussion

First, we give an explanation for the reduction of the silicate feature in emission, before we discuss the possible contribution from bremsstrahlung emission from the hot inter-cloud gas and compare our modelling to previous models of clumpy tori.

3.4.1 Explanation for the reduction of the silicate feature

The results shown in the subsections before can be explained by the following model, which was partially already discussed by Nenkova et al. (2002). It is illustrated in Fig. 3.22, where red colour denotes directly illuminated clump surfaces. Many of the explained features can also be seen in the zoomed-in version of the surface brightness distributions of our standard model (Fig. 3.7) at inclination angles $\leq 30°$.

As already pointed out in Chapter 2, the SEDs of dust tori in the mid-infrared wavelength range are mainly determined by the inner few parsecs of the toroidal dust distribution. In each of the central clouds of the clumpy model, the dust temperature drops from the inner directly illuminated edge towards the cloud's outward looking surface.

With an inclination angle between the line of sight towards the observer and the symmetry axis

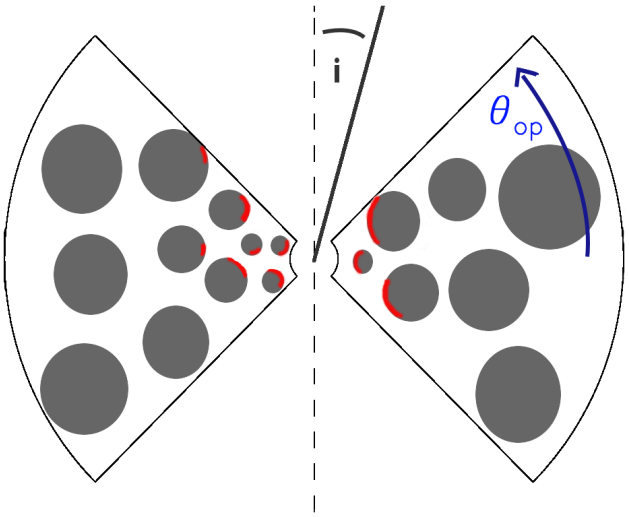

Figure 3.22: *Sketch of our clumpy torus model. Indicated in red are directly illuminated surfaces of the clumps. i is the inclination angle, $\theta_{\rm op}$ is the half opening angle of the torus.*

around $i = 90°$, we expect – for realistic volume filling factors – comparable features as in the continuous case. But the situation changes with decreasing inclination angle. Here, one has to distinguish between different cases:

① With a relatively high volume filling factor and a not too small extension of the clouds in the central region of the torus, it is likely that the directly illuminated part of most of the clouds is hidden from direct view by other clouds. Therefore, the directly illuminated surface area is reduced compared to the corresponding continuous model. As this area is responsible for the emission fraction of the silicate feature within the SED, it shows less SiO emission. In order to produce such a shadowing effect, clouds have to possess a large enough optical depth, which means that they have to be either small or massive ($\tau_{\rm clump} \propto m_{\rm clump}\, a_{\rm clump}^{-2}$, where $m_{\rm clump}$ is the mass of the clump).

② For the case of too small optical depth of clumps in the innermost region, we expect the silicate feature to appear in strong emission.

③ Another possibility to produce silicate features in emission is when the model possesses a small number of clumps in the inner part, making the shadowing effect inefficient.

Briefly speaking, the strength of the silicate feature is mainly determined by the distribution, size and optical depth of the clouds in the direct vicinity of the sublimation surface of the dust. We will see in the next section that this finding well explains the fact that Nenkova et al. (2002) and Dullemond & van Bemmel (2005) come to different conclusions concerning the reduction of the strength of the silicate feature due to clumpiness, as the distribution (and size) of their clouds differ.

3.4.2 Contribution from cooling due to bremsstrahlung within the hot inter-clump medium

As already briefly discussed in Sec. 3.1, the torus is actually made up of a multiphase medium. Within such a model, dusty and molecular clumps are embedded into a hot (with temperatures of the

order of 10^6 K, see Fig. 4.20), fully ionised surrounding medium of low density. In this temperature regime, the plasma cools via atomic line emission and continuous emission of bremsstrahlung. Here, we make an upper limit estimate only for the bremsstrahlung contribution to the spectral energy distribution of the torus – as we are only interested in the continuum radiation transport. The following assumptions are needed:

① Velocities of the electrons possess a thermal distribution.

② Fully ionised gas, only bremsstrahlung emission taken into account.

③ 100 % (upper limit estimate!) of the torus filled with hot gas (within the models of this paper, this corresponds to roughly $V_{\rm torus} \approx 370\,000\,{\rm pc}^3$).

④ No extinction due to dust and the bremsstrahlung emission is treated in an optically thin manner.

⑤ $\rho_{\rm gas} = 10^{-23}\,{\rm g/cm}^3$: This value results from the standard model of our hydrodynamic simulations. Compare to Chapter 4.

⑥ The hot gas possesses solar abundances, which results in a mean molecular weight of $\mu = 0.6$ and the number densities of electrons and ions are then given by $n_{\rm e} = 0.52\,n_{\rm tot}$ and $n_{\rm i} = 0.48\,n_{\rm tot}$, where $n_{\rm tot} = \frac{\rho_{\rm gas}}{\mu\,{\rm AMU}}$ is the total number density of gas particles and AMU is the atomic mass unit.

The emitted flux due to bremsstrahlung is given by (Rybicki & Lightman 1979):

$$\frac{dW}{dV\,dt\,d\nu} = \frac{2^5\,\pi\,\tilde{e}^6}{3\,m_{\rm e}\,c^3}\,\sqrt{\frac{2\,\pi}{3\,k_{\rm B}\,m_{\rm e}}}\,\frac{1}{\sqrt{T_{\rm gas}}}\,Z^2\,n_{\rm e}\,n_{\rm i}\,e^{-h\nu/k_{\rm B}T_{\rm gas}}\,\bar{g}_{\rm ff}, \tag{3.3}$$

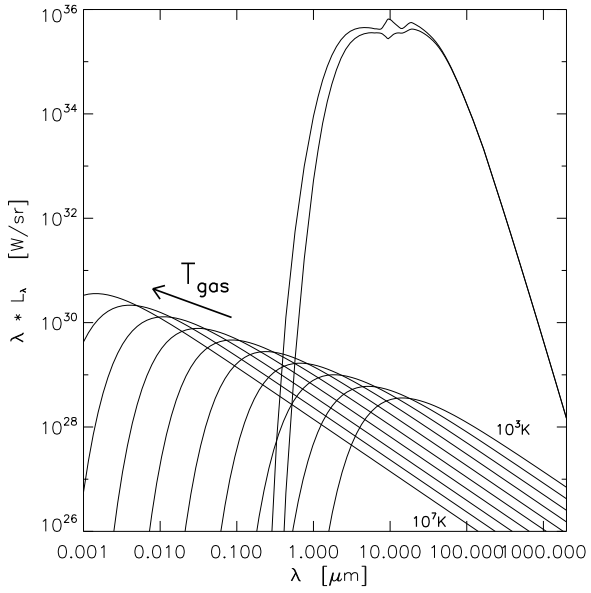

Figure 3.23: *Estimate (upper limits) of the SEDs of bremsstrahlung emission due to cooling of the hot inter-clump medium in one of our typical clumpy torus models. Shown are various examples for temperatures of the emitting plasma between* 10^3 *K and* 10^7 *K. For comparison, the face-on and edge-on view towards our clumpy standard model are shown.*

where $\tilde{e}$ is the charge and m_e is the mass of the electron. $\bar{g}_\mathrm{ff}$ is a *velocity averaged gaunt factor* which in a good order of magnitude estimation can be set to 1 (see Rybicki & Lightman 1979). As hydrogen is the main component of the gas mixture, the atomic number Z is set to 1 as well.

In our usual units and for the total volume of the torus V_torus, we obtain:

$$\lambda L_\lambda = \frac{1}{4\,\pi}\frac{2^5\,\pi\,\tilde{e}^6}{3\,m_\mathrm{e}\,c^3}\,\sqrt{\frac{2\,\pi}{3\,k_\mathrm{B}\,m_\mathrm{e}}}\,n_\mathrm{e}\,n_\mathrm{i}\,\frac{1}{\sqrt{T_\mathrm{gas}}}\,\nu\,e^{-h\nu/k_\mathrm{B}T_\mathrm{gas}}\,V_\mathrm{torus} \tag{3.4}$$

The resulting SEDs are plotted in Fig. 3.23 for gas temperatures ranging from 10^3 K to 10^7 K. Overplotted are the edge-on and face-on SED of our clumpy standard model. As can be seen from this, even for an upper limit estimate of emitted flux due to bremsstrahlung, there is no significant contribution to the SED of the torus. Therefore, we conclude that bremsstrahlung can be neglected in our continuum radiative transfer calculations, although important for longterm cooling processes of the hot inter-clump medium in our hydrodynamical simulations, but also more important at higher temperatures. At lower temperatures, cooling is still dominated by line emitting processes.

3.4.3 Comparison with other torus models

Results of Nenkova et al. (2002) - the pioneering work in the field of clumpy tori - are broadly consistent with the explanations given in Section 3.4.1 of this chapter.

Dullemond & van Bemmel (2005) model 2D *clumps* in form of rings with a two-dimensional radiative transfer code. In contradiction to all other simulations, no systematic reduction of the silicate feature due to clumpiness is found. The reason for this is understandable with the explanations given in Section 3.4.1, as their model features a very small clump number density in the central region and shadowing effects are rather small. Therefore, they find both, strengthening of the silicate feature and reduction, depending on the random ring distribution.

A comparison of our clumpy standard model and two other random cloud distributions with simulations of Hönig et al. (2006) is shown in Fig. 3.24. They follow a different, multi-step approach: 2D radiative transfer calculations of individual clouds at different positions and with various illumination patterns within the torus are carried out. In a second step, the spectral energy distribution of the total system is calculated. The cloud distribution and parameters like optical depth or size arise from an accretion scenario of self-gravitating clouds close to the shear limit (Vollmer et al. 2004; Beckert & Duschl 2004). The advantage of this approach is that resolution problems can be overcome, as only 2D real radiative transfer calculations of single clumps are needed. Characteristic for their modelling are small cloud sizes with very high optical depths in the inner part of the torus and a large number of clumps. For comparison, a cloud at the sublimation radius of their model has a radial size of $R_\mathrm{cloud} = 0.02$ pc with an optical depth of $\tau_{0.55\,\mu\mathrm{m}} \approx 250$. In our standard model, clouds at the sublimation radius are four times larger and possess an optical depth of only $\tau_{0.55\,\mu\mathrm{m}} \approx 3$. The large number of small clumps leads to quasi-continuously looking surface brightness distributions in the inner part of the tori. The large optical depth in the innermost part in combination with the large number density there, reduces the silicate feature significantly by shadowing with respect to their single clump calculations. Their finding that the silicate emission feature can further be reduced when increasing the number density of clumps in the innermost part perfectly fits to the model presented in Section 3.4.1. Deviations between the two approaches in Fig. 3.24 are due to the approximately eight times larger primary luminosity and the larger optical depth, at least in

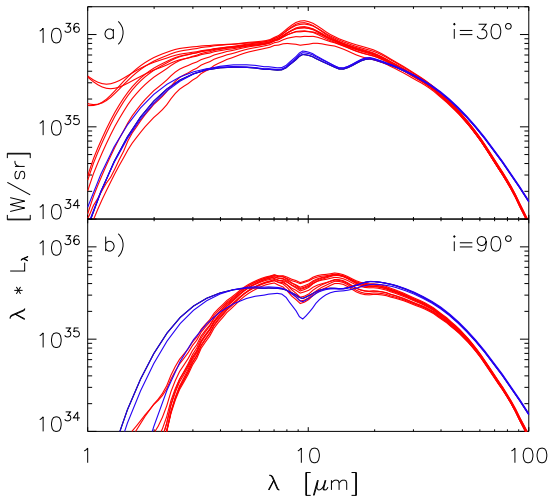

Figure 3.24: *Comparison of our clumpy standard model (blue lines) with the current standard model of simulations done by S. F. Hönig (private communication), shown by the red lines, for 10 different random realisations of their model. The latter are scaled with a factor of 2.2 in order to give rough agreement between the two models.*

the midplane of the Hönig et al. (2006) modelling compared to our standard model. This leads to relatively higher fluxes at short wavelengths compared to long wavelengths for the $i = 30°$-case (Fig. 3.24a) and to more extinction within the midplane and, therefore, a shift of the Wien branch towards longer wavelengths (see Fig. 3.24).

3.5 MIDI interferometry

Even with the largest single-dish telescopes, it is impossible to directly resolve the dust torus of the nearest Seyfert galaxies, with apparent sizes of less than 50 mas for the warm component (Jaffe et al. 2004). With them, spatial resolutions of around 100 mas can be reached. Therefore, interferometric measurements are needed. Recently, Jaffe et al. (2004) succeeded for the first time to resolve the dusty structure around an AGN in the mid-infrared wavelength range. In this case, they probed the active nucleus of the nearby Seyfert II galaxy NGC 1068 with the help of the mid-infrared interferometric instrument (MIDI, Leinert et al. 2003). It is attached to the European Southern Observatory's (ESO's) Very Large Telescope Interferometer (VLTI) on Cerro Paranal in Chile. Its main objective is the coherent combination of the beams of two 8.2 m diameter Unit Telescopes (UT) in order to obtain structural properties of the observed objects at high angular resolution. A spatial resolution of up to $\lambda/(2\,B) \approx 10$ mas at a wavelength of $\lambda = 10\,\mu$m can be obtained for the largest possible separation of two Unit Telescopes of $B \approx 130$ m. Operating in the N-band ($8-13.5\,\mu$m), it is perfectly suited to detect thermal emission of dust in the innermost parts of nearby Seyfert galaxies. MIDI is designed as a classical Michelson-Interferometer. Being a two-element beam combining instrument, it measures so-called visibility amplitudes. Visibility is defined as the ratio between the correlated flux and the total flux. Its interpretation is not straightforward, since no direct image can be reconstructed. Therefore, a model has to be assumed, which can then be compared to the visibility data. MIDI works in dispersed mode, which means that visibilities within the whole wavelength range are derived. The dust emission is probed depending on the

orientation of the projected baseline. Whereas the real baseline is fixed by the positions of the four UT-telescopes, the projected baseline changes due to earth's rotation. Therefore, a large number of different projected baseline sizes and orientations are available. Point-like objects result in a visibility of one, as the correlated flux equals the total flux. The more extended the object, the smaller the visibility. With the help of a density distribution, surface brightness distributions in the mid-infrared can be calculated by applying a radiative transfer code. A Fourier transform then yields the visibility information, depending on the baseline orientation and length within the so-called *U-V-plane* (or *Fourier-plane*), derived by the Fourier transform.

The main goal of the following analysis is to investigate, whether MIDI can distinguish between clumpy and continuous torus models of the kind presented above. Furthermore, we try to derive characteristic features of the respective models.

3.5.1 Model visibilities

In Fig. 3.25, calculated visibilities for four inclinations of the continuous model observed at $\lambda = 12\,\mu$m are shown. Colour coded are various position angles of the baseline orientation (counted anti-clockwise from the projected torus axis). Due to the axisymmetric setup, all lines coincide for the face-on case. For all other inclination angles, visibilities decrease until a position angle of 90° is reached and increase symmetrically again. This means that the torus appears elongated perpendicular to the torus axis at this wavelength. Fig. 3.26 shows the same study, but for the corresponding clumpy model. The basic behaviour is the same, but the visibilities show fine-structure and the scatter is much higher, especially visible in the comparison of the $i = 0°$ cases. Furthermore, whereas all of the curves of the continuous model are monotonically decreasing with baseline length, we see rising and falling values with increasing baseline length for one position angle in the clumpy case. In addition, for the continuous models, curves do not intersect, which is the case for clumpy models. However, to detect such fine-structure in observed MIDI data, a very high accuracy in the visibility measurements of the order of $\sigma_v \approx 0.02$ is required.

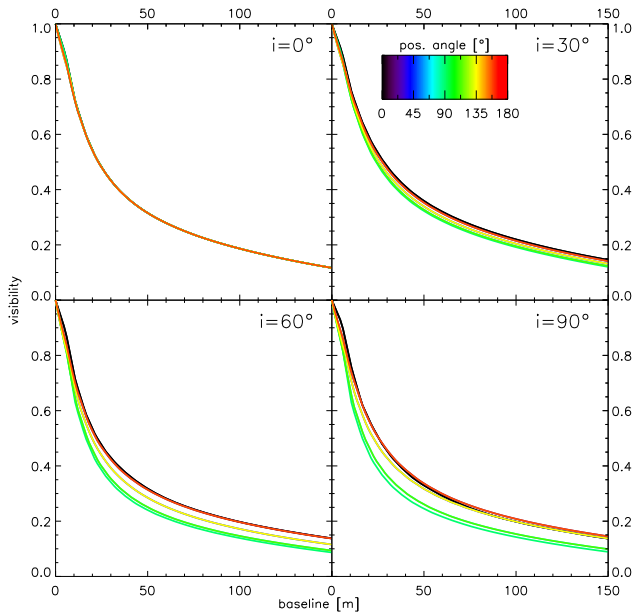

Figure 3.25: *Visibilities of the continuous model corresponding to our standard model at a wavelength of 12 µm plotted against the baseline. Colour coded are the position angles measured from the projected torus axis. Each panel shows a different inclination angle, as indicated in the upper right corner.*

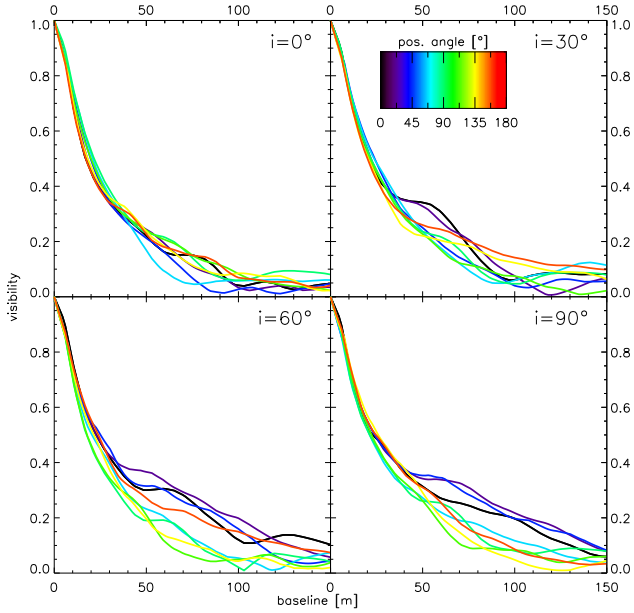

Figure 3.26: *Visibilities of our clumpy standard model at a wavelength of* 12 µm *plotted against the baseline. Colour coded are the position angles measured from the projected torus axis. Each panel shows a different inclination angle, as indicated in the upper right corner.*

In Fig. 3.27, the wavelength dependence of the visibility is shown. Each panel visualises a different position angle (counted anti-clockwise from the projected torus axis). The first two represent the case of the clumpy standard model and the third and fourth the continuous model. An inclination angle of 90° is used in all panels. Colour coded are three different wavelengths: 8.2 µm at the beginning of the MIDI-range (black line), 9.8 µm within the silicate feature (blue) and 12.6 µm at the end of the MIDI wavelength range (yellow), outside the silicate feature. Whereas the continuous model results in smooth curves (see also Fig. 3.25), lots of fine-structure is visible for the case of the clumpy model. Clumpy models generally appear more extended (higher visibilities) and the differences between the displayed wavelengths relative to the longest wavelength are smaller than in the continuous case.

Fig. 3.28 again shows visibilities for our clumpy standard model at 12 µm, plotted against the position angle (counter-clockwise from the projected torus axis). Colour-coded are baselines between 20 m and 100 m in steps of 20 m. A larger baseline means that structures are better resolved, leading to decreasing visibilities. For the case of inclination angles close to edge-on, the visibility distri-

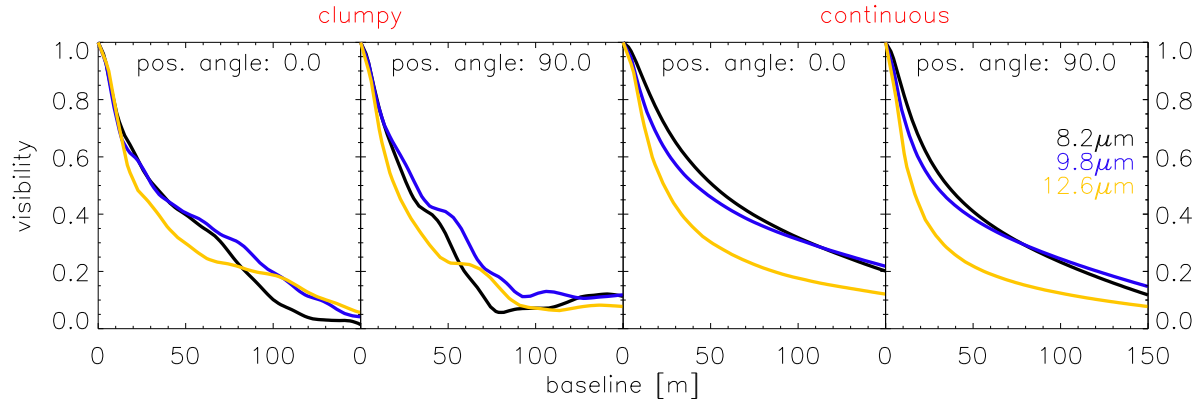

Figure 3.27: *Visibilities of our clumpy (first 2 panels) and continuous (last 2 panels) standard model at different wavelengths (colour coded), plotted against the baseline for the two position angles* 0° *(in torus axis direction) and* 90° *(along the midplane) for an edge-on view onto the torus (*$i = 90°$*).*

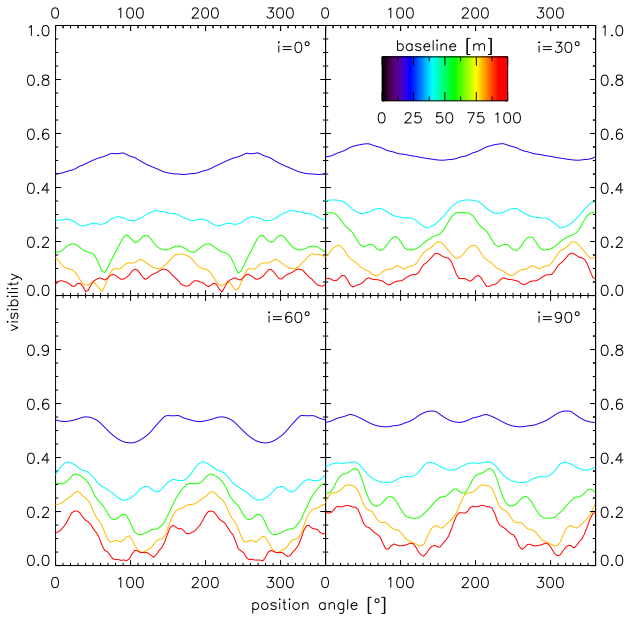

Figure 3.28: *Visibilities of our clumpy standard model at different inclination angles (as annotated in the upper right corner) plotted against the position angle for various baselines (colour coded) and a wavelength of* 12 µm.

bution changes from more or less flat to a characteristic oscillating distribution at longer baselines (from 60 m onwards) with minima around 100° and 300°. This means that our torus model seems to be more elongated within the equatorial plane and has the smallest width along the projected torus axis. But this only applies for the innermost part; the torus as a whole looks more or less spherically symmetric. At small inclination angles no such favoured size distribution is visible.

Fig. 3.29 shows dispersed visibilities of our standard model. As already seen before, the longer the baseline, the larger the resolution and, therefore, the smaller the visibility. From 0° position angle towards 90°, the amplitude of variation in the visibility information with wavelength increases and we see more and more fine-structure in the curves. This underlines the claim that the same kind of fine-structure in the observed MIDI data for the Circinus galaxy is a hint for clumpiness of the torus (Tristram et al. 2007).

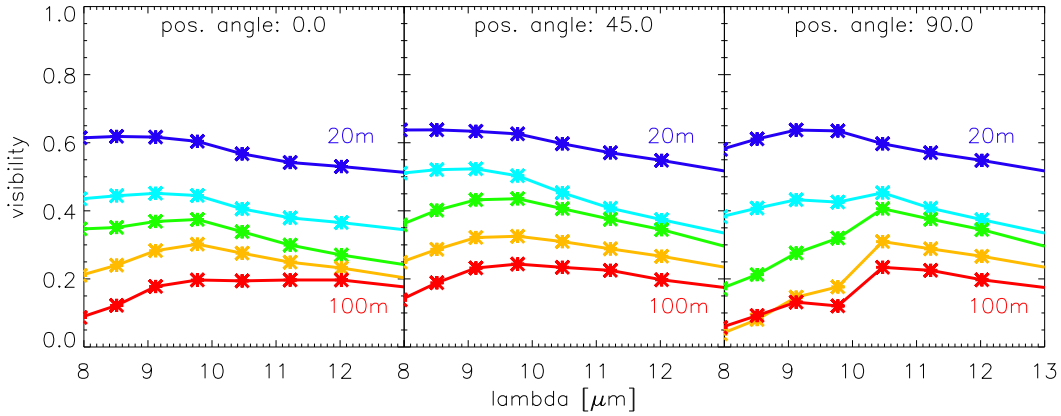

Figure 3.29: *Dispersed visibilities of our standard model at different position angles (as annotated) for various baselines (20, 40, 60, 80, 100 m) and an inclination angle of* 90°.

3.5.2 Comparison with MIDI-data for the Circinus galaxy

Unfortunately, a fitting procedure involving a huge parameter study is not possible with our current model, due to the very long computational times of the order of 30 to 40 hours per inclination angle (including calculation of the temperature distribution, the SED and surface brightness distribution). Therefore, we applied the following procedure: From our experience with modelling the SED of the Circinus galaxy with our previously used continuous *Turbulent Torus Models* (see Section 2.4.2), we took over the size of the object adapted there. Furthermore, we tried to stay as close to our clumpy standard model as possible (for the parameters of the clumpy standard model, compare to Table 3.1) and transferred the parameters α, β and a_0. The rest of the parameters were changed, in order to obtain the best possible adaptation of the data, within the investigated parameter range (see Table 3.3). The results are displayed in Fig. 3.30 for the case of the visibility comparison. Here, interferometric observations with MIDI (Tristram et al. 2007) for the Circinus galaxy (black) and our current clumpy Circinus model as described above and in Table 3.3 (yellow stars) is compared. In contrast to the above presentation of visibilities, single measurements of combinations of various baseline lengths and position angles are displayed in this plot. Furthermore, position angle now refers to the angle measured from north in counter-clockwise direction. The torus axis has a position angle of approximately $-45°$ according to this definition. The black numbers denote the baseline length (given in m) of the corresponding data point. From the approximate correspondence of the model values with the data, one can see that the size of the emitting region at the two wavelengths seems to be adapted quite well. Most of the local extrema of the curve can be reproduced for the case of 9.1 µm. Larger deviations are visible for $\lambda = 12.0\,\mu$m. Partly, the good adaptation is due to the changes in baseline length. Larger baselines naturally result in smaller visibilities, as we are probing smaller and smaller structures (see also Fig. 3.26). Larger visibilities for smaller or equal baselines and similar position angle, therefore, have to be due to those curves in Fig. 3.26 with increasing visibility with baseline or a very inhomogeneous distribution of dust with position angle. Both can be interpreted as signs of clumpiness. The spectral energy distribution of the same model is overplotted over current high resolution data in Fig. 3.31. Data was obtained with the NACO camera at the VLT and corrected for foreground extinction by $A_V = 6$ mag (Prieto et al. 2004). Different symbols refer to various aperture sizes (see figure caption). The red line shows the MIDI total photometry (Tristram et al. 2007) and the black line is our Circinus model as discussed above for an aperture of 0.4″ in radius, whereas the dotted line denotes the same model, but calculated for an aperture of 1.0″ (comparable to the aperture of the yellow triangle data point). Both modelled

Parameter	Value	Parameter	Value
$R_{\rm sub}$	0.6 pc	$N_{\rm clump}$	500
$R_{\rm out}$	30 pc	β	1.0
$\theta_{\rm op}$	65°	a_0	0.2 pc
$\left\langle \tau^{\rm equ}_{9.7\,\mu{\rm m}} \right\rangle_\phi$	3.9	$\tau_{9.7\,\mu{\rm m}}$	0.96
$M_{\rm BH}$	$1.7 \cdot 10^6\, M_\odot$	$L_{\rm disk}/L_{\rm edd}$	30%
α	-0.5		

Table 3.3: *Circinus model parameters: For an explanation of the parameters see Section 3.2 and 3.1.* $M_{\rm BH}$ *is the mass of the central black hole (Greenhill et al. 2003) and* $L_{\rm disk}/L_{\rm edd}$ *is the Eddington luminosity ratio resulting for the assumed luminosity of the central source.*

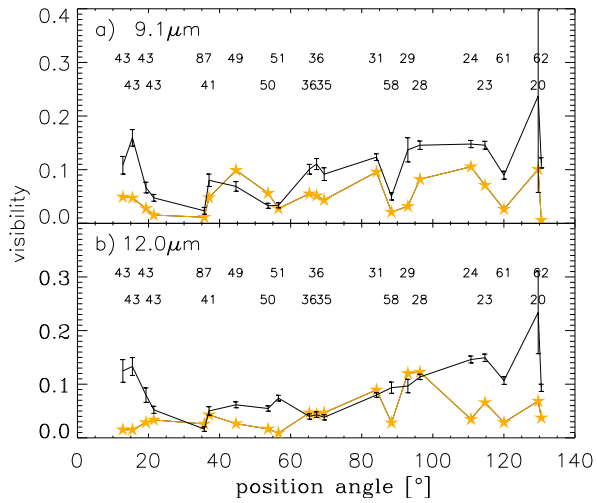

Figure 3.30: *Comparison of model visibilities (yellow lines) for an azimuthal viewing angle of $\phi = 225°$ with MIDI observations for two different wavelengths. Baseline information for all data points is given above the data. Data courtesy of Tristram et al. (2007).*

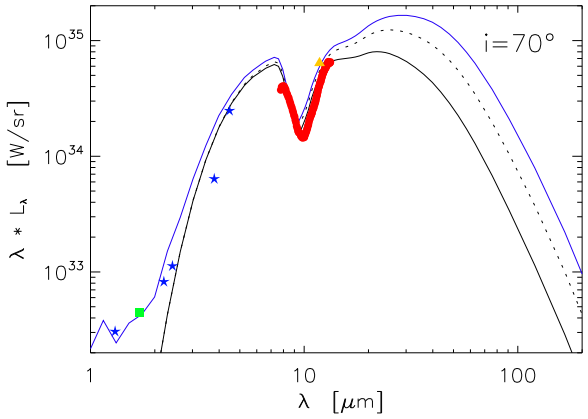

Figure 3.31: *Comparison of model SEDs with data for the Circinus galaxy. Different symbols refer to various aperture radii: blue stars – 0.38″, green rectangle – 0.1″ and yellow triangle – 1.0″ (data courtesy of Prieto et al. 2004). The red line shows the total MIDI photometry (Tristram et al. 2007). Our model (see model parameters in Table 3.3) is calculated for an aperture radius of 0.4″ (solid line) and 1.0″ (dotted line).*

SEDs are pure dust reemission. Stellar radiation is included for the case of the blue solid line, where additionally no aperture correction is applied. In contradiction to our homogeneous Circinus model in Section 2.4.2, enough stellar radiation can be observed in order to explain the turnover of the SED at small wavelengths and we do not need to assume scattering by material (dust and electrons) within the torus funnel. As can be seen from these viewgraphs, our model is able to qualitatively explain the spectral energy distribution as well as the visibility information.

3.6 Conclusions

In this section, we implemented a new clumpy torus model in three dimensions. For computational reasons, a wedge-like shaped disk is used. In the discussion of our results, we put special emphasis on the comparison with continuous models in terms of the appearance of the silicate feature, as well as the differentiation between them with the help of the mid-infrared interferometer MIDI.

In Chapter 2, we already found that the SEDs of AGN tori in the mid-infrared wavelength range are mainly determined by the innermost part of the torus. With the help of the presented clumpy torus models, this claim could be further strengthened. According to these simulations, the silicate feature strength is mainly determined by the number density and distribution, as well as the optical depth of clumps in the inner region. With a high enough optical depth of the clouds in the inner part, shadowing effects can take place, which hide the primarily illuminated cloud surfaces from direct view and, thereby, reduce the silicate feature in emission. At the same time, enough lines of sight with low optical depth remain so that only weak absorption features result for the edge-on case. Continuous models with special and unrealistic morphologies (like the here used wedge-shaped tori) are also able to weaken the silicate emission feature for the face-on view, but fail to simultaneously account for moderate absorption features, when looking edge-on onto the torus.

Due to the large clumps in our model, appreciable scatter in spectral energy distributions for different random realisations of the torus are expected. A contrary effect is caused by the small optical depth of the single clumps and also of many lines of sight towards the centre. Direct comparison between calculated visibilities for clumpy and the corresponding continuous models show that clumpy models naturally possess more fine-structure, which can partly be resolved by MIDI. But at the current state of our modelling, one has to be cautious with these interpretations, as a higher spatial resolution, as well as number of photon packages would be desirable.

We also showed that these kind of models are able to qualitatively describe the available visibility and high resolution spectroscopic data of the Circinus galaxy at the same time. Currently, it is one of the best studied Seyfert galaxies in terms of mid-infrared visibility measurements. Noteworthy, the decreasing slope of the SED at short wavelengths can be described with our clumpy model, whereas it was at odds with the continuous model described in Section 2.

Chapter 4

Hydrodynamic models of tori

4.1 Introduction

As already discussed in Chapter 2, the origin, shape and evolution of the observed obscuring material around AGN is still under debate. One of the major problems in this field is the stabilising mechanism to sustain the vertical scale height of the torus. But it is not only the obscuration for which this gas and dust distribution is needed, but it also constitutes the reservoir of material for the feeding of the central black hole. Due to the very complicated astrophysical processes, which are thought to happen in centres of AGN and the sparse knowledge of them, no global models of the central parsecs of AGN and the gas and dust dynamics exist so far. Therefore, one goal of this part of our work is to combine the knowledge we have - be it observationally or from theoretical work - and put it together to a more complete picture of the behaviour of nuclear gas und dust. We will test a global, hydrodynamical realisation of an extended TTM-model (see Section 2.2.1) with the help of numerical simulations and to confront it with observational facts. Eventually, this model should account for the obscuration as well as the feeding of the central source. Furthermore, the combination of hydrodynamic simulations and subsequent radiative transfer calculations has never been done before. But only this procedure enables us to probe our models with observations. In this work, we focus on low-luminosity AGN (Seyfert galaxies), as they are more abundant in the local universe and, therefore, their nuclear regions are accessible via current generation interferometric instruments.

Roughly 50-80% of low luminosity AGN host nuclear star clusters in their centres (Peng et al. 2006). In our simulations, we assume that it was built up during a short-duration starburst and the stellar density is distributed according to a Plummer (Plummer 1911) profile. After this, the stellar population (often referred to as a coeval stellar population - *CSP*) evolves. The most massive stars end their lives very fast – after only a few million years – in supernova type II explosions. This is a very violent phase of the evolution of this cluster, which might result in a partial evacuation of the stellar cluster from its gas and dust content, which remained from the initial cluster formation scenario or mass loss during the first million years of cluster evolution. After this phase, our simulations start, featuring mass input mainly due to planetary nebulae injections and energy input from supernovae, partly balanced by optically thin radiative cooling.

Before we present our model in more detail, the most important physical concepts will be discussed.

4.2 Theoretical concepts needed in our simulations

In this section, we first present the equations of non-ideal hydrodynamics, the so-called Navier-Stokes equations and introduce some hydrodynamical concepts, needed for the further understanding. A discussion of the numerical realisation with the help of the TRAMP-code follows.

4.2.1 Basic equations

The equations of non-ideal hydrodynamics are the so-called Navier-Stokes equations. They are a system of non-linear conservation laws, describing the dynamics of a compressible and viscous material, like gas or liquid and can be expressed in terms of the *primitive variables* (also called *physical variables*): density $\rho(\vec{x},t)$, pressure $P(\vec{x},t)$ (or temperature $T(\vec{x},t)$) and velocity $\vec{u}(\vec{x},t)$. Another possibility is to describe the state of the flow with the help of the *conserved variables*: density $\rho(\vec{x},t)$, momentum vector $\vec{p}(\vec{x},t)$ and internal energy per unit mass $e(\vec{x},t)$. The usage of conserved quantities has two main advantages:

① They naturally result from the derivation of the fundamental laws of conservation of mass, Newton's Second Law and the law of conservation of energy, as long as no source terms are present.

② Computationally, so-called *conservative methods* are applicable for the case of conservative representation of the Navier-Stokes equations.

In the conservative, integral form for the case of spherical coordinates, the Navier-Stokes equations can be expressed in compact notation as:

$$\partial_t \int_V \vec{W}\, dV + \int_{\partial V} \vec{W}\vec{u}\cdot\vec{n}\, dS = \int_V \sum_i \vec{f}_i, \tag{4.1}$$

where $\vec{W} = \left[\rho,\ p_r,\ l_\theta,\ l_\phi,\ \rho\,\epsilon\right]$ denotes the state vector of the conserved quantities density, radial momentum, angular momentum in meridional and azimuthal direction and energy density. Being conservation equations, the change of a conserved quantity in time (first term left hand side) has to be balanced by the transport of this quantity (so-called advection) through the surface ∂V of the treated volume V (second term left hand side) and the source terms, given on the right hand side. Advection happens with the velocity $\vec{u} = \left[p_r/\rho,\ l_\theta/(r\,\rho),\ l_\phi/(\rho\, r\, \cos\theta)\right]$.

For the case of high Reynolds numbers, for which the effects of body forces, viscous stresses and heat flux are negligible, the Navier-Stokes equations reduce to the time-dependent Euler equations, a system of non-linear hyperbolic conservation laws. This is also the case for our simulations. Furthermore, according to Balbus et al. (1994), molecular viscosity does not contribute to turbulent transport within accretion disks. The only effect it causes is to act as an energy sink, responsible for thermalization at the high wavenumber end of the energy spectrum. Therefore, they conclude that for large-scale simulations of accretion disk turbulence, an explicit representation of viscosity is not needed. This can be transferred to our simulations of AGN tori. Often, viscosity (e. g. given as tensor viscosity) is included in order to allow for additional transport effects, which are not explicitly modelled (e. g. accounting for magnetically driven angular momentum transport in pure hydrodynamic simulations).

The source terms differ, depending on the conserved quantity, as well as the physics taken into account. Here, only a short summary is given, while they will be described in more detail in Sect. 4.3. Concerning the continuity equation (conservation law for density ρ), the source terms are given by mass-loss of evolving stars (as discussed in Section 4.3.2) and supernova mass input (Sect. 4.3.4). The conservation equations for momentum contain the following source terms on the right hand side: centrifugal forces, gravitational forces, which in our simulations are made up of a point-like Newtonian potential due to the black hole and a *Plummer* potential, caused by the nuclear stellar distribution (see Section 2.2.1), pressure gradient forces, forces due to the injection of planetary nebulae (see Sect. 4.3.2). Concerning the energy equation, important source terms are given by pressure work, energy input due to supernova explosions (see Section 4.3.4) and radiative losses according to optically thin cooling (see Section 4.3.5). Viscous forces and viscous dissipation are neglected, as discussed above.

Both sets of conservation laws (Navier-Stokes as well as Euler equations) cannot completely describe the state of a fluid, as - mathematically speaking - one supernumerous variable compared to the number of equations exists. Therefore, a so-called *closure relation* is needed additionally. Physically, this means that some information about the nature of the material has to be involved. To do this, thermodynamical relations are used, which link internal energy with pressure, temperature and density. This results in a so-called *equation of state* (EOS), as the relationship changes from substance to substance. For the case of solving the time-dependent Euler equations, a P-v-e-relationship (pressure, specific[1] volume and specific internal energy) is needed only. This can be given for instance with a *calorical equation of state*, expressable in the form $e = e(P, v)$. For the case of this work, we use the EOS for *calorically ideal gases*, as it is usually done for the case of astrophysical gases:

$$e = \frac{P}{\rho\,(\gamma - 1)} \tag{4.2}$$

where γ is the (in our case constant) adiabatic index, which depends on the particular gas under consideration. Deviations from this description are expected for example for degenerate matter, as present in white dwarfs or neutron stars. As we are also interested in the temperature, we additionally need to relate pressure and density with temperature (in a P-v-T-relationship), which can be given via a *thermal equation of state* for ideal gases:

$$T = \frac{P\,V}{n\,R}. \tag{4.3}$$

Here, V denotes the volume, n the number of moles within this volume V and $R = 8.1344 \cdot 10^7\,\mathrm{erg\,mol^{-1}\,K^{-1}}$ is the *Universal Gas Constant*.

Some more thermodynamical relations are needed for the interpretation of our simulations. This is first of all the (specific) heat capacity. It is defined as the ratio between the heat dQ added to the system and the change of temperature it causes: $c = \frac{dQ}{dT}$. Depending on the kind of the

[1] specific always means per unit mass, if not stated otherwise

process – either happening at constant pressure or at constant volume – different relations between thermodynamical potentials can be applied, finally resulting in the expressions:

$$c_p = T \left(\frac{\partial s}{\partial T}\right)_p \qquad c_v = T \left(\frac{\partial s}{\partial T}\right)_v , \tag{4.4}$$

$$\tag{4.5}$$

where s is the specific entropy and c_p, c_v are the specific heat capacities at constant pressure and volume respectively.

Generally, the specific heat at constant pressure exceeds the specific heat at constant volume, as the addition of heat also causes expansion of the gas at constant pressure, yielding smaller temperature changes. For the case of an ideal gas, the difference equals the universal gas constant:

$$c_p - c_v = R \tag{4.6}$$

From *Molecular Theory* and the *principle of equipartition* of energy, one can deduce the internal energy of every molecule of the fluid, which is equipartitionally distributed over all degrees of freedom F of the molecule (or atom). Degrees of freedom result from translation, rotation and vibration. This results in the specific (per mole) energy of the gas

$$e = \frac{1}{2} F R T \tag{4.7}$$

and a description of the adiabatic exponent in terms of degrees of freedom of the molecules or atoms:

$$\gamma = \frac{F + 2}{F}. \tag{4.8}$$

As our gas mainly consists of atomic hydrogen, the number of degrees of freedom possesses the lowermost value of three translational degrees of freedom and hence, a value $\gamma = \frac{5}{3}$ is used.

Of fundamental interest for the study of hydrodynamical flows is furthermore the speed of sound, as it divides between regimes of different flow behaviour. Exerting from a caloric equation of state, the (equilibrium) speed of sound is defined as

$$a_s = \sqrt{\left(\frac{\partial P}{\partial \rho}\right)_s} \tag{4.9}$$

Again with the help of thermodynamical relations and under the assumption of an ideal gas and the thermal equation of state given above, it can be rewritten as:

$$a_s = \sqrt{\frac{\gamma P}{\rho}} \tag{4.10}$$

The speed of sound is of the order of the mean thermal speed of the ions of the gas. The following approximate expression can be given:

$$a_s \approx 10 \sqrt{\frac{T}{10^4\,\mathrm{K}}} \frac{\mathrm{km}}{\mathrm{s}} \tag{4.11}$$

This is the velocity, at which pressure disturbances travel through the fluid. Therefore, it limits the rapidity with which it can respond to pressure changes. This means that for the case of supersonic flows, pressure gradients have only little effect on the flow, in contradiction to subsonic flows, which behave as if in hydrostatic equilibrium (in first order approximation).

More detailed reviews of hydrodynamical concepts as well as thermodynamic relations involved in our simulations can be found in Toro (1997).

4.2.2 Numerical realisation - The TRAMP code

For our simulations, we use the 3D radiation hydrodynamics code TRAMP (Kley 1989; Klahr 1998; Klahr et al. 1999). In the following section, a brief overview over the numerical scheme and the features of TRAMP is given, before the new implementations are discussed in the Sections 4.3.2, 4.3.4 and 4.3.5.

TRAMP is implemented on a *staggered mesh*, see Fig. 4.1. This means that scalar quantities are defined in the cell centres and vector quantities on the cell faces. As our simulated objects are rotating tori, which have increasing scale heights in radial direction, spherical coordinates are used. In polar as well as azimuthal direction, they are equipartitionally subdivided, whereas the cell width in radial direction increases linearly with radius, resulting in a logarithmic grid. This has several advantages:

① Cells have comparable width in all coordinate directions, like the cubes in the cartesian case.

② The resolution increases towards the centre. This is needed, as appearing structures are expected to grow with radial size due to the different conditions in the inner and outer regions of the model space. Furthermore, higher central resolution is mandatory for subsequent radiative transfer modelling, as here, steep temperature gradients close to the heating source (the central accretion disk) need to be well resolved.

The numerical implementation is similar to the Zeus-code (Stone & Norman 1992a,b; Stone et al. 1992). Equations of non-ideal hydrodynamics are solved with the help of the *Operator Splitting*-technique. This means that in a multi-step approach, first the transport part (*advection step*) – equation 4.1 with zero right hand side – is solved. In the*force step*, changes of the hydrodynamic state due to pressure, gravitational and viscous forces is taken into account, before in the last step changes in energy are computed. This is not only numerically advantageous, but in every later step, already partially updated values are taken into account, resulting in a more stable behaviour. Therefore, the method is often referred to as semi-second order in time (see Rozyczka 1985). Additional source terms are treated in a separate step. For the advection step, the monotonic transport scheme of van Leer (1977) is applied, which is a spatially second-order-accurate upwind method. It discretises equations in the finite volume description. Compared to the *finite difference* description, this has the main advantage that advected quantities are locally and globally conserved. The force step is calculated using a finite difference discretisation.

The dynamical time-step is given by a fraction (the so-called *CFL-number*) of the Courant-Friedrich-Levy (CFL) time-step (Courant & Friedrichs 1948; Ritchmyer & Morton 1967):

$$\Delta t \leq min_{i,j}\left(\frac{(\Delta x)_i^j}{|u_i^j| + c_a^j}\right), \tag{4.12}$$

where u_i^j is the local fluid velocity of the i-th coordinate direction and the j-th grid cell, $(\Delta x)_i^j$ is the grid spacing of grid cell j in i-th coordinate direction and c_a^j is the local adiabatic speed of sound within cell j. The minimum is taken over all grid cells and coordinate directions. Resulting from a stability analysis (Ferziger & Perić, M. 1996), it assures that propagation of information is limited to one grid-cell per integration time-step. For the sake of global stability, the condition is additionally multiplied with the mentioned *CFL-number* c_{CFL}, which is empirically determined and was chosen to be $c_{\mathrm{CFL}} = 0.5$ in our simulations. A too large value leads to oscillations in the flow pattern, resulting from the non-linear behaviour of the Navier-Stokes or Euler equations, especially in more than one dimension.

Numerical problems appear, when supersonic motions lead to shocks, which lead to discontinuities in the variables. This can be handled by introducing so-called artificial viscosity (see Section 4.2.6 for a more detailed description), which smears out discontinuities over several cells and, thereby, results in the correct generation of entropy in the shock, the correct shock velocities and suppresses post shock oscillations. Artificial viscosity can either be applied in terms of a tensor viscosity or as an additional contribution to the pressure. For the case of the simulations presented in this work, we used the latter description. Then, the usual pressure is substituted by the sum of (thermal) pressure p and the artificial pressure q:

$$q = c_{\mathrm{av}}\,\rho\,(\Delta x)^2\ [min(\nabla \cdot u, 0)]^2\,. \tag{4.13}$$

Here Δx is the size of the grid cell and c_{av} determines the strength of the artificial viscosity, e. g. roughly the number of grid cells over which a shock is smeared out. The non-linearity of

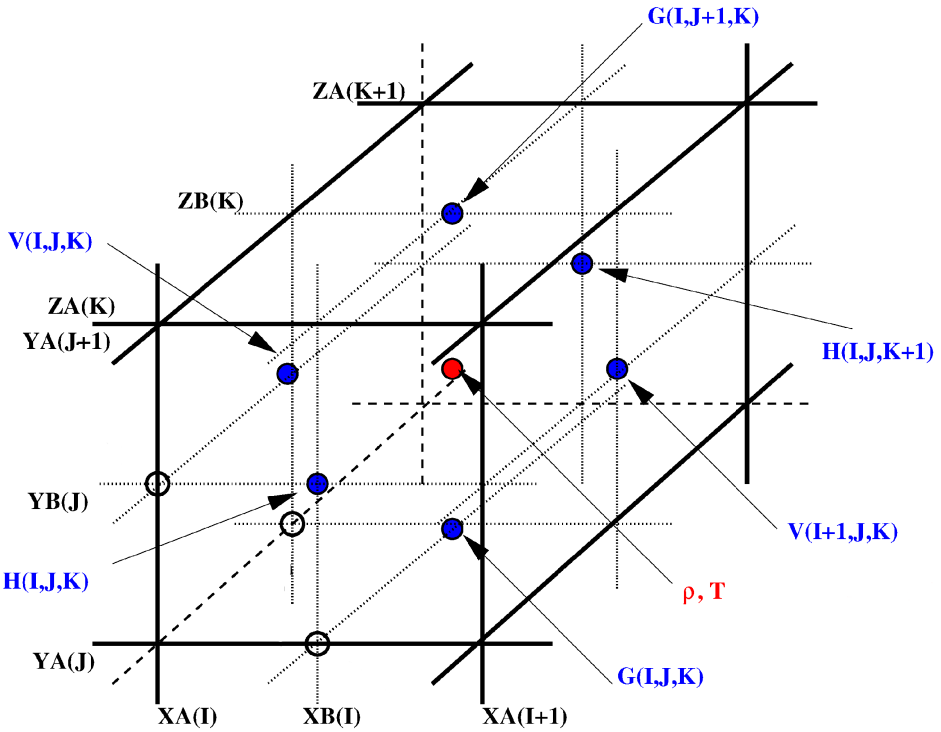

Figure 4.1: *Staggered mesh of the finite volume description. Scalars (e. g. ρ – given in red letters) are defined in the cell centres, whereas vector quantities (e. g. $\vec{u} = (V, G, H)$ – blue letters) are given on the cell faces. Figure taken from Klahr (1998).*

the equation ensures that the artificial viscosity is large in shocks, but negligible elsewhere.

A more detailed description of all of the features of TRAMP can be found in Kley (1989), Klahr (1998) and Klahr et al. (1999).

4.2.3 Domain decomposition

In order to gain resolution and to increase the CFL-timestep, we split the whole computational domain into three parts: the inner part ranges from 0.2 pc to 2.0 pc, the middle part from 1.0 pc to 10.0 pc and the outer part from 5.0 pc to 50.0 pc. Towards the centre, the size of the single cells decrease (logarithmic grid) and additionally the obtained velocities increase due to the presence of the central gravitational potential and the conservation of angular momentum of infalling material. This leads to ever smaller timesteps according to the *CFL*-condition (see equation 4.12). Therefore, we are able to calculate a much longer time period for the outer domain with the same number of CPU hours and the same grid size, compared to the inner domain. On the other hand, further in, processes act on much shorter timescales and only a shorter time evolution is needed in order to obtain a steady state. Therefore, we calculate 10 orbits[2] for the outer domain, but only the last orbit for the middle domain and one tenth of an orbit for the innermost part. This leads to a comparable amount of CPU time of approximately one weak per domain.

In a first step, the outer domain is calculated. The physical state of material at the position of the outer boundary of the middle model is stored in a file after a certain time difference Δt_{boun}. Outflow boundary conditions are used radially inwards as well as outwards. During the calculation of the middle domain in the second step, the inner radial boundary is set to outflow, whereas the outer boundary is set by the afore stored quantities, which can result in in- or outflowing material, due to the overlap of the domains. To do this, within every timestep, the outer ghost cells are set to interpolated[3] values from the outer domain. At the same time, physical quantities advected across the position of the outer boundary of the inner domain are stored. In the last step, the same is done for the innermost model. For the analysis and the subsequent radiative transfer calculations, the three domains are combined again.

This procedure is a reasonable approximation, as in most of the simulations we observe infall of gas towards the inner region. Partly outflowing material can be taken into account, as the domains have a quite large overlapping region. Small problems arise in simulations, which feature outflowing material through the boundaries between the domains, but they produce no significant effects.

4.2.4 Initial condition of the hydrodynamical simulations

In order to study the newly introduced physical effects (supernova heating, discrete mass input and optically thin cooling), a hydrodynamically stable initial condition is needed. For the case of our effective potential – made up of the nuclear star cluster, the black hole and the additional centrifugal potential due to orbital rotation – this is provided by the isothermal *Turbulent Torus Model* (see Section 2.2.1).

[2] Orbit always refers to a global orbit, measured at the torus radius at $R_{\mathrm{T}} = 5\,\mathrm{pc}$ and corresponds to a real time of approximately $1.2 \cdot 10^5$ yr.

[3] a linear interpolation in time is used

A conical volume around the rotation axis with a half opening angle of 4° needs to be cut out, because the funnel region of the turbulent torus model is dynamically unstable. If not cut out, it would lead to unphysically high velocities and temperatures due to infalling material towards the midplane, causing numerical problems.

As will be shown later in Section 4.5.2, the definition of the initial condition is uncritical, as due to the large mass input and violent behaviour of supernova injections and cooling, the initial conditions are washed out on short timescales, much shorter than our calculated time, even for the innermost domain.

4.2.5 Boundary conditions

Boundary cells are always problematic in numerical simulations. Therefore, so-called *ghost-cells* are used. They do not belong to the physically modelled domain of the simulations, but also take part in the advection as well as the force step. Special conditions can be applied to these cells depending on the desired behaviour of the flow pattern at the borders, in order to get physically results.

For the simulations in this work, we use periodic boundary conditions in ϕ direction, as we are only modelling a range of 90° for this coordinate. This is reasonable for a rotating structure. Material leaving the model space will enter it immediately again at the opposite ϕ-border. In θ-direction, as well as for the inner boundary in radial direction, outflow boundary conditions are applied. This means, that mass is allowed to flow out of the integration domain, but no material can get back into it. This implementation is often referred to as a *continuative* boundary. This means, that the values of the ghost cells are set such, that the normal derivatives at the boundary equal to zero for all quantities. This intends to present a smooth continuation of the flow through the boundary. In the simulations shown here, this is realised by keeping the mass flow and the pressure constant at the boundary cells. For a spherical grid, the first condition means that corrections need to be applied, as the size of the cells change in radial and θ direction. This can be done by multiplying with the ratio of the squares of the radii of the cells at the radial boundary and the ratio of the cosines of the cells for the θ boundary. These corrections can either be applied to the velocity components only or to the gas density and the temperature, in order to assure that the gas pressure ($P = \frac{\rho}{\mu} R\,T$) is kept constant as well. Within these zero gradient conditions, the normal velocity components only have a vanishing gradient, if the flow is directed outward of the computational domain. Otherwise they are set to zero. The factors correspond to the solid angle volume element: $d\Omega = \cos(\theta)\, r^2\, d\theta\, d\phi\, dr$. The cosine is used, as our θ-angle starts from the x-axis and not from the positive y-axis.

Problems with this simple boundary conditions can occur for the case of sound waves propagating out of the computational domain, which leads to partly reflection of these waves. Better techniques try to measure the speed and direction of these waves reaching the boundary and then apply boundary conditions trying to avoid reflection. Therefore, they are sometimes called radiation boundary conditions. But this is not the case in our simulations.

The outer radial boundary of the outer domain also allows for outflow in the same manner as described above. For the middle and inner domain, the outer radial boundaries are determined by the stored values of the outer and middle domain respectively, as described in Section 4.2.3.

4.2.6 Artificial viscosity

Supernova explosions and the ejection of planetary nebulae in cold material or any supersonic motion in our simulations causes the propagation of shock fronts. Mathematically, they can be treated as discontinuities in the physical quantities. This naturally causes problems in the numerical implementation, as these sharp discontinuities can not be resolved. Within the shock fronts – due to conservation laws – kinetic energy has to be transformed into heat, what can be done by viscous dissipation. Applying an unphysically large amount of viscosity in the medium causes a large amount of dissipation and, therefore, a smearing out of the shock front to a width which can then be resolved. This additional viscosity is known as artificial viscosity. Too small artificial viscosities can lead to post-shock oscillations in the velocity or to unphysical behaviour especially of velocities in low density regions. The implementation of a nonlinear artificial viscosity guarantees that it is strong in shocks and negligible elsewhere (see equation 4.13).

4.2.7 Numerical viscosity

Whereas artificial viscosity was introduced in order to get numerically stable simulations when shock waves appear in the medium, numerical viscosity is an unwanted numerical phenomenon, which appears due to numerical approximations in the different steps of the calculation. The numerical error can be determined by subtracting the physical hydrodynamical equations from the discretised equations. The leading terms are usually quadratic in the cell spacing and one distinguishes between dispersive (leading to oscillations in the solution) and diffusive (leading to smoothing of gradients) errors. In the TRAMP code, the dispersive errors are minimised, whereas some diffusive errors remain. During the advection, momentum exchange is calculated by adding the advected value to the value of momentum already in the cell, which leads to a smoothing of the flow. As this is done every timestep, in order to transport the flow, it induces something like a diffusion of the flow, similar to an additional viscosity.

4.2.8 Dust models for radiative transfer of hydrodynamic simulations

As already discussed in Section 2.3.1, radiative transfer calculations of three dimensional clumpy configurations are computationally very expensive and also resource intense calculations. This is even more the case for our hydrodynamic simulations, as the appearing filamentary structure needs to be well resolved within a large enough grid. Therefore, the test described in Sec. 2.3.1 has been expanded to smaller numbers of grains and for a continuous wedge-like model (the standard continuous model from Chapter 3). See this chapter for a detailed description of the deviations between the solid line (15-grain-model) and the dotted line (averaged grain properties) in Fig. 4.2. In this section, we additionally reduce the number of grains from 5 per chemistry to 2 (dashed line) and 1 (dash-dotted line). The resulting differences are only marginal for the face-on case. Larger deviations are visible at 90° for the dashed-dotted line, but only at short wavelengths. This is again caused by the less pronounced layering of dust grains. As larger grains are missing, the inner radius is shifted slightly further out, causing a smaller optical depth towards the $\tau = 1$-surface and, therefore, a shift of the Wien branch towards shorter wavelengths. As the inner surface is mainly shielded from direct view in the face-on case, hardly any effect is visible there.

As a conclusion for simulations with the necessity of very high resolution, one can say that a

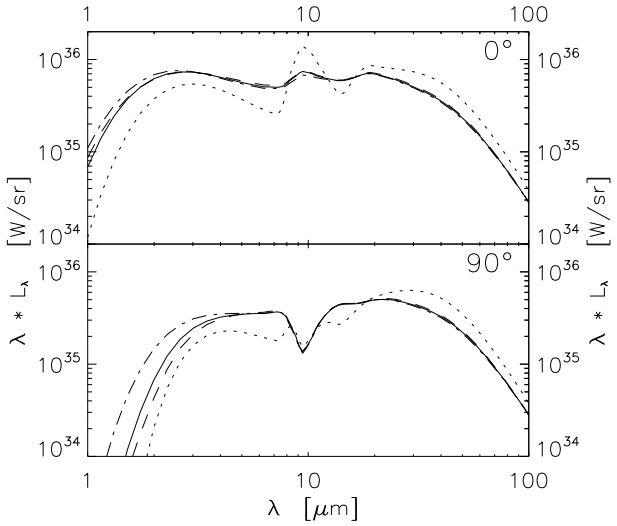

Figure 4.2: *Dependence on different dust models with the standard continuous model: split into 15 dust grains (solid line), one grain with averaged properties (dotted line), split into 6 dust grains (dashed line) and into 3 (dash-dotted line).*

dust model made-up of 2 grain sizes (maximum and minimum of the distribution) seems to be an adequate representation.

4.2.9 Turbulence

As pointed out by Breitschwerdt & de Avillez (2006) and also explained in Appendix A, turbulence in the ISM does not only provide an additional pressure source, but it is also highly important for the dynamics of the ISM. It acts on small as well as on large scales, where it plays a completely opposite role. On global scales, it provides support against gravity by setting up an additional *turbulent* pressure, whereas on small scales, it promotes collapse of the cold gas. It also shows up in enhanced mixing of fluid elements and, thereby, provides a means to have large amounts of mass in the thermally unstable regime. H I Arecibo Survey observations by Heiles & Troland (2003) find 48% of the *Warm Neutral Medium* in the thermally unstable regime between 500 and 5000 K. Similar results ($\approx$ 60%) are found in simulations (Breitschwerdt & de Avillez 2006). There are many sources in the ISM providing shear flows, finally leading to turbulent behaviour, e. g. stellar outflows, jets, thermal instability, supernova, etc. Energetically the most important one is supernova energy input (Mac Low & Klessen 2004).

Turbulence affects a very large temperature, as well as density range. Both, large and small eddies exist at the same time. Therefore, very high resolution in combination with large dynamic ranges in density and temperature are mandatory for a realistic simulation of ISM turbulence. In our simulations, turbulent behaviour is visible in a dense nuclear disk, which forms in the vicinity of the torus radius (see Section 4.5.5).

So-called Reynolds stresses can be used to characterise it's behaviour by determining the strength of turbulence and the amount of angular momentum transport caused by it.

Transport properties of the turbulence

Transport of angular momentum due to turbulence can be measured by means of a turbulent or eddy viscosity (see also Lynden-Bell & Pringle 1974), which can be done with the help of the *Reynolds stress tensor*, which is defined as the stress tensor in a fluid due to the random turbulent fluctuations in fluid momentum. The stress itself can be found by averaging over these fluctuations. First of all, the velocity can be decomposed into its mean value plus departures therefrom

$$\vec{u} = \overline{u}\,\hat{u} + \vec{\delta u}, \tag{4.14}$$

where bars mean averaging over time and space and $\hat{u}$ is the unit vector pointing in direction of the flow. Introducing this into the Euler or Navier-Stokes equations, they can be split into an average and fluctuating part. Doing this, a stress appears on the right hand side, namely the Reynolds stress, which can be written as:

$$W_{ij} = \overline{\delta u_j\, \delta(\rho\, u_i)}. \tag{4.15}$$

The Reynolds stresses represent the mean force (per unit area) imposed on the mean flow by turbulent fluctuations. In analogy to the kinetic gas theory, Reynolds stresses are split into an isotropic (*turbulent*) pressure part – namely the diagonal-components of the tensor – and an off-diagonal part, which is the turbulent viscosity.

Turbulent transport in a nonmagnetized disk can now be quantified by the $R\phi$-component of the turbulent stress tensor W (e. g. Cabot & Pollack (1992), Kato & Yoshizawa (1993), Balbus et al. (1994), Klahr & Bodenheimer 2003):

$$W_{R\phi} = \overline{\delta u_\phi\, \delta(\rho\, u_R)} \tag{4.16}$$

$$= \overline{\rho\, u_\phi\, u_R} - \overline{u_\phi}\,\overline{\rho\, u_R}, \tag{4.17}$$

where $R = r\cos(\theta)$ is the cylindrical radius. For positive values of $W_{R\phi}$, angular momentum is transported outwards. Scaling this turbulent stress tensor with the average pressure in the midplane – given by $P = \overline{\rho}\, c_s^2$ – results in the so-called α-stresses. For the case of the $R\phi$-component, the classical Shakura-Sunyaev-α-value[4] results:

$$\alpha = A_{R\phi} = \frac{W_{R\phi}}{\overline{\rho}\, c_s^2} = \frac{\overline{\delta u_\phi\, \delta(\rho\, u_R)}}{\overline{\rho}\, c_s^2}, \tag{4.18}$$

This is the α-value of an effective viscosity, which would cause the same amount of angular momentum transport by viscous diffusion in a laminar flow. But in our simulations, it is actually caused by turbulent motion of the gas.

[4] in the Shakura-Sunyaev alpha-viscosity model, the viscous stress tensor is assumed to scale with the local gas pressure with an unspecified proportionality constant $\alpha < 1$.

Similar to these considerations, the turbulent Mach number can be derived, which is then given by the square-root of the sum of the on-diagonal elements of the α-stress tensor and represents the strength of the turbulence:

$$M = \sqrt{A_{rr} + A_{\theta\theta} + A_{\phi\phi}} \tag{4.19}$$

The single on-diagonal components, corresponding to the square of the turbulent Mach number in a certain direction, give us a measure of the isotropy of the turbulence:

$$A_{rr} = \frac{\overline{(\delta u_R)^2}}{c_s^2}, \tag{4.20}$$

$$A_{\theta\theta} = \frac{\overline{(\delta u_R)^2}}{c_s^2}, \tag{4.21}$$

$$A_{\phi\phi} = \frac{\overline{(\delta u_R)^2}}{c_s^2}. \tag{4.22}$$

4.3 The model and its realisation

A short overview over the model we are realising was already given in the introduction (Section 4.1). After providing some more details, the implemented input of gas and energy, as well as the cooling function will be described in this section.

4.3.1 Overall model

According to observations, a large number of low luminosity AGN host nuclear star clusters in their centres. We model this in form of a Plummer profile (Plummer 1911) and assume that it was built up during a short-duration starburst. The first phase of evolution is expected to be very violent, where supernova type II explosions might evacuate more or less the whole cluster from gas, either remaining from the creation of the nuclear star distribution or from mass loss of evolving stars. According to our population synthesis modelling with the starburst 99-code (Leitherer et al. 1999; Vázquez & Leitherer 2005), this phase takes approximately 40 million years. Within about the same time period, double systems of lower mass stars have been able to form. According to models which include binary systems (de Donder & Vanbeveren 2003), the rate of supernova type Ia explosions – arising from double degenerate systems – begins to rise steeply and it dominates the input of energy of the coeval stellar population from then on[5].

The main mass loss mechanism is now the ejection of planetary nebulae by stars in the intermediate mass range (from 1.5 to 8 $M_\odot$, Kwok 2005). As we do not trace stellar evolution explicitly, the mass input of a single planetary nebula is fixed and occurs instantly. As the nuclear star cluster is mainly stabilised by its velocity dispersion, this random velocity is transferred to the ejected blobs of gas, together with the rotational velocity of the central star cluster.

[5] SN Ia appear later, as their progenitors (white dwarfs in binary systems) have to form first.

There will also be material transported into the simulated domain of the active galactic nucleus from further out of the galaxy. Prominent examples are dusty mini-spirals, of which some have been discovered by NACO (Prieto et al. 2005) or HST-ACS observations (Hubble Space Telescope – Advanced Camera for Surveys). Simulations (Maciejewski 2006) show that with the help of such nuclear spirals, enough gas inflow can be produced in order to power luminous nearby AGN. At present, this kind of gas input is not considered in our simulations. The idea is to check, whether input due to stellar evolution of such nuclear clusters, which are conveniently found in Seyfert galaxies, is already enough to produce tori with column densities (for the edge-on case) similar to observed ones. But it is expected that infalling material from further out will suffer the same fate as planetary nebulae (PN) in our picture, namely streaming inwards.

The total time of our runs is 10 orbits at the torus radius ($R_{\mathrm{T}} = 5\ pc$), which corresponds to $1.2 \cdot 10^6$ Myr. This is sufficiently long to avoid memory effects from the initial condition and at that point, a global dynamical equilibrium concerning the total mass and total energy is reached for the outer domain. In the middle and inner domain, the calculated time evolution of one and 0.1 orbits at the torus radius respectively, is not long enough to reach a global dynamical equilibrium state. However, a longer time evolution was not possible within reasonable computational times. For details see discussion below.

4.3.2 Input of gas (dust)

In our simulations, we assume that a nuclear star cluster is built up during a short-duration starburst, which forms a so-called *coeval stellar population* (CSP). Stars of all masses loose material during their lifetime. This can be in the form of winds of different strengths. For the case of high-mass stars also supernova type II explosions are taken into account in the procedure described below. The mass loss mainly happens within short periods of the life time of the star (e. g. at the tip of the Red Giant Branch).

In principle, the time dependence of the mass loss rate of a coeval stellar population can be calculated, if the stellar initial mass function (IMF) $\psi(m_i)$ and the time dependence of the mass loss rate of individual stars $\dot{m}(t, m_i)$ is known:

$$\dot{M}(t) = \int_{m_{min}}^{m_{max}} \dot{m}(t, m_i)\, \psi(m_i)\, dm_i \tag{4.23}$$

Unfortunately, both of them are not known in detail. Jungwiert et al. (2001) use a number of simplifying assumptions for the calculation of their model. The various phases of mass loss are summarised in one delta peak for the intermediate mass stars (IMS) and the high mass stars (HMS) and two delta peaks for low mass stars (LMS). For the IMS the delta peak represents the AGB (*Asymptotic Giant Branch*) wind peak and for the HMS the SN explosions plus winds. For the LMS, it represents the wind loss at the tips of the RGB (*Red Giant Branch*) and AGB. For the IMF, they use a power-law with three slopes (0.2, 1.7 and 1.3 for initial mass ranges of 0.1-1 $M_\odot$, 1-10 $M_\odot$ and 10-100 $M_\odot$) as given by Scalo (1998), representing an average of recently published IMFs.

With this, the solving of the equation of stellar mass loss (4.23) reduces to the knowledge of the IMF, the stellar initial-final mass relation and the stellar lifetime-mass relation. For the latter two,

Jungwiert et al. (2001) use the Padua stellar evolutionary models (Bressan et al. 1993; Marigo et al. 1996).

With this procedure, an approximate, normalised mass loss rate function, appropriate for our simulations can be derived:

$$\dot{M}(t)_{\mathrm{n}} = \frac{5.55 \cdot 10^{-2}}{t + 5.04 \cdot 10^{6}\,\mathrm{yr}}, \tag{4.24}$$

where the subscript n denotes that it is normalised to the initial mass of the *Coeval Stellar Population* (CSP).

This leads to a normalised mass loss rate of $1.2 \cdot 10^{-9}\, M_{\odot}\, yr^{-1}\, M_{\odot}^{-1}$ at the beginning of our simulations (after 40 Myr). It is obvious that this procedure includes quite large uncertainties. Comparing it to another approach to calculate mass loss given by Mathews & Brighenti (2003), differences of a factor of 2 can be found. Their calculation was originally done for the simulation of elliptical galaxies. They obtain their result by assuming an aging single burst stellar population with a Salpeter initial mass function. These calculations lead to the following specific mass loss rate of the stars:

$$\alpha_{*} = 4.7 \cdot 10^{-20} \left(\frac{t + t_{\mathrm{zero}}}{t_{\mathrm{n}}} \right)^{-1.3} \frac{1}{\mathrm{s}} \text{with } t_{\mathrm{n}} = 13\,\mathrm{Gyrs} \tag{4.25}$$

Further uncertainties arise from the initial mass function. Recent observations tend to find rather top heavy IMFs in the centres of galaxies. This means that the amount of more massive stars is increased compared to low-mass stars. It has been shown for the centre of the Milky Way (Stolte et al. 2002, 2005; Nayakshin et al. 2006; Paumard et al. 2006), the Andromeda galaxy (Bender et al. 2005) as well as more distant galaxies (Scalo 1990; Elmegreen 2005). Therefore, actually higher mass loss rates are expected.

To calculate the mass input within our simulations, these rates have to be multiplied with the local stellar density. Numerically, mass injection means a source term in the continuity equation as well as the momentum equation, when taking the ejection velocity of the blob into account. Within our simulations, the injection of mass is modelled with the following method: We make similar assumptions as above, namely that the injection of mass appears as a delta peak at a certain time. As the main mass input at the time of our simulations is given by the ejection of planetary nebulae, we further refer to this mass input mechanism as the planetary nebulae injection, although all mass loss effects mentioned above are included. According to the mass injection rate, which is fixed at the value given above, we check every timestep, how many planetary nebulae with mass m_{PN} have to be injected within the whole model space. The residual time is transferred to the next timestep. The position of the ejecting star is chosen randomly following the distribution of stellar mass. The ejection velocity of the gaseous blobs (planetary nebulae) is chosen such that it matches the velocity dispersion of the stars in the central star cluster, which is assumed to be constant, as in the assumption of the turbulent equation of state in the TTM-model. Overlayed is the rotational velocity of the stellar cluster stars, also taken over from the TTM-model, see Section 2.2.1.

All of the ejected planetary nebulae have the same gas mass in our simulations, as we cannot follow the evolution of single stars directly. Therefore, we calculated the mean mass by weighing

the initial-final mass relation (given by Weidemann 2000) with the Initial Mass Function (IMF), which in this mass regime is well approximated by a Salpeter-like function (Weidner & Kroupa 2006): $\frac{dm}{dt} \propto m^{-2.5}$. This leads to an average mass of 2.2 $M_\odot$ per planetary nebula. Within the simulations shown in this work, this mass is distributed homogeneously over 3^3 cells surrounding the randomly chosen position.

A detailed modelling of the temperature structure of a planetary nebulae is beyond the possibilities of our current resolution. As it will finally thermally merge with the surrounding gas on short timescales, we choose the temperature to be the same as the gas in the cells where they are injected. This refers to the fact that we would need tremendously higher spatial resolution in order to allow for the small-scale physical processes, which would lead to a thermalization of the gas.

4.3.3 Planetary nebulae

Similar to the AGN phenomenon, planetary nebulae are active all along the electromagnetic spectrum. Their name derives from their appearance as faint disks, resembling images of Uranus or Neptune, when the first one (NGC 6853) was discovered by Messier in 1784.

According to stellar evolutionary models, most of the stars with initial masses between 1 and 8 $M_\odot$ will go through the planetary nebula phase and end their lives as white dwarfs[6]. Despite this large range in initial masses, all white dwarfs have very similar masses, close to 0.6 $M_\odot$ (Weidemann 1990). Therefore, large amounts of mass are lost to the ISM, part of which is in form of such planetary nebulae.

[6]provided they are single stars or belong to a wide binary system

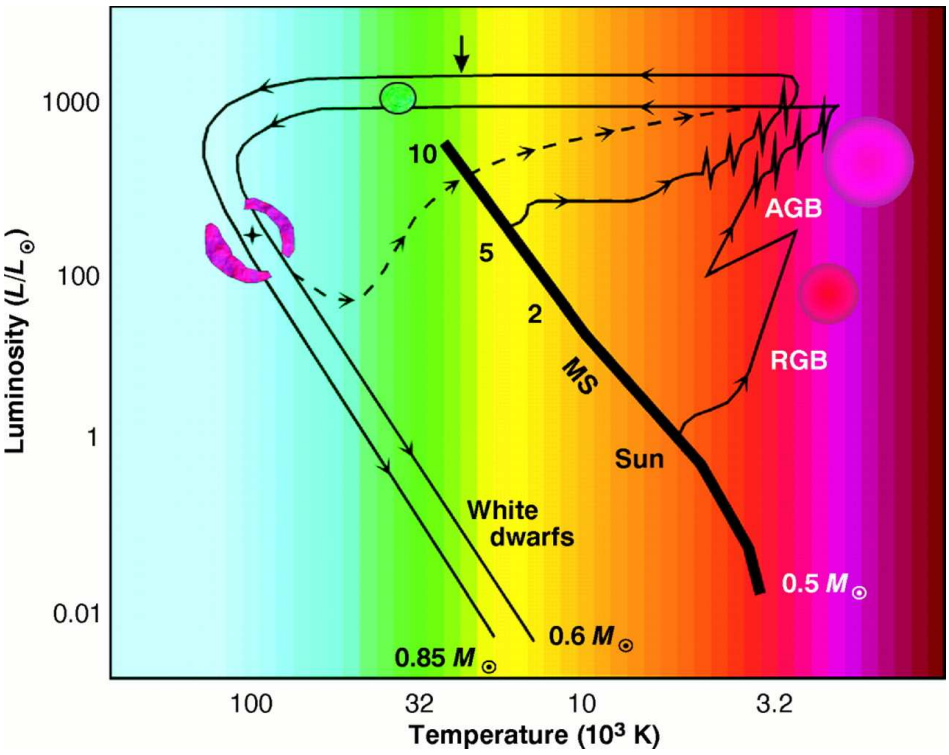

Figure 4.3: *Two examples of stellar evolutionary tracks in the* Hertzsprung-Russel *Diagram (HRD), which go through the phase of planetary nebula ejection and end in the white dwarf state. Numbers along the main sequence (MS) denote masses of the stars in $M_\odot$. The dashed line describes a so-called born-again scenario, where He above the core is reignited, which brings the star back to the tip of the AGB-phase. Taken from Weinberger & Kerber (1997).*

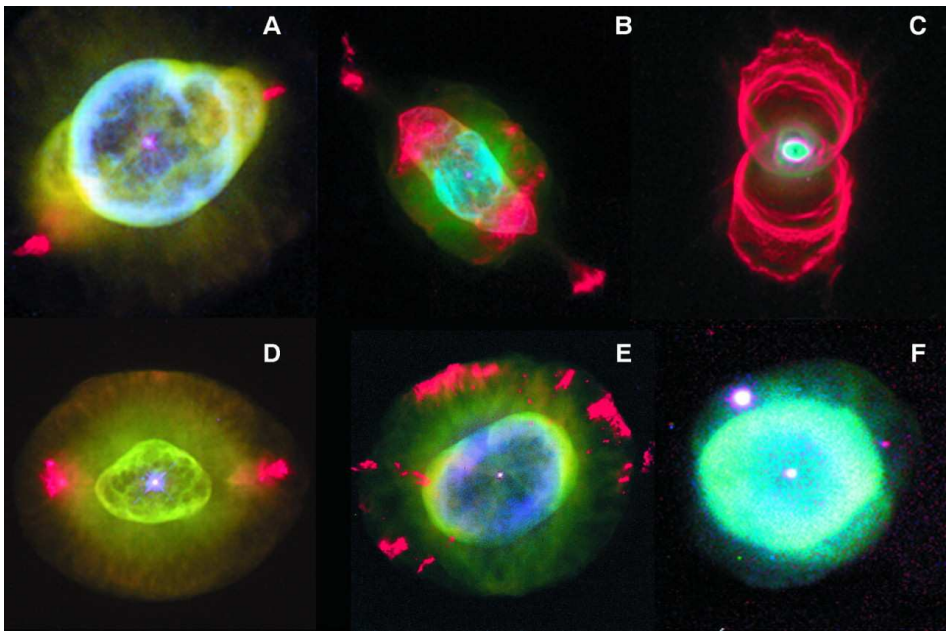

Figure 4.4: *Examples for various morphologies of planetary nebulae. Shown are colour composite images of [N II] emission in red, H I emission in green and [O III] emission in blue: (***A***) NGC 3242, (***B***) NGC 7009, (***C***) MyCn 18, (***D***) NGC 6826, (***E***) NGC 7662 and (***F***) NGC 2610. Images were observed with the Hubble Space Telescope, except of (***F***) which was taken with the* 2.1 *m telescope of Kitt Peak National Observatory. Figure copied from Weinberger & Kerber (1997).*

Typical evolutionary paths of such stars are shown in Fig. 4.3 in the HERTZSPRUNG-RUSSEL diagram. When a population of stars is born, they occupy the Main Sequence (MS) in this diagram, while they are powered by nuclear fusion of hydrogen. Their position on this sequence as well as their entire evolution mainly depends on their mass and composition (metalicity content). After the hydrogen abundance is reduced to approximately 10% – the duration differs by orders of magnitude in time – helium burning starts in the core, while hydrogen burns in the shell of the star. This leads to an inflation of the star and it evolves along the Red Giant Branch (RGB) sequence. When it enters the AGB-phase (*Asymptotic Giant Branch*), the star alternately burns H or He in shells above an electron-degenerate C, O and Ne core, leading to thermal pulses, showing up as jumps in the HR-diagram. Convective mixing then leads to transport of heavier elements (C,O and Ne) from the core into the atmosphere. There, dust grains are able to form and radiation pressure exerted on them leads to a stellar wind. This wind increases as the luminosity of the central star increases and eventually, a hole expanding envelope can be ejected from the contracting stellar remnant. The star evolves towards higher temperatures (to the left) and when it reaches approximately 30 000 K, photons are able to cause photoionisation of the expelled shell and the planetary nebula is observable at optical wavelengths from now on. This is indicated by the vertical arrow in Fig. 4.3. The morphology of this new born nebula depends mainly on the mass loss mechanism of the star and how the envelope is expelled. Also fast gas particles from the central star at later stages shape the nebula further. Thereby, it mirrors the physical condition within the planetary nebula. Also interaction with the surrounding medium is possible.

Examples for various morphologies are given in Fig. 4.4. (**A**) belongs to the class of bipolar nebulae, whereas the rest of the images are elliptical nebulae with various strengths of ellipticity. Binary systems and rotation of the precursor stars are hold responsible for these asymmetric appearances of the nebulae. But the main shaping of the planetary nebulae is done by the interaction of a fast

wind with the remnant shell from the AGB stage. These fast winds will generate shock waves, forming a bubble of a few million Kelvin hot gas inside the PN (as was observed with ROSAT). Surrounding the gaseous nebula (with approximately 10 000 K), neutral gas – containing H and CO – as well as dust can be observed, challenging theoretical models. The conundrum – comparable to AGN tori – can also be explained by inhomogeneities within the structure of the nebulae in form of small scale clumps, which have already been observed e. g. in the Helix nebula.

After 10 000 to 50 000 years, the PN mixes with the surrounding ISM and is too faint to be observable, because the fast wind from the central star fades away.

4.3.4 Heating due to supernova explosions

As explained before, type II supernovae from the nuclear star cluster occur very early after the formation of the nuclear star cluster (e.g. a 40 $M_\odot$ mass star lives only about 5 Myr) and are not considered in our models, which start after this phase.

We are interested in the rate of type Ia supernovae. It rises at roughly the time, when the SN II-rate drops – a result found in population synthesis modelling including binary systems (de Donder & Vanbeveren 2003). SN Ia are expected to be most important for the energy input from the cluster at later stages, when our simulations start. According to today's theoretical understanding, SN Ia are thought to be thermonuclear disruptions of accreting white dwarfs (WD). There are different scenarios, which might lead to a SN Ia explosion, although there are many uncertainties. The most important ones are sketched in Fig. 4.5. All of them start with a main sequence binary system. The primary star needs to be in the mass range between 4-10 $M_\odot$, so that it develops to the AGB-stage and forms a degenerate CO core. After filling up its Roche-lobe, a common envelope is formed and a CO white dwarf develops. Depending on the separation of the two and the mass of the remaining main sequence star, two scenarios can be distinguished. For masses larger than 4 $M_\odot$ a pair of white dwarfs is finally formed. If the two WDs merge due to angular momentum losses via gravitational wave radiation, a Chandrasekhar mass ($\approx 1.4\,M_\odot$)[7] may accumulate and the scenario might lead to a SN Ia explosion (branch A in Fig. 4.5). This is also called the double degenerate (DD) scenario. The second scenario is appropriate for a secondary star in the mass range between 2.5 and 4.0 $M_\odot$. This star eventually becomes a He star, fills its Roche lobe and, thereby, transfers mass to the white dwarf. If this accreted He layer ignites, it compresses the core and may lead to the ignition of carbon, although at sub-Chandrasekhar masses. This scenario is labelled B in Fig. 4.5 and is called *edge-lit detonation* (ELD). Currently, it is at odds with observations, although theoretically predicted. Finally, if the secondary has a mass below 2-3 $M_\odot$, it has the ability to fill its Roche lobe within the main sequence or subgiant phase and can transfer enough mass on the white dwarf so that it reaches the Chandrasekhar mass limit (branch C in Fig. 4.5).

The determination of SN Ia rates for such a nuclear stellar system is complicated. Observations exist only for few galaxies and, therefore, have to rely on low number statistics. A recent publication by Sullivan et al. (2006) describes the SN Ia rate for young and old stellar populations and find that it can be well represented by the sum of $5.3 \pm 1.1 \cdot 10^{-14}$ SNe yr$^{-1} M_\odot^{-1}$ (old populations of stars) and $3.9 \pm 0.7 \cdot 10^{-4}$ SNe yr$^{-1}(M_\odot\, yr^{-1})^{-1}$ of star formation for a young population of stars. For the total mass of our nuclear cluster of $1.9 \cdot 10^9\ M_\odot$ and an assumed duration of the starburst of 40 Myr, this results in a SN Ia rate of $1.8 \cdot 10^{-2}$SNe yr^{-1}. Due to the large uncertainties in theoretical derivation

[7] The Chandrasekhar mass is the maximum mass, which can be supported by electron degeneracy pressure.

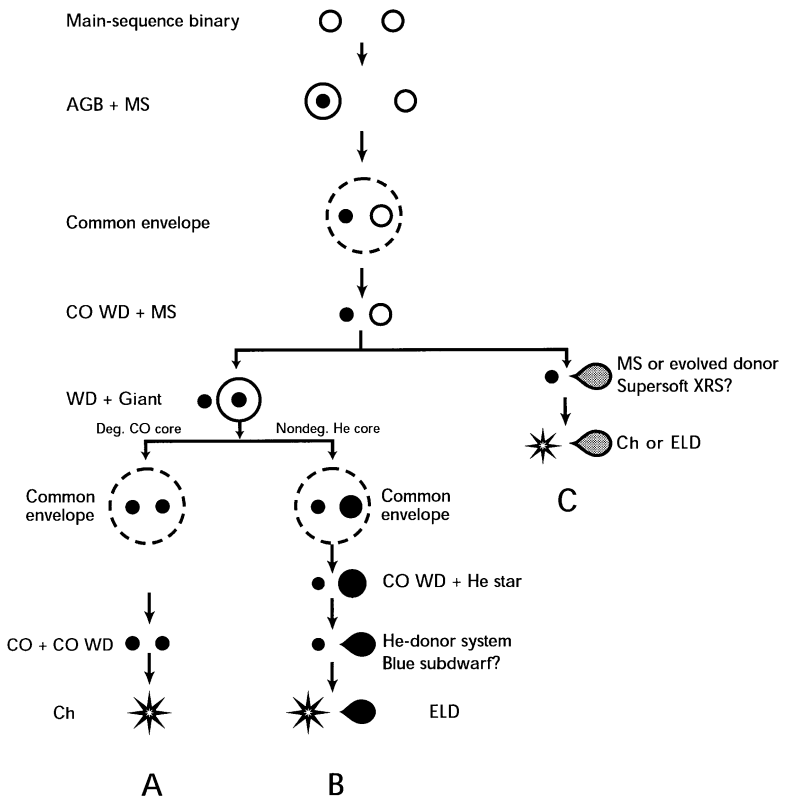

Figure 4.5: *Evolutionary scenarios for the most frequent potential progenitors of SNe Ia. Ch: accumulation of a Chandrasekhar mass by a white dwarf and central carbon ignition. ELD: accumulation of 0.15 of He on top of a sub-Chandrasekhar mass white dwarf. See text for details. Figure taken from Yungelson & Livio (2000).*

of supernova rates and as it is doubtful whether the observational derivations are appropriate for our simulations, we consider the SN Ia rate a more or less free parameter within our models.

In a starburst scenario within nuclei of Seyfert galaxies, Wada & Norman (2002) use a large rate of roughly 100× our SN-rate, namely 1 SN detonation per year, restricted to a narrow strap around the midplane. This is motivated by violent star formation within a dense gas disk in the galactic midplane, accounting for SN II explosions. For a discussion of their model, see Section 4.9.

After a SN-rate parameter study, a value of 10^{-10} SNe $M_{\odot}^{-1}\, yr^{-1}$ was chosen for our standard model. It is assumed to be constant in our simulations, as only a short time evolution (1.2 Myr) is possible at the moment. From the supernova rate for the whole model space, the number of supernovae exploding in each timestep can be determined. Residual time is added up to the next timestep. If a supernova is launched, the position is determined randomly. The energy is injected into a single cell in the form of thermal energy. Additionally a mass of 1.4 $M_{\odot}$ is added to this cell, also ensuring numerical stability.

Hydrodynamic simulations of single supernova explosions within different environments were undertaken by Thornton et al. (1998). They took the 10^{51}ergs (Chevalier 1977; Abbott 1982; Woosley & Weaver 1986; Heiles 1987), which are associated with the lightcurve and kinetic energy output of type Ia and type II supernovae explosions and used this as the total initial energy (kinetic plus thermal) in their simulations. They find that the total energies of the remnants in the late stages of their expansion range between $9.0 \cdot 10^{49}$ ergs and $3.0 \cdot 10^{50}$ ergs with a typical case being $1.0 \cdot 10^{50}$ ergs.

In these simulations, the amount of SN energy input into the ISM is a sensitive function of the surrounding density and metalicity. The total energy available in kinetic and thermal energy is the greatest in the limiting cases of low density and low metalicity, which is due to the lower cooling rates in these environments. Therefore, a larger amount of energy remains in the remnants. In concordance with these simulational results and with Navarro & White (1993), we use an efficiency of $\eta_{\rm SN} = 0.1$, reducing the input of thermal energy.

One problem with adding the SN energy discretely as thermal energy is that for the case of large gas densities, most of this energy is lost due to the implemented optically thin radiative cooling curve ($\Lambda_{\rm cool} \propto \rho^2$). Depending on the gas density, this can happen within a few Courant timesteps and causes that no blast wave forms. Therefore, thermal energy is simply radiated away and cannot be transformed to kinetic energy. In order to overcome these problems, several ideas have been proposed:

1. Thacker & Couchman (2001) use an artificial time delay in cooling of the cells, where the energy has been injected.
2. Navarro & White (1993) assign the energy directly to kinetic energy of the explosion shell.
3. Joung & Mac Low (2006) choose the radius of the explosion sphere so that gas densities are sufficiently low that radiative losses within the spheres are negligible. Therefore no artificial cooling delay has to be applied.

The Joung & Mac Low (2006) model is not suitable for us, as these radii can get fairly high, sometimes close to the extension of our computational domain. When the energy is directly provided in form of kinetic energy of an expanding shell, very high resolution is necessary. Therefore, we use the possibility of the artificial time delay in cooling.

4.3.5 Cooling

A mixture of neutral and ionised gas mainly cools via the transformation of kinetic energy to radiation via collisional processes. This also means that the efficiency of cooling is a sensitive function of the constituents of the gas. The radiation can only escape, if the medium is optically thin for these wavelengths, otherwise cooling is inefficient.

Fig. 4.6 shows the effective radiative cooling curve applied in our simulations, provided by Richard Wünsch (private communication). Originally, it was created by Michal Rozyczka and Guillermo Tenorio-Tagle (unpublished work) using the code Cloudy (Ferland 1993) and later it was updated by Tomek Plewa with the help of Cloudy version 84.06 (Plewa 1995; Ferland et al. 1998). Cloudy is a spectral synthesis code to calculate fully physical conditions within an astrophysical plasma. It predicts the emitted spectrum by taking a large number of microphysical processes into account, which set the ionisation states, the population of excited states and the electron temperature. When the current cooling curves presented in this thesis were computed, the code included 13 elements: H, He, C, N, O, Ne, Na, Al, Si, S, Ar, Fe and Ni with solar abundances taken from Grevesse & Anders (1989) and Grevesse & Noels (1993). A hydrogen and heavy element molecule network as described in Hollenbach & McKee (1989), Ferland et al. (1994) and Ferland & Persson (1989) was applied. For the case of our cooling curve, a purely collisionally ionised optically thin plasma with solar abundances was used.

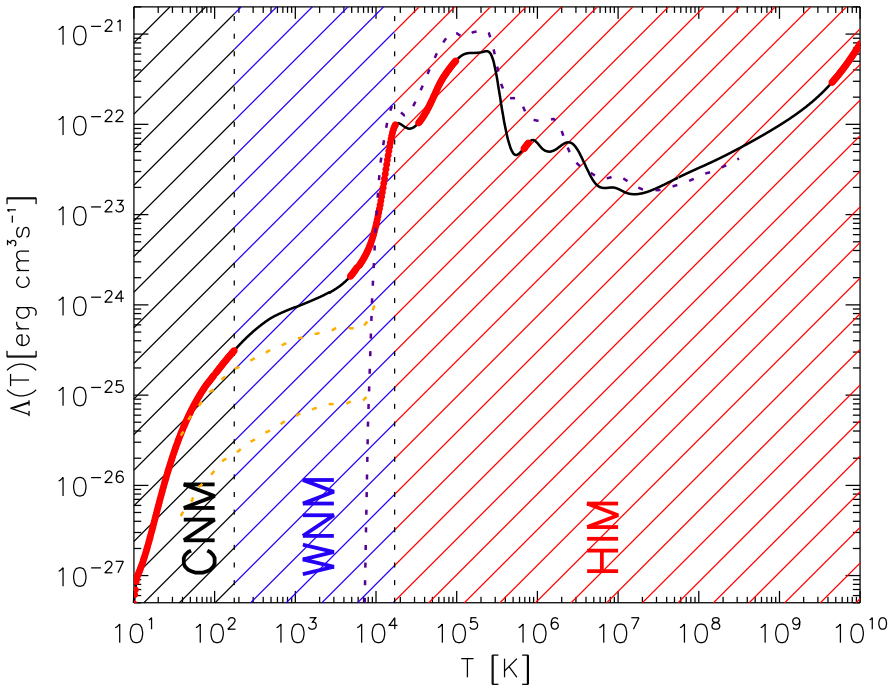

Figure 4.6: *Cooling curve. The hatched regions denote three temperature regimes: cold neutral medium (CNM), warm neutral medium (WNM) and hot ionised medium (HIM). Indicated in red are the thermally stable parts of the cooling curve. Dashed lines refer to cooling curves used by other groups, see text.*

Following Joung & Mac Low (2006), such a gas is thermally stable, where the slope in logarithmic display is steeper or equal to one. For the case of our cooling function, we find five distinct stable regions: 10 – 175 K, 4 814 – 17 403 K, 33 781 – 97 221 K, $6.82 \cdot 10^5$ – $7.72 \cdot 10^5$ K and $4.47 \cdot 10^9$ – $1.00 \cdot 10^{10}$ K. They are marked with the thick red line in Fig. 4.6. Overplotted as dotted lines are the often used cooling functions from Dalgarno & McCray (1972) – where only the part below 10^4 K is shown – given in yellow (with ionisation fractions of 0.1 for the upper curve and 0.01 for the lower one). The violet dotted line results from equilibrium ionisation cooling, calculated by Sutherland & Dopita (1993) for the case of solar metalicity. As can be seen from this, the cooling curves are in rather good agreement in the high temperature regime (above the ionisation temperature of hydrogen at around 10^4 K. At temperatures lower than 10^4 K, the values of the assumed cooling curves are most uncertain, as in this temperature regime, the approximation of thermal equilibrium is usually not valid. Therefore, large deviations exist between the different calculational methods. It is also a matter of debate, which ionisation fraction to assume for the low temperature part. We decided for an ionisation fraction of 0.1 (upper yellow curve and black curve in 4.6) in concordance with de Avillez & Breitschwerdt (2004), whereas Joung & Mac Low (2006) assume an ionisation fraction of 0.01 (lower yellow curve). For temperatures lower than 10 K, we set the cooling rate to zero.

In order to give a better understanding of the shape of the cooling curve, the contributions of the 10 most abundant elements are depicted in Fig. 4.7a) for the case of a hot ($T > 10^4$ K), tenuous, optically thin plasma. It is taken from Boehringer & Hensler (1989), resulting from their code, which takes only 10 elements into account and includes a slightly different subset of microphysical processes compared to the Cloudy code. Therefore, some differences in the morphological shape

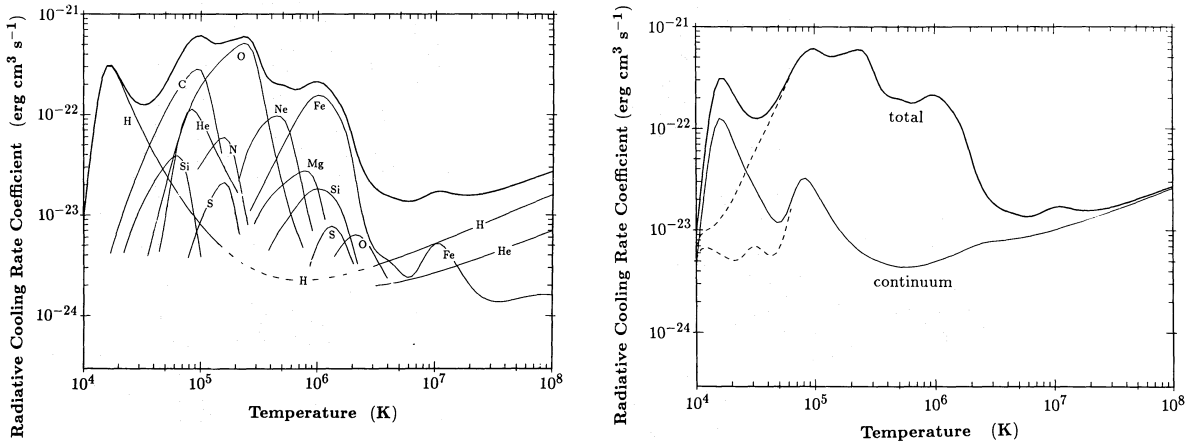

Figure 4.7: a) *Contribution of the different elements to the total cooling coefficient for solar abundances of elements.* **b)** *Contribution of the continuum emission processes (including free-free, two-photon and recombination radiation) to the total cooling function. Dashed curves include photoionisation of hydrogen. Figures taken from Boehringer & Hensler (1989).*

of the curve result. But the main features agree and are due to the same elements. These are namely H, C+He, O and Fe ions. Fig. 4.7b) displays the contribution of continuum radiation to the total cooling curve. At temperatures beyond $2.0 \cdot 10^7$ K, cooling is mainly determined by free-free emission, where mainly H and He ions are involved. The two peaks at roughly $1.5 \cdot 10^4$ K and $8.0 \cdot 10^4$ K are caused primarily by two-photon and recombination radiation. Therefore, below a certain metalicity threshold (below $10^{-3}\, Z_\odot$ for the stepsize given in Fig. 4.8), metalicity dependence vanishes, as continuum emission dominates at higher temperatures. Above this threshold, cooling delicately depends on the metal content. The more metals we have in our gas mixture, the more efficient the cooling is (see Fig. 4.8).

The cooling time is then given by

$$t_{\mathrm{cool}} = \frac{k_{\mathrm{B}}\, T}{n\, \Lambda_{\mathrm{cool}}\, (\gamma - 1)}, \tag{4.26}$$

where γ is the adiabatic index, Λ_{cool} is the cooling coefficient described above, k_{B} is the Boltzmann constant and n is the number density of gas.

In dense regions, it can be shorter than the Courant timestep. Therefore an implicit time-stepping method is applied for the cooling. Whenever the temperature decrease of one cell would be more than 10% of the initial temperature value of this cell, we iteratively reduce the temperature, by allowing only cooling of 10% at each step. With the help of this procedure, we are able to follow the shape of the cooling curve and unphysical jumps cannot occur. To do this, a cooling timestep is introduced with the advantage that the dynamical timestep remains untouched. Otherwise, dense regions could cause tiny dynamical timesteps and appreciably slow down the simulations.

Problems of this approach arise, when densities get very high. Then, the assumption of very small optical depth is not valid anymore and extinction effects should be taken into account.

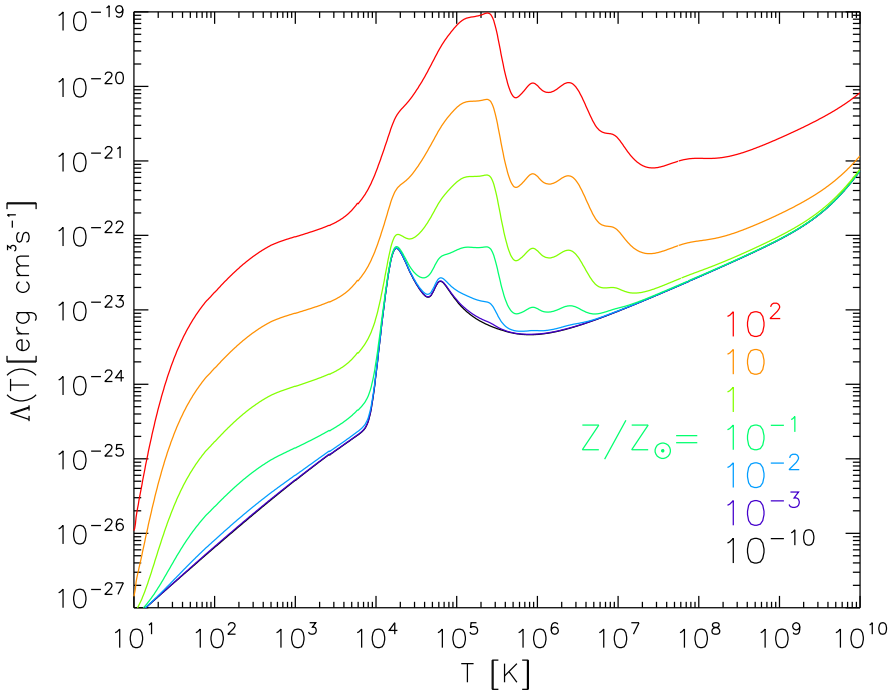

Figure 4.8: *Cooling curves for various metalicities, as indicated in the lower right corner, calculated with the Cloudy code (Ferland et al. 1998).*

4.4 Testing mass and energy injection

In this paragraph, we test the principal behaviour of the injection of planetary nebulae and their interaction within the model space. Only the idealised case of a homogeneous surrounding medium or a simple density distribution, stratified in one coordinate direction is taken into account. Cooling as well as effects due to our usual gravitational potential or the rotating model space are not allowed for, as only the principal behaviour is of interest here.

In contrast to all other simulations shown in this thesis, these simulations were done with the help of the PLUTO-code (Mignone et al. 2006) and using cartesian coordinates in 3 dimensions. A resolution of 50^3 grid cells, together with a range of 10 pc leads to a spatial resolution of 0.2 pc per grid cell, which corresponds to the resolution at a radial position of approximately 7 pc in our usual torus simulations.

In these simulations, planetary nebulae initially have a radial extent of 1 pc, a mass of 5 $M_\odot$ and a velocity of 140 km/s. The surrounding medium is homogeneous with a density of $1.0 \cdot 10^{-23}$g/cm^3, except for the one case of the stratified medium. We always show two sets of simulations. The first one with a temperature of the ambient medium (which is identical to the temperature of the injected mass of the PNe) of $2 \cdot 10^6$ K. This is roughly the value of the initial condition of our typical torus simulations. In the second case it is only 1000 K, corresponding to the warm neutral medium. Supernova injections are modelled as energy input only.

These simulations are meant to show the principal behaviour of these kind of interaction processes, in order to be able to interpret our global torus simulation.

4.4.1 Simulation of single planetary nebulae injections

In the first example, single planetary nebulae are injected, having a velocity component in positive diagonal direction within the x-y-plane. Depending on the temperature of the surrounding material, two cases can be separated, showing significantly different behaviour:

① **Supersonic injection velocity**
The case of low surrounding temperature (1000 K) is a typical example for supersonic (c_s = 5.5 km/s) behaviour (see Fig. 4.9): a bow shock is formed in front of the planetary nebula, whereas the region behind the object is nearly evacuated from gas. A diamond-ring like structure forms, with a shock wave surrounding it and a density enhancement due to the compressed planetary nebula in front, slightly behind the shock front. In the course of evolution, the ring shaped shock gets more and more elliptical and the density enhancement decreases, before it finally dissolves. The behaviour looks somehow similar to the case of a supernova explosion (see Sect. 4.4.3), although much less energetic and acting on longer timescales.

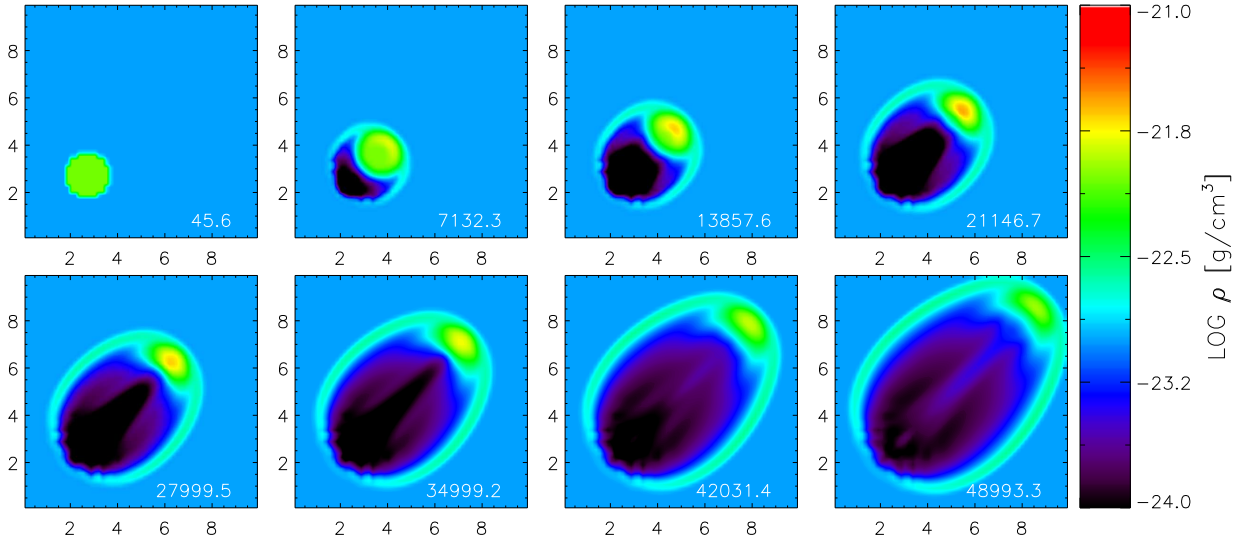

Figure 4.9: *Logarithmic density distributions of a model planetary nebula within a cold (1000 K), homogeneous medium (supersonic case). Time (lower right corner) is given in years. Displayed is a 2D slice through the 3D data cube.*

② **Subsonic injection velocity**
Scaling with the square root of the temperature, the sound speed increases significantly compared to the low temperature case and obtains values of the order of c_s = 250 km/s for a temperature of the surrounding medium of $2 \cdot 10^6$ K, much higher than the initial velocity of the planetary nebula (u_{ini} = 140 km/s). Therefore, its motion is in the subsonic regime and no shock wave is expected to form. As can be seen from Fig. 4.10, this is indeed the case, but other effects take place. The behaviour is similar to the RAYLEIGH-TAYLOR instability: In our case a denser blob of material moves through a less dense medium. Therefore, first a half-moon shaped object forms, and changes to a mushroom-shape with eddies forming at the edges.

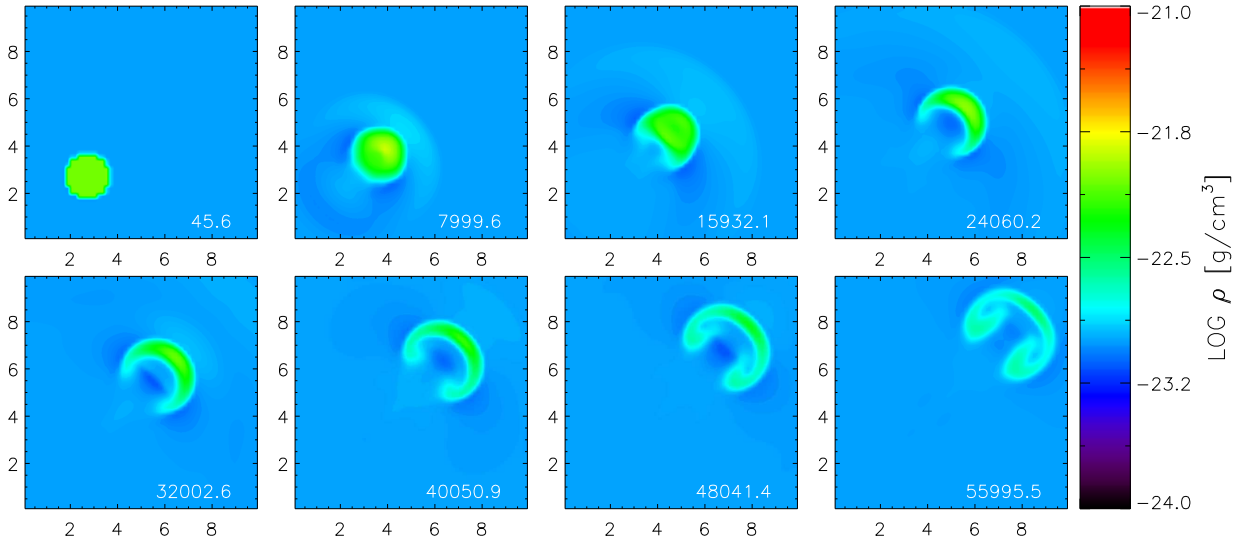

Figure 4.10: *Logarithmic density distributions of a model planetary nebulae within a hot, homogeneous medium (subsonic case). Time (lower right corner) is given in years.*

4.4.2 Interaction between two planetary nebulae

The large number of injected planetary nebulae as well as the presence of the large scale filamentary structure promotes frequent collisions between two planetary nebulae or with denser filaments. Therefore, the study of the impact of such interactions with the help of single processes within a homogeneous medium yields important insight for interpreting different stages of torus evolution. To study this, two planetary nebulae are ejected in opposite direction with a velocity of 140 km/s under an angle of 45° towards the x-axis.

Again, it can be divided into the sub- and supersonic case, where the single objects behave like described above.

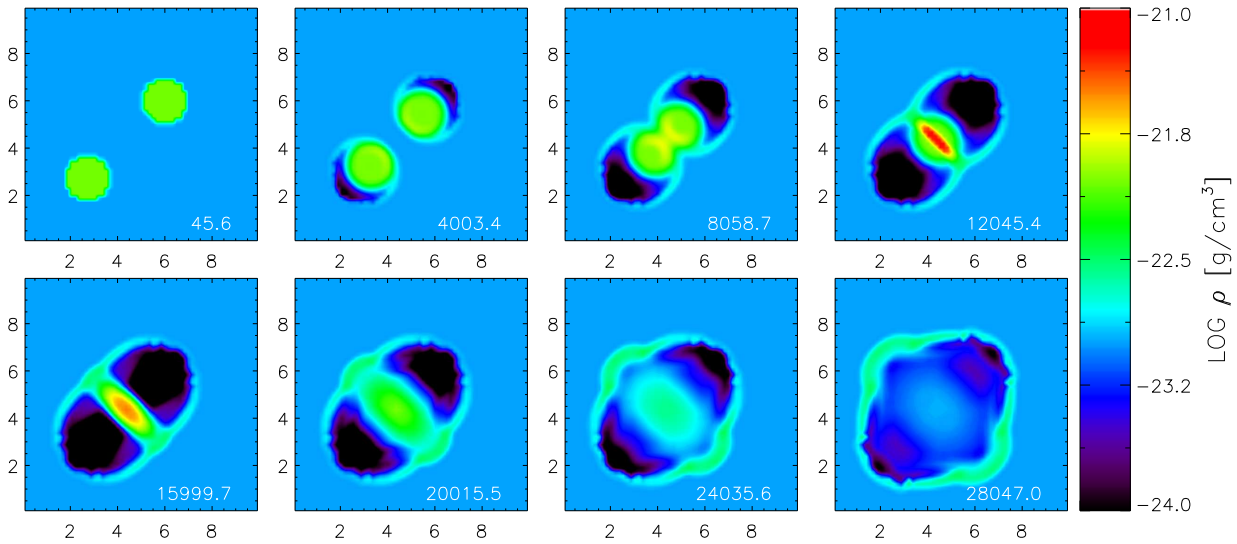

Figure 4.11: *Logarithmic density distributions of two model planetary nebulae interacting with one another within a cold (1000 K), homogeneous medium (supersonic case). Time (lower right corner) is given in years.*

① **Low surrounding temperature (Fig. 4.11)**
When the two still more or less spherical clouds collide with supersonic velocities, the density and temperature rise steeply at the interaction zone, leading to subsequent release of a shock wave propagating outwards and finally melting with the wrapping shock waves from the single PN-emissions. At later stages, this wrapping shock wave becomes more and more a spherical shell of density enhancement propagating outwards.

② **High surrounding temperature (Fig. 4.12)**
Fundamentally different is the subsonic case: as expected, the propagating spherical blobs disturb the surrounding medium (as well as the blobs themselves) much less, until they get in touch with each other. The actual interaction causes a flattening of the blobs. At later stages, they still flatten and thereby expand in orthogonal direction (relative to the interaction direction) and form a thin rigid filament with mushroom-like shaped ends, similar to the onset of Rayleigh-Taylor instability, as already described above.

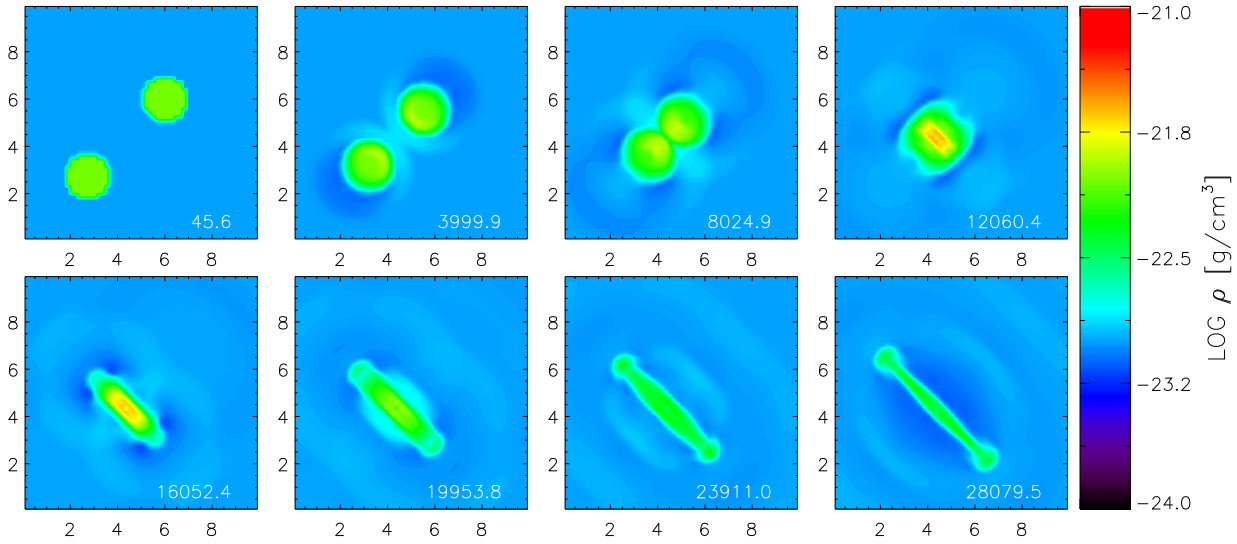

Figure 4.12: *Logarithmic density distributions of two model planetary nebulae interacting with one another within a hot ($2 \cdot 10^6$ K), homogeneous medium (subsonic case). Time (lower right corner) is given in years.*

Due to the small mean free path of planetary nebulae in our simulations, arising from the high rate of PN-input, the emerging filamentary structure and their further interaction with supernovae, the behaviour of these individual cases cannot be seen directly in our global simulations.

4.4.3 Simulation of single and interacting supernovae

The same study presented above for single planetary nebulae ejections is carried out for the case of supernova explosions. Being a much more energetic phenomenon with much larger velocities involved, both of the tested temperature regimes (1000 K and $2 \cdot 10^6$ K) show a similar, supersonic behaviour of expanding blast waves, which can be described reasonably well by the analytical Sedov blast wave solution (see Fig. 4.13) of Sedov (1959).

Only the case of two interacting supernova explosions at rest is shown here (see Fig. 4.14). Both temperature regimes display similar behaviour, as even in the high temperature test case

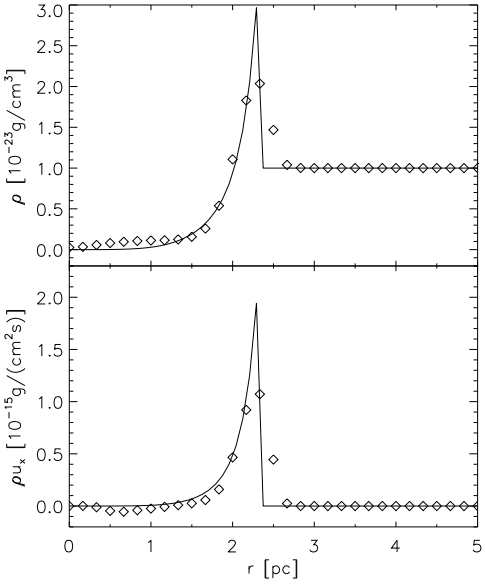

Figure 4.13: *Comparison of a single supernova explosion (diamonds) with the analytical Sedov blast wave solution (solid line). Shown are density (upper panel) and mass flux (lower panel) after an evolution time of 1000 years.*

($T = 2.0 \cdot 10^6\,K$), the velocities of the explosion front are well beyond the sound speed in the medium most of the time. The velocity peaks shortly after the explosion at a velocity of more than 1500 km/s in both simulations. Differences only occur at very late stages. As can be seen in Fig. 4.14, the shock waves of two nearby exploding supernovae merge to form a larger bubble, which at later stages develops into a spherical shell. A larger number of nearby explosions is able to form giant bubbles, known as superbubbles (e. g. McCray & Snow 1979; Tomisaka & Ikeuchi 1986; Tomisaka 1992). This is a phenomenon which can also be observed in the ISM and is normally due to associations of O and B stars.

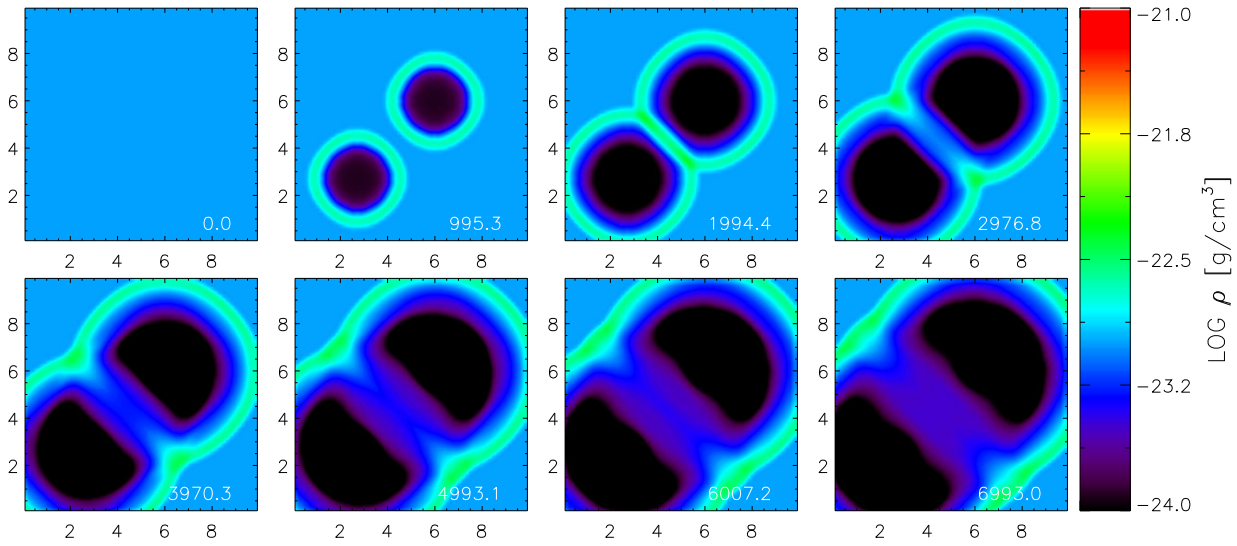

Figure 4.14: *Temporal evolution of a 2D-density slice through the 3D data cube showing two interacting supernova explosions. Time is given in years (see lower right corner).*

4.4.4 Supernova explosions in a stratified medium

Above, we showed that blast waves of a supernova explosion in a homogeneous medium expand spherically symmetric. A different behaviour can be observed in a vertically stratified medium. In our test case, the density rises logarithmically from the standard value of $1.0 \cdot 10^{-23}$ g/cm^3 up to 10^{-18} g/cm^3. The resulting simulation in terms of density can be seen in Fig. 4.15. The intersection of the horizontal and vertical line marks the origin of the supernova explosion (at rest). Density increases in upward direction and, therefore, the blast wave sweeps up material and further compresses the density stratification in this direction. But along the density gradient towards lower densities, the blast wave can propagate much faster and the bubble releases its hot gas in this direction. This temporal sequence of images also resembles the phenomenon known as the *galactic fountain process*, observable in galactic disks. There, several supernova explosions contribute to a superbubble. This bubble preferably propagates along the density gradient, away from the midplane of the disk, leading to release of hot gas into the halo and thereby reducing its volume filling factor within the galactic plane.

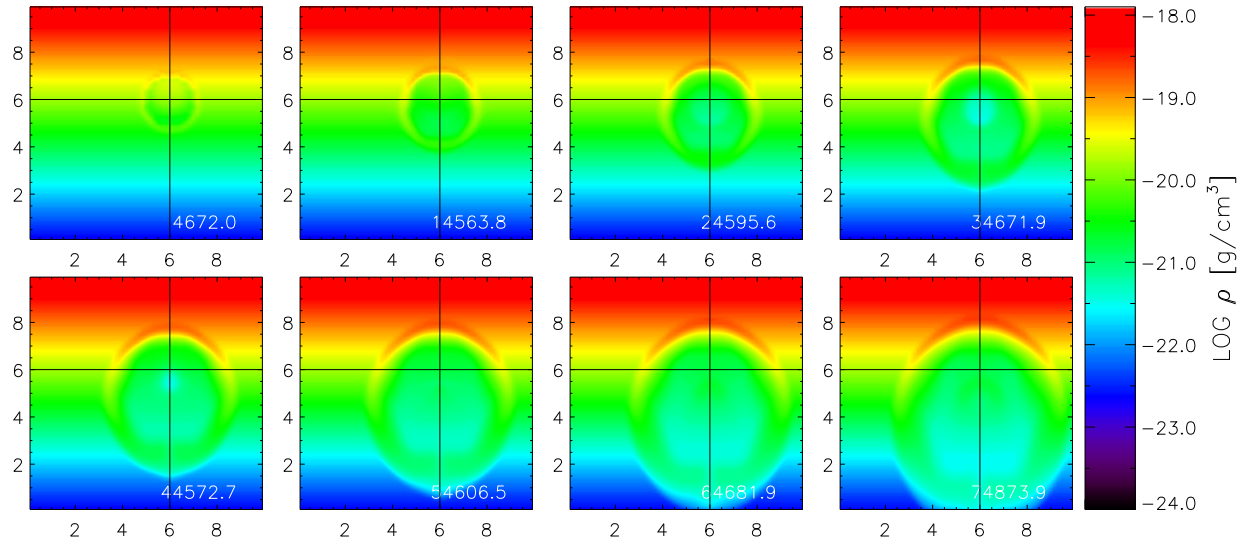

Figure 4.15: *Temporal evolution of a 2D-density slice (at the position of the explosion) through the 3D data cube showing a supernova explosion within a density stratified medium. Time is given in years (see lower right corner). The horizontal and vertical crossing lines give the midpoint of the explosion.*

4.5 Results and discussion

In the following sections, we show the results obtained with the ingredients mentioned before. First of all, the evolution of our standard model is shown in order to discuss the typical course of the evolution of such a torus model, before several parameter studies are presented.

4.5.1 Parameters of our standard hydrodynamic model

The parameters we use for our standard model are summarised in Table 4.1. Most of them have already been motivated in the last sections. For the remaining, short explanations are given in this paragraph.

The underlying gravitational potential is made up of two components:

① The potential of the nuclear star cluster with a total stellar mass of $M_* = 1.9 \cdot 10^9\, M_\odot$, which is modelled according to a Plummer distribution:

$$\phi_{\mathrm{Plummer}}(r) = -\frac{G\, M_*}{\sqrt{r^2 + R_\mathrm{c}^2}}. \tag{4.27}$$

② The Newtonian point-like potential of the nuclear black hole with a mass of $M_{\mathrm{BH}} = 6.64 \cdot 10^7\, M_\odot$:

$$\phi_{\mathrm{BH}}(r) = -\frac{G\, M_{\mathrm{BH}}}{r}. \tag{4.28}$$

Our initial condition comprises of a *TTM*-model similar to the one discussed in Chapter 2, but with a Plummer potential (as given above) and the parameters listed in Table 4.1. Additionally, the mass of the nuclear stellar cluster was determined with the help of the Jeans-equation to be $1.9 \cdot 10^9\, M_\odot$. The angular momentum of the stellar content, the gas in the initial condition as well as the injected gas follows the same distribution as given in equation 2.5, with a constant $\gamma = 0.5$ and a torus radius of $R_\mathrm{T} = 5\, pc$. In most of the simulations shown in this thesis, the turbulent pressure of the initial condition is substituted by a thermal pressure. For the case of our standard model, the velocity

Parameter	Value	Parameter	Value
M_*	$1.9 \cdot 10^9\, M_\odot$	γ	0.5
M_{BH}	$6.64 \cdot 10^7\, M_\odot$	T_{ini}	$2.0 \cdot 10^6$ K
$M_{\mathrm{gas}}^{\mathrm{ini}}$	$1.2 \cdot 10^4\, M_\odot$	mass loss rate	$6.0 \cdot 10^{-9}\, M_\odot/(yr\, M_\odot)$
R_c	25 pc	M_{PN}	$2.2\, M_\odot$
R_T	5 pc	supernova rate	$1.0 \cdot 10^{-10}$ SNe/(yr $M_\odot$)
R_{out}	50 pc	Γ	5/3
σ_*	165 km/s		

Table 4.1: *Parameters of our standard model. See text for explanations.*

dispersion of the assumed dust clouds in the *TTM*-model of $\sigma_* = 165$ km/s then corresponds to an initial temperature of $T_{\rm ini} = 2.0 \cdot 10^6$ K. The mass loss rate was chosen to be $6.0 \cdot 10^{-9}\, M_\odot/(yr\, M_\odot)$, which means a mass injection of $6.0 \cdot 10^{-9}$ solar masses of gas per year, normalised to one solar mass of stars. This follows the mass loss formalism presented by Jungwiert et al. (2001). Predictions of supernova rates involve larger uncertainties. For our standard model, we decided to use a SN-rate of 10^{-10} supernovae per year and $1\, M_\odot$ in stellar mass (see Section 4.3.4 for further discussion). As already discussed in Sect. 4.2.2, we apply the equation of ideal gas as a closing condition with an adiabatic index of an ideal monoatomic gas ($\Gamma = \frac{5}{3}$). The gas has solar abundances in our simulations, with a mean molecular weight, which changes from 0.6 (fully ionised gas with solar abundances) to 1.2, following a smooth transition at the ionisation temperature of hydrogen. Most of the simulations shown in this thesis ran for an evolutionary period of 10 orbits at the torus radius, corresponding to $1.2 \cdot 10^6$ yr. The total model space between 0.2 and 50 pc was decomposed into three parts: the inner part ranging from 0.2 to 2 pc, the middle part from 1 to 10 pc and the outer part from 5 to 50 pc (see Sect. 4.2.3).

Table 4.2 provides an overview over the parameter studies of our hydrodynamic simulations, which will be discussed in this thesis. Only the varied parameters are indicated. TOR 1 is our standard model, as described above.

In the following sections, first the principal evolution of our models is demonstrated and explained with the help of our standard model. Further, parameter studies are presented and a comparison between them is made. Please compare to the mentioned figures within this thesis and to the animations of the temporal evolution of the simulations provided on the enclosed DVD (see Appendix B).

4.5.2 Evolution of our standard model

The course of evolution of our standard model can best be seen in the animation provided on DVD (see also Appendix B), but the various stages described below are also depicted in Fig. 4.16. Within the first percent of an orbit at 5 pc, single injected blobs of material are visible, as well as the formation of single spherical cavities due to the explosion of supernovae. As discussed in Section 4.4.3, supernovae produce shock waves for the whole temperature regime of our simulations, whereas injected planetary nebulae show different behaviour. For hot surrounding material (the subsonic case), colliding streams tend to stick together and form long filaments. In cold material (supersonic behaviour), the formation of a common shock front surrounding the point of interaction is visible. All of these processes contribute to the formation of a filamentary structure. At the beginning – due to the hot ($\approx 2 \cdot 10^6$ K) initial condition, the first process dominates to form the first structures in combination with supernova explosions, mainly within 25 pc distance to the centre (the core radius of the nuclear star cluster). Compare to Fig. 4.16a. With ongoing evolution, these clumps merge and build up larger and denser filaments. The clumpy material is distributed more or less spherically symmetric, as is the distribution of stars, to which the SNe and PNe events are linked. These dense filaments cool on short timescales and due to the lack of pressure support (thermal as well as turbulent pressure from the stellar injection processes), gravity cannot be fully compensated by angular momentum and pulls them towards the minimum of the potential at a distance of 5 pc (the *torus radius*) within the midplane. Combined with this mechanism is the evolution of a toroidal structure and the opening of a narrow funnel along the rotation axis (Fig. 4.16b and c). Some explosions, appearing completely within the dense regions are able to disrupt the filaments,

Table 4.2: *Overview over the hydrodynamic torus models discussed in this chapter. TOR 1 is our standard model. Red color indicates the varied parameters relative to the standard model.*

Model Name	mass loss rate $10^{-9}\ M_\odot\, yr^{-1}\ M_\odot^{-1}$	supernova rate 10^{-10} SNe $yr^{-1}\ M_\odot^{-1}$	cooling	initial condition	stellar mass norm. const. $10^9\ M_\odot$
TOR 1	6.0	1.0	solar	TTM	1.9
TOR 2	2.4	1.0	solar	TTM	1.9
TOR 3	1.2	1.0	solar	TTM	1.9
TOR 4	6.0	2.0	solar	TTM	1.9
TOR 5	6.0	5.0	solar	TTM	1.9
TOR 6	6.0	10.0	solar	TTM	1.9
TOR 7	6.0	1.0	0.2 × solar	TTM	1.9
TOR 8	6.0	1.0	5.0 × solar	TTM	1.9
TOR 9	6.0	1.0	solar	empty model space	1.9
TOR 10	6.0	1.0	solar	cold initial condition, turbulent pressure	1.9
TOR 11	6.0	1.0	solar	TTM	0.66

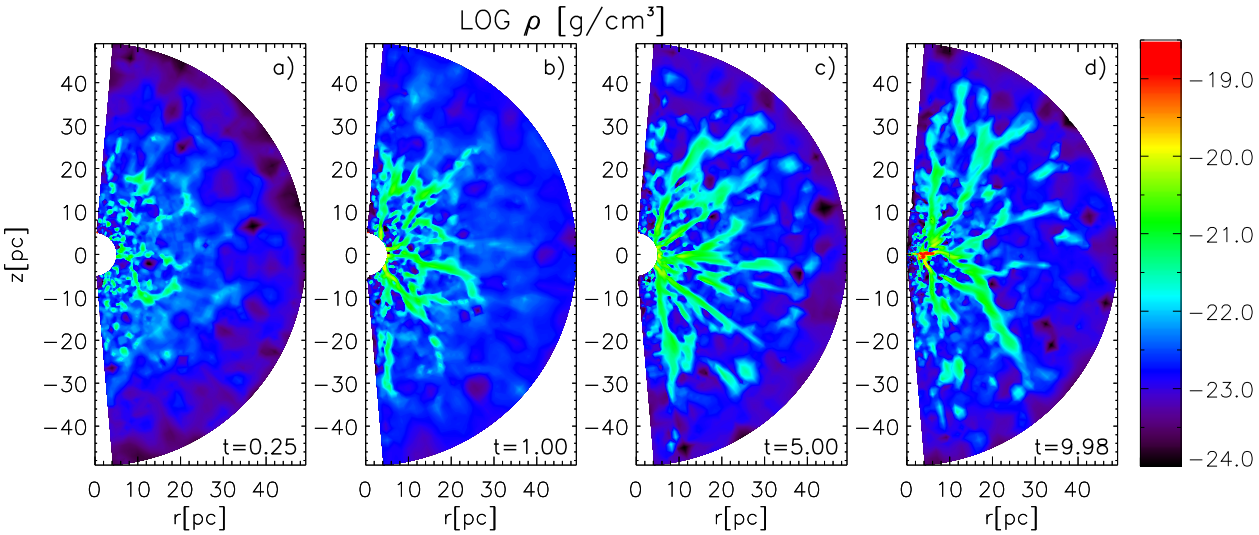

Figure 4.16: *Temporal evolution of the density in our standard hydrodynamic model, given in meridional slices of the torus. Shown are four stages of the torus at 0.25, 1.0, 5.0 and 10.0 orbits at 5 pc.*

but most supernova explosions rather help to form radial filaments by blowing away less dense material within the radial cavities (compare to Fig. 4.15). This effect is counterbalanced by the continuous feeding of material, which only depends on the radial direction. The further evolution is dominated by radial infalling, dense and cold filaments, whereas in the outer part, hot material is blown out of the computational domain (see discussion in Section 4.5.4). After 9 revolutions, we start calculating the middle part of our simulations. Already after a fraction of this one global orbit, material from the outer domain gathers around the minimum of the potential and a geometrically relatively thin, but optically thick disk evolves, which shows very turbulent behaviour (see Section 4.5.5). Material cannot proceed further in, as angular momentum needs to be transported outwards in order to overcome the angular momentum barrier. The disk in the midplane plays a crucial role in the comparison with the x-ray-silicate-feature strength relation (see Section 4.8.2).

The final stage of our standard model after 10 orbits is depicted in terms of density, temperature

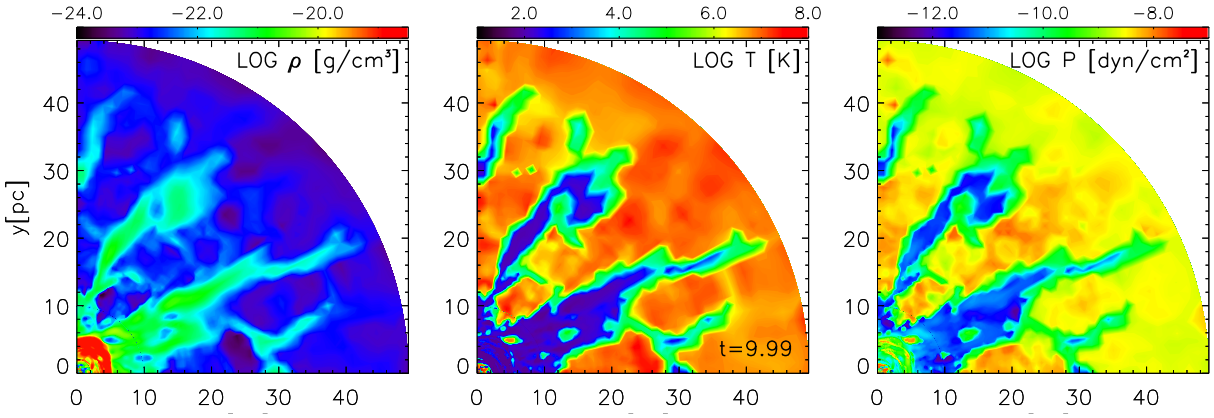

Figure 4.17: *State of the torus after roughly 10 orbits. Shown are from left to right the density distribution, the temperature distribution and the pressure distribution in an equatorial plane. All images are displayed with a logarithmic color scale.*

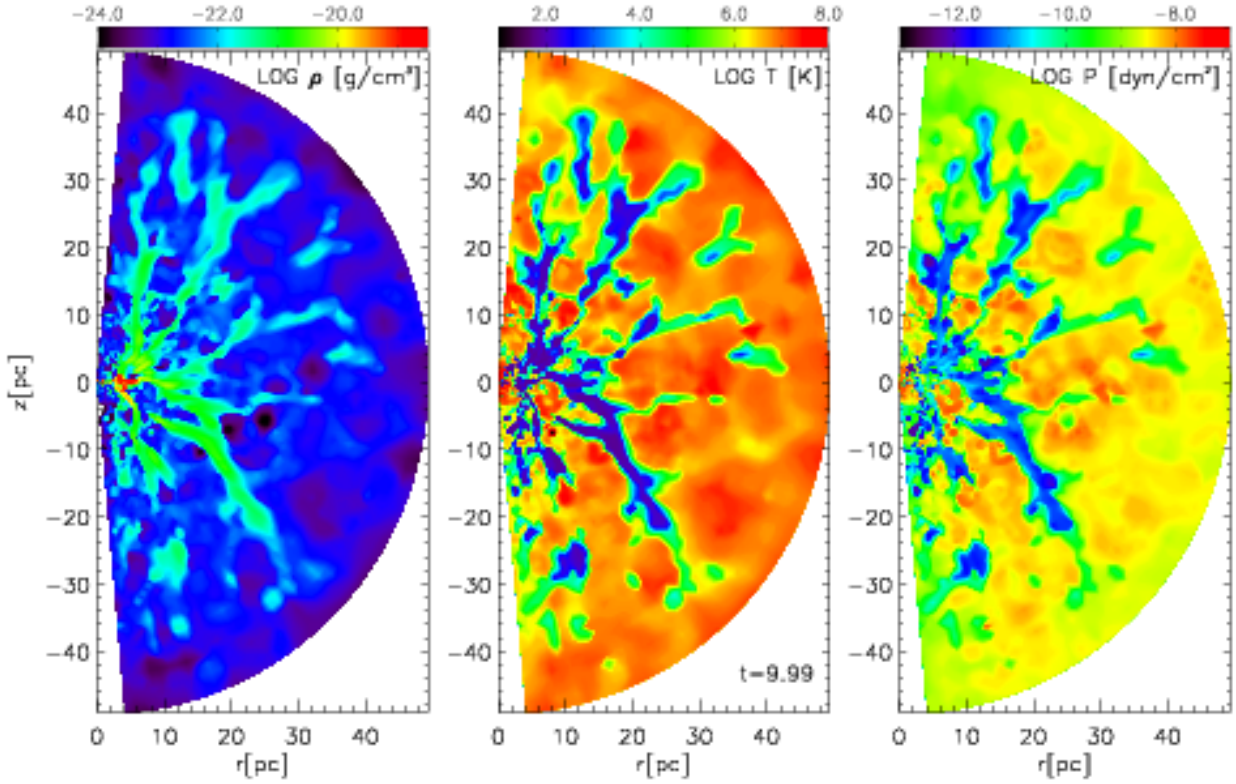

Figure 4.18: *State of the torus after roughly 10 orbits. Shown are from left to right the density distribution, the temperature distribution and the pressure distribution. All images are displayed with a logarithmic color scale.*

and pressure within an equatorial and meridional plane in Fig. 4.17 and Fig. 4.18. A multi-phase medium – concerning temperature – has formed, which will be discussed in detail in Section 4.5.4. It is obvious, that temperature and density are opposite in the sense that high density regions show low temperatures due to rapid cooling and hot regions possess low density as material has been blown away by supernova explosions. A large-scale filamentary structure pointing towards the torus centre forms as result of the interplay between infalling cool material and the concerted action of supernovae, blowing away low density material more easily, than dense filaments. The pressure distribution, spanning more than five orders of magnitude shows the absence of pressure equilibrium. This is an indication for ongoing thermal instability in the cold temperature regions and recent supernova activity in the hot temperature regime, leading to supersonic turbulence.

According to numerical simulations, one finds that supersonic turbulence decays quickly. This can also be seen in our simulations: The supersonic turbulence induced by supernovae and planetary nebulae decays quickly to smaller scales and is soon dissipated. This leads to the warm and hot medium and turbulent pressure (as assumed for our first approach with the TTM-model) is transformed to thermal pressure. This thermal pressure (for the case of the HIM) suppresses gas infall towards the centre at large velocities.

4.5.3 Evolution of the standard model without further gas and energy input

After an evolution of 10.12 orbits, we switch off the supernova and planetary nebula input with an e-folding time of 0.1 orbits. This means that after 0.1 orbits, the mass as well as supernova input rate has dropped by a factor of e^{-1}. The time is chosen such that we are numerically able to follow at least 10 times the e-folding time. As can be seen in the evolutionary sequence in Fig. 4.19, this leads to further infall and the outer part of the model space evacuates towards the central cavity, whereas material gathers at the angular momentum barrier in the middle domain. After evacuation of the outer domain and infall is not the dominating dynamical component in radial direction, our separation of the model space into 3 domains, which does not allow for advection through the two boundaries of the inner models in outward direction causes slight problems. A very faint borderline appears at 10 pc (only visible in the electronic version of the plot). The errors remain very small, due to the large overlapping region between the domains (1-2 pc and 5-10 pc).

After roughly 2 orbits, most of the torus has dissolved and only fairly tenuous, but filamentary and very turbulent structures reside within approximately 15 pc, toroidally distributed. The timescale seen in this evolution has to be compared to the free fall timescale. The free fall time from a distance of 50 pc amounts to approximately 0.75 orbits. This can be prolonged due to fast rotation.

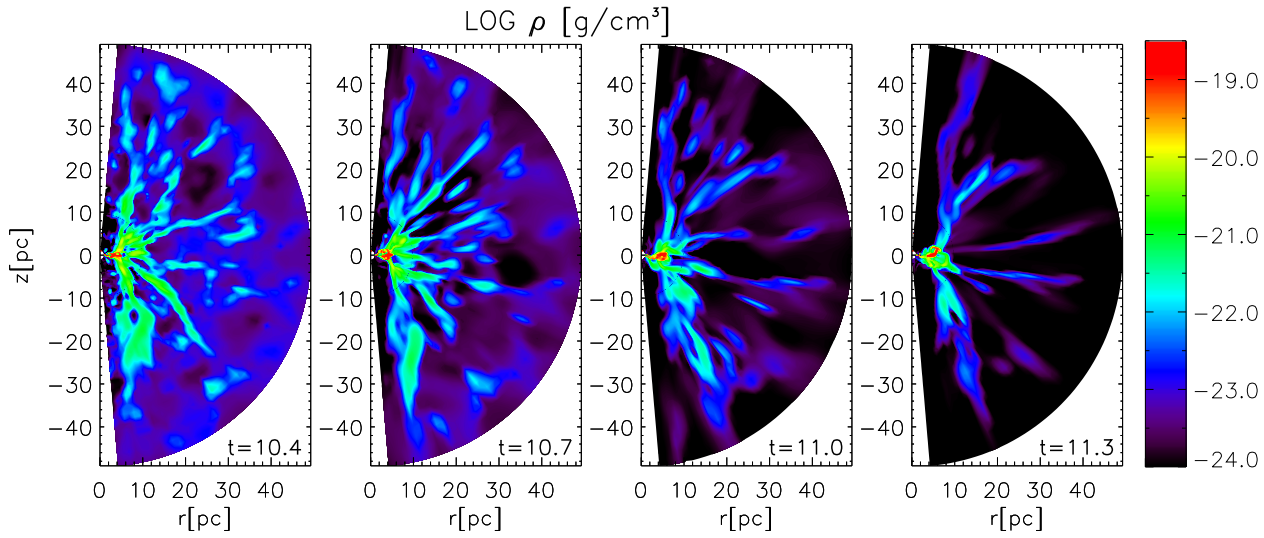

Figure 4.19: *Further evolution after switching off supernova as well as mass input with an e-folding time of 0.1 orbits. Shown is the logarithmic density distribution at 10.4, 10.7, 11.0 and 11.3 orbits.*

4.5.4 Multiphase medium

Already McKee & Ostriker (1977) and McKee (1990) proposed the first coherent and global model of the ISM. Within an analytical framework, they coined the so-called three-phase model (or MO-model named after their initials) of the ISM which consists of a cold neutral medium (CNM), a warm ionised (WIM) and neutral medium (WNM) and a hot ionised medium (HIM), also often referred to as the hot intercloud medium. In disagreement with our simulations and e. g. simulations done by Breitschwerdt & de Avillez (2006), one assumption of the theory is pressure equilibrium between these temperature phases. The whole system is regulated via supernova explosions in their

scenario. Components are converted into one another by means of physical reactions like radiative cooling, heat conduction, photoionisation and evaporation.

Following Joung & Mac Low (2006), we divide these phases at the onset of the thermally stable regime towards small temperatures at 175 K and at the ionisation temperature of hydrogen at $1.7 \cdot 10^4$ K (compare to Fig. 4.6) and, therefore, abbreviate them with CNM, WNM and HIM.

Fig. 4.20 shows phase diagrams for the three spatial subregimes (inner part blue, middle part green, outer part red) and the whole model space (black) of simulation TOR 1 after 10 orbits. First of all, an overview over the characteristic behaviour of each curve for the total model space (black curve) is given, before we discuss differences between the three curves of the single domains. The hatched regions indicate thermally stable parts of the cooling curve (see Section 4.3.5). Capital letters (A-F) denote the 6 bumps in the probability density function for gas temperature. C and D as well as the small excess E can be directly related to the stable regions of the cooling curve, because the time spent in each temperature range is proportional to the inverse of the cooling function (Gerola et al. 1974). At these temperatures, gas cools comparatively slow and therefore assembles in these regimes. The explanation for the maximum B is identical. The minimum between A and B evolves, because gas at these temperatures is mostly located in dense clumps. As cooling goes with density squared, it can cool quite fast, although the cooling curve indicates thermally stable behaviour. F can be explained by the permanent input of energy caused by supernova explosions. Due to this constant stirring and energy input mechanism, a large fraction of gas can reside in the thermally unstable regime, as the different temperature phases are constantly mixed and the hot temperature gets fed by input of energy. This effect occurs even stronger in simulations of the ISM further

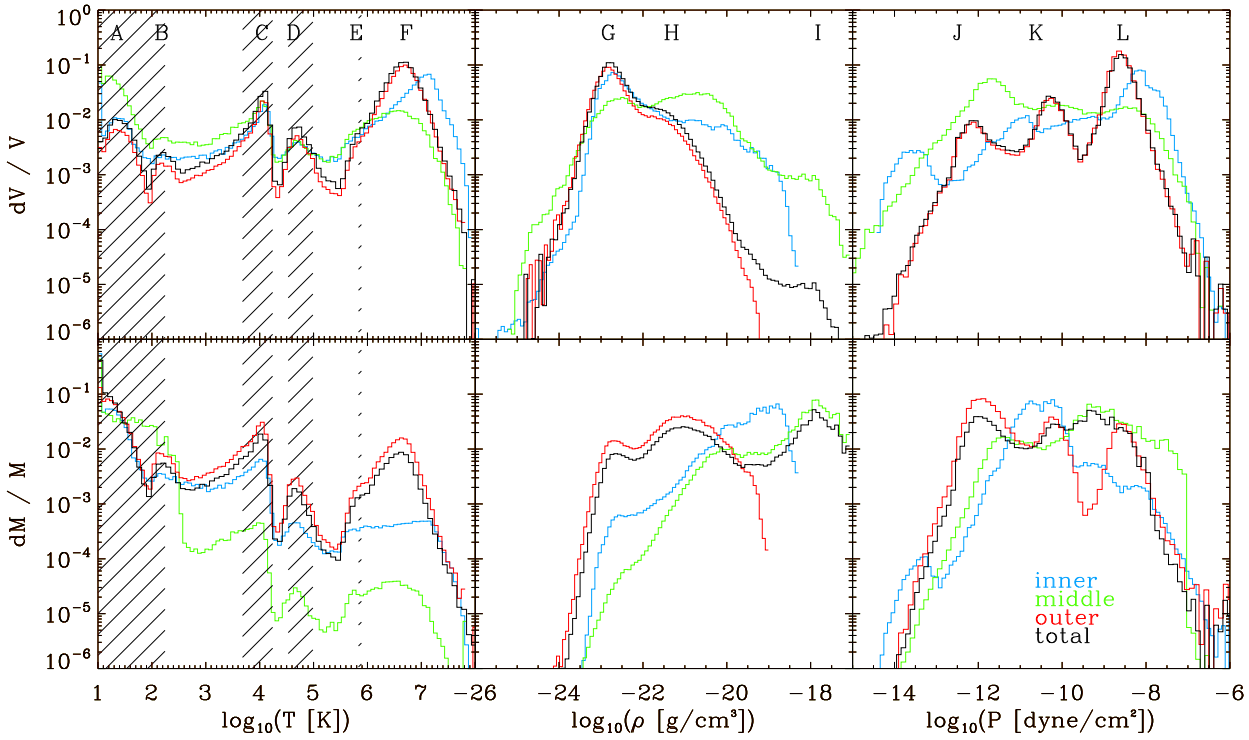

Figure 4.20: *Comparison between phase diagrams of inner (blue), middle (green) and outer (red) simulation of model TOR 1 after evolution of 10 orbits. Additionally, the complete model (without overlapping volumes) is shown in black. The hatched regions indicate thermally stable regimes according to the cooling curve (see Fig. 4.6).*

outside the nuclear galactic region, as densities are lower there. Looking at the mass distribution of the various temperature phases, a similar curve is obtained, but tilted, as most of the mass is concentrated in the cold temperature regime, but the hot gas fills most of the volume. This is as expected: supernova explosions blow away material and fill the remaining cavity with hot gas, whereas mass rich blobs cool down on short timescales.

The second column in Fig. 4.20 shows histograms of volume und mass fractions plotted against the gas density. Concerning the mass distribution, three local maxima are visible (labelled G,H,I). This behaviour can again be explained by the shape of the cooling curve and the energy input. Mainly inelastic interactions of clumps and blast waves from supernova explosions pile up material, which cools on short timescales. This loss of thermal pressure promotes further infall and thereby increases the density close to the torus radius, settling into a rotationally supported dense disk. This is visible in feature I - dominant in mass, but unimportant in volume and not visible in the outer domain (red curve). Therefore, it had enough time to cool to temperatures of the stable branch below 175 K and, though, corresponds to the leftmost stable area in the left column, containing the two features A and B. In contrast to this, feature G can be accounted to regions, where supernova explosions happened recently clearing the volume of most of the gas and heating it to high temperatures. In the left column, this corresponds to maximum F. The bump (H) in between arises from material in the large scale filaments, which is in the process of settling down and thereby cooling. This is evident, as it only shows up in the outer domain (red) and the total phase diagrams (black).

The distribution of mass and volume with respect to pressure is shown in the right column of Fig. 4.20. As can be seen from this and also from two-dimensional cuts through the pressure distribution in Fig. 4.18 and Fig. 4.17, the assumption of pressure equilibrium is not valid in our simulations. This is in concordance with recent observations. Jenkins & Tripp (2006) find variations in the pressure of the diffuse, cold neutral medium in a range of $500\,\mathrm{K\,cm^{-3}} < P/\mathrm{k_B} < 4000\,\mathrm{K\,cm^{-3}}$. This is done with the help of C I absorption lines, measured towards the ultraviolet spectra of a number of roughly 100 hot stars, taken from the HST archive. The population of the upper two of the three fine-structure levels of atomic carbon is regulated by collisional (de-)excitation balanced by spontaneous decay and, therefore, can be used as a measure of the local temperature and density and hence, pressure.

Pressure equilibrium between the different temperature phases was not only assumed in the first analytical model of McKee & Ostriker (1977), but near pressure equilibrium was also found in some simulations (e. g. Joung & Mac Low 2006). Breitschwerdt & de Avillez (2006) instead find huge pressure variations within the simulated ISM of up to four orders of magnitude on parsec scale. Their explanation for this is that pressure equilibrium can only be obtained, if there is enough time for relaxation of the processes, which promote mass and energy exchange between these phases (like radiative cooling, supernova heating, etc.). The most important process though is turbulent mixing, as the ISM possesses a very high Reynolds number. As turbulent mixing occurs supersonically in a compressible medium, pressure waves are not able to establish pressure equilibrium in the flow.

Instead of one single and sharp peak (when in pressure equilibrium), we obtain three local maxima for the case of the total domain (black curve in the right column of Fig. 4.20). We interpret this as follows: the system tries to find an equilibrium state, which results in the peak in the middle (K). Peak L can be allocated to non-equilibrium states caused by recent supernova-explosions, resulting in the highest pressures of the simulation and filling a large volume. This is the same component causing peak F and G as well. The evolving pressure also depends on the efficiency of

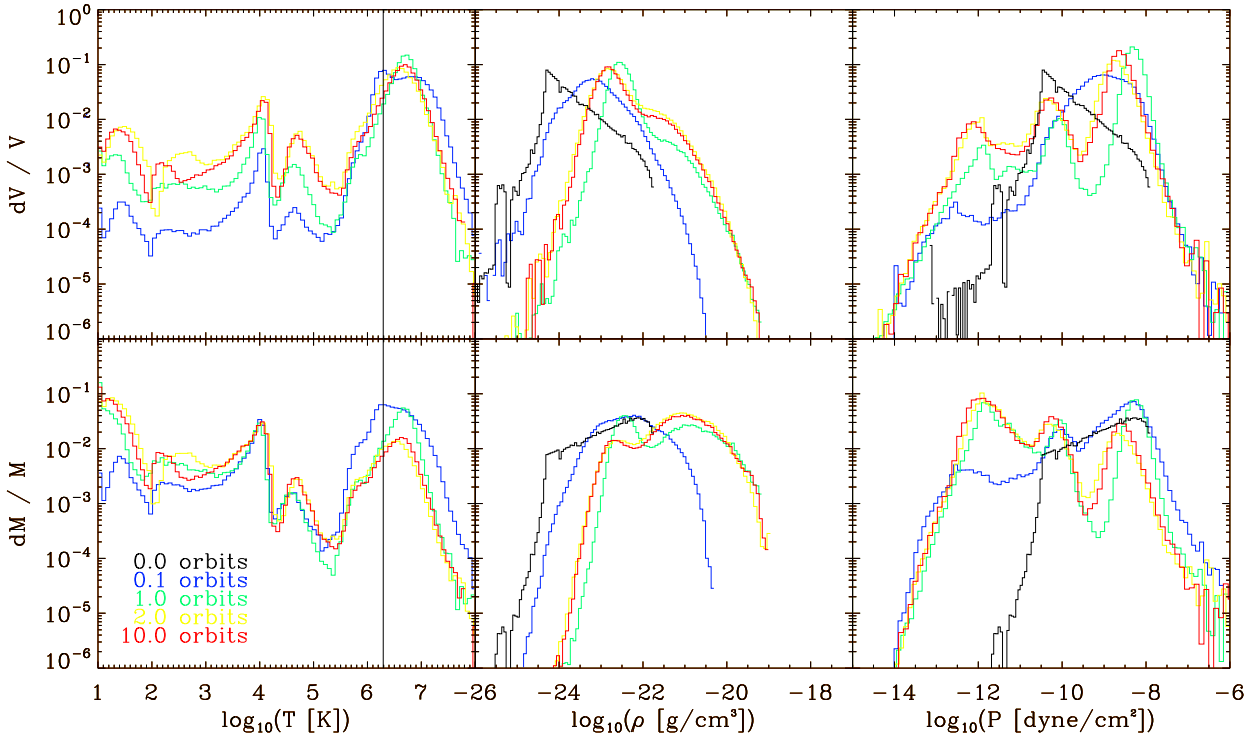

Figure 4.21: *Temporal evolution of phase diagrams for the outer simulation of model TOR 1. The black line denotes the initial condition.*

the conversion of the introduced thermal energy into kinetic energy, sweeping away material and, thereby, triggers deviations from a global pressure equilibrium value. Deviations from a global equilibrium pressure value towards small pressure (J) is a sign of ongoing thermal instability within the fast cooling, densest regions of the flow (see also discussion in Joung & Mac Low 2006). These deviations are also visible in Fig. 4.18, where cold and dense regions correspond to low pressure states and hot and tenuous regions to high pressure.

Additionally shown in Fig. 4.20 is the decomposition into our three spatial domains (inner – blue, middle – green, outer – red). In the first column, curves show similar behaviours. The largest deviations are visible for the middle domain. This is where the dense disk forms within the midplane, occupying a large volume and particularly mass fraction of this part of the computational domain. Supernova explosions are less frequent due to the smaller volume and therefore, peak F is much smaller. But these explosions are more violent in a sense, that they can blow large fractions of the material out of the domain on these small scales. Nevertheless, curves of the temporal evolution converge, as can be seen in Fig. 4.22. The same holds true for planetary nebulae injections. This can also be seen in the relatively large scatter of these curves on small time scales, visible in Fig. 4.23. Concerning the differences in density population, the same is true. Here, the dense disk of the middle model even dominates the total mass per density bin at high densities. Comparing with the distribution of masses with pressure of the inner model, it seems that most of the mass is in pressure equilibrium. But one has to keep in mind that these kind of comparisons between our three spatial domains are problematic, as in the inner domains no dynamically steady state is reached within the evolution we can follow so far. Up to now, more material is transported into this domain than can be accreted through the inner radial boundary.

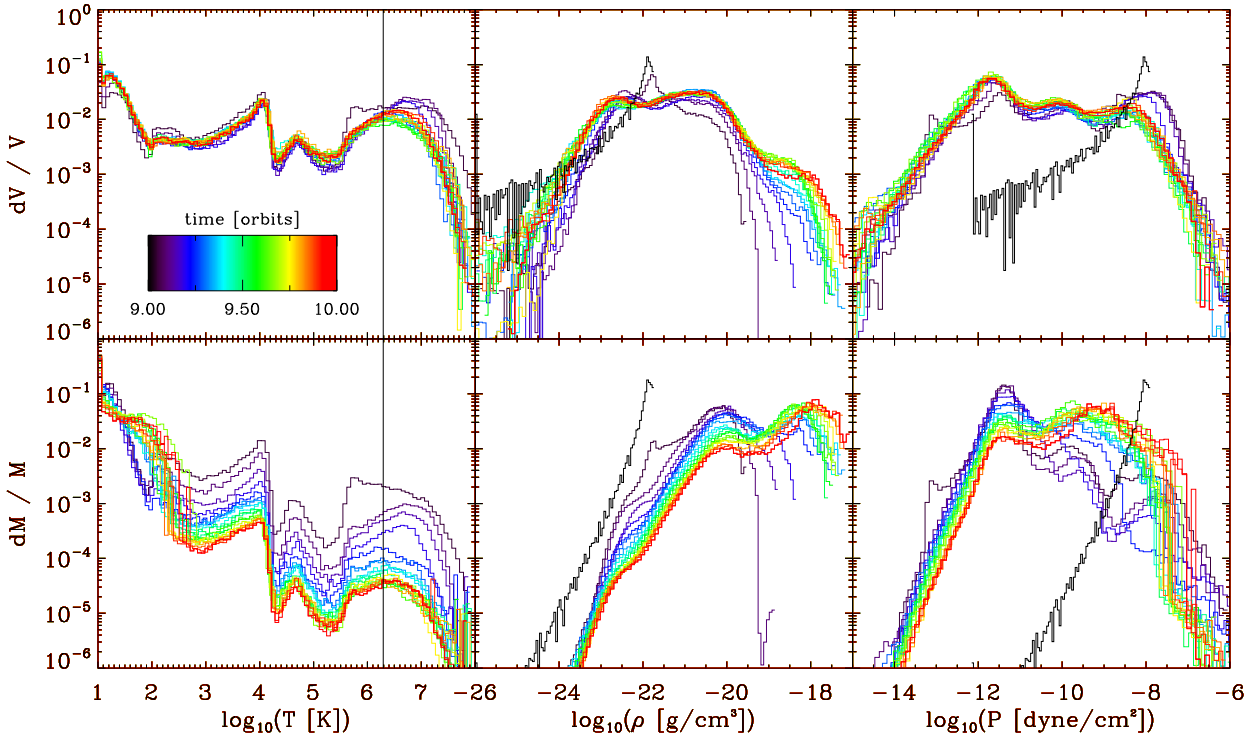

Figure 4.22: *Temporal evolution of phase diagrams for the middle simulation of model TOR 1. The black line denotes the initial condition.*

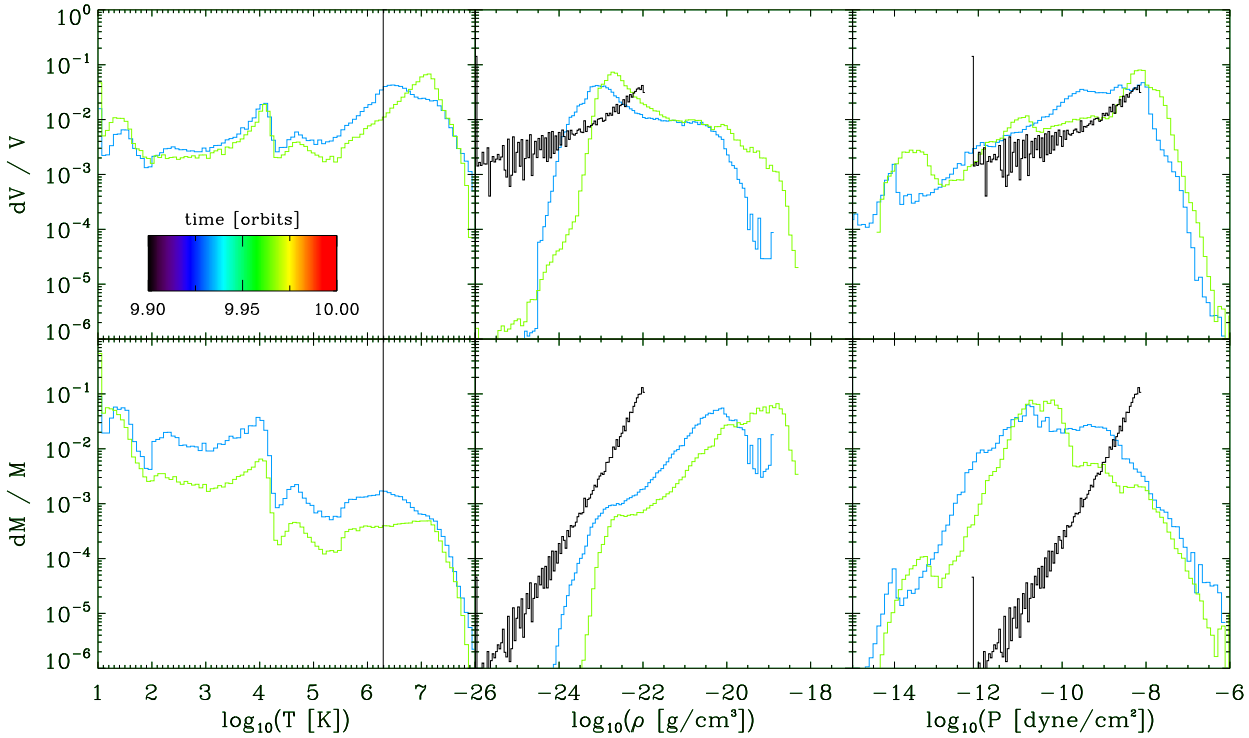

Figure 4.23: *Temporal evolution of phase diagrams for the inner simulation of model TOR 1. The black line denotes the initial condition.*

Looking at the temporal evolution of the phase diagrams one can see in all three domains (Fig. 4.21, Fig. 4.22 and Fig. 4.23) the conversion from the isothermal initial condition towards the discussed

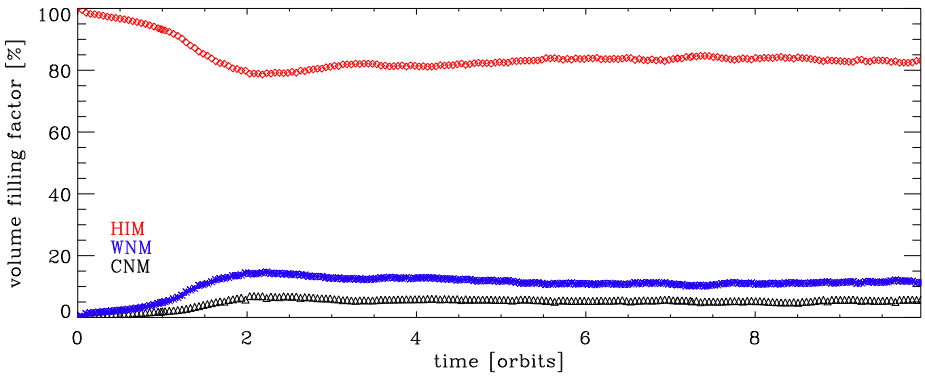

Figure 4.24: *Time dependence of the volume filling factors of the three different temperature regimes: HIM - red, WNM - blue and CNM - black.*

final solution, which in turn depends on the cooling curve, the energy and mass input as well as the position of the angular momentum barrier.

Volume filling factors

After evaluation of the temporal evolution of volume filling factors for the different temperature regimes, Fig. 4.24 results for the outer domain. Starting from the hot isothermal initial condition, cooling and energy input compete, until after three orbits, a dynamical equilibrium is reached. This leads to a distribution in volume of 83.3% for the HIM, 11.3% for the WNM and 5.4% for the CNM. Due to thermal instability and supernovae which blow away gas, the situation looks different for the relative contributions to the total mass (see Fig. 4.25). The hot gas is diluted on short timescales, as blast waves and mass input yield blobs of dense gas, which cool fast. Finally the majority of mass is in the cold (60.4%) and the warm regime (22.6%), while only 16.9% of the total mass corresponds to the hot medium, which fills 83.3% of the model space. Evaluating only the midplane of the model space, we obtain similar results. A comparison is given in Table 4.3.

The analytical model of McKee & Ostriker (1977) also predicts a very high volume filling factor of approximately 70% for the hot medium in the ISM within the galactic plane. In contrast to this, observations tend to much smaller values of rather a few percent (e. g. Brinks & Bajaja 1986). For the case of the ISM within the galactic plane, these low values can be obtained with the help of a

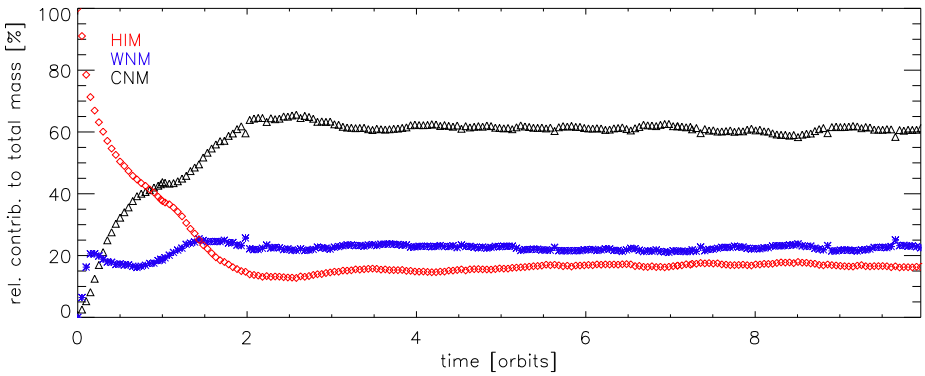

Figure 4.25: *Time dependence of the relative contributions of the three different temperature regimes to the total mass: HIM - red, WNM - blue and CNM - black.*

	total		midplane	
	vol. fill.	rel. mass contribution	vol. fill.	rel. mass contribution
HIM	83.3	16.9	81.4	17.4
WNM	11.3	22.6	12.7	23.5
CNM	5.4	60.4	5.9	59.0

Table 4.3: *Volume filling factors and relative contributions of the different temperature phases to the total mass for the whole model space and restricted to the midplane after 10 orbits evolution, given in %.*

so-called galactic fountain process or chimney model (Norman & Ikeuchi 1989). According to it, outbursting superbubbles (resulting from the concerted action of supernova explosions emanating from associations of O and B stars) produce a chimney-like structure, enabling the exchange of energy and mass between the disk and the halo. Within this process, hot gas is transferred to the halo, thereby reducing the volume filling factor of the disk. The same holds true for buoyant outflows from supernova remnants (SNRs). Taking these effects into account, Breitschwerdt & de Avillez (2006) find volume filling factors as low as 17.8% for the case of a Galactic supernova rate and only 43.6% for supernova rates as high as 16 times the Galactic value[8]. However, the situation in our simulations is different, as we are focusing our attention to the central part of galaxies. The spherically symmetric potential and the spherically distributed input of energy and mass from a massive stellar cluster yield much larger gas densities and establish a converging flow towards the minimum of the potential. Therefore, the reduction of the hot filling fraction due to escaping buoyant bubbles is not visible in our calculations. Furthermore, our models do not feature OB-associations, as in our model, we chose a smooth stellar distribution within the cluster.

Dynamical state of the multiphase medium

In the following section a number of physical parameters, determining the state of the gas flow of our simulations is presented. One should note that despite of the turbulent mass and energy feeding, all of the displayed quantities reach steady state values after already less than three orbits.

The dynamical state of the gas can be characterised by the mass weighted average velocity dispersion, whereas the averaging is done for all cells for the θ and r components and the ϕ component is only averaged in r and θ direction:

$$\langle\sigma\rangle = \sqrt{\frac{\Sigma_{i=0}^{N_{\rm cell}} \left[\left(v_i^r, v_i^\theta, v_i^\phi\right) - \left(\langle v_r\rangle_{r,\theta,\phi}, \langle v_\theta\rangle_{r,\theta,\phi}, \langle v_\phi\rangle_{r,\theta}\right)\right]^2 m_i}{\Sigma_{i=0}^{N_{\rm cell}} m_i}} \tag{4.29}$$

This is done for the three different partitions separately in Fig. 4.26. Again, after 3 orbits, a steady state is reached and the σ-values in the outer domain are fairly constant with a mean value of 160 km/s in the last 2 orbits. Despite the low number statistics for the inner and middle part of the simulation, a trend towards higher mean velocity dispersions in the inner parts seems to exist. The time averaged values - indicated by horizontal lines in the particular colours - then reach 204 km/s in the middle part to 297 km/s in the innermost part. Indicated with the yellow line is the velocity

[8]Breitschwerdt & de Avillez (2006) use a different partitioning into ISM temperature phases compared to our definition, but borders of the hot temperature regime are roughly comparable.

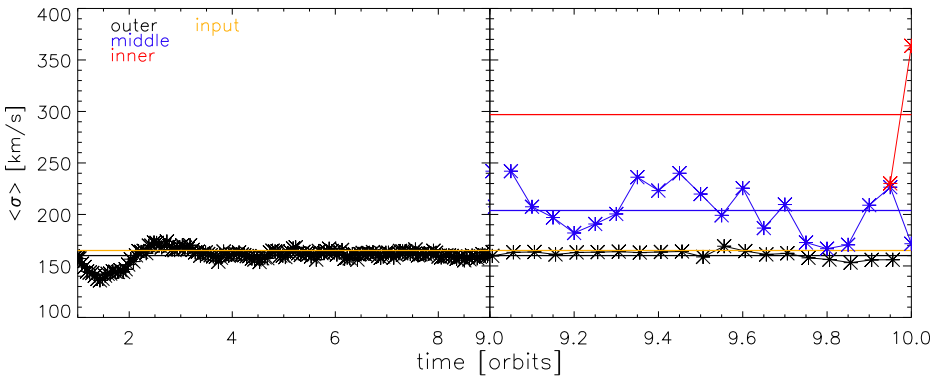

Figure 4.26: *Time dependence of average velocity dispersion for the three different partitions (black - outer, blue - middle and red - inner) of the model space of model TOR 1. Horizontal lines denote the particular time average over the whole computational time. Averages are: 160 km/s (outer), 204 km/s (middle) and 297 km/s (inner). The yellow line is the velocity dispersion of the stars within the cluster, with which the planetary nebulae are injected into the computational domain. See text for further explanation.*

dispersion of the hydrostatic equilibrium solution for the underlying effective potential (165 km/s). The outer mean value is slightly lower, whereas the middle and inner values are much higher. This indicates that on large scales (in the outer part), the mass input (which is done with a velocity dispersion as indicated by the yellow line) dominates the dynamical state. σ is smaller due to interaction of injected planetary nebulae with others and with other blobs or filaments of material already present in direction of the ejected new born planetary nebula. Due to the smaller occupied volume, in the parts of the domain further in, the dynamics of the gas seems to be dominated by other processes than the feeding of mass. Thereby, the highly turbulent disk and supernova stirring (more violent on smaller scales) may play crucial roles in enhancing unordered motion. Further, they cause large deviations from the mean value. Again, this has to be taken with caution, as no steady state is reached in the middle and inner domain.

Fig. 4.27 results, when the same analysis is done for the three main temperature phases (CNM, WNM, HIM), as indicated in the cooling curve in Fig. 4.6. All of the graphs lie significantly below the total value. This is an indication, that the different flow patterns of the individual temperature

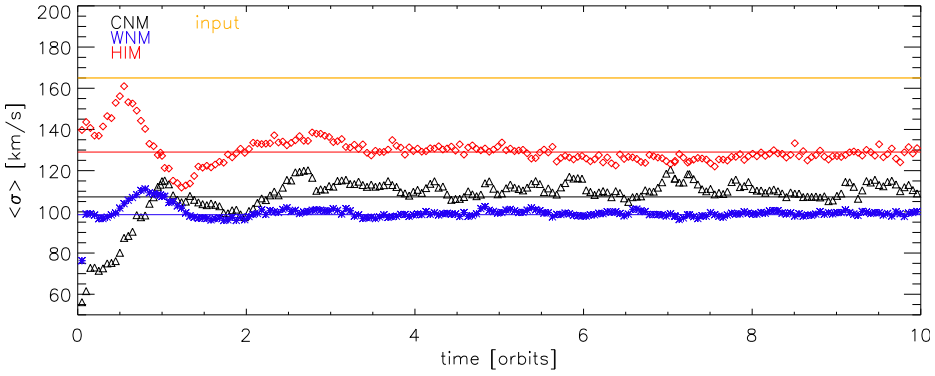

Figure 4.27: *Time dependence of average velocity dispersion for the three different temperature phases (black - CNM, blue - WNM and red - HIM) of model TOR 1. Horizontal lines denote the particular time average over the whole computational time. The average values are* 107.3 *km/s (CNM),* 98.6 *km/s (WNM) and* 129.0 *km/s (HIM). The yellow line is the initial value. See text for further explanation.*

regimes significantly alters the total dispersion of all three phases (Fig. 4.26). Cool material streams radially inwards much faster than the hot gas, as will be discussed in more detail below. As mass injection happens with the local gas temperature, it is hard to disentangle it from stirring due to supernova explosions in this analysis. But as expected, the hot medium possesses the highest velocity dispersion of around 129 km/s, whereas the CNM (107 km/s) and WNM (99 km/s) appear in reverse order. The reason for this might be the large radial velocities of cold blobs of gas.

In order to determine the main driving force of the ISM flow and also the turbulence, Fig. 4.28 shows the volume weighted ram pressure in comparison to the volume weighted thermal pressure for the three domains and altogether, plotted against the temperature. In concordance with Breitschwerdt & de Avillez (2005), we find dominance of ram pressure for low temperatures, whereas for temperatures higher than approximately 10^6 K thermal pressure is the driving force of the flows, at least in the outer domain. Further in, ram pressure possesses orders of magnitude higher values, as the radial flow speed increases towards the minimum of the potential and the black hole and we see fast rotation within the forming inner disk. In the picture of pure thermal pressure balance (as done in the TTM-model initial condition), the thermal pressure also increases towards the minimum of the potential well, as can be seen in Fig. 4.28, too. Therefore, the intersection between thermal and ram pressure is further shifted to larger temperatures, when considering only the middle or inner part. Summarising, one can see in graph 4.28 that with increasing temperature, the flow pattern changes from a directed streaming (large ram pressure, low thermal pressure) towards a random motion dominated flow without preferential direction (high thermal pressure, low ram pressure).

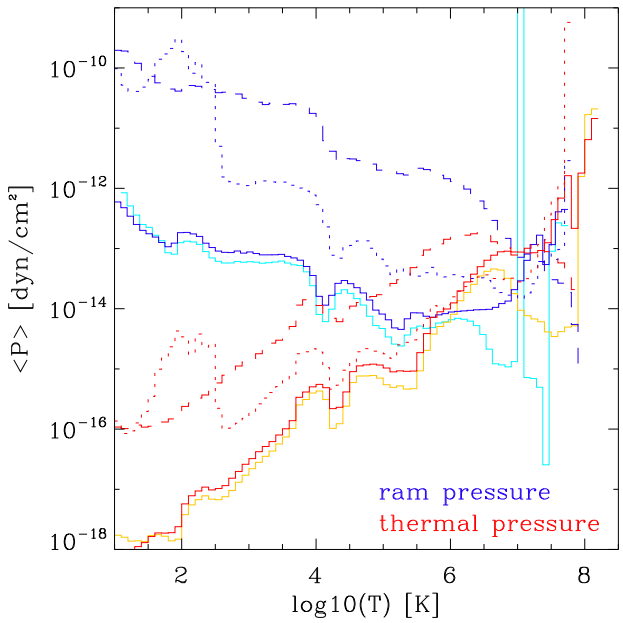

Figure 4.28: *Comparison of thermal pressure (red) with ram pressure (blue), averaged over the outer domain (solid), the middle (dotted) and the inner domain (dashed). Lines in turquoise and yellow denote the total domain.*

Fig. 4.29 shows the mass accretion rate towards the inner edge of the outer domain plotted against time and separated into HIM, WNM and CNM. As can be seen from this, practically only cold material is transported inwards over the inner boundary. During the first orbit, it rises steeply, before the slope decreases and nearly constant values of approximately 2.0 $M_\odot$/yr for the CNM, 0.02 $M_\odot$/yr for the WNM and 0.001 $M_\odot$/yr for the HIM are reached, already two orbits after starting the mass and energy input. This accretion rate in the outer domain corresponds well to the mass

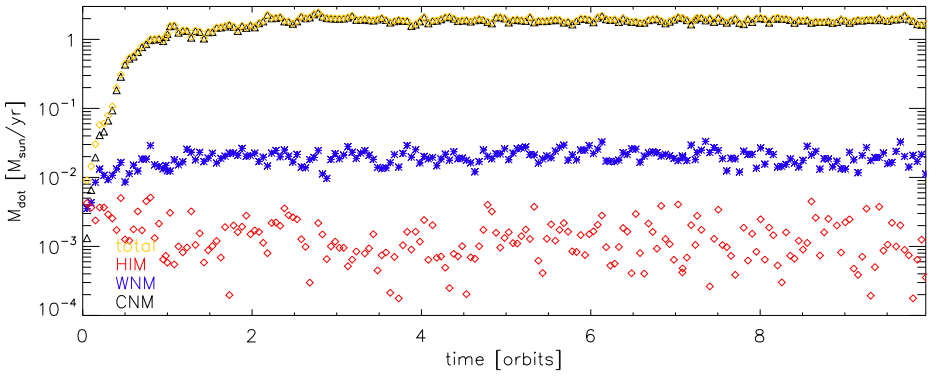

Figure 4.29: *Mass accretion rate through the inner boundary of the outer domain in solar mass per year plotted against time. Separated into the three different phases: HIM (red), WNM (blue), CNM (black) and the total of all three (yellow).*

input due to planetary nebulae injections and supernova explosions.

According to magneto-hydrodynamic simulations for the case of optically thin accretion tori (Hawley 2000), a large fraction of this inflowing material on large scale is re-ejected by a wind exerting from the accretion disk, driven outwards mainly by magnetic pressure. Therefore, the accretion rate towards the black hole is expected to be reduced appreciably, but this would still yield super-Eddington accretion rates for the case of the central black hole with a mass of $6.64 \cdot 10^7\, M_\odot$ in our model. This is clearly too high compared to typical accretion rates of Seyfert galaxies ranging between a few percent up to a few ten percent of the Eddington value. At the moment, this material accumulates at the angular momentum barrier and part of it is accreted. Therefore, either a smaller accretion rate is needed or the mass input process has to stall at a certain time. A more detailed analysis of this problem and the dependence of the accretion rate on our model parameters is given in Section 4.7.

Fig. 4.30 shows the temporal evolution of the total mass of the outer model. As we start with a hot isothermal initial condition, the total mass is dominated by the hot temperature phase until almost one orbit. It rises at the beginning, as our mass input happens at the local gas temperature and supernova type Ia also result in a mass input of $1.4\, M_\odot$ per event. The cold gas only gains mass via cooling of warmer gas in the beginning of the simulation, but with a growing volume occupation, mass input due to planetary nebulae becomes more and more important and the gas mass increases

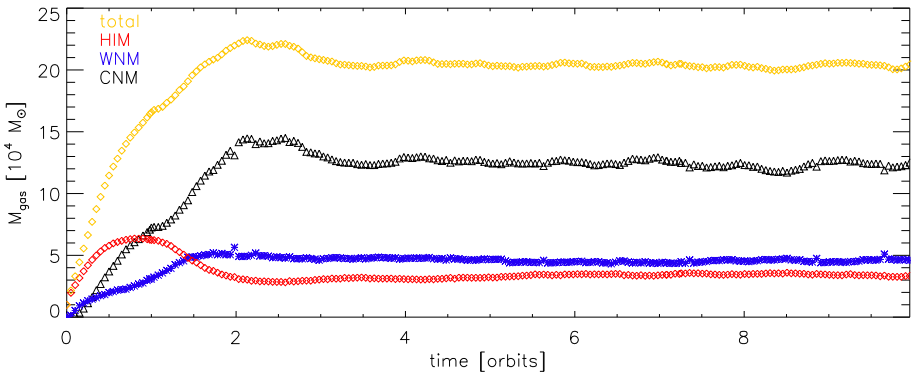

Figure 4.30: *Gas mass in the outer domain in units of* $10^4\, M_\odot$ *plotted against time, separated into the three different phases: HIM (red), WNM (blue), CNM (black) and the total of all three (yellow).*

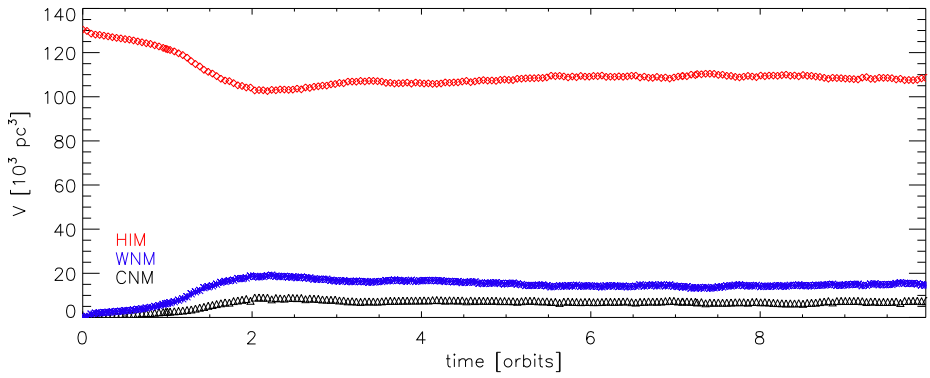

Figure 4.31: *Evolution of the volumes of different phases. Averages are: 6 508* pc^3 *(CNM), 13 834* pc^3 *(WNM), 110 108* pc^3 *(HIM).*

steeply. After about 3 orbits, the total, as well as the separated gas masses reach their steady state value. This is roughly 20 times the initial value ($10^4\ M_\odot$) for the total mass, $12 \cdot 10^4\ M_\odot$ for the cold gas, $5 \cdot 10^4\ M_\odot$ for the warm component and $3 \cdot 10^4\ M_\odot$ for the hot ionised gas. In this dynamical equilibrium, mass input is mainly balanced by accretion of material through the inner boundary, as this is also the location of the torus radius.

As already discussed before, Fig. 4.31 shows again the distribution of volume. Clearly, the hot temperature regime occupies most of the spherical model space (more than 80% when steady state is reached).

Looking at the temporal evolution of the radial velocities (see Fig. 4.32), the picture of the interplay between supernovae, planetary nebula injections and cooling, as described in Section 4.5.2, is quantified. Clearly, the hot tenuous medium is able to provide the largest thermal pressure, which helps to slow down the infall towards the mass centre. This is less the case for the warm and not the case for the cold material. Therefore, cold material sinks to the bottom of the potential, accelerating to an averaged radial velocity of 213 km/s, whereas warm material reaches only 119 km/s and hot ionised material merely 51 km/s. The reason for the coexistence of these large differences lies in the formation of the previously discussed long filaments, which link the outer part of the torus with the innermost region and provide a possibility for sustaining such different velocities of the three components. Due to lacking resolution in the outer part, we are not able to see Kelvin-Helmholtz or Rayleigh-Taylor instabilities in such kind of global simulations. Actually, they are expected to

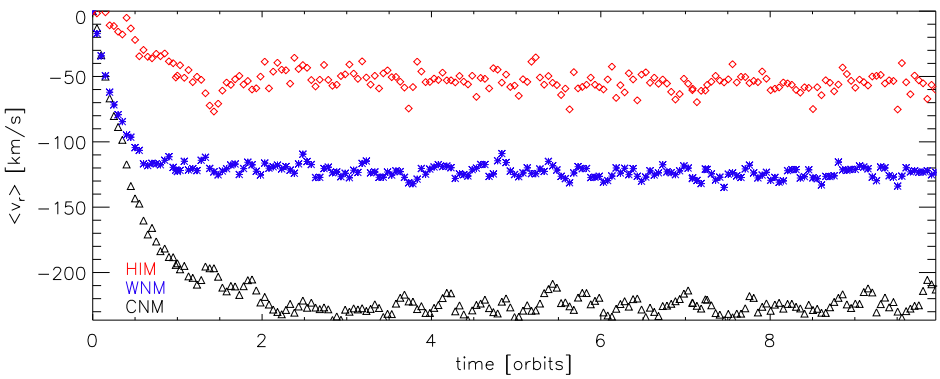

Figure 4.32: *Temporal evolution of the radial component of the gas velocity, split into HIM (red), WNM (blue) and CNM (black). Negative velocities indicate inflow.*

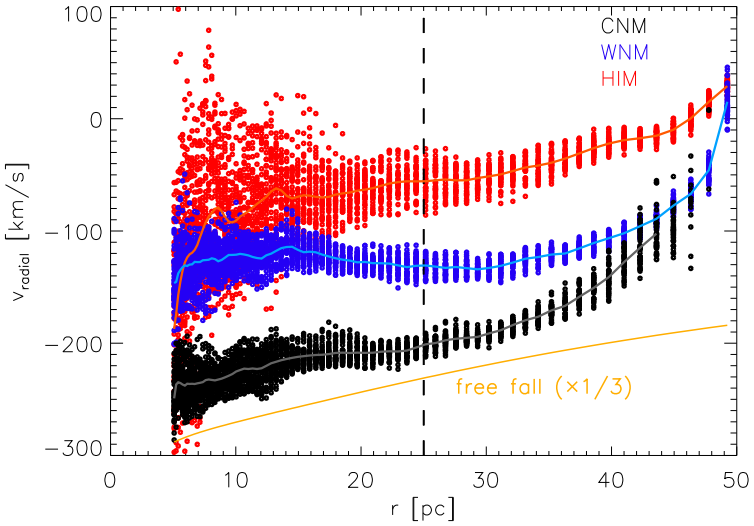

Figure 4.33: *Radial velocities of the outer model between 8 and 10 orbits, separated into temperature phases. The yellow line represents the free fall velocity (v_{ff}), scaled with a factor of* 1/3*, the dashed line symbolises the location of the core radius of the stellar distribution. The vertical stripes in the outer region are visible due to the logarithmically spaced radial grid and directly reflect the spatial resolution there.*

increase turbulence and promote further mixing of the temperature phases.

As supernova explosions are less effective in dense regions, these cold flows are hard to stop or to fragment further. It only happens from time to time, but after a short time, the flow revives again. This is visible in the animated evolutionary sequences given on DVD (see Appendix B).

Fig. 4.33 shows the radial dependence of the radial velocity, averaged over all angles θ and ϕ and separated into the three temperature components (see graph). For an integration time between 8 and 10 orbits, the data is plotted every 0.05 orbits. Given in yellow is the free fall velocity of a test particle within the total gravitational potential of the black hole and the star cluster, scaled down by a factor of three (mind that rotation is not included in this free fall velocity calculation!). It

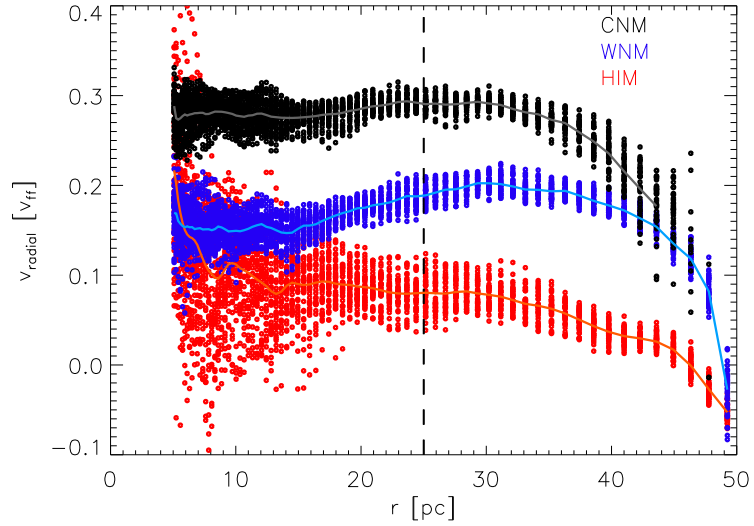

Figure 4.34: *Radial velocities of the outer model between 8 and 10 orbits, separated into temperature phases and plotted relative to the free fall velocity.*

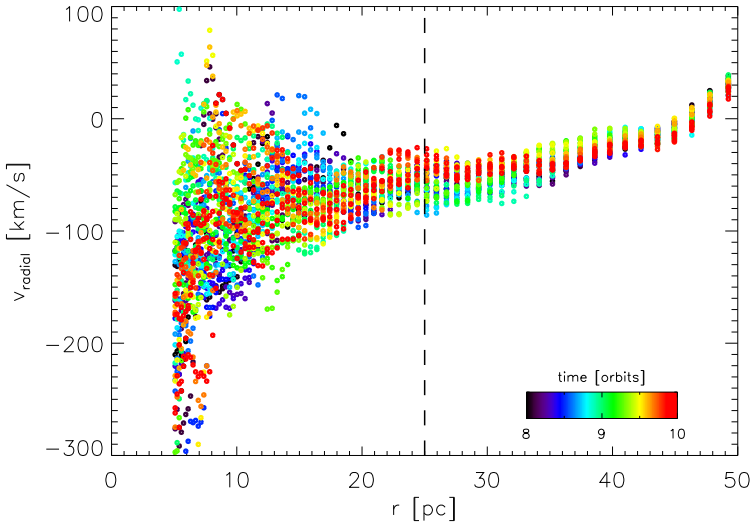

Figure 4.35: *Radial velocities of the HIM of the outer model between 8 and 10 orbits.*

rises towards the centre due to increasing stellar density as well as the presence of the supermassive black hole. Further remarkable is that the distributions have similar slopes compared to the free fall velocity. The CNM reaches radial velocities of up to 30% of the free fall velocity, the WNM approximately 15% and the HIM 10% (see also Fig. 4.34) are reached. Therefore, the initial assumption of a mechanical equilibrium of the gas, which was used in the analytical description of the Turbulent Torus Model appears to approximately be valid only for the hot gas. The other components show large deviations from mechanical equilibrium. This is a further indication that the turbulent motion of the gas, which is introduced into the gas at roughly parsec scale (resolution dependent for the case of planetary nebulae) due to the turbulent velocity dispersion of the mass blobs and expanding supernova blast waves, is mainly injected into the hot medium. The larger scattering of the radial velocity values at small radial distances to the centre at higher temperatures further underlays this reasoning. Within this scattering, no clear temporal trend is visible, as can be seen in the color-coding of Fig. 4.35.

4.5.5 Formation of a turbulent disk

A general overview over the effects of turbulence within the ISM has been given in the introduction 4.2.9. In this section, we apply this to describe the formation and behaviour of a nuclear turbulent disk in the direct vicinity of the torus radius, which plays a crucial role concerning observational quantities (which will e. g. be discussed in Section 4.8.2).

A detailed turbulence analysis is beyond the scope of this work. As we are mainly focussing on testing the proposed model for the build-up of AGN-tori, in this first model, only the main physical effects are taken into account. For the realistic modelling of ISM turbulence, further physical effects are needed: magnetic fields, self-gravity, radiative transfer, etc.

Fig. 4.36 and 4.37 show the temporal evolution of density within the midplane and a meridional plane, respectively. Time starts after 9 orbits, until when only the evolution of the outer domain has been traced. For the middle part, we start with the isothermal initial condition, which is washed out after a fraction of an orbit already. The dynamical evolution is mainly determined by mass inflow

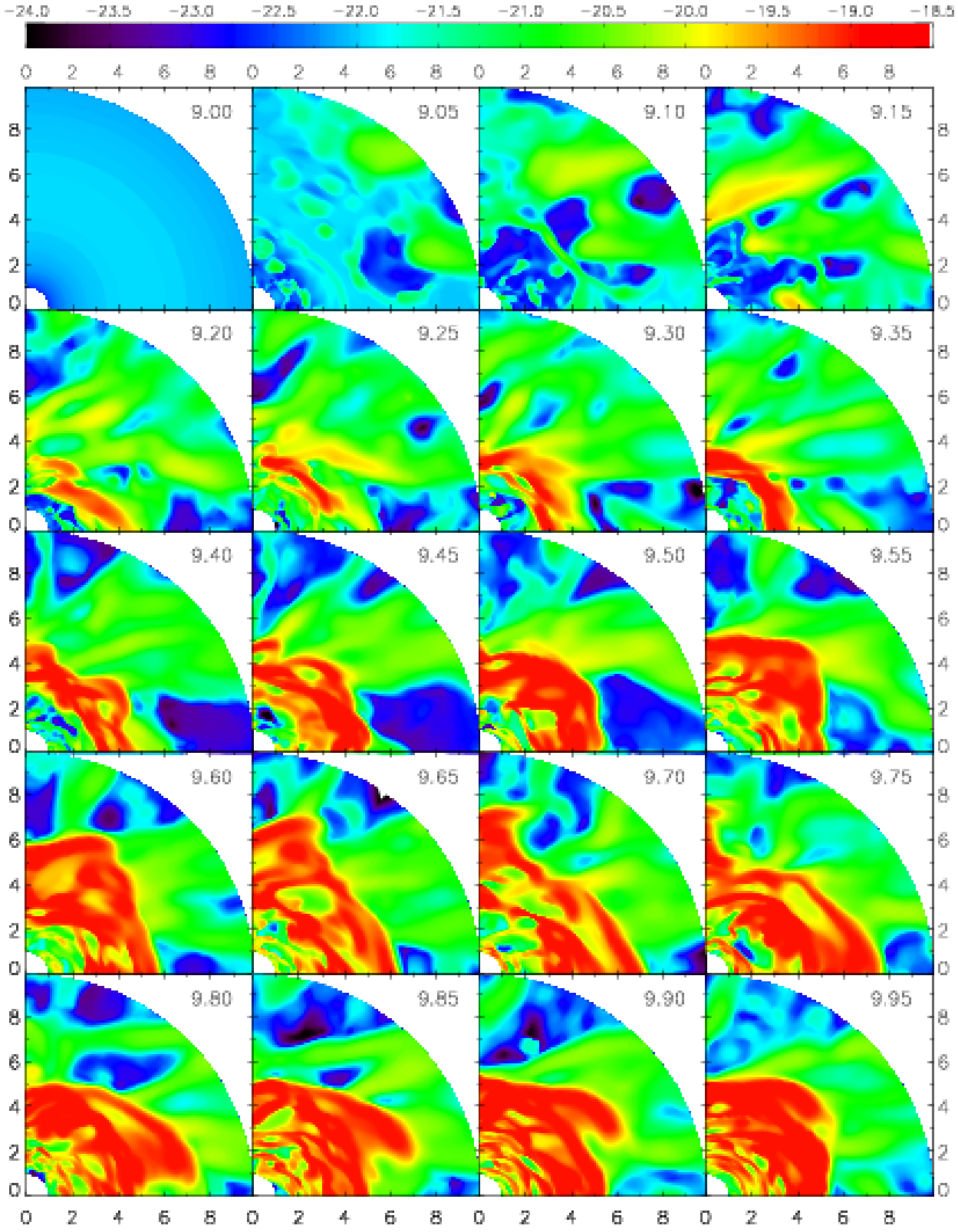

Figure 4.36: *Formation of a turbulent, geometrically thin disk in the midplane. Shown is the logarithm of the density in units of g/*cm^3 *as a cut through the midplane. Time is given in orbits at the torus radius (*5 *pc). Labels are given in pc.*

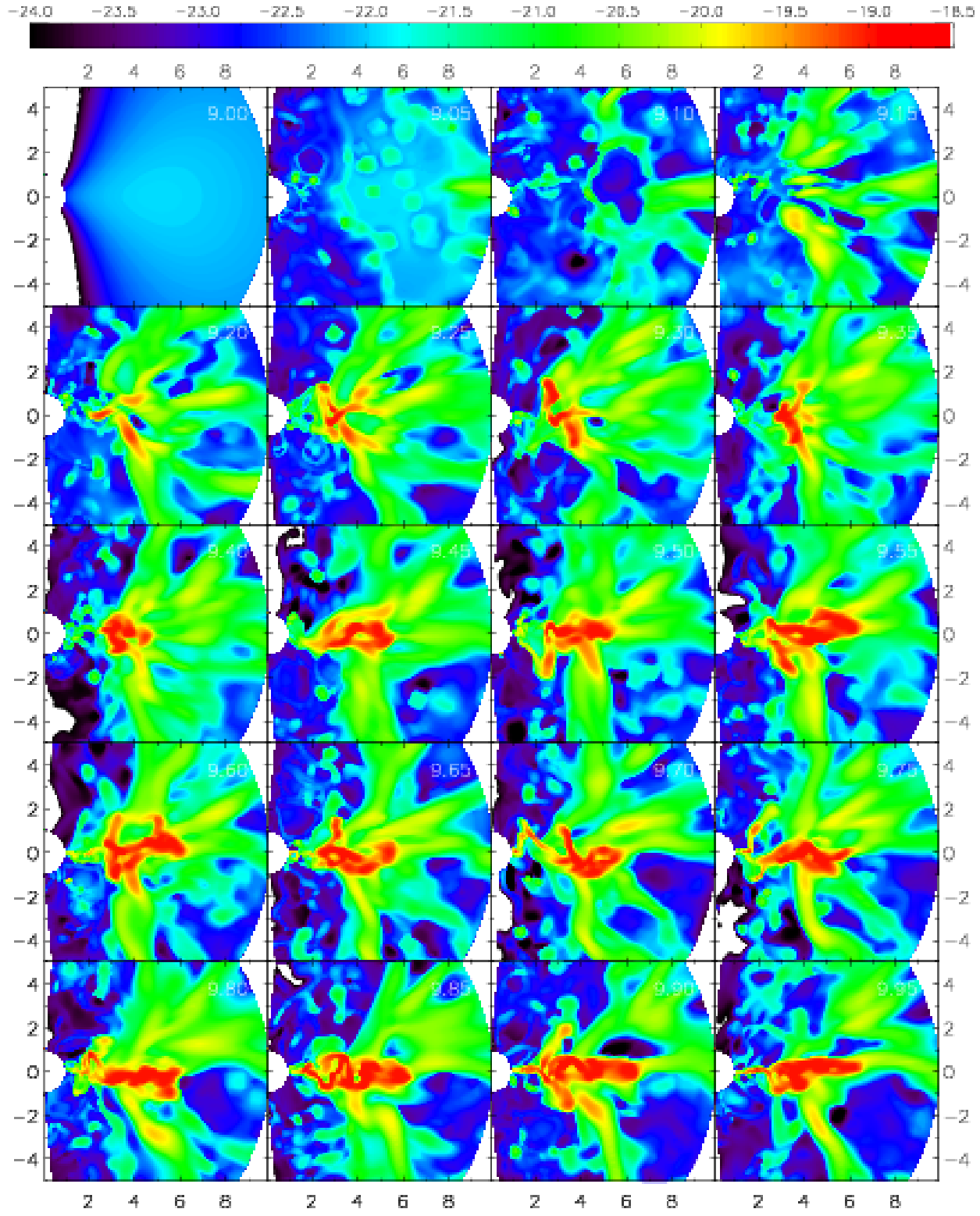

Figure 4.37: *Formation of a turbulent, geometrically thin disk in the midplane. Shown is the logarithm of the density in units of g/*cm^3 *as a cut through a meridional plane. Time is given in orbits at the torus radius (5 pc). Labels are given in pc.*

through the outer radial boundary. This material arrives as well in form of broad streams as also in blobs and filaments of material and gets structured by supernova explosions and planetary nebulae. This can be best seen in the snapshot of the midplane (Fig. 4.36) after 9.05 and 9.10 orbits. Single planetary nebulae are visible as well as shock waves from supernova explosions within the tenuous medium of the initial condition (compare to Fig. 4.14). Especially mind the shock waves coming from small radii and the shock wave from the big bubble at approximately 6 pc, which collide after 9.1 orbits and form a thin filamentary structure, as expected. After 9.15 orbits, it is already partially destroyed by inward-moving streams, dragging along material. Whereas in the first images of this sequence, single events (planetary nebulae and supernova detonations) are visible, it soon gets washed out by the interaction between inflowing material with gas already present. In snapshot 9.20, enough material has assembled in this part of the model space, so that a first disk can form. As more and more material falls onto it, a turbulent, fluffy disk emerges between the inner boundary and roughly 6 or 7 pc. Remarkable is the filamentary structure of the disk, showing strings of material, elongated in azimuthal direction. The reason for the filamentary nature of the material is identical to what has been discussed for the outer domain. The difference is that the main stream of material is now directed in azimuthal direction and not in radial direction (see Section 4.5.4) and, therefore, material streams are elongated in azimuthal direction. To recall, supernova blast waves will soon get stuck in very dense material and, therefore, blow channels in these directions, where densities are lower (compare to Fig. 4.15). This is known as the chimney effect in the ISM of (stratified) galactic disks, finally leading to the evolution of a galactic fountain process, transferring hot gas from the disk to the halo.

In summary, what we see is a collapse from a geometrically thick torus (here the outer part is most important) to a geometrically thin disk (which mainly lives in the middle domain). The initial torus is mainly (thermal) pressure (and partly rotation) supported and, therefore, collapses due to radiative cooling processes in the dense filaments, as cooling and heating of the gas is locally unbalanced within the course of the simulations. This finally forms the thin disk in the vicinity of the minimum of the gravitational potential. Thermal pressure does not play a role anymore, as it has cooled to temperatures of less than 100 K and reaches in some regions even our minimal temperature of 10 K. The scale height is now determined by random motions of the filamentary disk, often referred to as a turbulent pressure (like in our continuous TTM-models) and rotation. A cusp-like structure forms automatically in the inner part, due to the underlying gravitational potential and the rotation. This cusp ends into turbulent thin accretion tongues, pointing into the inner domain. Due to the angular momentum barrier, material cannot move further in, except angular momentum can be transferred outwards. As shown in the next section, this can be done by the turbulent flow in the inner part of the disk.

Characterisation of turbulence in the disk

In this section, we analyse the turbulence in the inner, dense disk described before. Especially interesting is the strength of the obtained hydrodynamical turbulence and the transport properties connected with it, which lead to further accretion of gas. The underlying turbulence theory is given in Section 4.2.9 and will only be applied here.

Shown in Fig. 4.38 are the normalised Reynolds stresses and corresponding Mach numbers of the turbulence observed in the middle domain of model TOR 1. Values correspond to an azimuthal, vertical and time-average over the whole temporal evolution, shown in Fig. 4.36 and 4.37. Radial

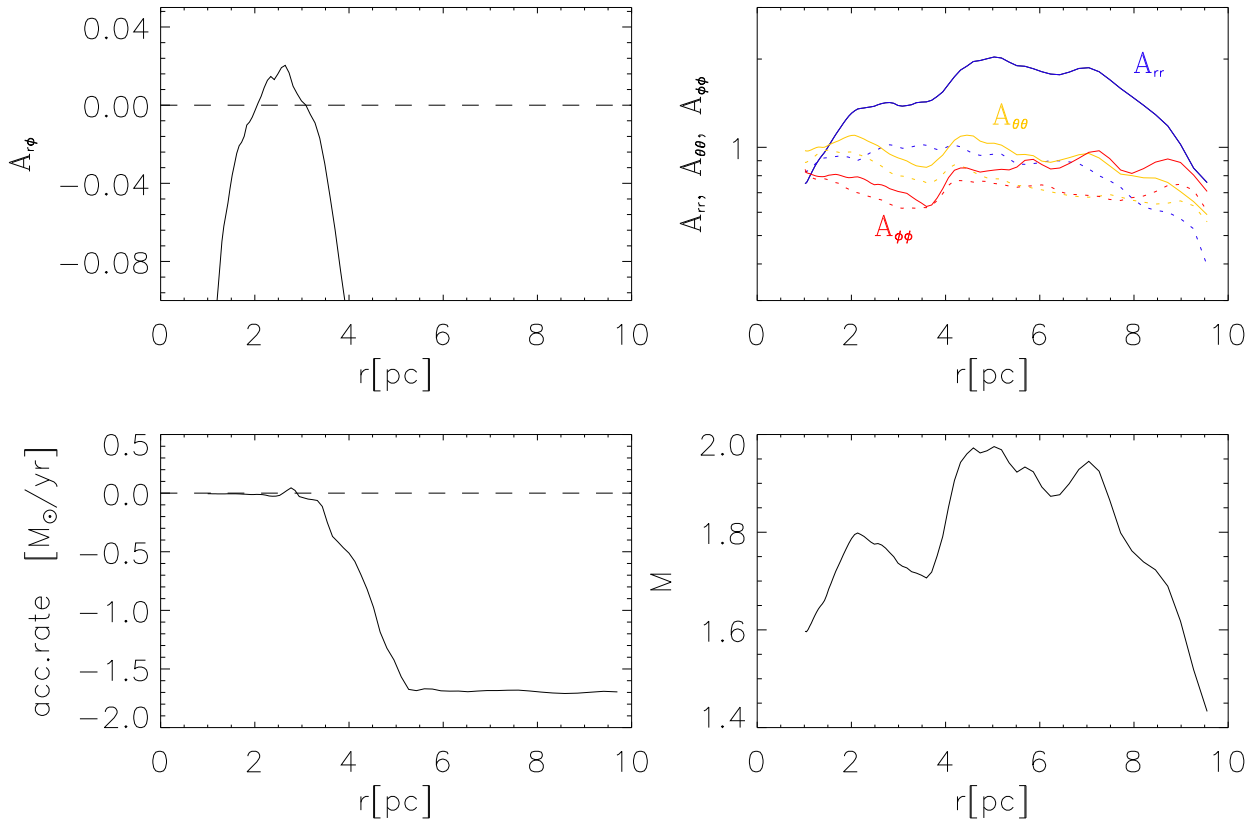

Figure 4.38: *Measurements of turbulence for the middle domain of model TOR 1: vertically, azimuthally and time-averaged Reynolds stresses for the whole evolution shown in Fig. 4.36 and 4.37, as well as average mass accretion rate and turbulent Mach number. See text for further explanation.*

variations are partly due to temporal and spatial events, which are not averaged out due to the short time period. As discussed in Section 4.2.9, on-diagonal elements (plotted in the upper right panel of Fig. 4.38) describe the strength of turbulence in different direction and are thereby also a measure of the isotropy of turbulence. For the case of our disk, turbulence decreases from supersonic for the radial case (A_{rr}, blue solid line) over sonic conditions in vertical direction ($A_{\theta\theta}$, yellow solid line) to subsonic turbulence in azimuthal direction ($A_{\phi\phi}$, red solid line). The reason for this might be due to the radially infalling material from the outer boundary acting as a source of turbulence within the minimum of the potential. This can also be seen from the result for the same simulation, but without taking radially infalling matter from the outer domain into account (given as dotted lines). Whereas the yellow and red lines show only small changes, the blue lines deviate by a large amount. Turbulence in azimuthal direction seems to be suppressed due to the fast rotation of the disk. Altogether, moderately super-sonic turbulence results, with Mach numbers between 1.4 and 2.0 (see lower right panel in Fig. 4.38). This is as expected for such kind of cold and thin accretion disks. Concerning mass transport (lower left panel), one can see that all over the domain, mass is transported inwards. Larger amounts in the outer part, where it is driven by infalling material from the outer domain. Only the inner part shows a small amount of material transported inwards by angular momentum transfer with α-values ($A_{r\phi}$) of the order of 2% (upper left panel). In our simulations, hydrodynamic turbulence is the only source of angular momentum transport. These processes lead to accretion in the form of thin turbulent streams of gas, as visible in the meridional cuts (Fig. 4.37). Time averaged accretion rates at the inner boundary of the middle domain amount from $10^{-4} M_\odot$/yr to $10^{-2} M_\odot$/yr (see lower left panel of Fig. 4.38). If all of the material would

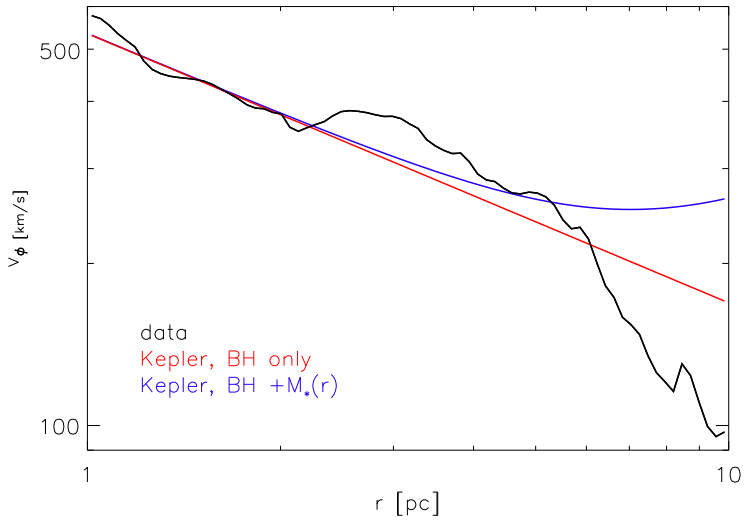

Figure 4.39: *Comparison of azimuthally averaged rotation velocity within the midplane of the turbulent disk of the middle domain (black line) with the Keplerian velocity due to the central black hole and the stellar cluster (blue curve). The red line indicates the Keplerian velocity when only the black hole is taken into account.*

reach the centre, this would yield a luminosity between $6.8 \cdot 10^{-2}$ % and 6.8 % of the Eddington luminosity of our central black hole of $6.64 \cdot 10^7\, M_\odot$. The problem in the outer part is that the disk forms within the last few timesteps and is still dominated by infalling matter. This can also be seen in Fig. 4.39, where the azimuthally averaged rotation velocity in the midplane of the disk (black curve) is compared to the Keplerian velocity due to the central black hole and the stellar cluster (blue line). The red line shows the Keplerian velocity, when only the central black hole is taken into account. Therefore, the averaging procedure for the transport characteristics does not make sense and leads to negative values for α. Within this sequence, no steady state can be obtained. A longer time evolution is needed here.

4.6 From hydrodynamic models to observables

The basic procedure of our effort of simulating gas dynamics in core regions of active galaxies can be divided into several steps: First of all, hydrodynamic simulations are carried out with the help of the TRAMP code as described above, with a spatial segmentation into three domains, which are successively calculated. In a subsequent step, these three domains are reassembled for certain timesteps. In order to subsequently perform continuum radiative transfer calculations, the obtained gas densities have to be transformed into dust densities. This is done by applying a constant gas-to-dust ratio to those patches of the gas distribution, where temperatures are below the sublimation temperatures of the various grain species. Two separate sublimation temperatures for the graphite (1500 K) and silicate (1000 K) component are taken into account. We decided to use a gas-to-dust-ratio of 250 in our simulations, which was motivated as follows. The gas-to-dust ratio of the local galactic surrounding was determined to be approximately 160 (Sodroski et al. 1994), whereas in external galaxies, ratios as high as 1000 where found. However, these measurements were recently questioned by Mayya & Rengarajan (1997) and they reduced them to values within a factor of two of the local ISM value. Towards active centres of galaxies, we expect an increased ratio, as dust is likely to be destroyed in the harsh environment close to the energy source. Thus, a value of 250 seems to be reasonable. Grain-size dependent sublimation is only considered during the radiative transfer calculations and, therefore, only for dust in the close vicinity of the AGN. Here, we split the dust opacity model into 6 different grains, made up of the largest (0.25 µm) and the

smallest (0.005 µm) grain of the MRN-size distribution and the three grain species (for details see Section 4.2.8). For this purpose, it results in an opacity model of high enough accuracy. As radiative transfer calculations are very time- and memory consuming, the grid from the hydrodynamic simulations - made up of all three portions as described above - has to be transferred to a smaller grid, depending on the number of dust species calculated in one single run. A resolution of 114 grid cells in radial direction (instead of 181 for the composed hydrodynamic model), 61 grid cells in θ direction (instead of 94 in the hydrodynamic models) and 128 in ϕ-direction (instead of 49 per quadrant in our hydrodynamic models) is possible with our current computers. Within these simulations, temperatures from the hydrodynamic simulations are not taken into account, but the dust is solely heated by the central AGN. From the resulting temperature distribution, observable quantities can be derived, in the usual second step of the two-step approach of MC3D. These are spectral energy distributions and images at various wavelengths of the dust reradiation. In a last step, surface brightness distributions will enable us to calculate visibilities in order to compare to recent mid-infrared interferometric observations.

However, at the current state of our modelling, one has to be cautious with the results of the subsequent radiative transfer calculations, as a higher spatial resolution would be desirable, in order to better resolve the fine structures of the hydrodynamical calculations and their partially steep density gradients. Furthermore, we are limited with the number of photon packages used in the Monte Carlo radiative transfer (determination of the temperature distribution), which has appreciable consequences on the signal to noise ratio of the single grain temperature distributions (6 different temperature distributions are calculated). This is especially the case for the much higher optical depths close to the midplane ($\tau_{9.7\,\mu m}$ of several hundred) of these simulations in contrast to the simulations shown in Chapter 2 and 3. It also causes problems with our procedure of determining the sublimation radii of the various dust species, leading to unphysically high temperatures in a number of grid cells (a fraction of 0.0006 of the cells have a temperature more than 20% higher than the grain's sublimation temperature in our standard model). Despite the large noise within single temperature distributions, our tests with ten times the number of photons (see Fig. 4.40a) and with a factor of roughly 3 decreased number of grid cells (see Fig. 4.40b) yield comparable spectral energy distributions for all calculated inclination angles of our standard model. One reason for this is that for the determination of the spectral energy distributions, all single temperature distributions are taken into account. The resolution test for the whole model space results in a much better

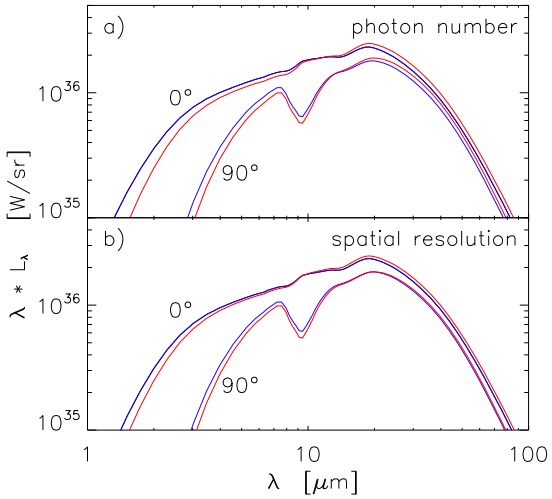

Figure 4.40: *Quality study for radiative transfer models of the standard hydrodynamic model (TOR 1):*
a) *Dependence on the photon number: our standard model (blue line) and 10 times more photon packages (red line).* **b)** *Dependence on spatial resolution: our standard model (blue line) and the same model, but with roughly a factor of three less grid cells.*

agreement compared to the single clump case in Chapter 3. For further information see discussion in Section 3.2.3.

4.6.1 Observing the standard hydrodynamic model

Fig. 4.41 shows an inclination angle study of images at 12 µm of the final stage (after 10 orbits) of our standard hydrodynamic model. Shown is the dust reemission and the central radiation of the face-on case ($i = 0°$), $i = 30°$, $i = 60°$ and the edge-on case ($i = 90°$) for an azimuthal angle of $\phi = 45°$. Even at an inclination angle of 60°, the central source is still the brightest spot at these ϕ-angles, but it vanishes behind the dense nuclear disk at larger inclination angles (90°). The dense nuclear disk is the second brightest, characteristic for our models. As expected, it does not appear smooth, but the filamentary structure is partly visible, as well as a slight nuclear spiral structure (only visible in the high-resolution electronic version), caused by the differential rotation of the disk. Due to the large optical depth at intermediate inclination angles, the torus shows an asymmetric structure with respect to the midplane, as only the upper direct illuminated funnel wall is visible. Objects of that kind could correspond to the case, when only one ionisation cone is visible in observations, e. g. NGC 1068 or NGC 5728 (see Fig. 1.4). The same holds true for the 60° inclination. Here, as well as in the edge-on case, *shadows* of dense – in most cases radially inward moving – filaments are visible. The anisotropic radiation source (preferentially emitting in vertical direction) also contributes to the vertically elongated bright regions and enhances the dark lanes in the midplane.

In Fig. 4.42, spectral energy distributions of the standard hydrodynamical model are presented in form of pure dust reemission spectra. As concluded in Section 2.5, the innermost part is crucial for the determination of the determination of spectral energy distributions. Due to the turbulent structure of the dense nuclear disk close to the midplane and the filaments and blobs of high density gas within or close to the funnel region (compare to Fig. 4.37), our proposed model for the reduction of the silicate feature in emission (Section 3.4.1) works perfectly and only a moderate emission band with a strength of 0.09 is visible at 9.7 µm. We define silicate feature strength in accordance with Shi et al. (2006) as

$$\Delta_{\text{feature}} = \frac{F_{\text{feat}} - F_{\text{cont}}}{F_{\text{cont}}}. \tag{4.30}$$

(for further explanation, we refer to Section 4.8.2). With increasing inclination angle, it changes

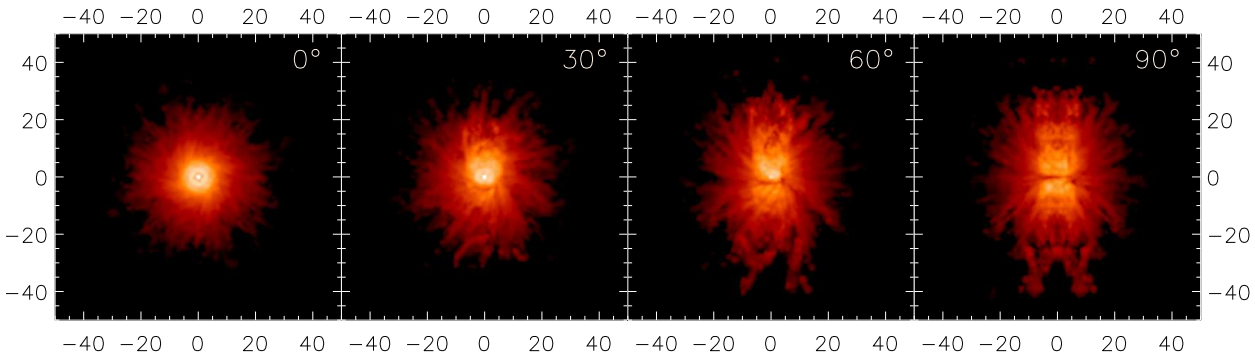

Figure 4.41: *Images of the standard hydrodynamic model at* 12µm. *Shown are the inclination angles* 0°, 30°, 60° *and* 90° *with a logarithmic color scale. Labels are given in pc.*

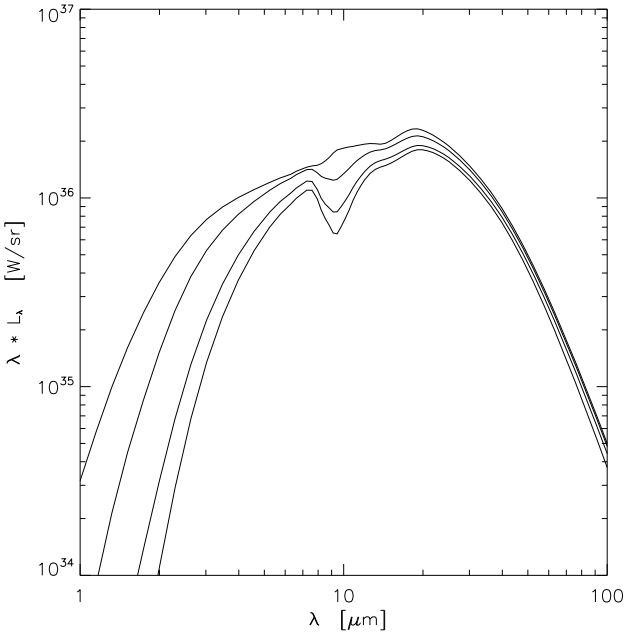

Figure 4.42: *Spectral energy distributions of the standard hydrodynamic model. Shown are again the inclination angles* 0°*,* 30°*,* 60° *and* 90° *(top to bottom).*

to moderate absorption: -0.18 for 30°, -0.39 for 60° and -0.50 for 90°. This is remarkable, as the same average optical depth within the midplane ($< \tau_{9.7\,\mu m} >_{equ} \approx$ 403.2!!) would cause much deeper absorption – which has never been observed – for the case of a torus with continuous dust distribution. This is possible, as the silicate emission feature is produced within a volume, elongated along the funnel region. The appearance of the silicate feature is due to a mixture of emission and absorption and, therefore, existing channels of low absorption towards the observer (though leading to silicate emission features) can also contribute to the final morphology of the silicate feature.

Finally, one has to be cautious, when interpreting observables for single lines of sight, as we expect quite large changes in these quantities for different ϕ-angles. But after all, one viewing angle is what we see in single galactic nuclei and for statistical statements, we have a far too small sample of nearby objects, which we are able to resolve with the most up-to-date interferometric instruments in the mid-infrared.

4.7 Parameter studies

In this section, we study the main parameters of our model, namely the mass injection rate and the supernova rate. As cooling delicately depends on the metalicity, we also vary the amount of cooling. Subsequently, the behaviour of different initial conditions, as well as the dependence on the mass of the stellar cluster is tested.

4.7.1 Mass injection rate

The mass injection rate is increased starting from model TOR 3 by a factor of 2 (TOR 2) and 5 (TOR 1 - the standard model). Fig. 4.43 displays meridional slices of this study after approximately 10 orbits. From row to row, the mass loss rate increases. The columns display the density, temperature and pressure in logarithmical scaling. Within this sequence it is clearly visible that

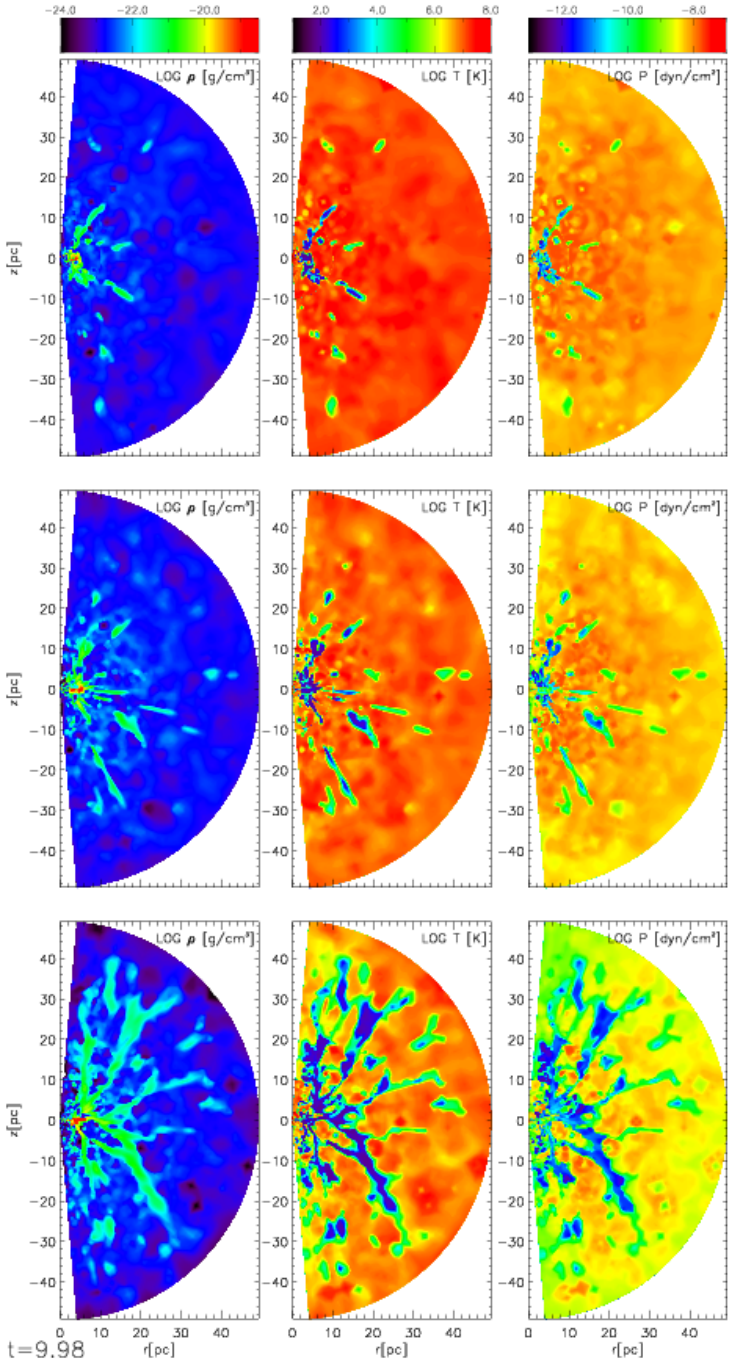

Figure 4.43: *Meridional slices in density (first column), temperature (second column) and pressure (third column) at low (upper row), medium and high mass loss rate (third row, standard model).*

simulations with mass input at high rates show a lot more structures appearing on large scales. The disappearance of structures can be accounted for by the unbalance of heating and cooling in the outer part and, therefore, material is blown outwards (see Fig. 4.46).

Additionally, the successive calculation of the middle and inner domain after the outer domain gets less exact, when the ratio of supernova rate and mass loss rate increases. Then, large fluctuations in the radial velocity exist (see below) and, therefore, material also flows in outward direction over the boundaries between the domains, which cannot be taken into account within our approximative

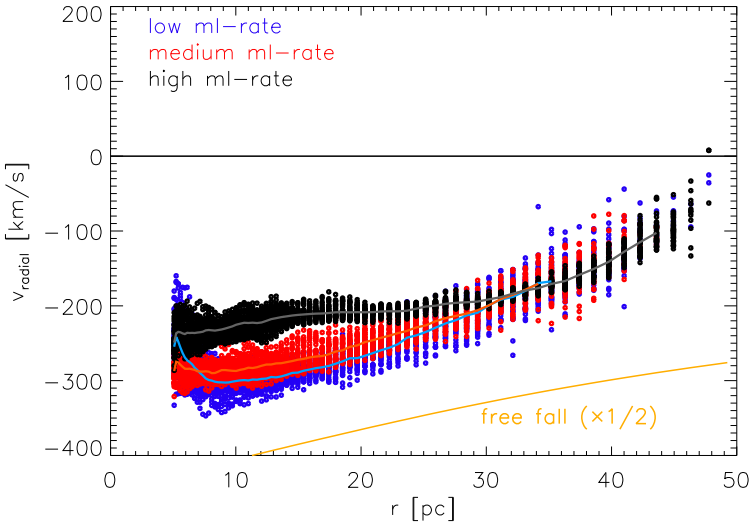

Figure 4.44: *Comparison of radial velocities within the mass loss rate study for the CNM between orbit 8 and 10. Lines represent time-averaged (orbits 8-10) values.*

handling of the domain decomposition, although we have a large overlap of the simulations towards the next inner domain. However, the effects are very small and it leads only to a faint, ring-like feature at 10 pc radius, getting less evident at smaller ratios (second and third row, but only visible in the electronic version of this plot).

Fig. 4.44, 4.45 and 4.46 show the radial dependence of the radial velocity (averaged over angles θ and ϕ) of the three models in comparison. Model TOR 3 (low mass loss rate) is given in blue, TOR 2 (medium mass loss rate) in red and TOR 1 (high mass loss rate) in black. Again, all values between 8 and 10 orbits of the outer domain are shown (dots), displaying an increasing spread of values towards the inner part. In addition, time averaged curves are given as overlaid coloured line plots. Whereas cold (Fig. 4.44) and warm material (Fig. 4.45) flows radially inward, we get a clear separation into inflowing and outflowing gas for the case of the HIM (Fig. 4.46).

The *transition radius* between outflowing material in the outer part and material being accreted in the inner part, grows with decreasing mass loss rate in our simulations. This means that only in a narrow range in radius, a balance of forces is acquired in radial direction. Further outwards, the gradient of thermal pressure of the relatively tenuous gas there pushes the gas outwards, a phenomenon visible in the form of galactic winds (for a recent review see Veilleux et al. 2005).

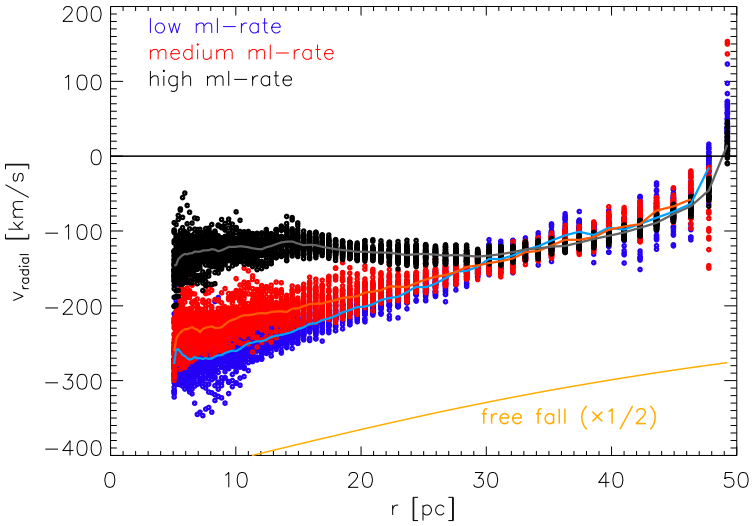

Figure 4.45: *Comparison of radial velocities within the mass loss rate study for the WNM between orbit 8 and 10. Lines represent time-averaged (orbits 8-10) values.*

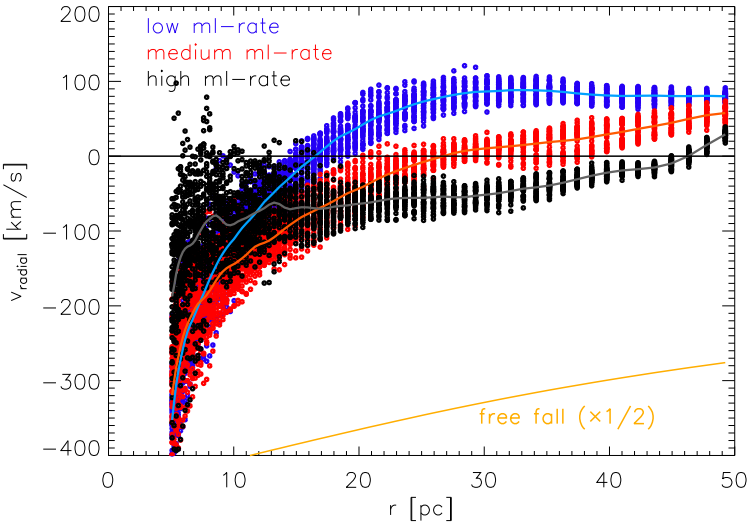

Figure 4.46: *Comparison of radial velocities within the mass loss rate study for the HIM between orbit 8 and 10. Lines represent time-averaged (orbits 8-10) values.*

Further in, pressure needs to be higher in order to balance the growing gravitational pull closer to the centre, but supernova explosions heat the material too little, as density increases towards the centre (see Fig. 5.1c). Additionally, dense material cools much faster ($\Lambda_{\rm cool} \propto \rho^2$!), loosing even more pressure. As density increases even faster towards smaller radii for the case of higher mass loss, the *transition radius* moves further inwards. Beyond the *transition radius* (inwards), models with higher mass loss rates show a flattening of the radial velocity, which is caused by the additional turbulent pressure component, provided by the mass input. This is even more visible for the case of the WNM. Concerning the CNM, the dependence weakens, as inflow velocities exceed the velocity dispersion of the injected clouds.

Fig. 4.47 displays the *accretion rate per cell*[9] for the model with the smallest mass loss rate, averaged over the ϕ-direction. This is of special interest, as for this simulation, we can see a clear change of sign of the radial velocity at approximately 16 pc (see Fig. 4.46) for the case of the HIM. We already discussed the global behaviour, namely that we see practically only infalling material for the case of cold and warm material, but outflow as well as accretion for the HIM. Most notably in this figure is that for the cold and warm material, regions of equal accretion rate per cell (enhanced compared to their surrounding) lie on a small number of radial rays, now emphasised by the ϕ-averaging process (compare to Fig. 4.43). The HIM-case is clearly distinct from the two other cases. Here, a separation into cylindrical regions appears. This is an indication for the driving mechanism of the hot flow. It seems that the stirring due to supernova heating and cloud-cloud interactions enables angular momentum transport in outward direction, similar to the assumption in the torus accretion scenario described by Vollmer et al. (2004) and Beckert & Duschl (2004), where turbulent cloud interactions produce effective viscosity and thereby a means of angular momentum transport, leading to a geometrically thick accretion flow, the torus.

Fig. 4.48 compares phase distribution functions of the mass loss rate study. The change of the curves is as expected for a higher rate of mass feeding. In summary this is (compare to Section 4.5.4):

- **first column:** the volume and mass of the hottest part of the gas decreases in favour of colder material, again caused by rapid cooling ($\Lambda_{\rm cool} \propto \rho^2$), when increasing the mass loss rate.

[9] *Accretion rate per cell* is printed in italic letters here, as it shows positive and negative values. Positive values denote outflowing material, according to our definition.

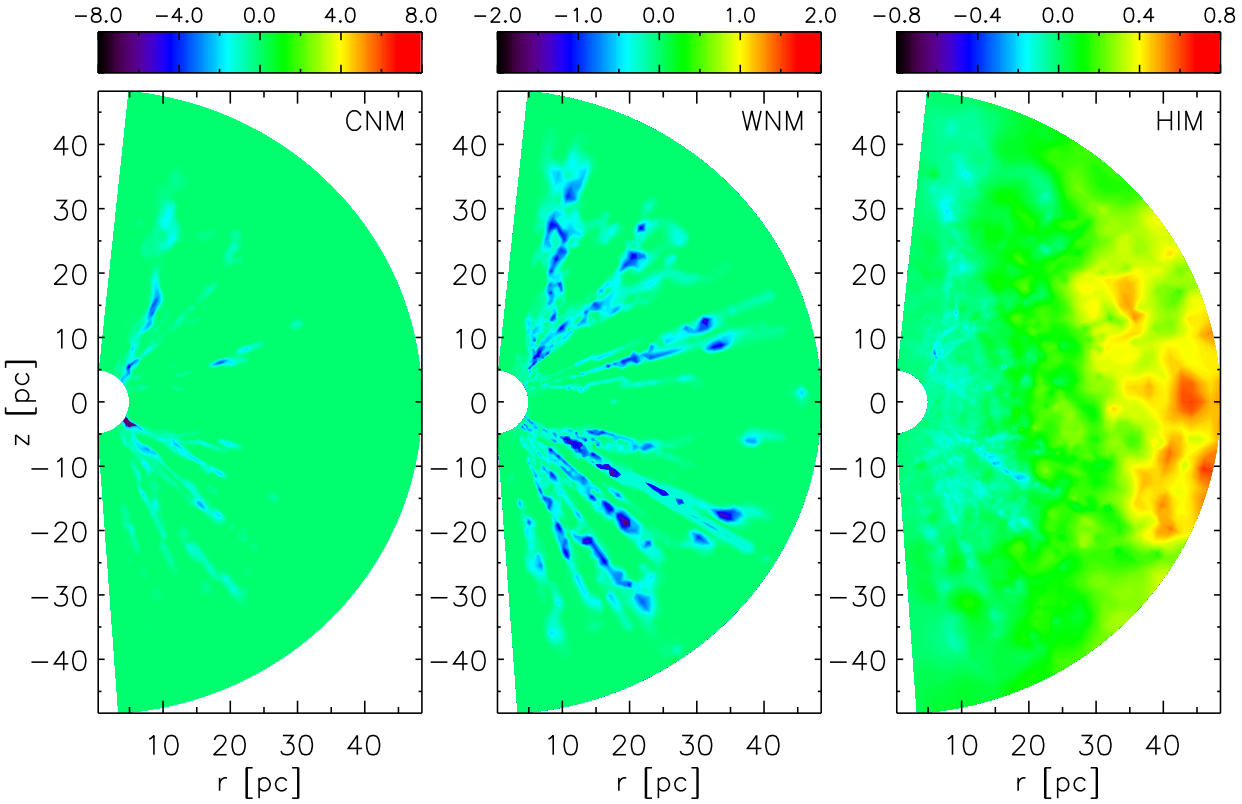

Figure 4.47: *Mass accretion rate per cell, averaged over ϕ-direction for the model with the lowest mass loss rate (TOR 1). Mind the different color scales, accretion rates are given in units of* 10^{-4} $M_{\odot}$*/yr. Positive accretion rates denote outflowing material.*

- **second column:** increased mass input promotes clumping of material, denser filaments form, especially visible in volume in the high density blobs and in mass in the decreasing amount of low density gas.
- **third column:** following our description in Section 4.5.4, the amount of mass undergoing thermal instability increases with enhanced mass input, while the amount of material in pressure equilibrium stays nearly constant (the equilibrium pressure seems to be shifted) and we see less gas which has recently suffered an effective supernova explosion. Effective in this sense refers to the smaller impact of supernova input, when exploding in a dense environment.

Furthermore remarkable is the change in observable quantities. Shown in Fig. 4.49 are the corresponding spectral energy distributions for one single ϕ orientation and face-on (upper panel) as well as edge-on viewing angle (lower panel) for high mass loss rate (solid line – the standard model), intermediate (dashed) and low mass loss rate (dotted). In the face-on case (upper panel), the silicate feature height is comparable for our standard model and the model with the smallest mass loss rate. For those two, values of 0.1 are derived with the help of the analysis as described in Section 4.8.2. The intermediate mass loss rate simulation yields a more pronounced feature with a value of roughly 0.3. For the case of our standard model, much more filamentary structure exists, also reaching out into the torus funnel region (see also Fig. 4.37). Therefore, shadowing effects are much more effective and help to significantly smear out the feature (see Section 3.4.1). This again shows that the feature height is determined by fine structure close to the central region. In both

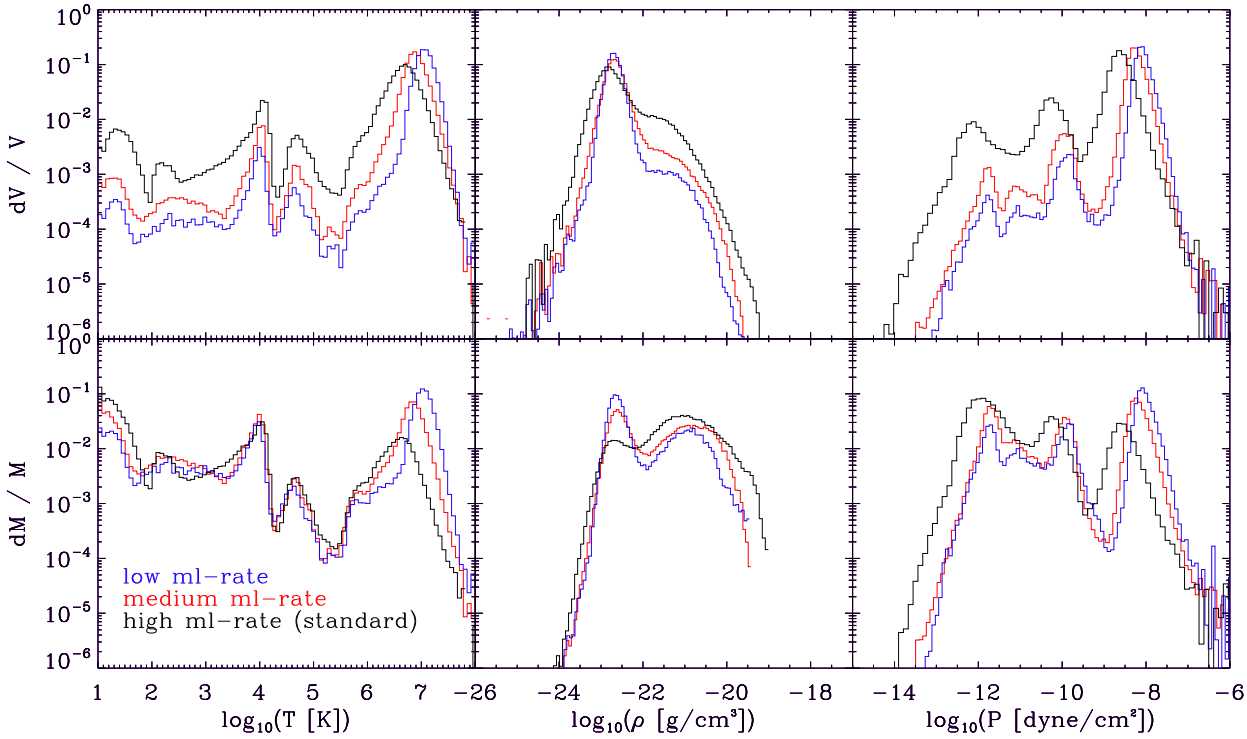

Figure 4.48: *Phase diagrams comparing different mass loss rates, as indicated in the legend in the lower left corner.*

panels, the larger dust mass in the standard model leads to more flux at longer wavelengths and additionally to an earlier cut-off at short wavelengths and a much deeper silicate absorption feature (-0.51) for the edge-on case.

Images at 12 µm (Fig. 4.50) closely resemble the density distribution of this study (compare to

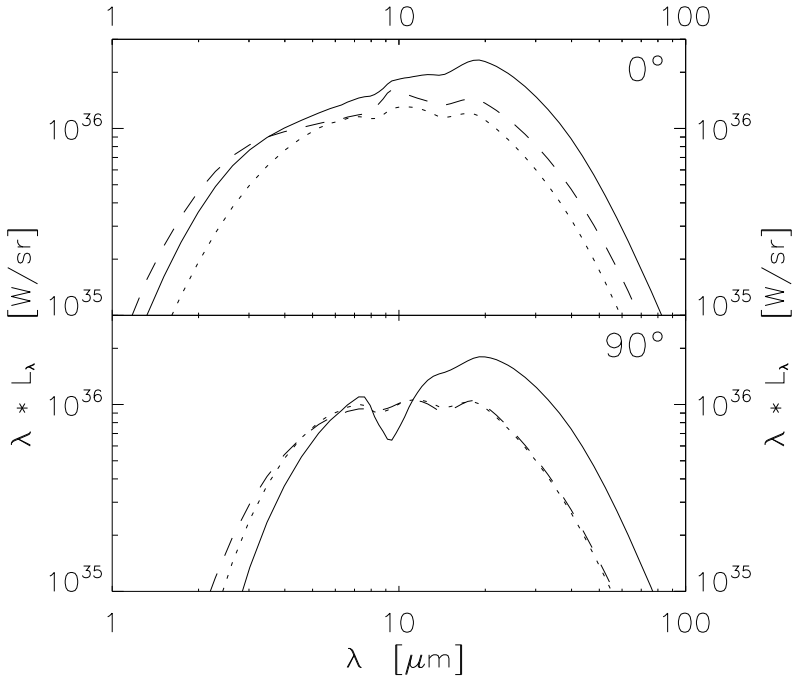

Figure 4.49: *Comparison of spectral energy distributions of the mass loss rate study at face-on (upper panel) and edge-on view (lower panel):* $1.2 \cdot 10^{-9}\, M_\odot\, \mathrm{yr}^{-1}\, M_\odot^{-1}$ *mass loss rate (dotted line), twice this rate (dashed line) and five times this rate (solid line – the standard model).*

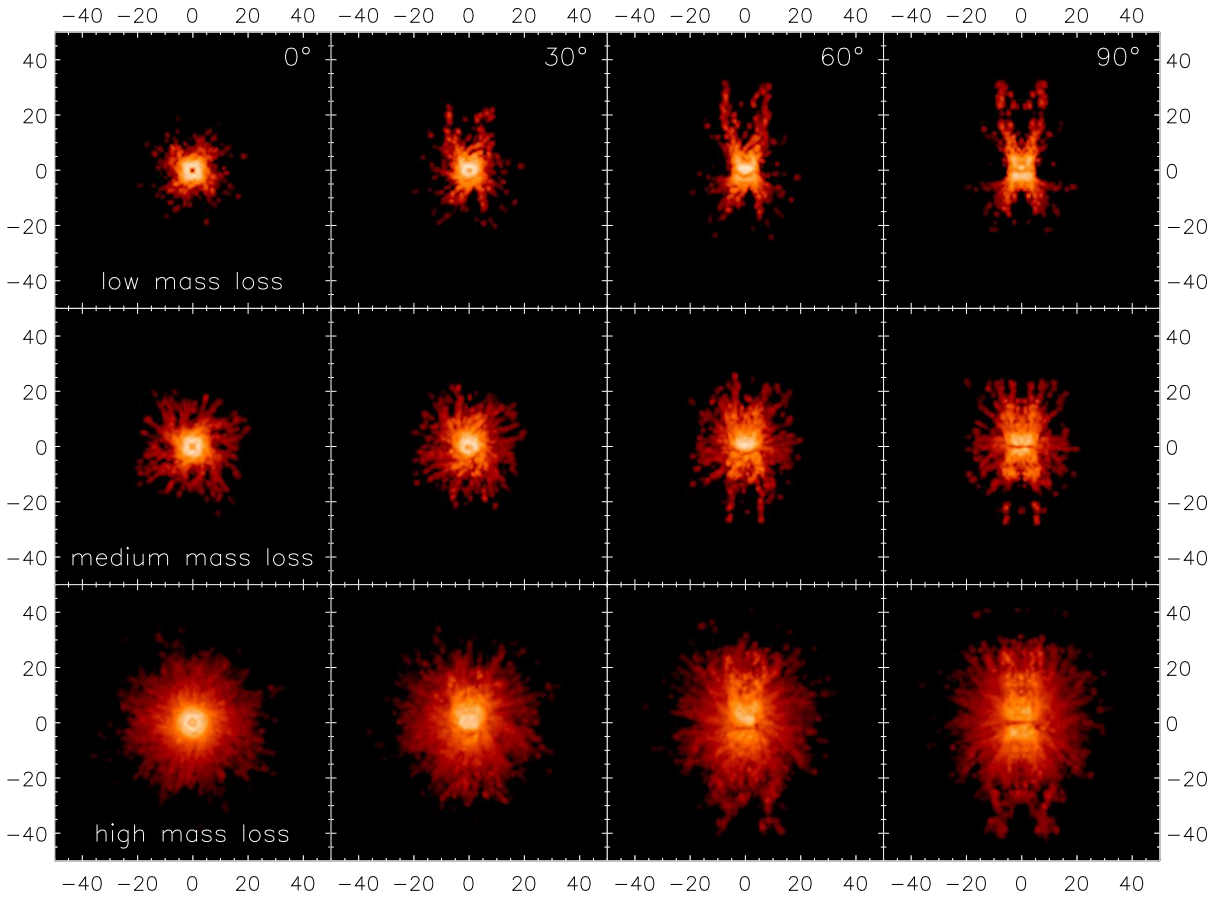

Figure 4.50: *Comparison of images at* 12 µm *of the mass loss rate study at inclination angles of* 0° *(*1st *column),* 30° *(*2nd *column),* 60° *(*3rd *column) and* 90° *(*4th *column):* $1.2 \cdot 10^{-9}\, M_\odot\, \mathrm{yr}^{-1}\, M_\odot^{-1}$ *mass loss rate (*1st *row), twice this rate (*2nd *row) and five times this rate (*3rd *– the standard model).*

Fig. 4.43). At inclination angles close to face-on (first and second column), the thick disk is visible, which finally causes asymmetric appearance of the images with respect to the midplane at intermediate inclination angles and the dark central lane in the midplane at edge-on-view. The central lane is enhanced by the anisotropic radiation characteristic of the primary source. With increasing mass loss rate, the images appear overall larger at this wavelength. For the case of edge-on view onto the torus, we observe an elongation in direction of the axis of rotation. It is caused by the large filaments close to the funnel. This could be of interest for the comparison with interferometric observations.

4.7.2 Supernova rate

In this parameter study, we examine the influences of changing the supernova rate. Starting with our standard model (TOR 1), we successively increase the supernova rate by factors of 2 (TOR 4), 5 (TOR 5) and 10 (TOR 6).

Meridional slices of this parameter study are given in Fig. 4.51. In different columns, from left to

right, the supernova rate increases. Different rows show density, temperature and pressure maps. With increasing supernova rate, the volume filling factor of the hot temperature gas increases drastically, where material has been swept away. This happens mainly in the outer part, where the HIM is transported outwards for the models with high supernova rate (see Fig. 4.51). Further in, supernova explosions try to push material further inwards, until this pressure is finally balanced by the angular momentum barrier. Therefore, the few dense clouds and filaments visible in the 2D cut

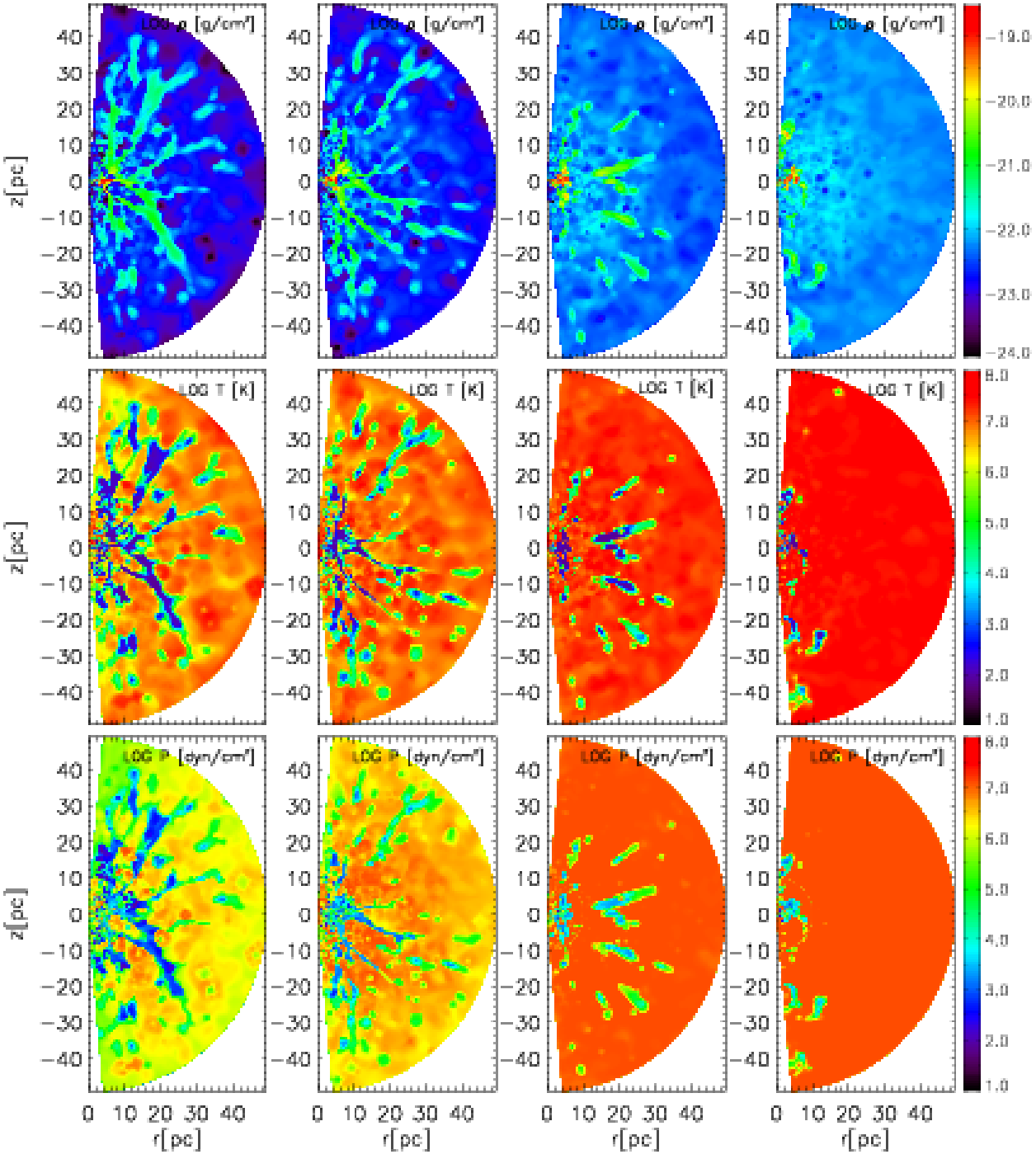

Figure 4.51: *Meridional slices of the supernova rate study. From left to right: our standard model, twice the supernova rate, five times the supernova rate and ten times the supernova rate. Shown are density, temperature and pressure distributions.*

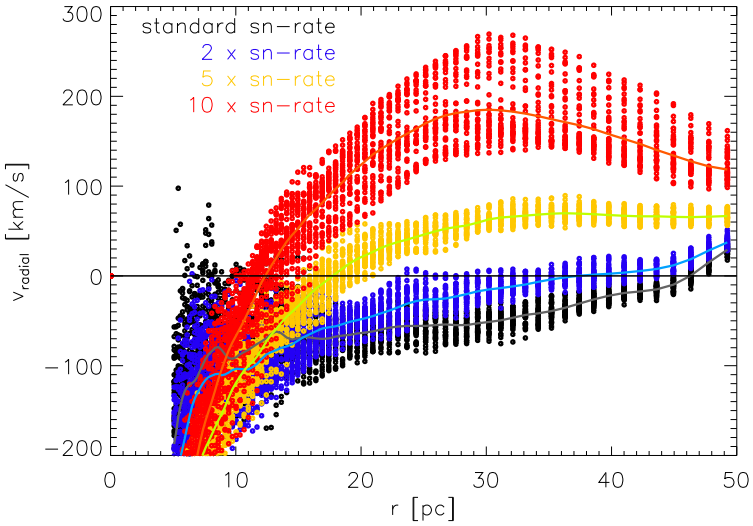

Figure 4.52: *Radial velocities of the supernova rate study: Our standard model (black), twice the supernova rate (blue), five times the supernova rate (yellow) and ten times the supernova rate (red) for the HIM-component.*

string up on a cylinder around the torus symmetry axis, unable to escape in horizontal direction inwards. The composition of structure increases when applying ever smaller supernova rates. For the case of the model with five times our standard value (3rd column), filaments appear nearly only radial, whereas at smaller rates, a more net-like structure builds up. This is a result of the velocity difference between material of different temperatures (see Fig. 4.53). Cold, dense gas is accreted, while hot gas is moving outward, thereby forming the streams of cold material. The maximal difference in these velocities is reached at approximately 25 pc for the case of the highest supernova rate of our study, which corresponds to the core radius of the stellar distribution. At this point, the radial velocity of the hot gas drops steeply and turns into an inward motion.

4.7.3 Cooling rate

As can be seen from Fig. 4.8, the cooling function depends delicately on the metalicity of the medium. The larger the metalicity, the larger the cooling rates (see discussion in 4.3.5). Therefore, to account for the uncertainty of the metal abundances within AGN tori material, we decreased (model TOR 7) and increased (model TOR 8) the cooling rate by a factor of 5 in each case.

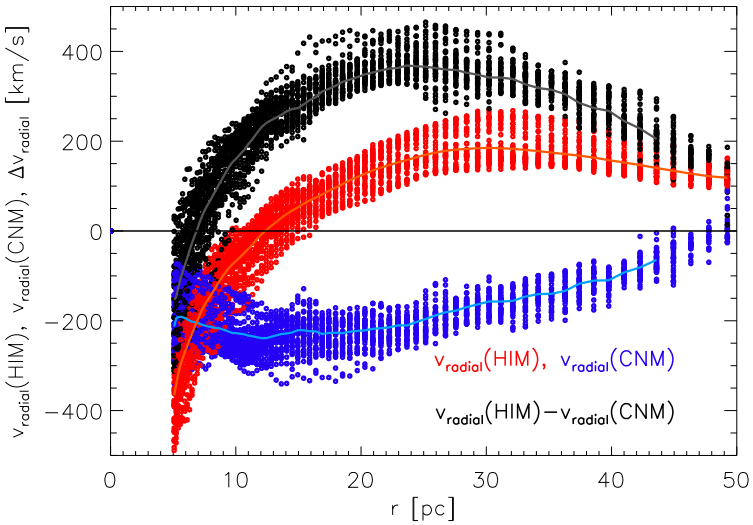

Figure 4.53: *Difference between radial velocities of the HIM- and CNM-component of the gas for the case of the highest supernova rate.*

Fig. 4.54 shows density and temperature distributions for the low and high cooling rate after roughly 10 orbits. Also compare to the case of the standard model (e. g. left column in Fig. 4.51). The most striking difference appears in the thickness of the structures, especially visible in the temperature distributions, as for the case of higher cooling coefficients, also lower density material can cool on short timescales, whereas for the lower cooling efficiency, only the densest filaments are able to cool down to CNM-temperatures. When looking at the temporal evolution of the simulations (see animations on DVD - Appendix B), the strong cooling even succeeds to convert the hot initial condition to a cold toroidal structure. Effective heating by supernovae is mainly possible in the outskirts of the simulational domain and within the funnel. In this regions, we have less radial infall, as radial gravitational forces are lower and, therefore, densities are on average lower. This again means that supernovae can heat the gas to higher temperatures in these regions.

As can be seen from Fig. 4.55, the higher the cooling rate, the larger is the temporal scatter of radial velocities in the innermost region for the case of the HIM. This is clearly a sign of supernova induced turbulence. The flow pattern of the high-temperature regime is now really dominated by supernova explosions. Looking at the temperature maps again (see Fig. 4.54), we have for the case of stronger cooling a less filamented structure, but a clear spatial separation between hot and cold regions. Whereas the body of the torus has less than 1000 K, the surroundings as well as the funnel region possesses high temperatures, given by recent supernova action. When cooling is less efficient, the filamentary structure is embedded into hot, tenuous gas, which is barely able to cool, but gets energy input by supernova explosions. Inside the radially infalling bulk of the cold gas, it gets dragged along with this flow and significantly contributes within the averaging procedure in polar direction. Concerning radial infall velocities at colder temperatures, we get slightly smaller

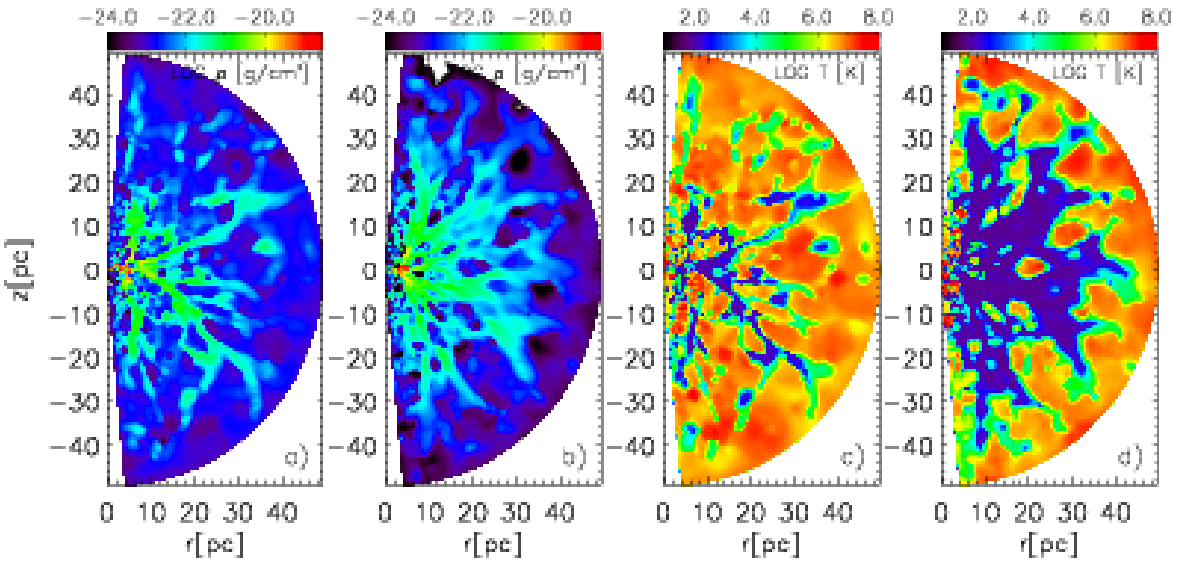

Figure 4.54: *Density (left two columns) and temperature (right two columns) maps for the cooling rate study: cooling rate decreased by a factor of 5 (a and c) and increased by a factor of 5 (b and d) compared to our standard model (TOR 1). Also compare to according images of our standard model (e. g. first column of Fig. 4.51).*

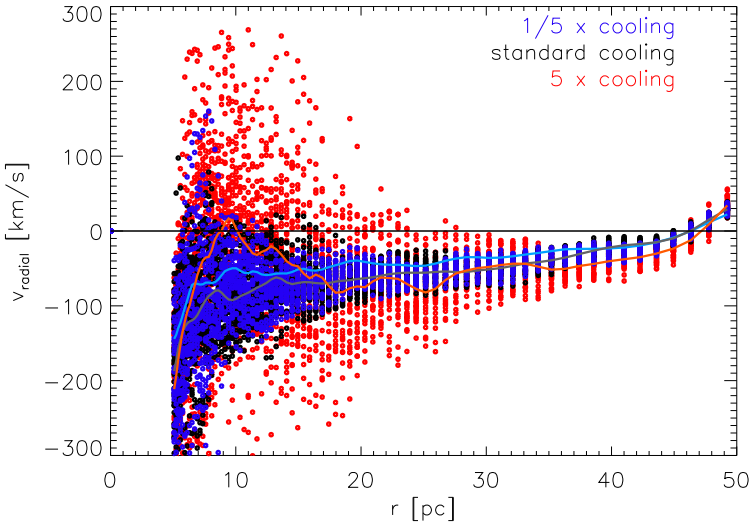

Figure 4.55: *Radial velocity distribution in radial direction, concerning the HIM-phase for varying cooling rates: our standard model's cooling rate (black), a five times smaller cooling rate (blue) and a five times higher cooling rate (red). Each dot for a given radial position belongs to a different simulational time.*

velocities for the case of a higher cooling rate, but this might also be biased by the averaging procedure and the fact that planetary nebula input happens at the local temperature.

4.7.4 (Nearly) empty initial condition & low initial temperature

In order to check the dependence of our results on the initial condition, in these simulations, we started from an empty model space. Empty in this sense means that it is homogeneously filled with gas with the lower density threshold value ($\rho = 10^{-26}\mathrm{g/cm^3}$). Numerical stability – despite supernova energy input – is guaranteed by the additional mass input of the usual 1.4 $M_\odot$ (see Section 4.3.4). As expected, the initial condition does not play any role in the evolution of the gaseous structures, as the final equilibrium value of the total mass (in the outer domain) is approximately 20 times higher than the initially distributed mass and is reached already after less than 3 orbits.

Additionally, this model features a very low initial temperature. Depending on the surrounding temperature, different behaviours of injected planetary nebulae as well as supernova explosions are expected (see Section 4.4.3 and 4.4.1 for a detailed discussion). But the memory of the initial condition is lost very quickly so that finally, very similar density distributions result. This again shows, that our simulations are insensitive to initial conditions.

4.7.5 Cold initial condition, turbulent pressure

Due to the large differences of planetary nebulae injections, depending on whether we are in the sub- or supersonic regime, we are checking the implications of starting with a cold ($T = 1000\,\mathrm{K}$) initial condition. In this simulation, gravitational and centrifugal forces are not balanced by forces due to thermal pressure in the initial condition, but with a turbulent pressure. It is applied by overlaying velocities for each cell, with a value equal to the velocity dispersion of the stars and randomly chosen directions. The imposed small-scale turbulence decays within a fraction of an

orbital period and is dissipated into heat, leading to a similar temperature distribution as in all of our other models. Additionally, the supernova input quickly heats the tenuous medium outside-in towards the minimum at the torus radius. Therefore, after a short while, we see identical behaviour, except for the first period in the direct vicinity of the torus radius. There, the appearing structures are thicker and the region is less filamented compared to our standard model. Later stages are again very similar to our standard model.

4.7.6 Mass of the star cluster

As discussed in Section 4.5.1, the stellar mass content of our models is determined by the Jeans equation. In this paragraph, we decrease this parameter, deviating from this equation. This is of interest, because changing the stellar mass content has the same effect on the supernova as well as the mass loss rate, leaving the ratio of both untouched.

Figures 4.56, 4.57 and 4.58 display the differences in radial velocity, again showing one data point for each timestep (every 5% of an orbital period). For the case of the HIM, a decrease of the transition radius between outflowing material and infalling gas is clearly visible for the case of the less massive stellar cluster.

For the case of higher stellar mass, we get a deeper potential well and the gravitational pull forces the material to reach higher velocities, although the supernova rate is increased by the same amount. The increasing transition radius is an indication that the outer part is dominated by gravitational infall, due to the fast cooling of material, which cannot be balanced globally by the supernova energy input.

In both cases a toroidal distribution of filaments pointing towards the centre is obtained in the outer domain. Further in, it is clear that a less dense disk forms, for the lower mass input case.

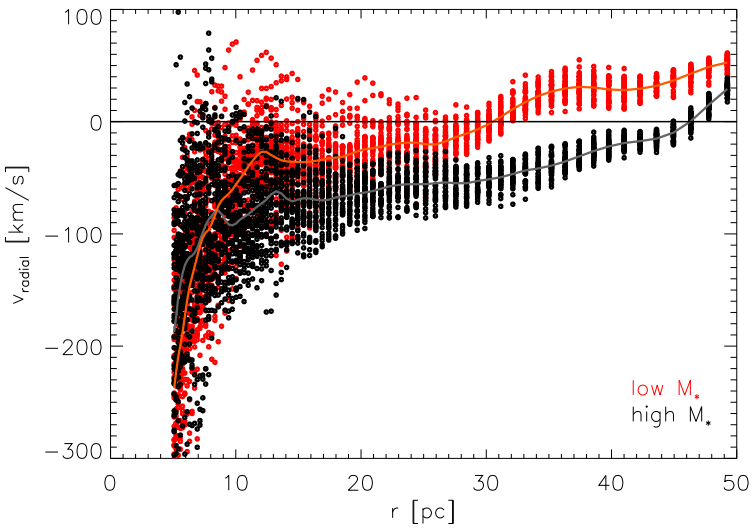

Figure 4.56: *Radial velocity distribution in radial direction, concerning the HIM-phase for varying total masses of the stellar cluster: our standard model's mass of stars (black -* $1.81 \cdot 10^9\ M_\odot$*) and an artificially reduced value (red -* $6.64 \cdot 10^8\ M_\odot$*).*

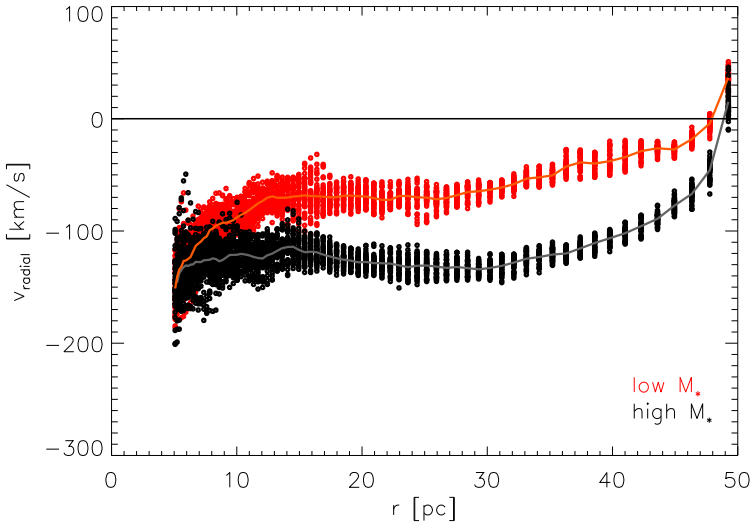

Figure 4.57: *Radial velocity distribution in radial direction, concerning the WNM-phase for varying total masses of the stellar cluster: our standard model's mass of stars (black -* $1.81 \cdot 10^9\ M_\odot$*) and an artificially reduced value (red -* $6.64 \cdot 10^8\ M_\odot$*).*

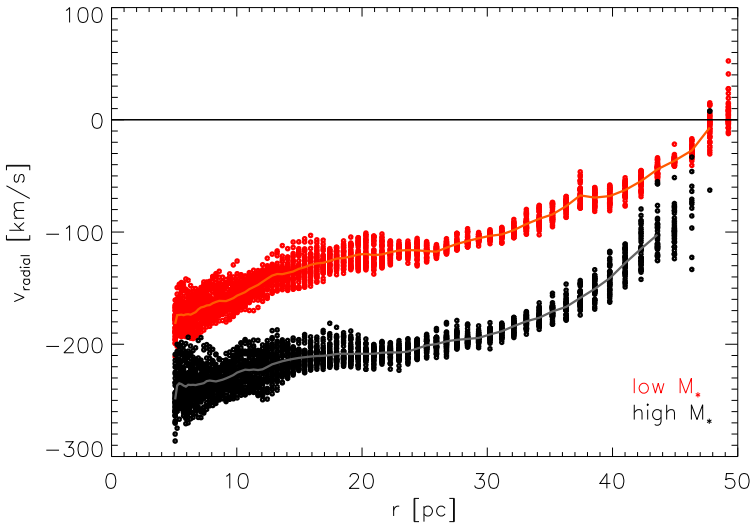

Figure 4.58: *Radial velocity distribution in radial direction, concerning the CNM-phase for varying total masses of the stellar cluster: our standard model's mass of stars (black -* $1.81 \cdot 10^9\ M_\odot$*) and an artificially reduced value (red -* $6.64 \cdot 10^8\ M_\odot$*).*

4.8 Comparison with data

In this section, we first of all compare the spectral energy distributions of our standard hydrodynamic model with observations of Seyfert galaxies. Additionally, we compare part of the parameter study with silicate feature strength and column density data derived from observations.

4.8.1 Comparison with Spitzer observations

Figure 4.59 shows a comparison of our standard hydrodynamic model with observations of two Seyfert galaxies with the Infra-Red Spectrograph (IRS) onboard the Spitzer Space Telescope, in high-sensitivity low resolution mode. The solid curve refers to a Seyfert type I sightline (an inclination angle of 0°), the dotted line is an intermediate inclination angle of 30° towards our standard hydrodynamic model. Shown in color are the mid-infrared SEDs of the two intermediate (type 1.5 according to NED[10], the NASA/IPAC Extragalactic Database) Seyfert galaxies NGC 4151 (blue solid line, Weedman et al. 2005) and Mrk 841 (red, H. W. W. Spoon, private communication). Both are scaled, in order to obtain similar fluxes as for our standard model, as we are only interested in a comparison of the shape of the curves. The face-on view towards our model shows the silicate feature in slight emission, whereas the 30°-inclination angle shows a self-absorbed silicate feature. For intermediate viewing angles between 0° and 30°, the correct feature height is expected to be visible. Deviations between observations and model are visible in a shift of the maximum of emission of our model towards slightly larger wavelengths, and a feature around 34 µm. The feature arises most likely from crystalline Forsterite in emission (H. W. W. Spoon, private communication). We do not include crystalline silicates within our dust model, hence the deviations.

As our SEDs do not result from a fitting procedure, this is a very noteworthy result. Especially because the physical parameters we use are meant to represent a typical Seyfert galaxy. The sharp decrease of the flux here results from missing cold dust in the outer part. Although these results are encouraging and in accordance with our expectations, one has to be cautious, as uncertainties arise from the radiative transfer procedure. But differences found in the study of spatial resolution as well as photon number do not change the conclusions drawn in this section, see discussion in Section 4.6.

[10] http://nedwww.ipac.caltech.edu

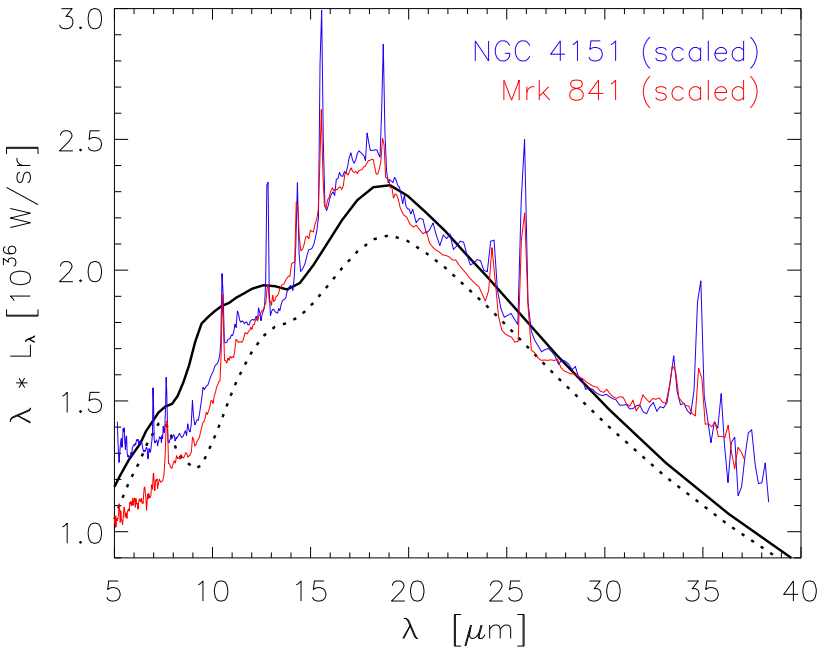

Figure 4.59: *Comparison of our standard model (solid line – $i = 0°$, dotted line – $i = 30°$) with IRS Spitzer observations of NGC 4151 (Weedman et al. 2005) and Mrk 841 (H. W. W. Spoon, private communication).*

4.8.2 Constraints from the measured X-ray HI column density silicate feature strength relation

The dusty torus mainly absorbs the optical and ultraviolet radiation from the active nucleus. As the extinction coefficients of our dust decrease shortwards and longwards of this wavelength range, the main source of opacity at shorter wavelengths (extreme UV to hard X-ray photons) is given by neutral hydrogen and neutral and singly ionised helium. This opacity is much smaller compared to the dust opacities. Therefore, a non-zero amount of X-ray photons can escape and provides thus the possibility to determine the hydrogen column density on the line of sight observationally. This is done by comparing the intrinsic AGN flux with the absorbed X-ray luminosity. A good measure for the intrinsic flux is the [O III] 5007 Å emission line, as it might be produced in the Narrow Line Region (NLR) beyond the torus opening and, therefore, is little affected by absorption within the torus. Hard X-ray photons are believed to result from a hot corona near the supermassive black hole. There, electrons reprocess low energy (UV-optical) photons from the accretion disk via Compton upscattering.

Gas and dust are distributed in slightly different ways, as can be seen in the comparison between the gas density and temperature distribution in Fig. 4.18 and Holwerda et al. (2005) point out for the case of radial dependencies in spiral galaxy disks. For the case of our hydrodynamic models, column densities are directly integrated along the line of sight. Only cells are considered, where the temperature is lower than the ionisation temperature of hydrogen. However, in our continuous models, we cannot take this into account. Therefore, we assume a constant gas-to-dust ratio of 250 (see discussion in Section 4.6), in order to calculate column densities from the continuous dust distributions.

As already discussed, we follow Shi et al. (2006) and quantify the silicate feature strength by its relative strength compared with the underlying continuum:

$$\Delta_{\mathrm{feature}} = \frac{F_{\mathrm{feat}} - F_{\mathrm{cont}}}{F_{\mathrm{cont}}}, \tag{4.31}$$

where F_{feat} is the flux within the silicate 10 μm feature and F_{cont} is the underlying continuum flux at the same wavelength. To do this, Shi et al. (2006) fit the underlying continuum with a spline to the SED-data, anchored at wavelengths between 5.0 and 7.5 μm and from 25.0 to 30.0 μm, well outside the silicate features at 9.7 μm and 18.5 μm and corresponding to the blue and red ends of the spectral range of Spitzer's Infra-Red Spectrograph (IRS). Thereby, they obtain a measure of the optical depth for the silicate emission (positive values) or absorption (negative values).

When analysing our simulations, we applied the same procedure, but changed the long wavelength range to reach up to 40.0 μm, in order to have the same number of simulated wavelengths as in the short wavelength range for the determination of the cubic spline. The value of the feature is taken at the wavelength, where the maximum distance between the spectrum and the fitted continuum is reached, as it can be appreciably shifted for the case of self-absorbed emission. Fig. 4.60 shows examples of this fitting procedure. Panel a) shows the case of a silicate emission feature, panel b) for self-absorbed emission feature and panel c) gives an example for deep silicate absorption. The 18.5 μm feature appears in emission for all three cases.

With the help of this procedure, our simulations can be compared directly to the observational data published in Shi et al. (2006). The Shi et al. (2006) sample shown in Fig. 4.61 comprises of 85 AGN of various types, for which Spitzer Infrared Spectrograph (IRS, Houck et al. 2004)

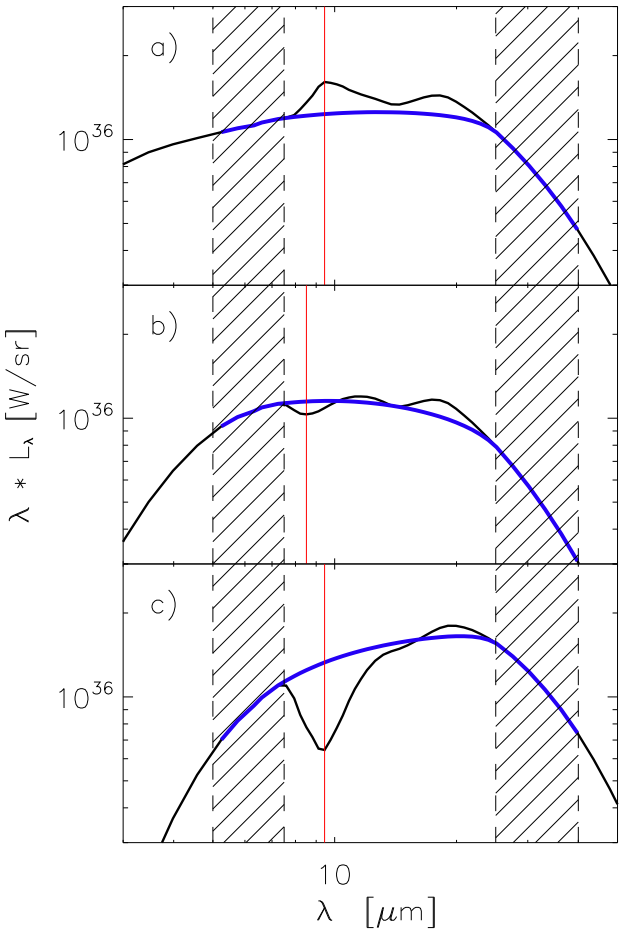

Figure 4.60: *Examples for the procedure of determining the silicate feature strength from simulated SEDs:* **a)** *a silicate feature in emission,* **b)** *a silicate feature in self-absorption and* **c)** *a silicate feature in absorption. The blue line shows the fitted cubic spline which is anchored in the hatched region and the red line denotes the position, where the feature strength is determined.*

observations or ground-based measurements from the Roche et al. (1991) sample (four objects) exist, as well as X-ray data. H I column densities are obtained from X-ray spectra taken from the Chandra data archive directly for 8 objects. For further 77 objects, column densities were collected from literature. A correlation was found between the silicate feature strength (see equation 4.31) and the X-ray absorption column density in a sense that low H I columns correspond to silicate emission and high columns correspond to silicate absorption:

$$\Delta_{\text{feature}} = 3.3 \pm 0.5 - (0.15 \pm 0.02) \cdot \log(N_{\text{H}}). \tag{4.32}$$

This is shown as the black line in Fig. 4.61. When they determine the correlation between the silicate feature strength and the X-ray column density data separately for the various types of AGN, a large scatter between them is found, as is also visible in the data ranges for each type of AGN (see Fig. 4.61). But all of them are comparable within the error ranges. Indicated in red is the correlation for Seyfert galaxies, given by:

$$\Delta_{\text{feature}} = 2.6 \pm 0.7 - (0.12 \pm 0.03) \cdot \log(N_{\text{H}}). \tag{4.33}$$

In Fig. 4.62, these correlations are compared to our simulations. The red solid line is again the linear fit to all Seyfert galaxies, and the black solid line corresponds to the whole sample of Shi et al. (2006). Colours of the symbols indicate inclination angle: blue – 0°, green – 30°, yellow – 60° and red – 90°. For the case of inclination angles without any dust along the line-of-sight, we assigned a value of $N_{\text{H}} = 10^{20}\,cm^{-2}$, taking foreground gas columns into account. Our hydrodynamic models

are given as stars, whereas the open stars correspond to our standard model and the filled stars are from the models of the supernova and mass loss rate study (compare to Section 4.7.1 and 4.7.2). The triangles denote results from our continuous TTM-model simulations. From these, we took our standard model and the models from the dust mass study (0.5, 2.0 and 4.0 times the mass of the standard model, see Section 2.3.7). Black triangles (together with one blue, green, yellow and red), belong to an inclination angle study (0°,10°,20°,30°,40°, 50°,60°,70°,80°,90° from left to right) of the TTM-model. Excluding the – somehow artificially added – values at $10^{20}\ cm^{-2}$, one can see that the hydrodynamical models agree quite well with the observed correlations, whereas the continuous models show a much to steep dependence. Although the emission features in the Seyfert I case are rather too pronounced, they are in good agreement with the two outlying galaxies NGC 7213 and PG 1351+640. Further, the silicate feature changes from emission to absorption within a very small range of column densities and it is also evident that column densities much higher than $10^{22}\ cm^{-2}$ cannot be reached, as they would cause unphysically high absorption depths of the silicate feature. A further concentration of the dust density towards the minimum of the potential within the midplane might cause a flattening of this distribution, but then, too narrow infrared bumps will be produced, see Schartmann (2003). This means that the observations presented in Shi et al. (2006) are in favour of clumpy models instead of continuous, concerning the models we investigated so far. At least, models are needed, which feature high column densities in combination with moderate emission as well as absorption features. In the hydrodynamical models presented in this thesis, this is possible due to the clumpy and filamentary nature of the dust distribution, which enables the coexistence of almost free lines of sight towards the inner region, where the silicate feature in emission is produced, together with highly obscured lines of sight. The highest column densities

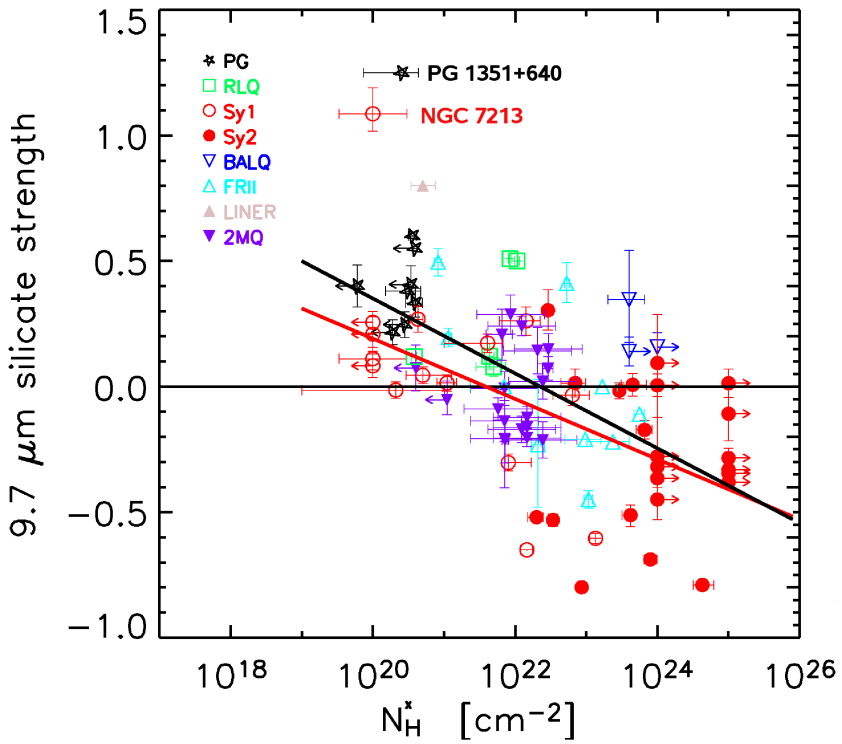

Figure 4.61: *Silicate feature strengths and X-ray column densities resulting from observational data. The various symbols refer to different types of objects. The black line indicates the linear fit to all objects, whereas the red line is fitted to Seyfert galaxies (type I and II) only. Figure courtesy of Shi et al. (2006).*

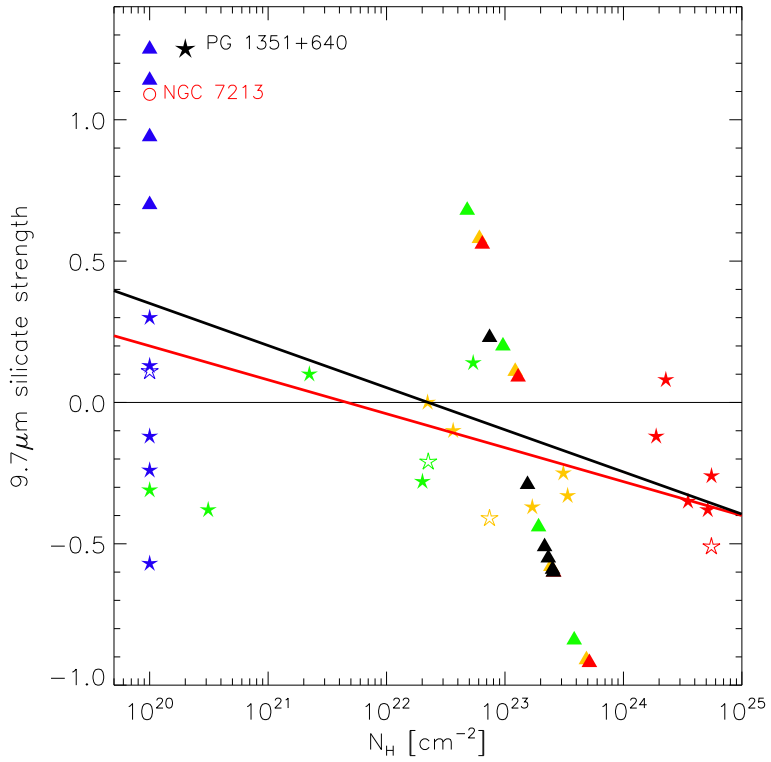

Figure 4.62: *Comparison of resulting silicate feature strengths and column densities of our hydromodels (standard model plus supernova and mass loss rate study) given as stars and the continuous TTM-models (standard model and dust mass study) given as triangles. The open stars denote our hydrodynamical standard model. Color denotes inclination angle (blue – 0°, green – 30°, yellow – 60°, red – 90°). The solid lines are linear fits to the observational data shown in Fig. 4.61 (black - all objects, red - Seyfert galaxy sample). The two outlying objects NGC 7213 and PG 1351+640 are given additionally.*

are reached for lines of sight through the dense and turbulent disk in our models. Furthermore, a remarkable consequence of this is the very tight linear correlation of the continuous models (omitting values with $N_{\mathrm{H}} = 10^{20}\,cm^{-2}$) and the broad distribution for the case of our (clumpy) hydrodynamical models. Therefore, the broad scatter in the observational data in Fig. 4.61 might really be taken as a case for clumpy models, as claimed in Shi et al. (2006). In the resolution and photon packages number study in Sect. 4.6, we find maximal deviations of the feature strength of ±0.05. These uncertainties do not change the conclusions we draw in this paragraph.

4.9 Comparison with an alternative model

Wada & Norman (2002) use an alternative approach to do global AGN torus simulations. They calculate the ISM especially in the nuclei of Seyfert galaxies with the assumption of starburst conditions. The torus scale height is supposed to be maintained by supernova type II explosions. As an initial condition, a geometrically thin, rotationally supported disk is used. Supernova type II explosions follow in situ star formation within these dense regions of the torus. Happening at a very high rate (1 SN per year within the cartesian model space of 64 × 64 × 32 pc), they are concentrated to a vertically thin layer around the midplane (SN-explosions are only allowed within

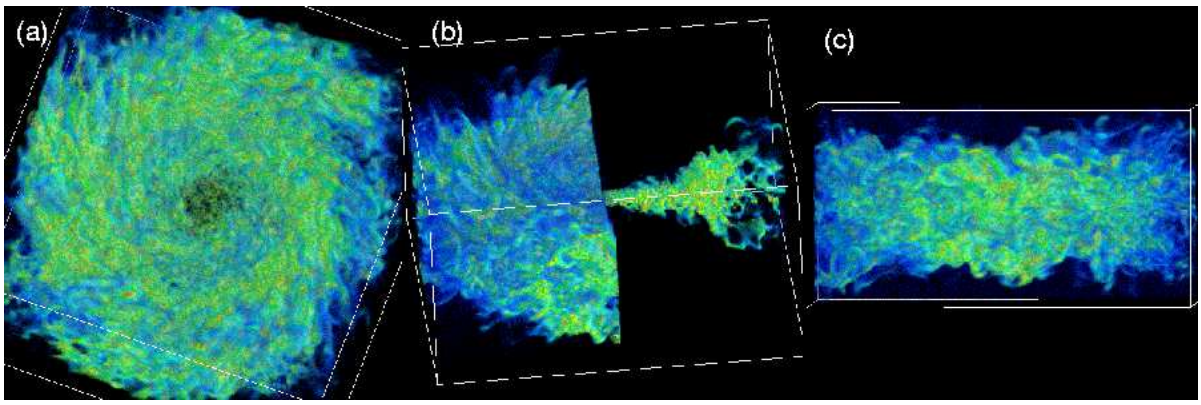

Figure 4.63: *Visualisations (volume rendering) of the 3D density distribution of the global Seyfert torus simulation done by Wada & Norman (2002). Red color represents high density regions, whereas blue color is low density gas.*

the central region for $|x|$,$|y| < 51$pc and $|z| < 4$pc). The concentration to the midplane is motivated by the fact that the gas densities are the highest there and, therefore, most of the star formation activity is expected to arise in the vicinity of the midplane. The orders of magnitude larger number of supernovae compared to our simulations leads to the evolution of smaller structures, as more supernova interactions take place, forming smaller filaments. Wada & Norman (2002) can show that the initially thin, rotationally supported disk gets puffed-up to a vertically thick torus (see Fig. 4.63), assuming the mentioned starburst conditions within the disk.

Comparing the evolving dust density distribution (Fig. 4.63) with our results, one can see that smaller structures appear on large scales, compared to our long filaments, streaming towards the central region, whereas the lack of pressure is the main driving force of these filaments towards the centre in our simulations, the filamentary structure in Wada & Norman (2002) evolves due to the violent energy input in the midplane, stirring up the dense gas disk. Also resolution effects may play a role in the outer part, as our logarithmically spaced radial grid concentrates on the inner part, whereas Wada & Norman (2002) use a cartesian grid.

In Fig. 4.64 and 4.65, the gas column densities, derived for all lines of sight of our hydrodynamic standard model and for the model of Wada & Norman (2002) are compared. In the latter, the range of column densities is much larger than in our models. Compared to observational data (see Section 4.8.2), the maximal values of our simulations are in good agreement. Missing values at the low column density end can be explained by additional material within the funnel region or in the foreground on the line of sight, which is not taken into account in our current simulations. The Wada & Norman (2002) torus seems to possess too large column densities within the midplane, which are not observed (compare to Fig. 4.61). But for the case of our simulations, it has to be taken into account that no steady state is reached and gas still accumulates in the midplane.

Such in situ star formation in the innermost parsec of spiral galaxies – as mentioned above – has been found in a part of a sample of 14 nearby (2-20 Mpc), late-type (Sbc+), edge-on spiral galaxies, observed with HST/ACS (Seth et al. 2006). They find multiple morphological stellar components in the centres with different colours, which are due to different ages of the stars. Three of the nine nuclear cluster candidates of the sample show a young stellar disk in addition to an older spheroidal component, which cannot be made by accretion of a globular cluster. Therefore, Seth et al. (2006) propose a model of ongoing nuclear cluster formation, in which stars form in a nuclear stellar disk. With ongoing time, the stars loose angular momentum and the disk converts

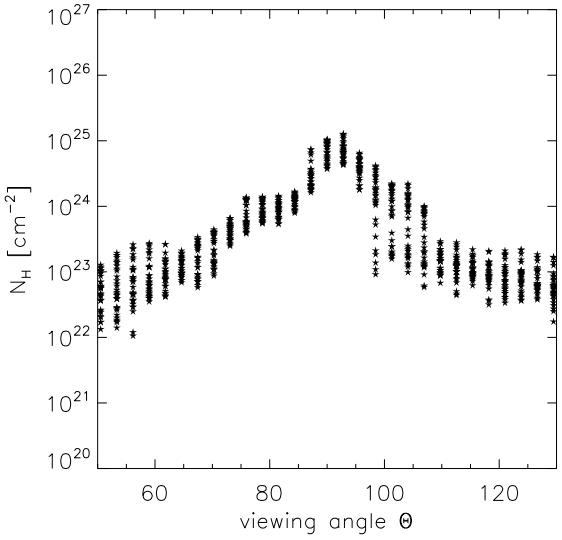

Figure 4.64: *Gas column densities as derived for our hydrodynamic standard model.*

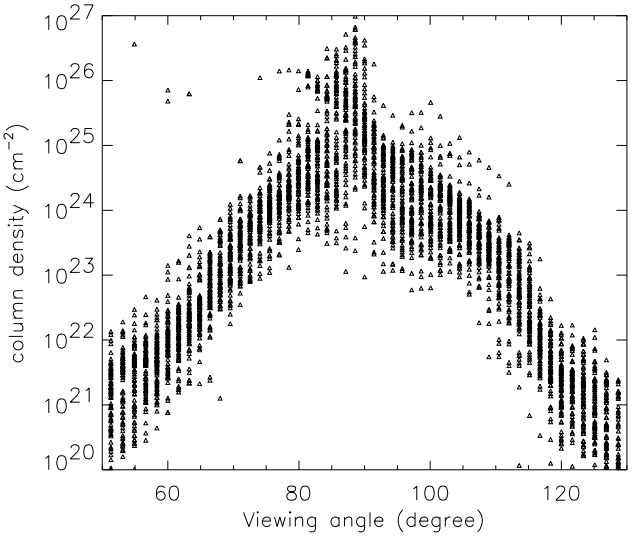

Figure 4.65: *Gas column densities as derived from the simulation done by (Wada & Norman 2002).*

into a spheroidal component.

4.10 Future work

Within this chapter, we presented a first approach towards self-consistent hydrodynamical models of gaseous AGN tori. Most important, a solution has been found, which is consistent with geometrical unification schemes and achieves similar obscuration effects compared to observations (see Section 4.8.2). Furthermore, some Seyfert I galaxy SEDs seem to be already explicable with the help of this physical model (see Section 4.8.1). Despite these promising results, it is necessary to include more physical effects in our simulations in order to overcome some problems. These main problems are accumulating mass close to the torus radius and a too small opening angle of the tori. The final goal of such simulations should be to include all of these effects, in order to attain a self-consistent picture of the evolution of gas and dust in the inner region of such nuclei. Some of these are listed in the following statement of items together with a brief discussion of the effects they are expected to cause. This can also be regarded as a TODO-list for future investigations:

① Most of the parameters we use in our simulations are constrained either by observations or by theoretical considerations. Unfortunately, some of them involve large uncertainties, like the inferred mass loss rate or the supernova rate, which is a more or less free parameter in our simulations. Especially for these two parameters, realistic population synthesis models for such a stellar cluster will help to better constrain them in future.

② Weak magnetic fields in combination with shear due to differential rotation would cause so-called magneto-rotational instability (MRI, see Balbus & Hawley 1991), which transports angular momentum and, therefore, triggers accretion towards the central region. Furthermore, enhanced magnetic pressure due to the amplification of magnetic fields can cause a

hydromagnetic outflow. According to magneto-hydrodynamical (MHD) simulations of optically thin accretion tori, a large fraction of the material accreted on large scales can be ejected within such a magnetically-driven wind. This wind will preferentially propagate within the dust-free cone of the torus and might help to broaden it. The additional magnetic pressure might even be the dominant component to the gas pressure for the case of low temperature regions (Heiles & Troland 2005; de Avillez & Breitschwerdt 2004). Furthermore, injected planetary nebulae themselves are magnetised. This first of all makes collisions between them more elastic and also causes injection of additional magnetic fields into the integration domain.

③ The next step is to include the radiation of the central accretion disk. First of all, it contributes to heating of the gas (mostly in the innermost part) and it provides an additional pressure as well. This radiation pressure will decrease the amount of matter streaming into the central cavity, but it will also power the outflow along the rotational axis, where densities are lower compared to the vertical direction. For a proper treatment, the implementation of an approximative solver of the radiative transfer equation is needed.

④ As described in Section 4.5.5, part of the gas gathers in a geometrically thin, but dense disk in the midplane, at the minimum of the potential well. Such disks are able to form stars (Nayakshin et al. 2006; Paumard et al. 2006). Though it is difficult to model this complex phenomenon, as for a self-consistent approach, the interplay between self-gravity, thermodynamics of gas and magnetohydrodynamics has to be taken into account, leading to so-called gravoturbulent fragmentation (recent reviews can be found in Larson (2003), Mac Low & Klessen (2004) or Ballesteros-Paredes et al. 2006). It is a crucial physical process, as subsequent supernova type II explosions might partly disrupt the evolving dense and geometrically thin turbulent disk in the innermost few parsec of most of our simulations. The rate of SN II in this scenario might even outnumber SN Ia explosions (see Wada & Norman 2002).

⑤ At the moment, we only consider gas in our simulations. Subsequent to our hydrodynamical simulations, a constant gas-to-dust ratio is applied, where gas temperatures are below the dust sublimation temperatures. The dust density distribution is then streamed to MC3D to do radiative transfer calculations. This assumes that gas and dust follow the same spatial distribution, which is only approximately the case. For more realistic dust distributions, a two-fluid medium (gas and dust) has to be simulated, with all interactions between them carefully taken into account.

⑥ With our serial code at hand, we are able to calculate an evolutionary period of roughly 1.2 Myrs, while typical evolutionary times of such systems are of the order of 10 to 100 Myrs. Furthermore, a domain decomposition as explained in Section 4.2.3 is needed to gain resolution. This works fine, as most of the flow is directed inwards. But a simulation of the whole computational domain for most of the evolutionary time would be desirable, but would require to speed up our code by one to two orders of magnitude.

In the outer part of our domain decomposition, mass injection is balanced by accretion of gas through the inner boundary surface. This material then assembles at the angular momentum barrier in the middle domain, where only part of it can be further accreted due to turbulent viscous processes, transporting angular momentum outwards. This is one of the major problems of our current modelling effort, which we think can be overcome by the proper inclusion of missing physical effects like magnetic fields and radiative pressure as described above.

4.11 Conclusions

We presented a physical model for the evolution of gaseous tori in Seyfert galaxies, in which stellar evolution of a young nuclear cluster triggers mass injection mainly due to planetary nebulae and injection of energy from supernova explosions. The resulting density and temperature structure of the gas is subsequently streamed to the radiative transfer code MC3D in order to obtain observables (spectral energy and surface brightness distributions), which are then compared to recent observations. Within the course of the simulations, a highly dynamical multiphase medium evolves, which is comparable to high resolution models of the supernova-driven turbulent ISM in galaxies (Breitschwerdt & de Avillez 2006; Joung & Mac Low 2006). There, blast waves from supernovae explosions sweep up the ISM by transferring kinetic energy to the gas, which leads to the subsequent formation of thin shells. These shells interact with one another and with other filaments. This, together with radiative cooling produces cold clumps. In our scenario, the ISM is constantly refilled by stellar evolutionary mass loss processes following the distribution of stars in the nuclear star cluster. Therefore, the main structuring agent of the ISM is the interplay between mass input, supernova blast waves locally sweeping away the ISM and the stream of cold gas towards the centre.
Within this scenario, cold dense clouds and filaments, where dust can exist, form naturally. The implemented optically thin cooling reduces thermal pressure and, therefore, material streams towards the minimum of the potential. This forms long radial filaments, with lots of substructure due to interaction processes. In concordance with MHD simulations of the ISM by Breitschwerdt & de Avillez (2006), we find absence of pressure equilibrium of the temperature phases within the computational domain. This is a result of supersonic motions and turbulence as well as cooling, resulting in shorter timescales compared to relaxation processes. Although no pressure equilibrium can be reached, the flow (at least in the outer part of the domain) is in a global dynamical equilibrium state. The characteristics of this equilibrium delicately depends on the driving parameters like energy input (supernova rate) and mass input rate, as well as the gravitational potential, the cooling curve and rotation. Furthermore, we find completely different velocities and streaming patterns for the various temperature phases. Whereas cold material tends to move towards the centre, the radial velocity of the hot ionised medium possesses a zero point. The inner part moves slightly inwards, whereas the outer part streams through the outer boundary of the model space, contributing to a supernova driven wind into the host galaxy. Depending on the ratio between supernova rate and mass loss rate, this zero point shifts towards smaller radii for higher ratios and towards larger radii (even beyond our outer radial boundary), when mass input dominates over supernova heating. For very high supernova-rates, we observe outflow solutions for the hot gas component, as might be expected during the initial supernova type II phase shortly after the birth of the stellar population.

Subsequent to the hydrodynamical simulations, we compute spectral energy distributions and mid-infrared images, which can then be compared to observations. A comparison with spectral energy data from the Spitzer satellite shows that already our hydrodynamical standard model (for the case of small inclination angles) describes one class of Spitzer-SEDs fairly well (see Fig. 4.59), without the necessity of any finetuning of parameters. For example the two intermediate type Seyfert galaxies NGC 4151 as well as Mrk 841 belong to this class (see Fig. 4.59). The success of the comparison with the silicate feature strength to HI column density relation for the hydrodynamical models and the failure of the tested continuous TTM-models leads to the important conclusion that the presence of a density enhancement within the equatorial plane in combination with a clumpy or filamentary structure surrounding it is needed in order to get agreement with observational data.

Otherwise, large X-ray column densities cannot simultaneously be obtained together with moderate optical depths at viewing angles within the midplane. The latter are guaranteed by almost dust-free lines of sight towards the inner part of the torus close to the funnel, where the silicate feature in emission is produced and contributes to a less pronounced silicate feature in absorption.

Since the flow pattern we observe in our simulations can already explain many features of AGN tori, we feel encouraged to implement further processes and port it to a fully parallelised MHD-code, which will then allow for detailed quantitative comparisons with observational data, especially with current mid-infrared interferometric observations (MIDI) in the range of 8 to 13 μm, which allow to resolve the inner morphology of such tori. Furthermore, we expect to overcome problems of the assembly of large amounts of mass within the turbulent disk by means of magnetic and probably radiative transfer effects. Therefore, we think that Seyfert tori appear naturally during a specific development stage of a young nuclear star cluster, if stellar evolutionary effects are taken into account.

As final goal, we plan to start the model from the formation of the nuclear star cluster (after rapid accretion of gas into the central parsec), then follow the process of a violently (that is at some 10% of the Eddington rate) accreting black hole, to later, more quiescent phases, where the lack of circum-nuclear gas starves the black hole while a new gas reservoir may build up again further out.

Chapter 5

Summary and concluding remarks

The central goal of this work was to get further understanding of the distribution of gas and dust in the inner few parsecs of Active Galactic Nuclei. This is of great interest, as the existence of a geometrically thick torus is still under debate. These circum-nuclear gas and dust *tori* are held responsible for providing the geometrical separation between type I and type II galaxies as distinguished in observations. Apart from its role in these unifying schemes, the torus is thought to provide the gas reservoir for fuelling of the central engine of these galaxies. With the advent of mid-infrared interferometry with MIDI at the VLTI we are entering an exciting phase of torus-related research, as for the first time, observations with sub-parsec resolutions are able to resolve the central dust distribution of nearby Seyfert galaxies. Even higher resolutions (well below 0.1 pc) and proper images are possible in the near-infrared with AMBER at the VLTI.

In this thesis, we presented a multi-step approach towards more realistic simulations of AGN tori. Figure 5.1 tries to visualise the three model families we considered by showing their different dust density distributions.

Model 1 used the density distribution predicted by the analytical *Turbulent Torus Model* (Camenzind 1995), which is based on astrophysical assumptions about a nuclear star cluster and the dust mass in this region (Fig. 5.1a). Mass ejection of an aging nuclear stellar cluster provides the necessary turbulent motion of gas clouds to keep the scaleheight of the torus. The gravitational potential of this cluster as well as the black hole, together with rotation form an effective potential. The density distribution (see Fig. 5.1a) results from a balance of these forces with pressure forces due to the clouds' turbulent motion, taken over from the *hot* nuclear stellar system. With the help of the 3D radiative transfer code MC3D (Wolf et al. 1999), spectral energy distributions (SEDs) and surface brightness distributions were calculated. The results of this approach are in good agreement with the gross features as well of recent large aperture observations as of high spatial resolution observations of the Circinus galaxy and NGC 1068. Furthermore, we found that the innermost part of the tori close to the central energy source is crucial for the determination of SEDs in the mid-infrared wavelength range. Therefore, any realistic model has to incorporate varying sublimation radii for different dust grain sizes and dust composition. One of the major problems, already known from previous studies of continuous tori is the strong silicate emission feature in model SEDs of face-on tori.

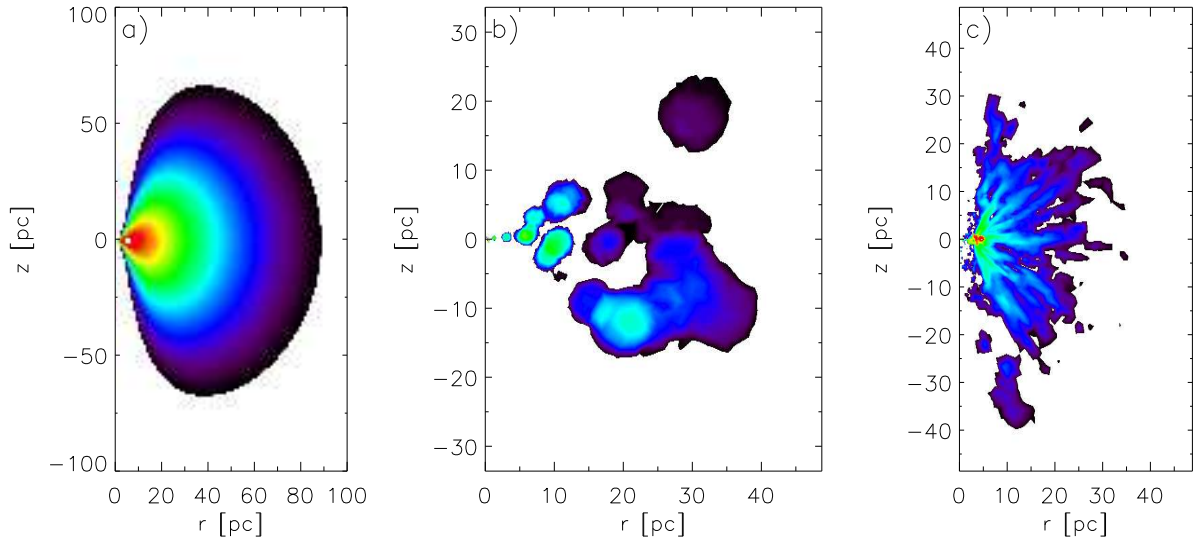

Figure 5.1: *Mean dust density distribution (averaged over* 45° *in* ϕ*) for the three model families considered so far (from left to right):* **Model 1:** *continuous density distribution as derived from an analytic Turbulent Torus Model (TTM, panel a),* **Model 2:** *clumpy torus models in which the dust clouds are distributed in a wedge-like geometry for computational reasons (b), and* **Model 3:** *fully hydrodynamic models, in which energy and mass is provided by supernovae and stellar mass loss in a young nuclear star cluster (c). Colours represent a logarithmic density scale, spanning two decades in (a), (b) and five decades in (c).*

Model 2, therefore, explored the most promising and physical solution already proposed by Krolik & Begelman (1988) to solve this conflict with the observations. Namely, to organise the dust in single clumps. To do this, we set up a three-dimensional model of the dust distribution in our MC3D simulations (see Fig. 5.1b), where clouds are randomly distributed within a wedge-like geometry. This had to be done for computational reasons, in order to gain resolution. Still, numerical effects may play a role in these kind of computations. The models show that the feature height is mainly determined by the size, distribution and optical depth of the innermost clumps of the torus. This is caused by shadowing effects of colder clouds on the line of sight. Predicted surface brightness distributions and SEDs are compared with high resolution spectral data and the very detailed interferometric MIDI observations of the Circinus galaxy.

In **Model 3** we investigated the hydrodynamical realisation of an extended version of the Turbulent Torus Model (compare left- and rightmost panel in Fig. 5.1). In these simulations, we assume that a young star cluster has emerged from a short starburst in the central region of the galaxy. The first phase of its evolution is very violent with a high rate of supernova type II detonations, where most of the gas is expected to be expelled from the nuclear region. During the further evolution, it transfers energy in form of supernovae as well as mass, mainly in form of planetary nebulae to the surrounding medium. We realise this scenario with the help of the hydrodynamics code TRAMP (Klahr et al. 1999). Energy input is provided by discrete supernova explosions, whose locations are randomly distributed, but according to the spatial distribution of stars within the cluster. The same distribution procedure is also applied for the discrete mass input in form of planetary nebulae, according to a mass loss rate given by Jungwiert et al. (2001). The ejected planetary nebulae take over the total velocity of the star, from which they were ejected, given by the stellar velocity dispersion in a randomly chosen direction plus the overlayed orbital motion. The energy input from supernovae is partly balanced by radiative cooling of the gas. With these ingredients, a multi-phase medium forms, as shown in Fig. 5.2. A large-scale filamentary structure pointing towards the torus

centre develops as a result of the interplay between infalling cool material and the concerted action of supernovae, blowing away low density material more easily than dense filaments. Looking at the temporal evolution of the simulations, the *torus* is a highly dynamical system: its densest regions can be described as a filamentary flow of material towards the centre. Where densities are high enough, optically thin radiative cooling yields very rapid temperature decrease and, therefore, dust can exist in these filaments. Consequently, they can provide the high optical depth which is required to explain the distinction between type I and type II objects. It should be noted, however, that almost *open* sight-lines towards the centre might not only exist along the torus axis, but also from other directions. A further characteristic of these kind of simulations is the formation of a geometrically thin, but optically thick disk in the midplane, close to the torus radius. It is first of all important for the comparison with observations. Furthermore, it provides a means of turbulent transport of angular momentum in our simulations due to the turbulent motion of gas within this disk. This leads to accretion towards the central black hole of up to a few percent of the EDDINGTON accretion rate. With the help of various parameter studies, we find that the existence of a torus solution mainly depends on the ratio between the supernova and the mass injection rate. The different stationary states obtained within these studies might observationally correspond to different classes of AGN. Subsequent radiative transfer calculations with our standard model yield good comparison with two SEDs of Seyfert galaxies. Furthermore, in contrast to the previously discussed continuous torus model, this new approach is able to explain the observed correlation between silicate feature strength and X-ray column density data. Despite all uncertainties and problems, this gives us some confidence that we are on the right track, although much more detailed comparisons with observational data will be required to constrain our models. We think that some of the problems might be overcome with the inclusions of further physical effects. These are namely magnetic

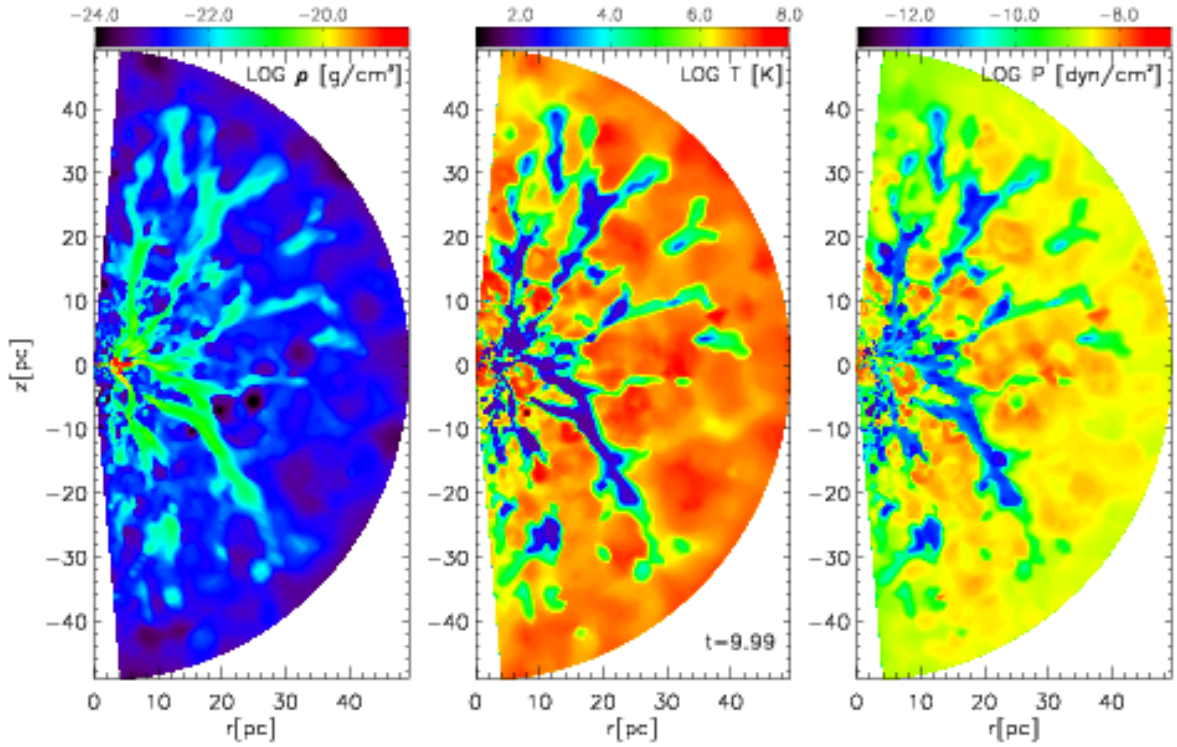

Figure 5.2: *From left to right: Density, temperature and pressure distribution of our standard hydrodynamic* **Model 3** *after an evolution of 10 orbital revolutions at a radius of 5 pc. The same meridional slice is shown in all three panels.*

fields and the radiation pressure of the central source. Additionally, with our serial code, we are limited as well in spatial resolution as in temporal evolution. Therefore, first attempts have been made to include the needed routines into a parallelised MHD code. This will enable us to gain resolution, as well as being able to calculate a longer time evolution of such tori. In future, these kind of simulations – adapted to the circumstances of individual galaxies – are necessary to be able to interpret recent and upcoming high resolution interferometric observations on sub-parsec scale with the Mid-infrared Interferometer (MIDI) or even with higher resolution (below 0.1 pc) in the near-infrared with the AMBER instrument, both at the VLTI.

Bibliography

Abbott, D. C. 1982, Astrophys. J., 263, 723

Antonucci, R. 1993, Ann. Rev. Astron. Astrophys., 31, 473

Antonucci, R. R. J. & Miller, J. S. 1985, Astrophys. J., 297, 621

Armstrong, J. W., Rickett, B. J., & Spangler, S. R. 1995, Astrophys. J., 443, 209

Avila-Reese, V. & Vázquez-Semadeni, E. 2001, Astrophys. J., 553, 645

Balbus, S. A., Gammie, C. F., & Hawley, J. F. 1994, Mon. Not. R. Astron. Soc., 271, 197

Balbus, S. A. & Hawley, J. F. 1991, Astrophys. J., 376, 214

Ballesteros-Paredes, J., Gazol, A., Kim, J., et al. 2006, Astrophys. J., 637, 384

Beckert, T. & Duschl, W. J. 2004, Astron. Astrophys., 426, 445

Bender, R., Kormendy, J., Bower, G., et al. 2005, Astrophys. J., 631, 280

Biferale, L., Lanotte, A. S., & Toschi, F. 2004, Physical Review Letters, 92, 094503

Bock, J. J., Neugebauer, G., Matthews, K., et al. 2000, The Astron. J., 120, 2904

Boehringer, H. & Hensler, G. 1989, Astron. Astrophys., 215, 147

Bohren, C. & Huffman, D. 1983, Absorption and Scattering of Light by Small Particles (New York: Wiley)

Böker, T., Laine, S., van der Marel, R. P., et al. 2002, The Astron. J., 123, 1389

Böker, T., Sarzi, M., McLaughlin, D. E., et al. 2004, The Astron. J., 127, 105

Bowyer, C. S., Field, G. B., & Mack, J. F. 1968, Nature, 217, 32

Breitschwerdt, D. & de Avillez, M. 2005, in The Magnetized Plasma in Galaxy Evolution, ed. K. T. Chyzy, K. Otmianowska-Mazur, M. Soida, & R.-J. Dettmar, 7–14

Breitschwerdt, D. & de Avillez, M. A. 2006, ArXiv Astrophysics e-prints

Bressan, A., Fagotto, F., Bertelli, G., & Chiosi, C. 1993, Astron. Astrophys. Suppl. Ser., 100, 647

Brinks, E. & Bajaja, E. 1986, Astron. Astrophys., 169, 14

Byun, Y.-I., Grillmair, C. J., Faber, S. M., et al. 1996, The Astron. J., 111, 1889

Cabot, W. & Pollack, J. B. 1992, Geophys. astrophys. fluid dyn., 64, 97

Camenzind, M. 1995, Reviews of Modern Astronomy, 8, 201

Camenzind, M. 2002/2003, Quasars and rotating Black Holes, lecture Notes WS 2002/2003, University of Heidelberg

Chevalier, R. A. 1977, Ann. Rev. Astron. Astrophys., 15, 175

Courant, R. & Friedrichs, K. O. 1948, Supersonic flow and shock waves (Pure and Applied Mathematics, New York: Interscience, 1948)

Crenshaw, D. M. & Kraemer, S. B. 2000, Astrophys. J., Lett., 532, L101

Dalgarno, A. & McCray, R. A. 1972, Ann. Rev. Astron. Astrophys., 10, 375

de Avillez, M. & Breitschwerdt, D. 2004, Astrophys. Space. Sci., 292, 207

de Avillez, M. A. & Breitschwerdt, D. 2005, Astron. Astrophys., 436, 585

de Donder, E. & Vanbeveren, D. 2003, New Astronomy, 8, 817

Draine, B. T. & Lee, H. M. 1984, Astrophys. J., 285, 89

Draine, B. T. & Malhotra, S. 1993, Astrophys. J., 414, 632

Dullemond, C. P. & van Bemmel, I. M. 2005, Astron. Astrophys., 436, 47

Elmegreen, B. G. 2005, in ASSL Vol. 329: Starbursts: From 30 Doradus to Lyman Break Galaxies, ed. R. de Grijs & R. M. González Delgado, 57

Elmegreen, B. G. & Scalo, J. 2004, Ann. Rev. Astron. Astrophys., 42, 211

Elvis, M., Wilkes, B. J., McDowell, J. C., et al. 1994, Astrophys. J., Suppl. Ser., 95, 1

Faber, S. M., Tremaine, S., Ajhar, E. A., et al. 1997a, The Astron. J., 114, 1771

Faber, S. M., Tremaine, S., Ajhar, E. A., et al. 1997b, The Astron. J., 114, 1771

Ferland, G. J. 1993, Hazy, A Brief Introduction to Cloudy 84 (University of Kentucky Internal Report, 565 pages)

Ferland, G. J., Fabian, A. C., & Johnstone, R. M. 1994, Mon. Not. R. Astron. Soc., 266, 399

Ferland, G. J., Korista, K. T., Verner, D. A., et al. 1998, Publ. Astron. Soc. Pac., 110, 761

Ferland, G. J. & Persson, S. E. 1989, Astrophys. J., 347, 656

Ferrarese, L. & Merritt, D. 2000, Astrophys. J., Lett., 539, L9

Ferziger, J. H. & Perić, M. 1996, Computational Methods for Fluid Dynamics (Berlin,New York: Springer-Verlag)

Frank, J., King, A., & Raine, D. J. 2002, Accretion Power in Astrophysics: Third Edition (Accretion Power in Astrophysics, by Juhan Frank and Andrew King and Derek Raine, pp. 398. ISBN 0521620538. Cambridge, UK: Cambridge University Press)

Freeman, K. C., Karlsson, B., Lynga, G., et al. 1977, Astron. Astrophys., 55, 445

Frisch, U. 1995, Turbulence. The legacy of A.N. Kolmogorov (Cambridge: Cambridge University Press)

Gaibler, V. 2004, Entwicklung des interstellaren Mediums in elliptischen Galaxien, diploma Thesis, Landessternwarte Heidelberg

Galliano, E., Alloin, D., Granato, G. L., & Villar-Martín, M. 2003, Astron. Astrophys., 412, 615

Gallimore, J. F. & Matthews, L. 2003, in ASP Conf. Ser. 290: Active Galactic Nuclei: From Central Engine to Host Galaxy, 501

Gebhardt, K., Bender, R., Bower, G., et al. 2000, Astrophys. J., Lett., 539, L13

Gebhardt, K., Richstone, D., Ajhar, E. A., et al. 1996, The Astron. J., 112, 105

Gerola, H., Kafatos, M., & McCray, R. 1974, Astrophys. J., 189, 55

Granato, G. L. & Danese, L. 1994, Mon. Not. R. Astron. Soc., 268, 235

Greenhill, L. J., Booth, R. S., Ellingsen, S. P., et al. 2003, Astrophys. J., 590, 162

Greenhill, L. J., Gwinn, C. R., Antonucci, R., & Barvainis, R. 1996, Astrophys. J., Lett., 472, L21

Grevesse, N. & Anders, E. 1989, in AIP Conf. Proc. 183: Cosmic Abundances of Matter, ed. C. J. Waddington, 1–8

Grevesse, N. & Noels, A. 1993, in Origin and evolution of the elements: proceedings of a symposium in honour of H. Reeves, held in Paris, June 22-25, 1992. Edited by N. Prantzos, E. Vangioni-Flam and M. Casse. Published by Cambridge University Press, Cambridge, England, 1993, p.14, ed. N. Prantzos, E. Vangioni-Flam, & M. Casse, 14

Günther, R. 2005, PhD thesis, Eberhard-Karls-Universität Tübingen

Hao, L., Spoon, H. W. W., Sloan, G. C., et al. 2005, Astrophys. J., Lett., 625, L75

Häring, N. & Rix, H.-W. 2004, Astrophys. J., Lett., 604, L89

Hawley, J. F. 2000, Astrophys. J., 528, 462

Heiles, C. 1987, Astrophys. J., 315, 555

Heiles, C. & Troland, T. H. 2003, Astrophys. J., 586, 1067

Heiles, C. & Troland, T. H. 2005, Astrophys. J., 624, 773

Henning, T. 1983, Astrophys. Space. Sci., 97, 405

Hernquist, L. 1990, Astrophys. J., 356, 359

Hollenbach, D. & McKee, C. F. 1989, Astrophys. J., 342, 306

Holwerda, B. W., González, R. A., Allen, R. J., & van der Kruit, P. C. 2005, Astron. Astrophys., 444, 101

Hönig, S. F., Beckert, T., Ohnaka, K., & Weigelt, G. 2006, Astron. Astrophys., 452, 459

Hopkins, P. F., Hernquist, L., Cox, T. J., et al. 2006, Astrophys. J., Suppl. Ser., 163, 1

Houck, J. R., Roellig, T. L., van Cleve, J., et al. 2004, Astrophys. J., Suppl. Ser., 154, 18

Hubeny, I., Agol, E., Blaes, O., & Krolik, J. H. 2000, Astrophys. J., 533, 710

Jaffe, W., Meisenheimer, K., Röttgering, H. J. A., et al. 2004, Nature, 429, 47

Jenkins, E. B. & Meloy, D. A. 1974, Astrophys. J., Lett., 193, L121

Jenkins, E. B. & Tripp, T. M. 2006, in IAU Symposium

Joung, M. K. R. & Mac Low, M.-M. 2006, ArXiv Astrophysics e-prints

Jungwiert, B., Combes, F., & Palouš, J. 2001, Astron. Astrophys., 376, 85

Kato, S. & Yoshizawa, A. 1993, Publ. Astron. Soc. Jpn., 45, 103

Kinney, A. L., Antonucci, R. R. J., Ward, M. J., Wilson, A. S., & Whittle, M. 1991, Astrophys. J., 377, 100

Klahr, H. H. 1998, PhD thesis, Friedrich-Schiller-Universität Jena

Klahr, H. H. & Bodenheimer, P. 2003, Astrophys. J., 582, 869

Klahr, H. H., Henning, T., & Kley, W. 1999, Astrophys. J., 514, 325

Kley, W. 1989, Astron. Astrophys., 208, 98

Kormendy, J. 1987, in IAU Symp. 127: Structure and Dynamics of Elliptical Galaxies, 17–34

Kraichnan, R. H. 1967, Physics of Fluids, 10, 1417

Krolik, J. H. 1999, Active galactic nuclei : from the central black hole to the galactic environment (Active galactic nuclei : from the central black hole to the galactic environment /Julian H. Krolik. Princeton, N. J. : Princeton University Press)

Krolik, J. H. & Begelman, M. C. 1988, Astrophys. J., 329, 702

Kwok, S. 2005, Journal of Korean Astronomical Society, 38, 271

Laor, A. & Draine, B. T. 1993, Astrophys. J., 402, 441

Larson, R. B. 2003, in ASP Conf. Ser. 287: Galactic Star Formation Across the Stellar Mass Spectrum, ed. J. M. De Buizer & N. S. van der Bliek, 65–80

Lauer, T. R., Ajhar, E. A., Byun, Y.-I., et al. 1995, The Astron. J., 110, 2622

Leinert, C., Graser, U., Waters, L. B. F. M., et al. 2003, in Interferometry for Optical Astronomy II. Edited by Wesley A. Traub . Proceedings of the SPIE, Volume 4838, pp. 893-904 (2003), 893–904

Leitherer, C., Schaerer, D., Goldader, J. D., et al. 1999, Astrophys. J., Suppl. Ser., 123, 3

Lynden-Bell, D. & Pringle, J. E. 1974, Mon. Not. R. Astron. Soc., 168, 603

Mac Low, M.-M. 1999, Astrophys. J., 524, 169

Mac Low, M.-M. & Klessen, R. S. 2004, Reviews of Modern Physics, 76, 125

Mac Low, M.-M., Klessen, R. S., Burkert, A., & Smith, M. D. 1998, Physical Review Letters, 80, 2754

Maciejewski, W. 2006, ArXiv Astrophysics e-prints

Maiolino, R., Marconi, A., Salvati, M., et al. 2001, Astron. Astrophys., 365, 28

Maiolino, R. & Rieke, G. H. 1995, Astrophys. J., 454, 95

Manners, J. C. 2002, PhD thesis, The University of Edinburgh

Manske, V., Henning, T., & Men'shchikov, A. B. 1998, Astron. Astrophys., 331, 52

Marco, O. & Brooks, K. J. 2003, Astron. Astrophys., 398, 101

Marigo, P., Bressan, A., & Chiosi, C. 1996, Astron. Astrophys., 313, 545

Mathews, W. G. & Brighenti, F. 2003, Ann. Rev. Astron. Astrophys., 41, 191

Mathis, J. S., Rumpl, W., & Nordsieck, K. H. 1977, Astrophys. J., 217, 425

Mayya, Y. D. & Rengarajan, T. N. 1997, The Astron. J., 114, 946

McCray, R. & Snow, Jr., T. P. 1979, Ann. Rev. Astron. Astrophys., 17, 213

McKee, C. F. 1990, in ASP Conf. Ser. 12: The Evolution of the Interstellar Medium, ed. L. Blitz, 3–29

McKee, C. F. & Ostriker, J. P. 1977, Astrophys. J., 218, 148

Meisenheimer, K., Tristram, K. R. W., Jaffe, W., et al. 2007, Astron. Astrophys., in preparation

Men'shchikov, A. B., Schertl, D., Tuthill, P. G., Weigelt, G., & Yungelson, L. R. 2002, Astron. Astrophys., 393, 867

Mignone, A., Bodo, G., Massaglia, S., et al. 2006, Astron. Astrophys., submitted

Miller, J. S., Goodrich, R. W., & Mathews, W. G. 1991, Astrophys. J., 378, 47

Navarro, J. F. & White, S. D. M. 1993, Mon. Not. R. Astron. Soc., 265, 271

Nayakshin, S., Dehnen, W., Cuadra, J., & Genzel, R. 2006, Mon. Not. R. Astron. Soc., 366, 1410

Nenkova, M., Ivezić, Ž., & Elitzur, M. 2002, Astrophys. J., Lett., 570, L9

Neugebauer, G., Green, R. F., Matthews, K., et al. 1987, Astrophys. J., Suppl. Ser., 63, 615

Norman, C. A. & Ikeuchi, S. 1989, Astrophys. J., 345, 372

Osterbrock, D. E. & Ferland, G. J. 2006, Astrophysics of gaseous nebulae and active galactic nuclei (Astrophysics of gaseous nebulae and active galactic nuclei, 2nd. ed. by D.E. Osterbrock and G.J. Ferland. Sausalito, CA: University Science Books, 2006)

Osterbrock, D. E. & Shaw, R. A. 1988, Astrophys. J., 327, 89

Padoan, P. & Nordlund, Å. 1999, Astrophys. J., 526, 279

Pascucci, I., Wolf, S., Steinacker, J., et al. 2004, Astron. Astrophys., 417, 793

Paumard, T., Genzel, R., Martins, F., et al. 2006, Astrophys. J., 643, 1011

Peng, E. W., Côté, P., Jordán, A., et al. 2006, Astrophys. J., 639, 838

Peterson, B. M. 1997, An introduction to active galactic nuclei (Cambridge, Cambridge University Press, 1997. 238 p.)

Pier, E. A. & Krolik, J. H. 1992, Astrophys. J., 401, 99

Pier, E. A. & Krolik, J. H. 1993, Astrophys. J., 418, 673

Plewa, T. 1995, Mon. Not. R. Astron. Soc., 275, 143

Plummer, H. C. 1911, Mon. Not. R. Astron. Soc., 71, 460

Poncelet, A., Perrin, G., & Sol, H. 2006, Astron. Astrophys., 450, 483

Press, W. H., Teukolsky, S. A., Vetterling, W. T., & Flannery, B. P. 1992, Numerical recipes in FORTRAN. The art of scientific computing (Cambridge: University Press, 2nd ed.)

Prieto, M. A., Maciejewski, W., & Reunanen, J. 2005, The Astron. J., 130, 1472

Prieto, M. A., Meisenheimer, K., Marco, O., et al. 2004, Astrophys. J., 614, 135

Rejkuba, M. 2004, Astron. Astrophys., 413, 903

Risaliti, G., Elvis, M., & Nicastro, F. 2002, Astrophys. J., 571, 234

Ritchmyer, R. D. & Morton, K. W. 1967, Difference methods for initial-value problems (Interscience Tracts in Pure and Applied Mathematics, New York: Interscience, 1967, 2nd ed.)

Robertson, B., Bullock, J. S., Cox, T. J., et al. 2006, Astrophys. J., 645, 986

Roche, P. F., Aitken, D. K., Smith, C. H., & Ward, M. J. 1991, Mon. Not. R. Astron. Soc., 248, 606

Rouan, D., Rigaut, F., Alloin, D., et al. 1998, Astron. Astrophys., 339, 687

Rozyczka, M. 1985, Astron. Astrophys., 143, 59

Ruiz, M., Efstathiou, A., Alexander, D. M., & Hough, J. 2001, Mon. Not. R. Astron. Soc., 325, 995

Rybicki, G. B. & Lightman, A. P. 1979, Radiative processes in astrophysics (New York, Wiley-Interscience, 1979. 393 p.)

Sanders, D. B., Phinney, E. S., Neugebauer, G., Soifer, B. T., & Matthews, K. 1989, Astrophys. J., 347, 29

Scalo, J. 1990, in ASSL Vol. 160: Windows on Galaxies, ed. G. Fabbiano, J. S. Gallagher, & A. Renzini, 125

Scalo, J. 1998, in ASP Conf. Ser. 142: The Stellar Initial Mass Function (38th Herstmonceux Conference), ed. G. Gilmore & D. Howell, 201

Scalo, J. & Elmegreen, B. G. 2004, Ann. Rev. Astron. Astrophys., 42, 275

Schartmann, M. 2003, Modelle für Staubtori in Aktiven Galaktischen Kernen, diploma Thesis, MPIA Heidelberg

Schartmann, M., Meisenheimer, K., Camenzind, M., Wolf, S., & Henning, T. 2005, Astron. Astrophys., 437, 861

Sedov, L. I. 1959, Similarity and Dimensional Methods in Mechanics (Similarity and Dimensional Methods in Mechanics, New York: Academic Press, 1959)

Seth, A. C., Dalcanton, J. J., Hodge, P. W., & Debattista, V. P. 2006, ArXiv Astrophysics e-prints

Shi, Y., Rieke, G. H., Hines, D. C., et al. 2006, ArXiv Astrophysics e-prints

Siebenmorgen, R., Haas, M., Krügel, E., & Schulz, B. 2005, Astron. Astrophys., 436, L5

Sodroski, T. J., Bennett, C., Boggess, N., et al. 1994, Astrophys. J., 428, 638

Stolte, A., Brandner, W., Grebel, E. K., Lenzen, R., & Lagrange, A.-M. 2005, Astrophys. J., Lett., 628, L113

Stolte, A., Grebel, E. K., Brandner, W., & Figer, D. F. 2002, Astron. Astrophys., 394, 459

Stone, J. M. & Balbus, S. A. 1996, Astrophys. J., 464, 364

Stone, J. M., Mihalas, D., & Norman, M. L. 1992, Astrophys. J., Suppl. Ser., 80, 819

Stone, J. M. & Norman, M. L. 1992a, Astrophys. J., Suppl. Ser., 80, 753

Stone, J. M. & Norman, M. L. 1992b, Astrophys. J., Suppl. Ser., 80, 791

Stone, J. M., Ostriker, E. C., & Gammie, C. F. 1998, Astrophys. J., Lett., 508, L99

Sturm, E., Schweitzer, M., Lutz, D., et al. 2005, Astrophys. J., Lett., 629, L21

Sullivan, M., Le Borgne, D., Pritchet, C. J., et al. 2006, Astrophys. J., 648, 868

Sutherland, R. S. & Dopita, M. A. 1993, Astrophys. J., Suppl. Ser., 88, 253

Thacker, R. J. & Couchman, H. M. P. 2001, Astrophys. J., Lett., 555, L17

Thatte, N., Quirrenbach, A., Genzel, R., Maiolino, R., & Tecza, M. 1997, Astrophys. J., 490, 238

Thornton, K., Gaudlitz, M., Janka, H.-T., & Steinmetz, M. 1998, Astrophys. J., 500, 95

Tomisaka, K. 1992, Publ. Astron. Soc. Jpn., 44, 177

Tomisaka, K. & Ikeuchi, S. 1986, Publ. Astron. Soc. Jpn., 38, 697

Toro, E. F. 1997, Riemann solvers and numerical methods for fluid dynamics: a practical introduction (Berlin, Springer-Verlag, 1997. 592 p.)

Tristram, K. R. W., Meisenheimer, K., Jaffe, W., et al. 2007, Astron. Astrophys., in preparation

Tuthill, P. G., Men'shchikov, A. B., Schertl, D., et al. 2002, Astron. Astrophys., 389, 889

Urry, C. M. & Padovani, P. 1995, Publ. Astron. Soc. Pac., 107, 803

van Bemmel, I. M. & Dullemond, C. P. 2003, Astron. Astrophys., 404, 1

van Leer, B. 1977, Journal of Computational Physics, 23, 276

Vanden Berk, D. E., Richards, G. T., Bauer, A., et al. 2001, The Astron. J., 122, 549

Vázquez, G. A. & Leitherer, C. 2005, Astrophys. J., 621, 695

Veilleux, S., Cecil, G., & Bland-Hawthorn, J. 2005, Ann. Rev. Astron. Astrophys., 43, 769

Vollmer, B., Beckert, T., & Duschl, W. J. 2004, Astron. Astrophys., 413, 949

von Weizsäcker, C. F. 1951, Astrophys. J., 114, 165

Wada, K. & Norman, C. A. 2002, Astrophys. J., Lett., 566, L21

Walcher, C. J., Häring, N., Böker, T., et al. 2004, in Coevolution of Black Holes and Galaxies

Ward, M. 2003, Active Galactic Nuclei, lecture held at the international school on *Black Holes in the Universe* in Cargèse (France)

Weedman, D. W., Hao, L., Higdon, S. J. U., et al. 2005, Astrophys. J., 633, 706

Weidemann, V. 1990, Ann. Rev. Astron. Astrophys., 28, 103

Weidemann, V. 2000, Astron. Astrophys., 363, 647

Weidner, C. & Kroupa, P. 2006, Mon. Not. R. Astron. Soc., 365, 1333

Weinberger, R. & Kerber, F. 1997, Science, 276, 1382

Weingartner, J. C. & Draine, B. T. 2001, Astrophys. J., 548, 296

Williams, L. L. R., Babul, A., & Dalcanton, J. J. 2004, Astrophys. J., 604, 18

Wilson, A. S., Braatz, J. A., Heckman, T. M., Krolik, J. H., & Miley, G. K. 1993, Astrophys. J., Lett., 419, L61

Wolf, S. 2001, PhD thesis, Friedrich-Schiller-Universität Jena

Wolf, S. 2003a, Astrophys. J., 582, 859

Wolf, S. 2003b, Computer Physics Communications, 150, 99

Wolf, S. & Henning, T. 1999, Astron. Astrophys., 341, 675

Wolf, S. & Henning, T. 2000, Computer Physics Communications, 132, 166

Wolf, S., Henning, T., & Stecklum, B. 1999, Astron. Astrophys., 349, 839

Woo, J. & Urry, C. M. 2002, Astrophys. J., 579, 530

Woosley, S. E. & Weaver, T. A. 1986, Ann. Rev. Astron. Astrophys., 24, 205

York, D. G. 1974, Astrophys. J., Lett., 193, L127

Yungelson, L. R. & Livio, M. 2000, Astrophys. J., 528, 108

Zhao, H. 1997, Mon. Not. R. Astron. Soc., 287, 525

Zheng, W., Kriss, G. A., Telfer, R. C., Grimes, J. P., & Davidsen, A. F. 1997, Astrophys. J., 475, 469

Zuckerman, B. & Palmer, P. 1974, Ann. Rev. Astron. Astrophys., 12, 279

Appendix A

The interstellar medium (ISM) and its theoretical description

All of our current knowledge about the interstellar medium (ISM) results either from observations of our direct vicinity, neighbouring galaxies or simulations. As the gas and dust composition of our objects is not directly accessible via observations, we have to set up our models in concordance with their findings.

According to observations, the ISM is highly turbulent with a Reynolds number of the order of 10^6 (de Avillez & Breitschwerdt 2005) and a Kolmogorov velocity spectrum in the gas over more than six orders of magnitude in length (Armstrong et al. 1995), which can be deduced from the electron density spectrum in the warm ionised medium. Furthermore, supra-thermal emission linewidths of giant molecular clouds (Zuckerman & Palmer 1974) in the ISM point towards supersonic random motions in this gas. Thus, the ISM can be described as a non-linear system, where complex phenomena can be seen, like phase transitions or the maintainance of a clumpy and filamentary structure made out of cold and warm gas and dust, formed by these highly turbulent flows. The main ingredients of this medium are gas in various temperature regimes, dust, magnetic fields and cosmic rays. Turbulent flows are kept alive by supernova explosions, stellar winds and stellar illumination. For the case of AGN tori, an additional contribution arises from the intense radiation of the central accretion disk and further AGN-related effects (see Section 1).

Active research on the ISM began after the discovery of the hot part of the ISM with the Copernicus satellite. These observations showed a diffuse, wide-spread O VI resonance line doublet in absorption towards background stars (Jenkins & Meloy 1974; York 1974). Following-up observations of diffuse soft X-ray emission below 2 keV (Bowyer et al. 1968), it was found that most of the emission below 0.5 keV must be mainly thermal emission of a hot plasma ($2 \cdot 10^5\,\mathrm{K} \leq T \leq 2 \cdot 10^6\,\mathrm{K}$), identified as the *Hot Ionised Medium* (HIM).

From the theoretical side, von Weizsäcker (1951) already proposed a model, which is still in concordance with our current knowledge. According to it, turbulence is stirred on large scales by differential rotation of the galaxies. This supersonic turbulence produces shock waves, which interact and form clouds. As the clouds move turbulently, they disperse quickly. The first coherent and global model was established by McKee & Ostriker (1977) (see also McKee 1990). According to it, the ISM is made up of three phases in pressure equilibrium, regulated by supernova explo-

sions. Physical reactions like radiative cooling, heat conduction, photoionisation and evaporation can transform one phase into one another. In this sense, the term *phase* denotes a stable branch in the $p - T$-diagram and thereby differs from the less strict definition we use, where it describes simply a certain range in temperature, as defined in Section 4.5.4. Independent from the inclusion of magnetic fields or not, supersonic turbulence – given as an initial condition – is found to decay on short timescales (often within a sound crossing time) in simulations of an isothermal or an adiabatic medium (Stone et al. 1998; Mac Low et al. 1998; Padoan & Nordlund 1999). Hence, constant stirring is needed. In the pioneering simulations, this was included uniformly distributed over the box in a narrow wave number range (so-called *Fourier forcing*), as e. g. done in Mac Low (1999). Recent simulations use so-called *discrete physical space forcing* in three dimensions, as decaying and forced regimes coexist within the ISM (Avila-Reese & Vázquez-Semadeni 2001) and it was shown that the resulting ISM structure in earlier simulations delicately depends on the forcing function (e. g. Biferale et al. 2004). Further, it is necessary to study turbulent flows in three dimensions. In 2D an inverse cascade of energy towards large scales occurs, as vortices merge to form larger ones. This is in contradiction to the 3D scenario (Kolmogorov turbulence), where the enstrophy (square of vorticity) decreases towards small scales (Kraichnan 1967; Frisch 1995). For a very detailed review of interstellar turbulence, see Elmegreen & Scalo (2004) and Scalo & Elmegreen (2004).

Most of the recent very detailed 3D simulations of the turbulent interstellar medium (ISM) are conducted in a small box within galactic disks, as for the detailed simulation of turbulence, very high spatial resolution is needed. Furthermore, this enables direct comparison of the results with observational studies. There, the gas distribution possesses lower gas densities as well as a different gravitational set-up compared to the direct environment of the nuclear galactic region we are simulating. Nonetheless, these simulations provide some of the know-how of discrete energy input due to supernova explosions, cooling in these media and other physical effects.

In these recent simulations, constant stirring is given by supernova explosions. This is needed to keep up the shear flows of large scale streams, which are thought to be the main reason for interstellar turbulence. Recent 3D simulations were done by Joung & Mac Low (2006), including vertical stratification (within the galactic disk), isolated and clustered supernovae (due to OB associations), cooling and background heating by surrounding stars, etc. Other simulations (de Avillez & Breitschwerdt 2005; Breitschwerdt & de Avillez 2005) additionally include magnetic fields and differ in some more details like cooling functions, background heating, etc. All of these simulations pos-

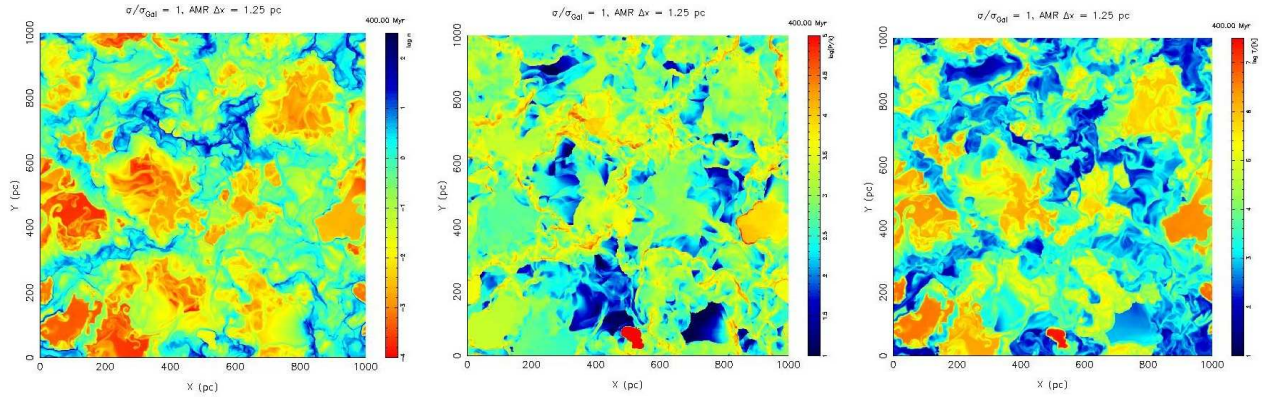

Figure A.1: *High resolution simulations of the ISM done by Breitschwerdt & de Avillez (2006): two-dimensional cuts through the 3D data cube. Shown are from left to right the number density n, the pressure P/k_B and the temperature T within the galactic plane in logarithmic scaling.*

sess very fine resolution and find qualitatively similar results: The observed clumpy and filamentary structure is recovered, although differences in the quantitative distribution of e. g. the temperature phases appear. This is due to the incorporation of different physical effects like self-gravity or magnetic fields.

The main results of these simulations can be summarised as follows (compare to Fig. A.1):

① The observed clumpy and filamentary structure can be recovered. Supernova-driven turbulence is the main structuring agent in these simulations by transferring kinetic energy to the ISM. In this picture, cold dense clouds and filaments form by colliding blast waves, which sweep up the ISM. The region in between is filled with hot but low density gas.

② Due to the density stratification, the gravitational field and the concerted action of supernovae, a global circulation (*galactic fountain*) develops, where hot gas streams away from and cold clumps fall back onto the midplane. This is a means for transferring hot gas from the galactic midplane into the halo. Thereby, it helps to bridge the discrepancy between observed and earlier simulated volume filling fractions of the temperature phases.

③ Simulations are roughly consistent with observed mass fractions and filling factors of different temperature phases. Deviations from observations can be seen in the vertical density profile. Too much gas is concentrated to the midplane, which they claim is caused by neglected pressure from magnetic fields and cosmic rays (Joung & Mac Low 2006).

④ High supernova rates lead to galactic outflows, which have been observed as well (for a recent review see Veilleux et al. 2005).

Appendix B

Additional material

Additional visualisations in form of animations of the density and temperature distributions of the evolution of the simulations as well as an electronic version of this thesis are provided on a DVD, together with additional parameter studies, not discussed in this thesis. An overview is given in start.html in the root directory of the DVD.

List of Figures

List of Tables

Acknowledgement

First of all, I would like to thank my supervisor Prof. Dr. Klaus Meisenheimer for giving me the possibility to work on this fascinating topic as well as all the discussion and friendly advice. I am also very grateful to Prof. Dr. Max Camenzind, Dr. Hubert Klahr, Dr. Sebastian Wolf and Prof. Dr. Thomas Henning, who guided my way during the last years with fruitful discussions and advice and helped me to get around the pitfalls of radiative transfer as well as hydrodynamical modelling. Furthermore, I would like to thank Prof. Dr. Hans-Walter Rix and Prof. Dr. Thomas Henning for giving me the opportunity to carry out this work at the Max-Planck-Institut für Astronomie. Furthermore, I am very thankful to Prof. Dr. Ralf Klessen for the appraisal of this thesis.

In addition to this, many people contributed in various ways to the final form of this thesis work. I am very grateful to (in random listing):

- The *AGN-connection*: Nadine Neumayer, Almudena Prieto and Konrad Tristram for discussion about AGN physics beyond dusty rings. Konrad also for advice and his routines to calculate visibilities from my simulations, sharing his expertise in MIDI interferometry and proof-reading of part of this thesis.
- Stefan Umbreit for constant advice and solutions for all computer- and numerics-related problems and his patience with me.
- The members of the theory group of Max Camenzind, especially Volker Gaibler, Steffen Brinkmann and Bernhard Keil for sharing their numerical and hydrodynamical expertise with me.
- My former and current office mates: Vernesa Smolčić, Jutta Stegmaier, Konrad Tristram, Stefan Umbreit, Stephan Birkmann, Ernest Krmpotic, Ulrich Klaas and the whole Elsässer laboratory for help, advice and distraction.
- Richard Wünsch and collaborators for the cooling function.
- Anders Johansen for his introduction into and the parameter file for the mpeg_encode routine to produce animations from a stack of images and for his introduction to the PIA-cluster.
- Kees Dullemond and Alexander Schegerer for many discussions on radiative transfer related problems.
- Henrik W. W. Spoon for his reduced Spitzer SEDs of Seyfert galaxies and discussion.
- Everybody who contributes to the exciting atmosphere of the MPIA.
- G.-L. Granato and S. F. Hönig for providing one of their radiative transfer models to compare to my simulations.
- All of my friends for encouraging words, distraction and enriching my social life outside the institute.

Last but not least I would like to thank my family who supported and encouraged me during my whole education so far. Thank you very much!